Electrodynamics of the Plasma Environment Induced Around Spacecraft in Low Earth Orbit: Three-dimensional Theory and Numerical Modeling

by

Nikolaos Achilleas Gatsonis

Ptychion Physics, Aristotelian University of Thessaloniki, 1983
M.S. Atmospheric Science, The University of Michigan, 1986
S.M. Aeronautics and Astronautics, Massachusetts Institute of Technology, 1987

SUBMITTED TO THE DEPARTMENT OF
AERONAUTICS AND ASTRONAUTICS
IN PARTIAL FULFILLMENT OF THE
REQUIREMENTS FOR THE DEGREE OF

Doctor of Philosophy

at the

Massachusetts Institute of Technology

September 1991

© Massachusetts Institute of Technology 1991. All rights reserved

Signature of Author ______________________________
Department of Aeronautics and Astronautics
June 1991

Certified by ______________________________
Professor Daniel E. Hastings
Thesis Supervisor, Department of Aeronautics and Astronautics

Certified by ______________________________
Dr. Tom Chang
Center for Space Research

Certified by ______________________________
Professor Mark Drela
Department of Aeronautics and Astronautics

Certified by ______________________________
Professor Manuel Martinez-Sanchez
Department of Aeronautics and Astronautics

Accepted by ______________________________
Professor Harold Y. Wachman
Chairman, Department Graduate Committee

MASS. INST. TECH.
SEP 24 1991

Electrodynamics of the Plasma Environment Induced Around Spacecraft in Low Earth Orbit: Three-dimensional Theory and Numerical Modeling

by

Nikolaos Achilleas Gatsonis

Submitted to the Department of Aeronautics and Astronautics on June 28, 1991
in partial fulfillment of the requirements for the degree of
Doctor of Philosophy in Physics of Fluids and Plasmas

Abstract

A study is presented of the electrodynamic interactions within the plasma environment induced around spacecraft in Low Earth Orbit. A fully three-dimensional theory and a computational model is developed for an artificial plasma cloud created by spacecraft with the potential of releasing neutrals and/or plasma into the ambient ionosphere.

A fluid model for the plasma transport is derived. The forces included in the momentum balance are due to electric fields, pressure, gravity, drag due to collisions and perturbative inertia terms. Generalized transport coefficients are derived. The equation for the perturbation electric field due to the presence of the plasma cloud is obtained. An analysis of boundary conditions is presented. The current closure with the use of a layer model is investigated; both Pedersen and inertia transverse currents are considered and the mapping process of the electric field is examined. The problem of Alfvén waves emitted by a moving plasma cloud is addressed. The relative contributions to the current closure of the Pedersen and the wave conductivities are discussed.

The numerical solution of the model equations is presented. The Flux Corrected Transport (FCT) scheme is used for the numerical solution of the hyperbolic continuity equations. This approach limits the artificial dissipation or dispersion arising in the numerical solution. The 3D-FCT algorithm, and the stability characteristics of the high and low order schemes used in the FCT are discussed. A computational example of a 3D wave convection demonstrates the ability of the 3D-FCT. The equation for the electrostatic potential is a three-dimensional nonself-adjoint elliptic equation with highly dissimilar coefficients. The numerical solution of the resulting large, sparse, asymmetric system of equations is discussed.

Initial time numerical simulations are performed. A water-bag plasma cloud model is used to demonstrate the current coupling process. The electrodynamics of Gaussian-like plasma clouds in the presence of a neutral cloud is examined. The effects of diffusion and the applied neutral wind are discussed. Releases which are stationary in the Earth frame or releases with neutral densities lower than the ambient result in plasma clouds which rotate slowly around the magnetic field while expanding quickly along it. For neutral densities higher than the ambient the plasma cloud develops a transverse drift of the order of the orbital velocity.

Simulations of typical spacecraft operations, such as thruster firings or effluent dumps, are performed and the created water plasma cloud is studied. It is shown that for time scales of interest in contamination studies the flow of neutrals is in the free molecular regime. The effects of altitude of the release, orientation of the thrust vector with regard to the magnetic field, and latitude are considered. It is shown that a large water ion cloud is formed with densities of the order of the ambient oxygen ions. It is predicted that the ambient oxygen forms depletion and enhancement regions. The electrostatic "snow-plow" effect, as well as the mapping of the electric field to other regions of the ionosphere, is demonstrated. The ambient plasma density is perturbed and forms "image" clouds. The ultraviolet radiation emission is shown to modify the signature of the spacecraft. It is argued that the model predicts qualitatively most of the observations. Quantitatively predictions are within the measured levels. Based on the model predictions several recommendations with regard to the design and operation of spacecraft are presented.

Thesis Supervisor: Professor Daniel E. Hastings
Title: Associate Professor of Aeronautics and Astronautics

Acknowledgements

I wish to express my graditude to everyone who has helped me in this endeavor. Most of all, I would like to thank my advisor Prof. Daniel Hastings. His encouragement, advice and enthusiasm made the time spent during my graduate studies at MIT most enjoyable. He has provided his inspiration, guidance and ideas over the years; his contribution to this work and my education in general will be always remembered and appreciated.

My sincere appreciation is extented to the members of my thesis committee for their willingness to share both their time and advice. Dr. Tom Chang of the Center for Space Research at MIT for his ideas and encouragement. Prof. Mark Drela for remaining a valuable source of advice in the numerical aspects of this work. Prof. Manuel Martinez-Sanchez for his critical comments and suggestions.

I would like to thank my thesis readers who graciously donated their time, Prof. Leon Trilling and Dr. David Cooke at the Phillips Laboratory. Thanks to Prof. Judson Baron for his interest in my work and education.

Thanks are due to all of my fellow students at the Space Power and Propulsion Laboratory. They have been a good company and valuable source of learning. David, Jong, Mengu, and Robie; Rodger and Eli, who deserve special thanks for keeping the computers running, Eric, and Damon; Knox who has been a fine company. I will miss my friends *Νικηφορος*, *Γιωργος* and *Γερασιμος*. To all of my friends outside school.

This work was partially supported by a Lockheed grant.

The biggest support came from my family, mother, *Κωστας*, *Μυρτω*, and most especially from *Μαρια*.

This work is dedicated to the memory of my father *Αχιλλεας*.

Contents

1 Introduction **18**

1.1 The LEO Ambient Space Environment 22

1.2 Spacecraft Induced Environment: A Review 26

1.3 Plasma Clouds in the Ionosphere : A Review 30

1.3.1 Plasma Clouds from Release Experiments 31

1.3.2 Plasma Clouds about Spacecraft 36

1.3.3 3-D Plasma Cloud Models 37

1.4 Research Approach 41

2 Fluid Model for the Plasma Motion **44**

2.1 Continuity and Momentum Equations 44

2.2 Solution of the Momentum Equation 48

2.2.1 The Correction to the Velocity due to Inertia 49

2.3 Perpendicular Plasma Motion 49

2.3.1 Electron Perpendicular Flow 49

2.3.2 Ion Perpendicular Flow 50

2.4 Parallel Plasma Motion 54

2.5 Collision Processes 57

2.5.1 Collisions between Charged Particles 57

2.5.2 Ion-Neutral Collisions 58

2.5.3 Electron-Neutral Elastic Collisions 61

2.5.4 Ambient Collision Frequencies 62

3 Electric Currents **64**

3.1 Current Balance 64

3.1.1 Equation for the Current Balance 69

3.2 Current Closure - Boundary Conditions 70

3.3 Current Closure with a Layer Model 74

3.3.1 Transverse Pedersen Current 74

3.3.2 Transverse Pedersen Currents and Alfvén Waves 78

3.3.3 Pedersen and Diffusion Currents 86

3.4 Generalized Charge Conservation Equation 88

4 Numerical Methods **92**

4.1 Numerical Solution of 3-D Hyperbolic Systems 92

4.1.1 3-D Flux-Corrected Transport 95

4.1.2 High Order Scheme 97

4.1.3 Low Order Algorithm: Donor Cell 100

4.1.4 A 3-D Computational Example 102

4.2 Numerical Solution of 3-D Elliptic Equations 107

4.2.1 Discrete Potential Equation 107

4.2.2 Solution of Sparse, Asymmetric Systems 112

5 3-D Current Closure: Initial Time Simulations **115**

5.1 Grid Configuration - Frames of Reference 116

5.2 Uniform Plasma Cloud 117

5.3 Nonuniform Plasma Cloud 125

5.3.1 Initial Conditions 125

5.3.2 The Unperturbed Electric Fields 125

5.3.3 3-D Diffusion in the Absence of Neutral Wind 128

5.3.4 3-D Diffusion with Unidirectional Neutral Wind 131

6 Neutral Flow Model **149**

6.1 Neutral Gas Releases in a Rarefied Background 149

6.1.1 Free Molecular Flow from a Pulsed Source 151
6.1.2 Diffusive Flow from a Pulsed Source 155
6.2 Neutral Flow from a Continuum Source 157

7 Induced Plasma Environment: Numerical Simulations 158
7.1 The Origin of the Contaminant Cloud 158
7.2 Chemistry within the Induced Environment 160
7.2.1 Implications of Chemistry on Numerical Stability 162
7.3 Radiation within the Induced Environment 164
7.4 Thruster Firings from Spacecraft 165
7.4.1 Altitude of $h = 250$ km 167
7.4.2 Altitude of $h = 450$ km 173
7.5 Release of Neutrals at Orbital Speeds 194
7.5.1 Altitude of $h = 250$ km 194
7.6 Conclusions - Comparisons with Data 199

8 Conclusions 208
8.1 Review of Findings 208
8.1.1 Contribution to Theory 208
8.1.2 Contributions to Numerical Modeling 212
8.1.3 Contributions to Applications - Theory 214
8.2 Recommendations for Spacecraft Operations 218
8.3 Recommendations for Further Research 219

A Description of the Computer Code 222
A.1 Flow Chart of the Code 222
A.2 Functional Description of Subroutines 223

List of Figures

1.1 Neutral density composition of the ionosphere. 24

1.2 Electron density for the daytime and nighttime ionosphere. 24

1.3 Ion composition of the ionosphere. 25

1.4 Neutral, Ion and Electron temperature of the ionosphere. 25

2.1 Fixed to earth and the field aligned system. 45

2.2 Ambient ionospheric collision frequencies 63

3.1 Ambient ionospheric conductivities 71

3.2 Bounding regions of the ionosphere 73

3.3 Layer model with a plasma cloud in applied electric and magnetic fields. 75

3.4 Stationary Alfvén waves about a moving conductor. 79

3.5 The Alfvén interaction length. 84

3.6 The ratio of $\Sigma^{\circ}_{bP}/\Sigma^{\circ}_{W}$ 84

3.7 Layer model for a plasma cloud under diffusion 87

4.1 Grid configuration used in the finite differencing of hyperbolic equations 94

4.2 Initial conditions for 3-D wave propagation example. 103

4.3 Low-order numerical solution for 3-d wave propagation 104

4.4 High-order numerical solution for 3-d wave propagation 105

4.5 FCT numerical solution for 3-d wave propagation 106

4.6 Grid configuration used in the finite differencing of the elliptic type of equation. 108

4.7 Grid configuration near a boundary. 111

5.1 Computational domain for a typical simulation. 118

5.2 Moving and stationary frame. 118

5.3 Conducting plasma sphere in applied $\mathbf{E_o}$ and $\mathbf{B}$ fields. 119

5.4 Plasma sphere:Electric and Velocity field 120

5.5 Shielding factor of a plasma sphere. 122

5.6 Parallel conductivity effects 123

5.7 The three-dimensional potential distribution of a plasma sphere. 124

5.8 Ambient electric field. 127

5.9 Potential on a midplane parallel to $\mathbf{B}$. Simulation parameters are: $h =$ 256 km, $N^o_{H_2O+} = 10^{12}$ m^{-3}, no neutral wind. 136

5.10 Analytical and numerical potential along $\mathbf{B}$. Simulation h= 256 km, $N^o_{H_2O+} = 10^{12}$ m^{-3}, no applied neutral wind. 136

5.11 Velocity of released ions on transverse to $\mathbf{B}$ planes. Simulation parameters are: $h = 256$ km, $N^o_{H_2O+} = 10^{12}$ m^{-3}, no neutral wind. 137

5.12 Velocity of ambient ions on transverse to $\mathbf{B}$ plane. Simulation parameters are: $h = 256$ km, $N^o_{H_2O+} = 10^{12}$ m^{-3}, no neutral wind. 138

5.13 Velocity of electrons, ambient and released ions on parallel to $\mathbf{B}$ planes. Simulation parameters are: $h = 256$ km, $N^o_{H_2O+} = 10^{12}$ m^{-3}, no neutral wind. 139

5.14 Potential on transverse to $\mathbf{B}$ planes. Simulation parameters are: $h =$ 256 km, $N^o_{H_2O} = 10^{14}$ m^{-3}, $N^o_{H_2O+} = 10^{11}$ m^{-3}, $\mathbf{U}_{H_2O} = -8\mathbf{x}$ km/s . . . 140

5.15 Velocity of released ions on transverse to $\mathbf{B}$ planes. Simulation parameters: $h = 256$ km, $N^o_{H_2O} = 10^{14}$ m^{-3}, $N^o_{H_2O+} = 10^{11}$ m^{-3}, $\mathbf{U}_{H_2O} = -8\mathbf{x}$ km/s. 141

5.16 Potential and velocity of the released ions on parallel to $\mathbf{B}$ midplane. Simulation parameters: $h = 256$ km, $N^o_{H_2O} = 10^{14}$ m^{-3}, $N^o_{H_2O+} = 10^{11}$ m^{-3}, $\mathbf{U}_{H_2O} = -8\mathbf{x}$ km/s. 142

5.17 Potential on transverse to $\mathbf{B}$ planes. Simulation parameters: $h = 256$ km, $N^o_{H_2O} = 10^{18}$ m^{-3}, $N^o_{H_2O+} = 10^{13}$ m^{-3}, $\mathbf{U}_{H_2O} = -8\mathbf{x}$ km/s. 143

5.18 Velocity of released ions on transverse to **B** planes. Simulation parameters: $h = 256$ km, $N^{\circ}_{H_2O} = 10^{18}$ m^{-3}, $N^{\circ}_{H_2O^+} = 10^{13}$ m^{-3}, $\mathbf{U}_{H_2O} = -8\mathbf{x}$ km/s. 144

5.19 Velocity of released ions on planes along **B**. Simulation parameters: $h = 256$ km, $N^{\circ}_{H_2O} = 10^{18}$ m^{-3}, $N^{\circ}_{H_2O^+} = 10^{13}$ m^{-3}, $\mathbf{U}_{H_2O} = -8\mathbf{x}$ km/s. 145

5.20 Central ion speed and electric field versus central density of the released ions and neutrals. 146

5.21 Rotation of the velocity vector versus altitude. 147

5.22 Ion velocity versus the altitude of the release 148

6.1 Flow regimes for H_2O, CO_2 and Ba released in the ionosphere. 152

6.2 Collision times between released H_2O, CO_2 and Ba and the ionospheric neutrals 153

6.3 Coordinate system in the neutral flow from a pulsed source. 155

7.1 H_2O density and velocity 0.25 s after the release. Thruster firing: $h =$ 250 km, $\mathbf{U}_s = -6\mathbf{x}$ km/s. 176

7.2 Density and velocity of H_2O^+ on transverse to **B** planes 0.25 s after the release. Thruster firing, $h = 250$ km, $\mathbf{U}_s = -6\mathbf{x}$ km/s. 177

7.3 Density and velocity of O^+ on transverse to **B** planes 0.25 s after the release. Thruster firing, $h = 250$ km, $\mathbf{U}_s = -6\mathbf{x}$ km/s. 178

7.4 Density and velocity of H_2O^+ on a midplane along **B** 0.25 s after the release. Thruster firing, $h = 250$ km, $\mathbf{U}_s = -6\mathbf{x}$ km/s. 179

7.5 Density and velocity of O^+ on a midplane along **B** 0.25 s after the release. Thruster firing, $h = 250$ km, $\mathbf{U}_s = -6\mathbf{x}$ km/s. 180

7.6 Potential on transverse to **B** planes 0.25 s after the release. Thruster firing, $h = 250$ km, $\mathbf{U}_s = -6\mathbf{x}$ km/s. 181

7.7 Electron density on transverse to **B** planes 0.25 after the release. Thruster firing: $h = 250$ km, $\mathbf{U}_s = -6\mathbf{x}$ km/s. 182

7.8 Height integrated UV emission 0.25 s after the thruster firing, $h = 250$ km, $\mathbf{U}_s = -6\mathbf{x}$ km/s. 183

7.9 Density and velocity of H_2O 0.25 s after the release. Thruster firing: h =250 km, $\mathbf{U}_s = -6\mathbf{x} + 2.4\mathbf{z}$ km/s. 184

7.10 Density and velocity of H_2O^+ on transverse to **B** planes 0.25 s after the release. Thruster firing, h =250 km, $\mathbf{U}_s = -6\mathbf{x} + 2.4\mathbf{z}$ km/s. 185

7.11 Density and velocity of H_2O^+ on a midplane along **B** 0.25 s after the thruster firing. h =250 km, $\mathbf{U}_s = -6\mathbf{x} + 2.4\mathbf{z}$ km/s 186

7.12 Density and velocity of O^+ on transverse to **B** planes 0.25 s after the release. Thruster firing, h =250 km, $\mathbf{U}_s = -6\mathbf{x} + 2.4\mathbf{z}$ km/s. 187

7.13 Density and velocity of O^+ on a midplane along **B** 0.25 s after the release. Thruster firing, h =250 km, $\mathbf{U}_s = -6\mathbf{x} + 2.4\mathbf{z}$ km/s. 188

7.14 Volume emission rate and height integrated emission intensity 0.25 s after the release. Thruster firing, $h = 250km$, $\mathbf{U}_s = -6\mathbf{x} + 2.4\mathbf{z}$ km/s. . 189

7.15 Density and velocity of H_2O^+ on transverse to **B** planes 0.25 s after the release. Thruster firing, h = 450 km, $\mathbf{U}_s = -6\mathbf{x} + 2.4\mathbf{z}$ km/s. 190

7.16 Density and velocity of H_2O^+ on a midplane along **B** 0.25 s after the release. Thruster firing, h = 450 km, $\mathbf{U}_s = -6\mathbf{x} + 2.4\mathbf{z}$ km/s. 191

7.17 Density and velocity of O^+ on a midplane along **B** 0.25 s after the release. Thruster firing, h = 450 km, $\mathbf{U}_s = -6\mathbf{x} + 2.4\mathbf{z}$ km/s. 192

7.18 Electron density on transverse to **B** planes 0.25 s after the release. Thruster firing, h = 450 km, $\mathbf{U}'_s = -6\mathbf{x} + 2.4\mathbf{z}$ km/s. 193

7.19 Density and velocity of H_2O^+ on transverse to **B** planes 0.2 s after the release. Orbital release, h = 250 km, $\mathbf{U}_s = -8\mathbf{x}$ km/s. 196

7.20 Density and velocity of O^+ on transverse to **B** planes 0.2 s after the release. Orbital release, h = 250 km, $\mathbf{U}_s = -8\mathbf{x}$ km/s. 197

7.21 Density and velocity of H_2O^+ on a midplane along **B** 0.2 s after the release. Orbital release, h = 250 km, $\mathbf{U}_s = -8\mathbf{x}$ km/s. 198

7.22 Maximum density of H_2O^+ and O^+ versus altitude. 203

7.23 The maximum integrated UV intensity versus altitude. 206

List of Tables

2.1 Cloud velocity and length scales 47

2.2 Maximum electron collision frequencies for momentum transfer and the collisionality ratio, in the F ionosphere. 50

2.3 Collision frequency ratio for limiting values of energy of the test particles, ϵ_α. 58

2.4 Polarizability of neutral gases 60

2.5 Momentum transfer ion-neutral charge exchange collision frequency . . 62

2.6 Momentum transfer electron-neutral collision frequency. 63

3.1 Ambient conductivities. 72

3.2 Cloud radius and the upper bound of the velocity for which wave conductance can be neglected. 83

3.3 Integrated Conductances for different ionospheric conditions. 86

5.1 Densities, conductivities and the shielding Factor (numerical) for a plasma sphere in an electric field 121

5.2 The contaminant mass of water with the corresponding central density. 131

6.1 Number of molecules of the released material Q_r and the corresponding mass. 151

6.2 The diffusion coefficient D and the radius of the neutral cloud at $t = \tau_D$. Data are for H_2O release at different altitudes. 156

7.1 Maximum time step for stability due to the charge exchange reaction . 163

7.2 Maximum time step for stability due to the electron recombination reaction 164
7.3 Parameters for thruster firing simulations. 166

Nomenclature

Symbol	Definition (SI units)
$A_{P,H,\|\|}$	Pedersen, Hall and Parallel components of property A
$A_{i\pm1/2,j,k}$	antidiffusive flux in the i direction
$A_{i,j\pm1/2,k}$	antidiffusive flux in the j direction
$A_{i,j,k\pm1/2}$	antidiffusive flux in the k direction
$\mathbf{B}$	magnetic field (T)
c_x, c_y, c_z	directional CFL numbers in the numerical integration
$C_{i\pm1/2,j,k}$	3D-FCT weighting coefficient in the i direction
$C_{i,j\pm1/2,k}$	3D-FCT weighting coefficient in the j direction
$C_{i,j,k\pm1/2}$	3D-FCT weighting coefficient in the k direction
$D^{J}_{t,P,H,\|\|}$	directional diffusion coefficient of species t associated with species j (m^2s^{-1})
$D_{tP,H,\|\|}$	total directional diffusion coefficient of species t (ms^{-1})
$\mathbf{E}$	electric field (Vm^{-1})
$\mathbf{E}_o$	ambient electric field (Vm^{-1})
$\mathbf{E}_m$	motional electric field (Vm^{-1})
$\mathbf{F}_t$	force on a species t (N)
$\mathbf{F}^{(iner)}$	force due to inertia (N)
$F^{H,L}_{i\pm1/2,j,k}$	transportive flux in the i direction based on a high (H) or low (L) order scheme
$G^{H,L}_{i,j\pm1/2,k}$	transportive flux in the j direction based on a high (H) or low (L) order scheme
$H^{H,L}_{i,j,k\pm1/2}$	transportive flux in the k direction based on a high (H) or low (L) order scheme
$\mathbf{g}$	gravity (ms^{-2})
h	altitude of release (km)

$\mathbf{I}$	current (A)
$I_{306.4}$	integrated volume emission rate (Rayleigh)
$\mathbf{J}$	total current density ($\mathrm{Cm^{-2}s^{-1}}$)
k_b	reaction rate in a reaction b ($\mathrm{m^3s^{-1}}$)
$k_{tP}, k_{tH}, k_{t\parallel}$	Pedersen, Hall, Parallel parameters
L_A	parallel interaction length based on Alfven wave (m)
$L_{\parallel}$	parallel interaction length based on conductivities (m)
m_t	mass of species t (kg)
M_t	mass of released material t (kg)
n_t, N_t	number density of species t ($\mathrm{m^{-3}}$)
P_t	pressure of species t ($\mathrm{kgm^{-1}s^{-2}}$)
$P^{\pm}_{i,j,k}$	sum of antidiffusive flux in or out a cell (i, j, k)
$Q^{\pm}_{i,j,k}$	maximum of antidiffusive flux in or out a cell (i, j, k)
q_t	charge of species t (C)
Q_r	number of released molecules
Q_o	total particle flux from a pulsed source ($\mathrm{s^{-1}}$)
$\mathbf{R}^b_t$	momentum transfer of species t in reaction b ($\mathrm{ms^{-2}}$)
S^b_t	production/loss term of species t in a reaction b ($\mathrm{m^{-3}s^{-1}}$)
T_t	temperature of species t (K)
$\mathbf{U}_n$	velocity of neutral n ($\mathrm{ms^{-1}}$)
$\mathbf{U}_s$	absolute source velocity of neutral ($\mathrm{ms^{-1}}$)
$\mathbf{U}'_s$	relative source velocity of neutral ($\mathrm{ms^{-1}}$)
U	state vector in hyperbolic equation
V_A	Alfven velocity ($\mathrm{ms^{-1}}$)
$\mathbf{V}_t$	velocity of species t ($\mathrm{ms^{-1}}$)
$\mathbf{V}_{t\perp}$	perpendicular to $\mathbf{B}$ velocity of species t ($\mathrm{ms^{-1}}$)
$\mathbf{V}_{t\parallel}$	parallel to $\mathbf{B}$ velocity of species t ($\mathrm{ms^{-1}}$)
$\mathbf{V}^b_t$	velocity of species t in reaction b($\mathrm{ms^{-1}}$)
$\mathbf{V}_o$	orbital velocity of spacecraft ($\mathrm{ms^{-1}}$)

$V_{i,j,k}$	volume of the element centered at the point (i,j,k) (m^{-3})
$w^t_{nP,H,\parallel}$	directional neutral wind coefficient of species t associated with neutral wind of species n
$W_{nP,H,\parallel}$	total directional neutral wind coefficient due to neutral wind of species n (m^{-3})

Greek Symbols	Definition (SI units)
α_o	equal mass radius (m)
$\alpha_\perp$	transverse length of a density perturbation (m)
β	plasma beta
$\beta^t_{P,H,\parallel}$	directional gravity coefficient of species t (s)
$B_{P,H,\parallel}$	total directional gravity coefficient (sm^{-3})
$\Gamma_{tP,H,\parallel}$	directional flux of species t ($m^{-2}s^{-1}$)
Δt	time step for numerical integration (s)
Δx_i	grid size in the i direction
Δy_j	grid size in the j direction
Δz_k	grid size in the k direction
$\delta\mathbf{V}$	velocity perturbation in the Alfven wave (ms^{-1})
$\delta\mathbf{B}$	magnetic perturbation in the Alfven wave (T)
$\delta\mathbf{E}$	electric field perturbation in the Alfven wave (Vm^{-1})
ϵ	perturbation electric field (Vm^{-1})
$\epsilon_{306.4}$	volume emission rate (photons $m^{-3}s^{-1}$)
θ_o, ϕ_o	polar and cone angles of the orbital velocity
θ_s, ϕ_s	polar and cone angles of the source velocity
κ_t	ratio of gyrofrequency to collision frequency of species t
λ	mean free path (m)
λ_D	Debye length (m)
$\lambda^\pm$	amplification factors of the numerical integration schemes
$\mu^t_{P,H,\parallel}$	directional mobility of species t ($Ckg^{-1}s$)
ν_{tj}	collision frequency of species t with species j (s^{-1})

ν_t^b	collision frequency of species t in a reaction b (s^{-1})
ν_t	total collision frequency of species t (s^{-1})
ρ	charge density (Cm^{-3})
$\sigma^t_{P,H,\|\|}$	directional conductivity of species t (S m^{-1})
σ_{ion}	ionization rate (s^{-1})
$\sigma_{P,H,\|\|}$	total directional conductivity (S m^{-1})
Σ^o_{bP}	Pedersen conductance of the unperturbed background plasma (S)
Σ_{bP}	Pedersen conductance of the perturbed background plasma (S)
Σ_{cP}	Pedersen conductance of the plasma cloud (S)
Σ^o_W	wave conductance of the unperturbed background plasma (S)
Σ_W	wave conductance of the perturbed background plasma (S)
τ_b	reaction time in chemical reaction b (s)
ϕ	perturbation potential (V)
Ω_t	gyrofrequency of species t (s^{-1})

Chapter 1

Introduction

The presence of a moving body in the ionosphere represents a disturbance in the ambient environment. We can distinguish between the *modified*, *contaminant* and the *induced* environments about a space vehicle. The modified environment represents the disturbance in the ambient ionosphere caused by the motion of the body. In addition to that, there is the contaminant environment. It consists of liquids, gases and solids originating at the vehicle as a result of operational or experimental activities or surface-environmental interactions. However, the above distinction is helpful only in identifying processes which contribute rather than define existing separate environments. The spacecraft flies within the induced environment. This is the result of an array of interactions between the modified and the contaminant environments. It consists of neutrals, ions, particulates and electromagnetic waves. The processes which determine the dynamical characteristics of the induced environment are electromagnetic and chemical in nature.

Since the early satellite flights, research and experiments have been devoted to the understanding of the nature and the processes within the induced environment. The Space Shuttle Orbiter (SSO) flights have provided clear evidence of the severe interactions between a space vehicle and the ambient ionosphere. The distinct characteristic of the SSO is that it is the largest vehicle ever flown, was used as a scientific platform and performed a series of operations. The study of the induced environment is extremely important. This environment affects the spacecraft, its surface and the sensors that it carries and, therefore, poses a serious question on the ability of the spacecraft to perform adequately. This is especially true for a vehicle which is expected to remain in space for a long period, like the proposed Space Station or a surveillance satellite. Therefore it is important to understand the characteristics of the induced environment.

It has become common practice to refer to the induced environment also as the *(contaminant) plasma cloud.* This descriptive term has been assigned to the morphology of the environment for more than merely semiological reasons. Spacecraft activities are not the only candidates for the creation of plasma clouds in the ionosphere. Long before the study of the spacecraft induced environment the space physics community was involved in the study of *artificial plasma clouds.* In what is referred to as the *chemical release or active experiments* neutrals are injected which upon their ionization create ions, i.e., a plasma cloud. The body of theories, computations and experiments in that area is vast and began almost three decades ago. The latest of this type of experiments is still under way with the series of Combined Release and Radiation Effects Satellite (CRRES) releases. The study of the spacecraft induced plasma clouds is a relatively new area of research and has been benefited enormously from the previous work on artificial clouds.

It is crucial to be able to model and predict the spacecraft induced environment because it:

- Contaminates and degrades the spacecraft surfaces and sensors.
- Affects space experiments and operations.
- Interacts with the solar arrays and other power systems.
- Contributes to the surface "glow".
- Emits radiation and modifies the signature of the spacecraft.
- Contributes to the differential charging of surfaces.

- Excites waves and plasma instabilities.

- Enhances the electrostatic noise in the vicinity of the spacecraft.

- Perturbs the ambient environment.

Another feature of the induced environment, that has become clear from the SSO flights experience, is the fact that it by itself represents an *active experiment* from which much can be understood about the plethora of plasma processes which are taking place. In that respect the study of the spacecraft induced environment benefits the space science objectives associated with the study of the release experiments in space. These objectives include but are not limited to:

- The estimation of ambient electric fields and neutral winds.

- The understanding of ionospheric phenomena related to current closure.

- The modeling of aurora and natural ionospheric irregularities, and ionospheric-magnetospheric electrodynamics.

- The investigation of basic plasma physics phenomena, waves and instabilities.

Review of the literature reveals that there has been a substantial improvement in the understanding of the mechanisms of the interactions whithin the induced environment. Effort has been put into the understanding of both the origin of the induced environment and the processes and interactions taking place within it.

In this work we focus our attention on the plasma cloud which is created about a space vehicle in Low Earth Orbit (LEO) in the altitude range between 120 and 650 km. The schematic of the process that we study is as follows: we consider a vehicle in LEO which creates a neutral cloud around it. The neutral cloud expands while undergoing chemical reactions which produce ions. The motion and composition of this plasma cloud is then a result of complicated chemical and electrodynamical processes. One can see that the schematic that we consider is quite general and, thus, can be applied to model processes such as outgassing or thruster firing. It can also be applied to another class of events, those of chemical release experiments. Thus, we can alternatively state that the purpose of this study is to obtain a three-dimensional (3-D) theory and a model for the motion of an artificial plasma cloud in the ionosphere. The details of the underlying assumptions and requirements of our model will be discussed later; however, the proposed schematic process serves as a framework to guide us in the study. The scope of this work is beyond a simple evaluation of the induced environment. Since this work is the first to address the 3-D aspects of the induced plasma environment and among the few 3-D simulations that have been carried out, important basic plasma physics phenomena must be addressed; in particular those related to the 3-D electrodynamics of plasma clouds. In this work we keep a balance by investigating basic plasma physics while aiming at engineering applications of interest.

In this introductory chapter we first present the ambient LEO plasma environment. We then review the literature of observations and experiments of the plasma and neutral cloud about a spacecraft. We will focus primarily on the SSO although similar studies have been undertaken during satellite flights; the SSO with its large plasma cloud provided the scientific community with an excellent opportunity for such studies. The review of the literature will provide a coherent background of the phenomena observed and also will reveal the current understanding that has been attained. Although we are to develop a "simplified" model of the contaminant cloud, our model must include and then be able to capture and reproduce some of the essential characteristics of the observations.

We then review the theory and the modeling of artificial plasma clouds in the ionosphere. We begin with plasma cloud experiments which have been historically the first attempt to study such phenomena. We review studies of ionospheric modification experiments which attempted to model neutral gas expansions and investigated the significant role of chemical interactions within the cloud. We also present studies on plasma jetting which focused on high speed plasma clouds, and we end the review with studies on contaminant clouds about space vehicles. In this review we highlight the basic theoretical assumptions of the models and the predictions obtained through the use of analytical or numerical techniques. This will reveal important developments, but it will also clarify the shortcomings. Finally, we present the underlying assumptions and the requirements of the 3-D plasma cloud model we develop in the current study.

1.1 The LEO Ambient Space Environment

In this study we are concerned with releases from spacecraft in LEO at altitudes from 150 km up to 650 km. This region is termed the thermosphere or F ionosphere if classified for its neutral or ion composition respectively. The composition of the ionosphere is influenced by processes such as photochemistry, solar radiation fluxes, transport and diffusion; one has to add to the above processes the dynamic interaction of the ionosphere with the atmosphere below and the magnetosphere above. All these result in an unsteady environment which may exhibits rapid changes and a variety of phenomena and interactions. The structure and motion of the ionosphere has been the subject of extensive research; however, this is beyond the scope of this study. We review here the ionospheric characteristics significant to our study. Measurements of the properties of the F ionosphere are determined from satellite observations and radar incoherent scatter data. For purposes that will become clear in the discussion of the current closure we include in the review the composition of the E ionosphere, the region between 100 and 150 km.

The major neutral species of the ionosphere are O, O_2, N_2, He, and H. From the altitude of 250 km and up to near 600 km the dominant neutral species is atomic oxygen. Above the 600 km altitude light species such as H and He dominate the gas. In the E region, however, neutral molecules like O_2 and N_2 dominate the neutral gas profiles. A typical profile calculated with the Mass Spectrometer Incoherent Scatter (MSIS) model for mid-latitude, summer, daytime and average solar activity conditions is shown in Figure 1.1. The MSIS model produces neutral temperature and density profiles [see *Hedin*, 1987 and references therein].

One of the most important plasma characteristics is the electron density, usually referred to as plasma density. The electron density shows considerable variation between daytime and nighttime conditions. A typical profile calculated with the International Reference Ionosphere (IRI) model for mid-latitude, summer, average solar activity conditions, is shown in Figure 1.2. The IRI produces electron density profiles and ion composition for given ionospheric conditions [*Rawer and Bradley*, 1987]. The electron density shows a peak at about 250 km with values as high 6×10^{11} m^{-3} occurring at noontime. During the night the density decreases considerably especially at lower altitudes. The stratification in the electron density reflects mainly the effect of the ultraviolet radiation that impinges on a neutral density profile that increases with decreasing altitude. The drastic density change between night and day at altitudes below 200 km also reflects the change of ionic composition at these altitudes. Typical ionospheric ionic profiles under the same conditions presented above are shown in Figure 1.3. The principal ion in the F region is O^+. In the E region NO^+ and O_2^+ dominate the plasma. Above the altitude of 1000 km the H^+ density exceeds that of the O^+. The ionic composition at altitudes above 150 km is sustained through the night. The drastic change in the plasma density of the E region is a consequence of the fast electron recombination time of the molecular ions which dominate this region. During the night the production of molecular ions is curtailed and rapid recombination reduces the plasma density. In the F region atomic ions sustain their profiles due to their slow recombination times.

The temperature characteristics of the ionosphere are quite variable and are shown for a typical case in Figure 1.4. Heating by absorption of the UV radiation is one of the important sources of energy in the ionosphere. The neutral temperature in general shows a very rapid increase from about 200 °K up to 1000 °K in the E and F-1 ionospheric regions. The ion temperature shows almost a linear increase from 500 to 2000 °K. Finally, the electron temperature after a steep increases up to about 300 km stays nearly constant at 2500 °K.

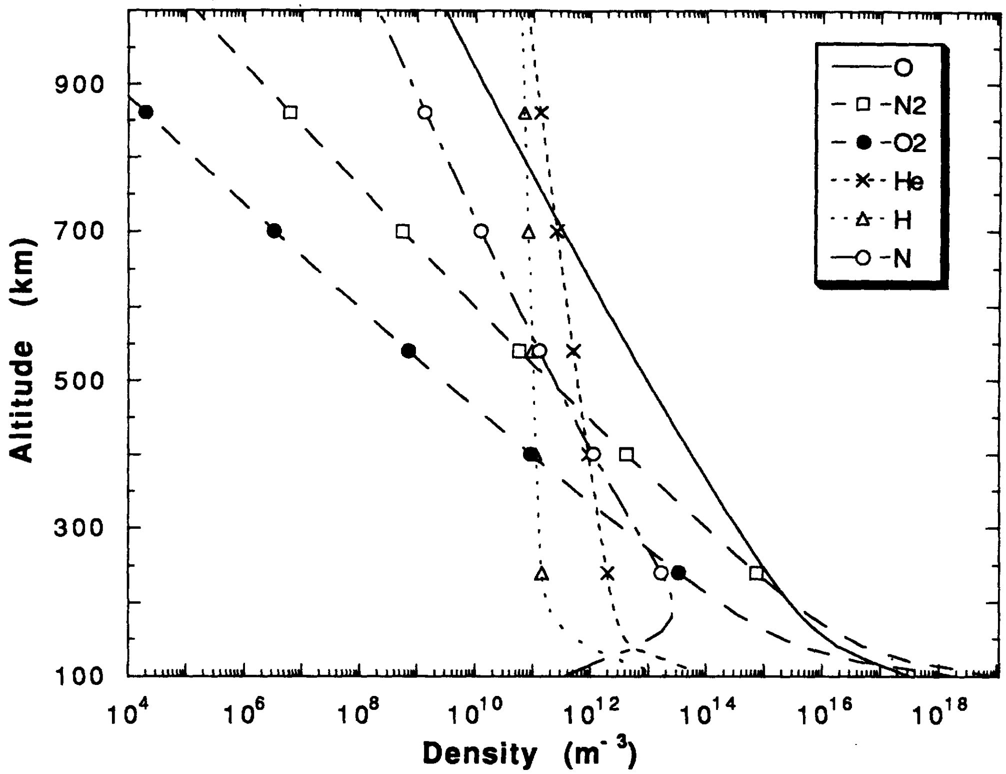

Figure 1.1: Neutral density composition of the ionosphere. MSIS model for mid-latitude, summer, daytime, average solar activity conditions.

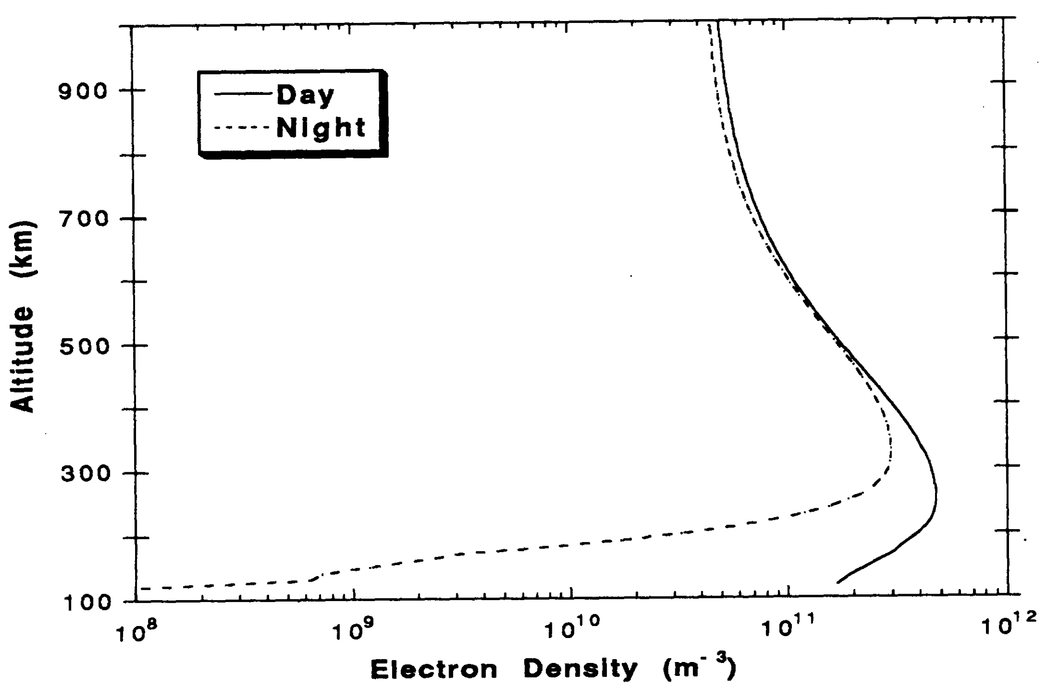

Figure 1.2: Electron density for the daytime and nighttime ionosphere. IRI model for mid-latitude, summer, average solar activity conditions.

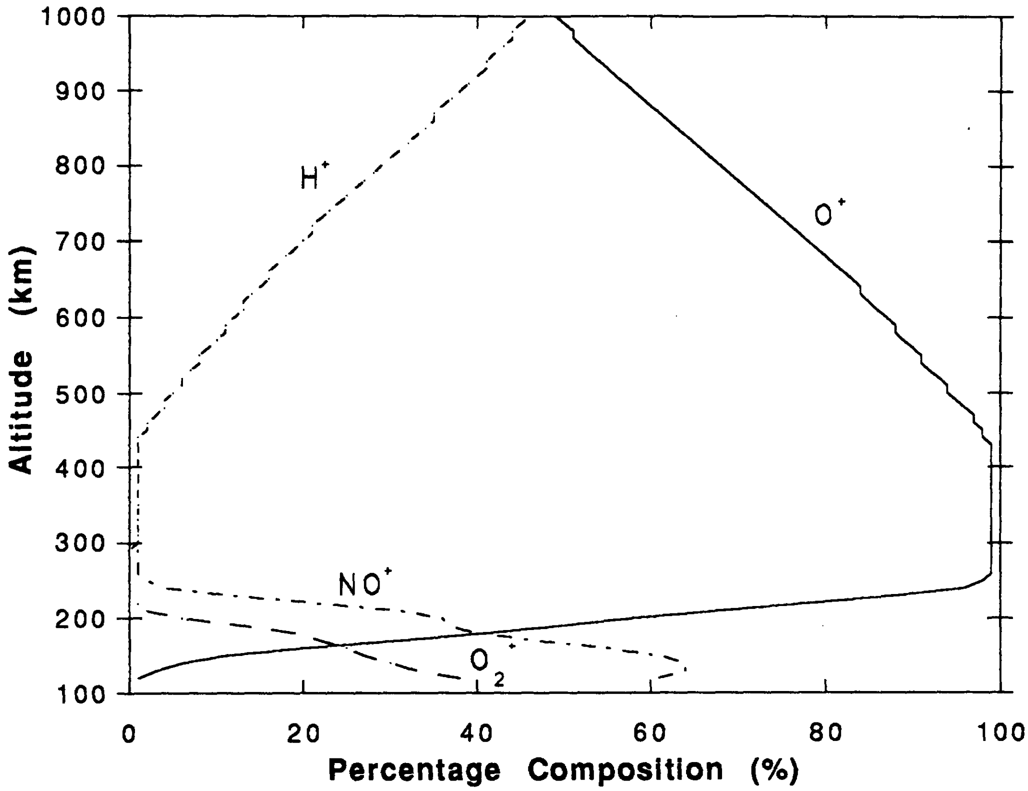

Figure 1.3: Ion composition of the ionosphere. IRI model for daytime, mid-latitude, summer, average solar activity conditions.

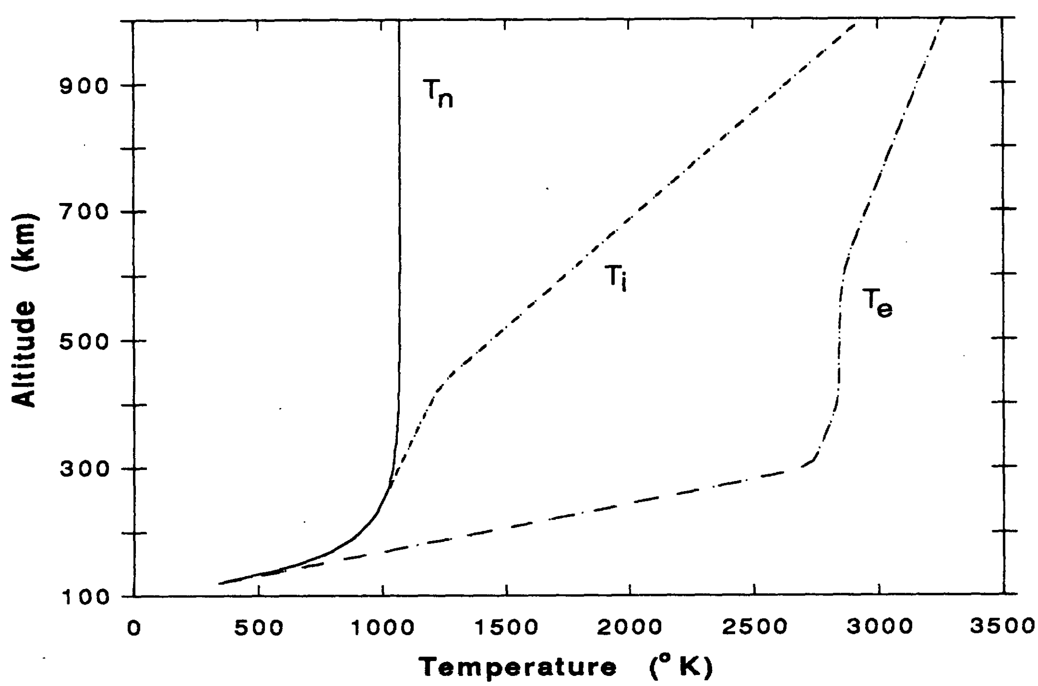

Figure 1.4: Neutral, ion and electron temperature in the ionosphere.

1.2 Spacecraft Induced Environment: A Review

Since the early spacecraft flights there have been observations that the ambient ionosphere surrounding a spacecraft is greatly modified. The cloud created about a spacecraft consists of neutrals and ions created through a variety of mechanisms. One can distinguish between ions and neutrals produced directly from the space vehicle and those which are produced in an array of chemical interactions between the contaminant cloud and the ambient environment. There are three major sources of the contaminant plasma cloud. The first is the outgassing of neutrals, the second is the rocket plume products from thruster firings, and the third is leakages and deliberate fluid dumps from the space vehicle. Upon their release the contaminants undergo chemical reactions with the background ionosphere and produce ion and neutral species.

Studies of the induced environment in the pre-SSO flight period concentrated on the modeling of outgassing and of thruster plume flow from small spacecrafts. The SSO was the largest vehicle flown with many operations that contributed to the creation of a large cloud about it. The SSO cloud was the subject of intense studies, both experimental and theoretical. These studies significantly increased our understanding of the phenomena within the induced environment by introducing and addressing new processes such as plasma transport, chemical interactions between the cloud species, and radiation emission from the cloud and the vehicle surfaces. Future spacecraft dedicated to complex missions and experiments may have a similar to the SSO potential of releasing large amounts of neutrals. It is this reason that prompted us into reviewing only the SSO studies.

Data from the STS-2,-3,-4 flights were reported by *Carignan and Miller* [1983]. They used a mass spectrometer located in the SSO bay. For the STS-4 flights it was also located above the orbiter. The major contaminant neutral was found to be water vapor, H_2O. It was found that water levels were high at the beginning of the flight and low at the end. The variation of the H_2O was attributed to the pre-flight conditions. Large fluxes of water were observed during thruster firings, water dumps and flush evaporator system releases. *Narcisi et al.* [1983] reported data from STS-3 on both the neutral and ion environment. Among the detected ions the dominant was found to be H_2O^+ formed via the charge exchange reaction $H_2O + O^+ \rightarrow H_2O^+ + O$. They also detected ions from exhaust gases such as N_2, NO^+ and OH^+. Among the detected neutrals H_2O was found to be the major contaminant. Exhaust products such as N_2 and H_2, were also detected. During thruster firings they observed significant perturbations of the particulate, gas and optical environment, as well as plasma depletions of one order of magnitude. One of the plasma phenomena within the disturbed environment about space vehicles was the existence of ion streams, associated with wake phenomena [*Henderson and Samir*, 1967]. On STS-3 the Plasma Diagnostic Package (PDP) was deployed 15 m above the orbiter and it detected the existence of ion streams at an angle of attack of almost 50° to the ram direction and outside of the wake [*Stone et al.*, 1983]. They speculated that the observed electrostatic noise might be the result of the electrodynamic interactions between the contaminant cloud and the ionosphere. An assessment of missions STS-1 through STS-4 was published by *Ehlers et al.* [1984]. They compared measurements of the contaminant environment with requirements and goals and concluded that the environment appears to be adequate. However, events such as thruster firings, water dumps, and flash evaporator releases contribute in a significant way to the build up of contaminants. It was suggested that during these events protection must be provided for some experiments under way on the SSO. *Shawhan et al.* [1984] presented measurements from the STS-3 flight (OSS-1 payload). They measured ambient species like O^+ and contaminant H_2O^+ which during water dumps reached densities comparable with those of the ambient. During thruster firings NO^+ was enhanced and perturbations of the electric field increased. Measurements of the orbiter potential showed it to vary by up to 5 V. Using data from the same payload *Raitt et al.* [1984] concluded that a number of factors make the orbiter an unfriendly platform for ambient ionospheric plasma observations. The plasma about the vehicle was shown to have a high degree of turbulence, higher than that observed around small satellites. They reported elevated electron temperatures up to 4000-5000 ° K in regions of high ion density and attempted to explain them with plasma instabilities occurring within the plasma cloud. An effort to explain plasma phenomena observed in the ram direction during the STS-3 flight was undertaken by *Siskind et al.* [1984]. They suggested that observations , such as high degree of turbulence, enhanced molecular ion densities, and thermal electrons with temperatures above 5000 °K can be attributed to plasma instabilities which are results of the motion of the outgassed cloud through the ionosphere. They suggested that chemistry within the SSO plasma cloud was responsible for the enhancement of ion densities while plasma processes were the cause for the elevated electron temperature; they also pointed out the similarity between the plasma cloud about spacecraft and those resulting from release experiments. On the basis of the same STS-3 data, *Pickett et al.* [1985] concentrated on the effects of chemical releases in the ionosphere. During water vapor releases the electrostatic noise was enhanced, plasma irregularities were increased along with perturbations of the spacecraft potential and pressures reached 10^{-4} torr, up three-orders from the ambient 10^{-7}. In their paper a clear effort was made to describe both the chemistry and the electrodynamics within the water cloud along with the suggestion that much can be gained from the study of release experiments. Further evidence of the severe interaction between the SSO outgassed cloud and the ionosphere appeared in measurements taken by an ion-neutral mass spectrometer during the STS-4 flight [*Hunton and Calo*, 1985]. The instrument detected ions such as O^+, H_2O^+ and H_3O^+ with energies less than 1.5 eV. *Hunton and Calo* suggested that these observations can be explained in terms of collisional scattering and chemical reactions within the outgassed cloud rather than purely plasma phenomena. They suggested that charge exchange reactions and bimolecular reactions, such as $H_2O^+ + H_2O \rightarrow H_3O^+ + OH$ are responsible for the large signals of H_2O^+ and H_3O^+. The authors suggested that, in contrast with small spacecraft, the SSO is expected to have a large contaminant cloud associated with it where both chemistry and electrodynamics play an important role. Such a comparison between observations in the wake of satellites and the wake of SSO was presented by *Murphy at al.* [1986]. The data from the PDP on board STS-3 revealed that phenomena like reduced plasma densities and elevated temperatures are observed within the SSO wake. They are strongly enhanced in comparison with satellite data. They criticized results presented by *Siskind et al.* [1985] concerning observations of high turbulence in the ram direction. They found that turbulence was high in regions with large pressure gradients, especially between ram and wake. They also stressed the fact that since there are only a few wake observations about large bodies, one has to be very careful because of possible instrumental errors. Therefore, comparison with observations on satellites and predictions from theoretical models are necessary. The effects of thruster firings on the composition of neutral gases within the SSO bay was the subject of the study presented by *Wulf and Von Zahn* [1986]. From measurements taken on board STS-41-B using a neutral mass spectrometer they confirmed previous results of high H_2O and NO levels. Other contaminants include N_2, CO and CO_2. The importance of their findings is that the intensity of the contamination depended strongly on the degree of direct impact of the thruster plume on a surface. Data taken by a retarding potential analyzer on board STS-3 were presented by *Reasoner et al.* [1986]. They showed that the SSO flying supersonically with respect to the ambient ions creates a Mach cone similar to the fluid dynamic case with significant departures from Maxwellian distributions. However,d the orbiter-ambient plasma interactions extend meters outside the Mach cone. It was concluded that valid ambient ionospheric observations can be made if the instruments are placed upstream at a distance greater than the ion gyroradii. A kinetic approach which incorporated outgassed cloud-ambient ionosphere interactions was presented by *Caledonia et al.* [1987]. It was shown that within the contaminant cloud the ratios of $[H_2O^+]/[O^+]$ and $[H_3O^+]/[H_2O^+]$ are related to $[H_2O]$, while the ratio $[CO_2^+]/[O^+]$ is related to $[CO_2]$. Each one of these ratios is related to a rate constant for chemistry and a time constant for the convective flow of the ions. They evaluated the rate constants using kinetic energies resulting from the velocity of the SSO. The drift velocities were evaluated using a fluid model which included parallel drift and chemical reactions. The calculated ratios of $[H_2O^+]/[O^+] = 0.1$ and $[H_3O^+]/[H_2O^+] = 0.2$ were consistent with a pressure of water vapor of 10^{-6} torr. A major contribution to the estimation of the extent of the contaminant cloud about the SSO came with observations taken during the Spacelab-2 mission and was presented in a paper by *Grebowsky et al.* [1987]. During that flight the PDP was flown as a free satellite while the SSO was maneuvered around it, so that measurements could be taken both in the ram and wake directions at distances of hundreds of meters. Ion measurements indicated that ions such as H_2O^+, NO^+ can be found for hundreds of meters both in the ram and the wake directions. Another result was that neutral gases originating at the SSO extend in all directions over distances of hundreds of meters. This evidence of a large contaminant cloud places in question the use of the SSO for any kind of ambient plasma observations. During the same free flight of the PDP, wave measurements showed broadband turbulence at frequencies of a few Hz to 10 kHz [*Gurnett et al.*, 1988]. The maximum intensity occurred in the downstream region and intensified during thruster firing. This broadband noise was attributed entirely to the outgassed cloud -ambient ionosphere interactions. The ions created within the cloud via charge exchange reaction result in a highly unstable velocity distribution as they move through the ionosphere. This pick-up process produces currents both perpendicular and parallel to the magnetic field which may be the cause of current driven electrostatic waves. The same electrostatic noise has also been observed during the artificial cloud release in the Active Magnetospheric Particle Tracer Explorers (AMPTE) mission, emhasizing the similarity between the two clouds.

1.3 Plasma Clouds in the Ionosphere : A Review

Artificial plasma clouds in the ionosphere may be the result of either experiments or contamination. Both incorporate similar physical and chemical processes. In the case of plasma cloud experiments, fast ionizing neutrals are injected, usually barium, which upon photoionization create an ion cloud. The study of the motion of such a cloud can reveal information about the ambient electric field and currents in the upper atmosphere, map the distant magnetic field and measure the ambient neutral winds. However, observations from the first experiments showed a vast variety of plasma dynamic phenomena and, thus, plasma clouds were used as experiments to study basic plasma phenomena such as plasma instabilities and plasma wave interactions. In this way the ambient ionosphere can serve as an excellent laboratory for plasma studies. Contaminant plasma clouds are the product of deliberate or accidental releases of neutrals or ions in the ionosphere. In that case too a neutral cloud is released and upon a series of chemical interactions a plasma cloud is created. The first studies of contaminant clouds started with the ionospheric modification experiments. Only very recently have there been studies particularly addressing the problem of the plasma cloud about the SSO. In the following review we address separately the various approaches to artificial cloud modeling. Theories and computations on plasma cloud experiments have explored the electrodynamic behavior and the instabilities of the plasma cloud. Studies on plasma jetting have been undertaken to account for the effects associated with high speed plasma clouds. Theories about ionospheric modification experiments have been developed to explain the chemistry and dynamical behavior of neutral gas expansions. Finally, studies of contaminant clouds about spacecraft have concentrated on the water plasma cloud observed about the SSO.

1.3.1 Plasma Clouds from Release Experiments

The first attempt to develop a theory of the motion of an artificial ion cloud and to explain experiments conducted in 1964, 1965 and 1966 has to be attributed to *Haerendel et al.* [1967]. From a simplified cylindrical model of an ion cloud of finite length they were able to estimate the ambient electric field and neutral winds in the ionosphere. A common feature of the artificial plasma clouds was the formation of striations, i.e., finger-like field aligned irregularities. *Simon* [1970] studied the instability produced by the effect of an applied electric field and a density gradient within a plasma cloud. At the same time *Linson and Workman* [1970] suggested another type of instability, the 'gradient drift', which eventually might result in striation formation. They predicted that the backside of the moving cloud would be unstable with a growth rate which was proportional to the ratio of the density gradient length and the velocity of the cloud. *Volk and Haerendel* [1971] performed a stability analysis of an ion cloud and introduced the notion of current balance within a cloud which is coupled with the background ionosphere. They also considered the short-circuit effect of the polarization current through Pedersen currents in the ambient ionosphere. In the same paper a discussion about *image clouds*, i.e., density and electric field variations in the ionosphere, appeared for the first time. *Perkins* [1973] showed that an instability in the form of rising and falling sheets of ionization may arise due to the $\mathbf{E} \times \mathbf{B}$ drift in the F region plasma if, in addition to the the east-west electric field a north-south component is applied. *Lloyd and Haerendel* [1973] performed the first two-dimensional (2-D) numerical calculation of the motion of a plasma cloud. They used a two-layer model, one for the ion cloud and the other for the ambient ionosphere, and modeled releases in both the E and F regions. It was concluded that releases in the E region drift with the ionosphere while releases in the F region are affected greatly by the presence of polarization fields within the cloud. It was also concluded that an altitude dependent neutral wind enhances the cloud's distortion while chemical recombination is insignificant. They performed numerical experiments introducing perturbations in their initial profiles and showed that clouds develop fingerlike striations, an observed feature of artificial ion clouds. *Perkins et al.* [1973] developed a 2-D field average model for a finite ion cloud. For a simple cylindrical cloud model they predicted that the cloud deformes like a dumbell due to the differential speeding of its regions. They considered large clouds, those in which the integrated conductivity is large compared with the ambient integrated conductivity, and showed that the formation of image striations does not affect the plasma dynamics considerably. It was concluded that both parallel conductivity and finite temperature yield a cutoff for the striation formation. In the same paper the assumption of equipotential magnetic field lines was questioned and it was suggested that it is valid for large clouds; for small clouds, however, the assumption is in question so that the 2-D approximation of the ion cloud-ionosphere system is not easily justified. In a companion paper *Zabusky et al.* [1973], solved numerically the system of the 2-D equations describing the motion of a large cloud for which the gyrofrequency is much greater than the ion-neutral collision frequency, i.e., $\Omega_i \gg \nu_{in}$. They considered various initial conditions and were able to reproduce many features of barium cloud experiments: finger-like striations, steepening backside and early elongation. A study of a small barium ion cloud was performed by *Goldman* *et al.* [1974] . They developed a 2-D model for the motion of both the cloud and the ionosphere and experimented using circular profiles as initial conditions. They showed the formation of image clouds in the ionosphere, and also that both clouds were rotated by an angle dependent upon the ratio of ion collision frequency to the ion gyrofrequency. Based on the model of *Goldman et al.* cited above, *Scannapieco et al.* [1974] performed a series of numerical calculations to investigate the effect of varying the ratio of the cloud to the background conductivity on the drift of a barium cloud. Small clouds showed rotation and elongation while large clouds showed steepening backside and enhancement of striations which became prominent in the image cloud first. A very important discussion on the accuracy of the numerical methods which were used to solve the system of ion cloud-ionosphere equations appeared in a paper by *Doles et al.* [1976]. They modeled releases at 150-200 km, ignored finite temperature effects and gravity and accounted for recombination taking place in the E region. With their line average 2-D, two level model they predicted rotation in the case of small clouds, drift in the $\mathbf{E} \times \mathbf{B}$ direction in the case of large clouds, backside steepening and striation formation. In contrast with *Haerendel et al.* [1973], they found that recombination was very significant in the cloud deformation. A significant feature in their numerical solution was the inclusion of grid adaptation in regions of high density and striation formation. In this study, as well as in a preceding one by *Zabusky and Doles* [1975], they severely criticized the results of the work by *Haerendel et al.* [1973] due to errors introduced in the numerical solution by inappropriate use of artificially imposed boundary conditions. Another problem in the numerical solution of continuity equations was that the solution could be corrupted by dispersive and dissipative methods. A step towards more accurate numerical schemes for the solution of hyperbolic equations was the introduction by *Zalesak* [1979] of the fully multidimensional Flux Corrected Transport technique. The new scheme was first incorporated in a model of the equatorial spread-F anomaly, [*Zalesak and Ossakow*, 1980], and since then it has become the standard method of solution of hyperbolic type of equations. *McDonald et al.* [1980], in an effort to explain plasma jetting experiments conducted in 1978, used a one-level, 2-D model and various ratios of the height-integrated Pedersen conductivities of the cloud to the ambient, Σ_c/Σ_a. They showed that small clouds develop structures rapidly due to gradient instability and that the time for the set-up of striations is a function of the Pedersen conductivity ratio. A significant contribution in the field came from a paper by *Goertz* [1980]. Although not directed to the modeling of ion cloud releases, Goertz's paper on the Io's interactions with the plasma of its torus presented a model for the field-aligned current carried by the Alfvén waves emanating from the moving Io-torus system. This configuration resembles very closely a moving ion cloud. Some other interesting but hard to explain features observed during ion cloud experiments were the development of structures of scales as small as 15 m, the formation of striations which were separated by almost 1 km and the persistence of these structures for hours ("freezing-up" phenomenon). *McDonald et al.* [1981] tried to derive a diffusion parameter which would trigger bifurcations in an ion cloud upon exceeding a specific value. They used a 2-D, field integrated Pedersen conductivity model, conductivity ratios from 2 to 30, and were able to observe freezing-up structures of kilometer size and predict lifetimes close to experimental data. In an attempt to further explain the "freezing" phenomenon *Zalesak et al.* [1983] proposed the "Pedersen leakage" mechanism. Ions, due to their finite mobility, separate from the electron cloud and, thus, lose their ability to structure further. Later, in 1985 *Zalesak et al.* using a two-level line integrated model simulated ion cloud releases including finite temperature, background incompressibility and uniform neutral wind. They were able to produce quasi-static structures hundreds of meters in diameter.

Plasma Jetting

Sperling [1983] extended the calculation of *Scholer* [1970] to study the case of plasma jetting in the ionosphere. He showed that the disturbance generated by the moving plasma cloud is both electrostatic and electromagnetic in nature. He pointed to the fact that ion-Pedersen currents and parallel electric fields invalidate the "frozen-in" magnetic field approximation. In higher altitude releases (500 km) the cloud is expected to drift over substantial distances and modify the magnetic field while the generated Alfvén waves are less subject to attenuation. A model of a barium release at an altitude of 350-450 km injected at orbital velocity was developed by *Mitchell et al.* [1985]. For the first time they introduced an accompanying neutral cloud and modeled its self-diffusive expansion. Their model was 2-D and included polarization currents and $\mathbf{E} \times \mathbf{B}$ drifts. Their model cloud, simulating a release similar to the CRRES experiment, drifted tens of kilometers across the magnetic field in accordance with observations made during the Buaro release experiments [*Simons et al.*, 1980]. Following this work, *Mitchell et al.* [1985] simulated for the first time instabilities in the inertial regime, i.e., $\nu_i \ll \omega$, where ν_i is the ion-neutral collision frequency and ω is the wave frequency of the $\mathbf{E}\times\mathbf{B}$ instability. They concluded that inertia $\mathbf{E} \times \mathbf{B}$ instabilities produce more isotropic striations and that the growth rate of the $\mathbf{E} \times \mathbf{B}$ instability is reduced when magnetospheric coupling is considered. The problem of image structuring in plasma jetting was examined by *Jacobson et al.* [1987]. The image process in the case of plasma jetting differs from the one described before in the sense that it is in the inertia and not in the collisional regime. In almost all models of ion clouds the ionosphere was considered as a closed system with insulators placed under the E region and above the F region. *Pudovkin et al.* [1987] considered a cloud released at auroral altitude which coupled electrically with the magnetosphere and showed that recombination inhibits the formation of large disturbances.

Ionospheric Modification

The effects of neutral gas injections in the ionosphere became a popular subject after the observation of a large *ionospheric hole* -a depletion in the ambient plasma density-createds by the exhaust of the Saturn V rocket. Initially, the observed depletion was attributed to the "snow plow" effects of the expanding gases of the exhaust plume but this mechanism was inadequate to explain the long duration and extent of the depletion. *Mendillo et al.* [1975] provided a theory where chemistry played the major role. The ambient O^+ rapidly reacts with H_2 or H_2O of the plume followed by dissosiative recombination of the molecular ions. The first model of diffusion of a chemically reacting neutral gas was provided by *Forbes and Mendillo* [1976]. In a subsequent paper the same authors [*Mendillo and Forbes*, 1978] examined the problem of creation of an O^+ hole and the formation of an electron depletion. In their calculation they demonstrated the effects of altitude of the release, the molecular weight of the released material, the quantity and the reactivity. The first treatment of both the ion and neutral clouds appeared in a paper by *Anderson and Bernhardt* [1978]. They simulated H_2 releases in the F region and modeled the effects of such a release by calculating densities of ion species as O^+, OH^+, H_2O^+ and H_3O^+. In their model they included production and loss of species by charge exchange, recombination and transport via $\mathbf{E} \times \mathbf{B}$. They also pointed to the fact that molecular releases may trigger a Rayleigh-Taylor gravitational instability. A 3-D model of a gas expansion in a nonuniform environment was presented by *Bernhardt* [1979] . He considered diffusion of neutral species and showed the effects of chemical reactions and wind shears on the neutral gas expansion. *Bernhardt* [1979] developed a model which applies to high-velocity neutral gas releases. *Yau et al.* [1985] presented a simulation of the Waterhole II and III experiments. They considered the explosive injection of H_2O, N and CO_2 and included charge exchange, dissociative recombination and three-body recombination reactions. Their model predicted the formation of a depletion and significant modification of the ambient ion composition. Their model, however, totally ignored plasma transport. Finally, an effort to tie both the neutral and ion dynamics in a directed release was undertaken by *Bernhardt et al.* [1988 a, b]. They used a fluid code to model the neutral gas dynamics for a release at an altitude of 320 km with initial velocity of 5 km/s. The predicted shock fronts were much smaller than the mean-free-path; consequently, this approach was unsuccessful since the background is too rarefied to justify the use of a fluid model. The model of the plasma dynamics included convection only along the magnetic field lines, steady state momentum, chemistry, and heat equations as well.

1.3.2 Plasma Clouds about Spacecraft

Elements of a theory of the dynamic behavior of contaminant clouds appeared in studies of observations taken on board the SSO and presented previously in this review. A study devoted to the water plasma cloud about a large space vehicle was undertaken by *Hastings et al.* [1988] and *Gatsonis* [1987]. Their model for the neutral cloud was derived from the outgassing of a spacecraft and was a simple spherically expanding cloud moving with the orbital velocity. The model for the ion cloud was 2-D, field-averaged, derived on the assumption that $\Omega_i \gg \nu_{in}$. The continuity equations for the O^+ and H_2O^+ included $\mathbf{E} \times \mathbf{B}$ drift and appropriate loss and production terms due to chemistry. They were able to calculate drift times for the ions, to predict striation formation, creation of ionospheric holes and polarization fields dependent upon the density of the plasma clouds. The instabilities whithin a water plasma cloud were investigated by *Mogstad* [1987]. Subsequently, *Eccles et al.* [1988] developed a similar 2-D model of a cold water plasma and studied the effects of chemistry in a systematic way. They showed that rotation is expected to deform the plasma clouds and also predicted very weak polarization. A new 2-D model was developed by *Hastings and Gatsonis* [1988]. It incorporated the theory of Alvén wings emanating from the moving cloud and investigated thoroughly the effects of parallel lengths on the structure and polarization of the cloud. The notion of parallel length in their model provided a mechanism for the cloud-ionosphere coupling. Their numerical simulations showed that dense clouds exhibit polarization and drift almost with the spacecraft while less dense clouds move backwards. Both develop striations and "dumbell" shapes predicted from other theories and observations as well. They also studied directed releases, highly asymmetric clouds which might be results of thruster firings and showed that rotation of the cloud was to be expected.

1.3.3 3-D Plasma Cloud Models

From the numerous 2-D studies, considerable understanding on the basic plasma physics processes regarding the plasma cloud evolution has been derived. However, the plasma cloud evolution is inherently a 3-D process and it has been long recognized that 3-D models are necessary. Phenomena which determine the electrodynamics, such as the parallel (to $\mathbf{B}$) expansion of the plasma cloud and the current coupling in a non-uniform ionosphere, can only be addressed with a fully 3-D model.

The major source of difficulty in addressing the 3-D evolution of a plasma cloud is the large ratio of the parallel to the perpendicular conductivities; for the ionosphere it is $\sigma_{\parallel}/\sigma_{\perp} \geq 10^6$. Ironically, it is this very anisotropy that suggested the derivation of the 2-D models which we reviewed in the previous section. Simply, it was assumed that the **B** lines are equipotentials, thus, parallel electric fields are impossible to set-up, and it was then possible to derive height-integrated equations for the (plasma) quantities of interest. However, it was recognized that this large ratio of conductivities is responsible for the process of *electric field mapping*: a perturbation electric field generated at some height in the ionosphere is mapped very effectively to other regions. The induced drifts in the ambient plasma result in a restructuring of the ambient density with the so called *image cloud* formation. Very early in the study of plasma clouds the development of layer models tried to provide an answer to the problem of the electrodynamic coupling between the cloud and other ionospheric regions. However, layer models are far from realistic. First, the ionosphere is varying with altitude and does not respond uniformly to applied density or electric field perturbations. Second, the plasma species within a density perturbation drift along and across the magnetic field due to the applied forces. Within the region of the plasma cloud, and probably outside, parallel electric fields are established dictating the evolution of the plasma structure. Therefore, one major outcome of the research effort in the last three decades is that the evolution of plasma clouds in the ionosphere is inherently a 3-D process and has to be addressed as such. In this work we shall investigate and elucidate some of the problems associated with 3-D modeling.

The first attempt to simulate 3-D plasma clouds was presented by *Voskoboynikov et al.* [1987]. The model equations they derived were based on the assumption of a weakly ionized plasma, thus, only ion-neutral collisions were included. They used the uniform background approximation. In their simulations they used arbitrary values for the perpendicular and parallel transport coefficients so that they became comparable in the two directions. In that way they avoided all the problems related with the anisotropy which characterizes the plasma evolution; however, it will be shown later in this work that proper theoretical and numerical treatment of the directional anisotropy must be the cornerstone of any 3-D analysis. Such approximations applied by the authors are far from the real ionospheric conditions and do not address the current coupling issue appropriately. For large clouds the parallel scale of the disturbance appeared to be comparable with the ionospheric scales. The main characteristics of their cloud evolution were the formation of ion and electron ellipsoids and depletions. They identified two separate processes with regard to the development of the electric field within the cloud: the first due to an applied external electric field and the second due to diffusion. However, their results can not be taken as representative of a real plasma cloud evolution but can only be used for the qualitative analysis of various plasma processes.

Zalesak et al. [1988] performed a very preliminary numerical calculation on a model developed by *Drake et al.* [1985]. With the use of a water bag model with circular cross section across and ellipsoidal along **B** they detected strong shear at the edges of the cloud. However, their results cannot be compared with a real cloud situation. Using the same analytical model *Drake et al.* [1988] examined the equilibrium and stability of 3-D clouds. They found that for a waterbag model the cloud rotated around the **B** axis and developed a sheared azimuthal plasma flow transverse to **B**. At equilibrium the potential is constituted by an ambipolar part and a polarization part due to a uniform neutral wind. Stability analysis showed that the $\mathbf{E} \times \mathbf{B}$ gradient drift instability can be stabilized by the shear of the azimuthal flow. Their conclusion was that striations in F region clouds should be stable to further bifurcations. Similar results were reported by *Zalesak et al.* [1990]. There are several problems with the above work. The clouds considered by these authors are very elongated structures along **B**. This is the result of a coordinate transformation done in order to achieve a system with isotropic conductivities. The water-bag model used is a very crude approximation to the density gradients that appear in a real cloud. Finally, the assumption of a uniform ionosphere neglects the ambient variability and, consequently, does not address the problem of current coupling correctly. It is then impossible to apply to real conditions where initially the cloud will have comparable lengths in the transverse and parallel directions. As it will be shown in this work the inclusion of finite lengths and of an altitude varying ionosphere is nontrivial and has significant impact on the plasma cloud evolution. Nevertheless, the analysis of the above authors is a valuable analytical tool since it simplifies and elucidates the very complex 3-D process associated with the evolution of a plasma cloud.

Gatsonis and Hastings [1990 and 1991] presented the theory and initial model simulations from a fully 3-D model which, along with other advances, accounted for a real nonuniform ionosphere and current coupling with other ionospheric regions. *Ma and Schunk* [1991] developed a 3-D model for a plasma cloud resulting from an artificial release in the ionosphere. The model was based on a simplification of a previously derived plasma transport theory. The major shortcoming is that it does not address the problem of current coupling appropriately. The background plasma is considered to be uniform and closure is enforced in the immediate vicinity of the cloud. It will be shown later in this work that it is necessary to account for the electrodynamic coupling of the cloud with other ionospheric layers since this is the process that determines the self-consistent electric fields within the cloud. It will also become apparent from our work that the nonuniform background is not a trivial extension to a uniform model, since it requires developments both in the theory and the numerics. Another simplification in their model is the neglect of the collision terms in the momentum associated with velocity differences between charged particles. However, the velocity difference between charged species can not be ignored, especially in neutral releases with large initial velocity. The model they developed included inertia terms perturbatively as well as an approximation to the stress tensor. In their simulations they used ion and neutral clouds initialized as Gaussians with prescribed density and length scales. Although ionization is included in their model the simulation was applied only to fully ionized clouds. In such cases the inclusion of a unidirectional neutral wind, although useful for analytical purposes, can not be substantiated physically. Also their neutral model -a Gaussian density distribution travelling with a unidirectional velocity- is far from the real conditions that occur during artificial release experiments. It is essential, and it will be clarified later in this work, to model the details of the neutral expansion if accurate data comparisons and predictions are to be made. Some of the effects captured in their work include the rotation of clouds about the **B** field and the rapid expansion along it. In the presence of a unidirectional neutral wind the cloud drifted in the direction of the applied wind with reduced speeds. In the ambient plasma they predicted the development of a hole and symmetric bumps due to the expansion of the plasma cloud.

1.4 Research Approach

The presence of an ion-neutral cloud in the ionosphere may be a result of a deliberate or experimental release, as explained in the introduction. A neutral cloud is produced through outgassing, thruster firing or experimental release. As it expands it reacts with the ambient ionospheric species and creates an ion cloud. The ion cloud in turn drifts across and along **B** while undergoing various electrodynamical and chemical interactions. Thus, a complete model of an artificial cloud should include models for *both* the neutral and ion cloud 3-D dynamics.

In the introduction we discussed the problems and identified the shortcomings of the models developed to date. Using this critical review as a guide for the requirements of a 3-D cloud model, we decided to start with as few simplifications as possible. Keeping the model general will enable us to identify the important mechanisms and also to apply it to a variety of ionospheric releases. There are several requirements for the model

- Finite lengths.

  Finite lengths in both the transverse and parallel directions is inherent to a 3-D model.

- Elastic Collisions.

  This is the mechanism for momentum transfer between the cloud and the ambient species. It requires the definition of all the collision processes as well as complete models for evaluating collision frequencies.

- Finite Temperature for the species

  Diffusion is an important mechanism for the drift and deformation of plasma clouds. In an applied **B** field, 3-D diffusion is a very non-isotropic process.

- Variable background neutral and ion densities.

  It has been long recognized that a plasma cloud connects electrically with other remote regions of the ionosphere. The role of the other ionospheric region in the drift of plasma non-uniformities is especially significant. An altitude varying ionosphere is therefore necessary to address the current coupling between the cloud and the ionosphere.

- Ambient neutral wind, electric fields and gravity

  They all affect the plasma transport and stability. To apply them it is necessary to have a model of the equilibrium ambient ionosphere.

- Chemistry.

  This is the mechanism for creation and depletion of the plasma species. It requires the knowledge of the complicated chemical interactions and the appropriate reaction rates for ionospheric conditions. There is a limitation in the complexity of the chemistry model imposed by the number of species which we are able to follow. Also, the issue of chemistry is related with that of the momentum transfer due to inelastic collisions.

- Variable initial conditions.

  The initial conditions of the release determine the cloud evolution.

- Model of the neutral flow.

  A detailed model of the 3-D expansion of the neutral gases within the plasma cloud is necessary. The neutral force is in many occasions the driving force of the plasma dynamics.

There are three aspects that are equally emphasized in this work:

- Theory development - Plasma Cloud Electrodynamics.

  We will present the detailed theoretical formulation of the problem. Emphasis will be placed on the current balance between the cloud and the background plasma. The current balance will determine the self-consistent electric fields and, subsequently, dictate the plasma cloud dynamics. Basic plasma electrodynamics associated with the 3-D character of the phenomena will be thoroughly investigated. Simple analytic models will be derived and will be used as guidelines to understand the complex fully 3-D numerical results.

- Computational Methods.

  The 3-D model equations will be solved numerically. This will require development and application of special computational methods. Two types of equations are to be solved: 3-D hyperbolic equations and a 3-D elliptic equation with very dissimilar coefficients.

- Applications.

  In the numerical simulations we will use realistic parameters from typical spacecraft operations that contribute to the formation of the plasma cloud. Model predictions will be discussed against existing experimental data. The results can be applied to the Shuttle, the Space Station or any other spacecraft with the potential of releasing neutrals and/or plasma into the ambient environment.

Chapter 2

Fluid Model for the Plasma Motion

We begin this chapter with the development of the fluid model for the plasma motion. We discuss the form of the continuity and momentum equations for the species considered. From the solution to the momentum equations we derive the velocity and present the plasma transport coefficients. Finally, we discuss the undergoing collision processes and present models for the evaluation of collision frequencies.

2.1 Continuity and Momentum Equations

We choose to work with two coordinate systems. Given the latitude of the release of the neutral cloud we construct an orthogonal coordinate system, fixed to the Earth system shown in Figure 2.1. In that system, **E** points to the east, **N** points to the north, and **H** refers to the altitude. This system allows us to include the spatial variability of the ambient ionospheric parameters. However, the coordinate system which is most suitable for analytical purposes is the field-aligned system. Given the latitude and altitude of the release, this system has its origin at the point of the release. The **z** axis is parallel to the local magnetic field line, the **y** axis is parallel to the **E** direction, and the **x** direction is perpendicular to both the **z** and **y** directions. A simple rotation enables us to move between the two coordinate systems.

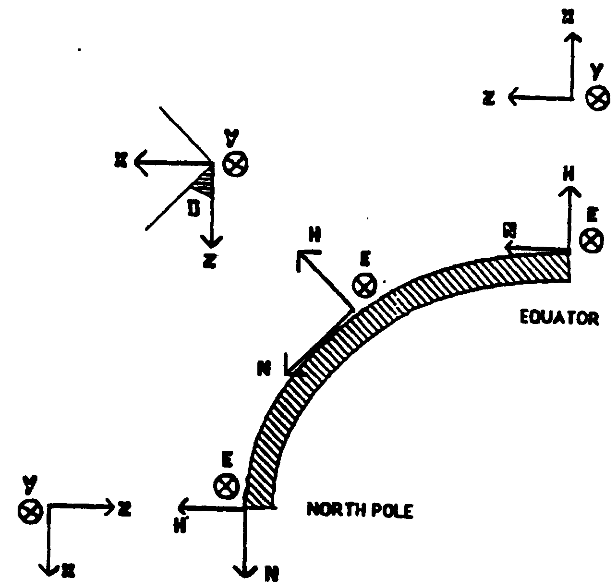

Figure 2.1: Fixed to earth and the field aligned system.

The ambient ionosphere in this study is assumed to be composed of O, He and H neutrals and O^+ ions. Given the latitude and time for the release we construct the neutral environment using the MSIS model and the electron density using the IRI model. We assume that the ambient ionosphere is quasineutral and thus take the O^+ with density equal to that of the electrons. This is a simplification to the altitude dependent ionic composition and implies that at altitudes below 250 km O_2^+ and NO^+ interact like O^+. For the temperatures we assumed isothermal ions and electrons with $T_{O^+} = 0.1$ eV and $T_e = 0.2$ eV respectively. Another important parameter in the dynamics of the ionosphere is the magnetic field. In all the applications in this study we considered an average value of $B = 0.35 \times 10^{-4}$ Tesla.

We take the plasma cloud to consist of contaminant ions with density n_{r^+} and velocity $\mathbf{V}_{r^+}$. The density of the ambient ions is n_{a^+}, and their velocity is $\mathbf{V}_{a^+}$ where $a^+ \equiv O^+$. Electrons have a density n_e and velocity $\mathbf{V}_e$. The continuity equation for any species $t = a^+, r^+, e$ is

$$\frac{\partial n_t}{\partial t} + \nabla \cdot (n_t \mathbf{V}_t) = \sum_b S_t^b \tag{2.1}$$

The term S_t^b on the right-hand side of the continuity equation is the production or loss rate of the species t due a chemical reaction b.

In the momentum balance we take into account electric fields, pressure forces, gravity, and all collisions.

$$\begin{aligned}\frac{\partial \mathbf{V}_t}{\partial t} + \mathbf{V}_t \cdot \nabla \mathbf{V}_t &= \frac{q_t}{m_t}(\mathbf{E} + \mathbf{V}_t \times \mathbf{B}) - \sum_{j \neq t} \nu_{tj}(\mathbf{V}_t - \mathbf{V}_j) - \sum_n \nu_{tn}(\mathbf{V}_t - \mathbf{U}_n) \\ &\quad - \frac{\nabla P_t}{n_t m_t} - \sum_b \mathbf{R}_t^b + \mathbf{g} \end{aligned} \tag{2.2}$$

Here $\mathbf{V}_t$ is the velocity, m_t is the mass of the species, $\mathbf{E}$ is the electric field, ν_{tj} is the collision frequency for momentum transfer between the charged species t and j, P_t is the pressure, ν_{tn} is the collision frequency for momentum transfer between the species t and a neutral n, and $\mathbf{g}$ is the gravitational acceleration. The term $\mathbf{R}_t^b$ accounts for the momentum transfer due to the inelastic collisions of the species t in a reaction b. A general operator for inelastic collisions is not available and depends on the specific reaction [*Burgers*, 1966; *Hastings and Gatsonis*, 1989]. The form of the operator used here is

$$\mathbf{R}_t^b = \frac{S_t^b}{n_t}(\mathbf{V}_t - \mathbf{V}_t^b) \tag{2.3}$$

where S_t^b is the rate of production or depletion of the species t in a reaction b and $\mathbf{V}_t^b$ is the velocity with which the species is created or lost in the reaction. We will discuss specific forms of the reactive operators in the applications considered in a Chapter 7.

A major simplification in the momentum equations for the plasma species can be achieved if we neglect the unsteady and inertia terms. Using a scaling analysis of the momentum equation we can compare the various acceleration terms containing the velocity of a species. In general we can write

Unsteady	Inertia	Lorentz	Pressure	Frictional
$\frac{V}{\tau}$	$\frac{V^2}{L}$	$\frac{qE}{m} + \Omega V$	$\frac{V_{th}^2}{L}$	νV

Here V is the nonuniform characteristic drift velocity, τ is the time scale for setting new forces on the plasma, L is a characteristic scale for velocity change and Ω is the gyrofrequency of the species t defined as $\Omega_t = q_t B/m_t$. With the assumption that the time scales of interest are much larger than the gyroperiod or the collision times, i.e., $\tau \gg \Omega^{-1}$ or ν^{-1} the unsteady term can be neglected. This assumption restricts the analysis to the low frequencies. The same condition is sufficient to allow the neglect of the off diagonal terms in the pressure tensure and, thus, take $P_t = n_t k T_t$. The inertia term, $\mathbf{V} \cdot \nabla \mathbf{V}$, can be neglected as long as $V/L \ll \Omega$ or $V/L \ll \nu$. This imposes a condition on the magnitude of the drift velocity. If this condition is satisfied, then the force balance is determined between the Lorentz, the frictional and the pressure terms. The electric field is still an unknown which has to be determined through the current balance. For typical contaminants or released materials the limiting magnitude of the drift velocity is shown in Table 2.1. The assumption of steady state momentum was

	$\Omega(\mathrm{s}^{-1})$	ΩL (km/s)	
		L =0.1 km	$L = 1$ km
H_2O^+	240	24	240
CO_2^+	100	10	100
Ba^+	32	3.2	32

Table 2.1: Gyrofrequency (s^{-1}), Maximum Drift Velocity (km/s) for different cloud scales L (km).

examined a posteriori for its validity. With the above approximations the momentum equations can be written in the following form

$$\frac{\mathbf{F}_t}{m_t} + \frac{q_t}{m_t}(\mathbf{V}_t \times \mathbf{B}) - (\nu_{ta} + \nu_{tr} + \sum_{j \neq t} \nu_{tj} + \nu_t^b)\mathbf{V}_t = 0 \tag{2.4}$$

where the force for the species t is

$$\mathbf{F}_t = q_t \mathbf{E} + m_t \nu_{ta} \mathbf{U}_a + m_t \nu_{tr} \mathbf{U}_r + m_t \nu_t^b \mathbf{V}_t^b + \sum_{j \neq t} m_t \nu_{tj} \mathbf{V}_j - \frac{\nabla P_t}{n_t} + m_t \mathbf{g} \tag{2.5}$$

The ambient neutral velocity, often in space plasma physics referred to as a wind, is denoted by $\mathbf{U}_a$ while the velocity of the released neutrals is $\mathbf{U}_r$. Note that by assuming that the ambient neutrals drift with the same velocity, then ν_{ta} accounts for collisions with all the neutral ambient species considered, i.e., $\nu_{ta} = \sum_n \nu_{tn}$. We have added also the term ν_t^b to be the collision frequency for momentum transfer due to the reaction b; using the definition of the reaction operator Eq. (2.3) $\nu_t^b = S_t^b/n_t$. This reaction term appears under the assumption that $\mathbf{V}_t \neq \mathbf{V}_t^b$. In the case where ions are created in a reaction with the velocity of the neutral, i.e., $\mathbf{V}_t^b = \mathbf{U}_r$ or $\mathbf{V}_t^b = \mathbf{U}_a$, the $\nu_{ta} = \sum_n \nu_{tn} + \nu_t^b$ and similarly $\nu_{tr} = \nu_{tr} + \nu_t^b$. The momentum equations written in this form allow us to define the total collision frequency for momentum transfer due to elastic collisions for any of the plasma species as

$$
\begin{aligned}
\nu_{a+} &= \sum_n \nu_{a+n} + \nu_{a+r} + \nu_{a+r+} + \nu_{a+e} + \sum_b \nu_{a+}^b && (2.6)\\
\nu_{r+} &= \sum_n \nu_{r+n} + \nu_{r+r} + \nu_{r+a+} + \nu_{r+e} + \sum_b \nu_{r+}^b && (2.7)\\
\nu_{e} &= \sum_n \nu_{en} + \nu_{er} + \nu_{ea+} + \nu_{er+} + \sum_b \nu_{e}^b && (2.8)
\end{aligned}
$$

where the summation index n is to be taken over the ambient neutrals.

2.2 Solution of the Momentum Equation

We have shown in (2.5) that the momentum equation for any species can be written in the form

$$\nu_t \mathbf{V}_t - \frac{q_t}{m_t}(\mathbf{V}_t \times \mathbf{B}) = \frac{\mathbf{F}_t}{m_t} \tag{2.9}$$

where ν_t is the total collision frequency. In the field-aligned system for any vector $\mathbf{A}$ we can write $\mathbf{A} = \mathbf{A}_\perp + \mathbf{A}_{||}$. With the use of vector identities we can obtain the velocity components

$$
\begin{aligned}
\mathbf{V}_{t\perp} &= k_{tP}\mathbf{F}_{t\perp} + k_{tH}\mathbf{F}_{t\perp} \times \mathbf{b}\\
\mathbf{V}_{t||} &= k_{t||}\mathbf{F}_{t||} && (2.10)
\end{aligned}
$$

where, $k_{tP} = \kappa_t/q_t B(1 + \kappa_t^2)$ is the Pedersen coefficient, $k_{tH} = \kappa_t^2/q_t B(1 + \kappa_t^2)$ is the Hall coefficient, and $k_{t||} = 1/m_t\nu_t$ is the parallel coefficient. For a given force these coefficients will give the appropriate transport coefficient, i.e., they express the response of the plasma to a given force. In the above expressions, $\kappa_t = \Omega_t/\nu_t$ is the ratio of the gyrofrequency to the total collision frequency. The above solution for the velocity for a species t, although exact, is not in closed form since it contains the velocities of the other species through the force term $\mathbf{F}_t$.

2.2.1 The Correction to the Velocity due to Inertia

We proceed to evaluate the unsteady and inertia terms perturbately. The velocity of the species t as given by Eq.(2.10) is the solution to the momentum equation under the approximation $d\mathbf{V}_t/dt \simeq 0$. If $\mathbf{V}_t$ is known we can evaluate the correction due to this approximation. Note that the term $d\mathbf{V}_t/dt$ is formally the error in the momentum equation due to the steady-state approximation- here we refer to it as the substantial derivative.

$$\tilde{\mathbf{F}}^{(\mathrm{iner})} = \left(\frac{\partial \mathbf{V}_t}{\partial t} + \mathbf{V}_t \cdot \nabla \mathbf{V}_t\right) m_t \tag{2.11}$$

With $\tilde{\mathbf{F}}_t^{(\mathrm{iner})}$ known we can use Eq.(2.10) to write for the correction to the velocity

$$\begin{aligned} \widetilde{\mathbf{V}}_{t\perp}^{(\mathrm{iner})} &= k_{tP}\tilde{\mathbf{F}}_{t\perp}^{(\mathrm{iner})} + k_{tH}\tilde{\mathbf{F}}_{t\perp}^{(\mathrm{iner})} \times \mathbf{b} \\ \widetilde{\mathbf{V}}_{t\|}^{(\mathrm{iner})} &= k_{t\|}\tilde{\mathbf{F}}_{t\|}^{(\mathrm{iner})} \end{aligned} \tag{2.12}$$

The role of the unsteady and inertia terms in the current balance will be addressed in the discussion of the current closure.

2.3 Perpendicular Plasma Motion

2.3.1 Electron Perpendicular Flow

For the perpendicular component of the electron velocity we can write using (2.10)

$$\mathbf{V}_{e\perp} = k_{eP}\mathbf{F}_{e\perp} + k_{eH}\mathbf{F}_{e\perp} \times \mathbf{b} \tag{2.13}$$

This expression can be further simplified by examining the magnitude of the collisionality ratio for electrons at altitudes between 100 and 1000 km for both the ambient and cloud conditions. The electron gyrofrequency is $\Omega_e = -7 \times 10^6$. The plasma cloud is assumed to have a maximum neutral density of 10^{18} m^{-3} and a maximum ion density of 10^{14} m^{-3}. The densities considered here are orders of magnitude larger than those observed about the Shuttle or similar vehicles. Typical contaminant Shuttle densities are $N_{H_2O} \sim 10^{16}$ m^{-3} and $N_{H_2O+} \sim 10^{11}$ m^{-3}. The maximum collision frequencies based on models presented in a subsequent section are shown in Table 2.2. We see that for both the ambient and the cloud conditions the collisionality ratio is

Ambient		Cloud	
$\nu_{eO}(s^{-1})$	1000	$\nu_{eH_2O}(s^{-1})$	2×10^5
$\nu_{eO^+}(s^{-1})$	100	$\nu_{eH_2O^+}(s^{-1})$	3.5×10^5
$\kappa_e \geq$	7×10^3		20

Table 2.2: Maximum electron collision frequencies for momentum transfer and the collisionality ratio, in the F ionosphere.

very large, i.e., $|\kappa_e| \gg 1$. From the definition of the Hall and Pedersen coefficients it is easy to show that

$$\left|\frac{k_{Pe}}{k_{He}}\right| = \left|\frac{1}{\kappa_e}\right| \ll 1 \tag{2.14}$$

The Pedersen term in the perpendicular electron velocity can be neglected since it will be much smaller than the Hall term. Furthermore, since we expect that for both ambient and cloud conditions $\left|\frac{\nu_{et}}{\Omega_e}\right| \ll 1$, we can neglect in the electron velocity all the contributions from the ion and neutral collisions, as well as from gravity, so that the velocity can be written finally as

$$\begin{bmatrix} V_{ex} \\ V_{ey} \end{bmatrix} = \begin{bmatrix} 0 & -\mu_H^e \\ \mu_H^e & 0 \end{bmatrix} \begin{bmatrix} E_x \\ E_y \end{bmatrix} - \begin{bmatrix} 0 & -D_{eH}^e \\ D_{eH}^e & 0 \end{bmatrix} \begin{bmatrix} \frac{1}{n_e}\frac{\partial n_e}{\partial x} \\ \frac{1}{n_e}\frac{\partial n_e}{\partial y} \end{bmatrix} \tag{2.15}$$

where $\mu_H^e = -\frac{1}{B}\frac{\kappa_e^2}{1+\kappa_e^2}$ is the electron Hall mobility (in Cs/kg) and $D_{eH} = -\frac{kT_e}{q_e B}\frac{\kappa_e^2}{1+\kappa_e^2}$ is the Hall electron diffusivity due to electron density gradients (in m²/s).

2.3.2 Ion Perpendicular Flow

In the ion momentum equations we write the force terms as

$$\mathbf{F}_{t\perp} = \mathbf{f}_{t\perp} + m_t\nu_{tj}\mathbf{V}_{j\perp} \tag{2.16}$$

where $j = a^+, r^+ \neq t$ and the components $\mathbf{f}_{t\perp}$ in the force is given by

$$\mathbf{f}_{t\perp} = q_t\mathbf{E}_\perp + m_t\nu_{te}\mathbf{V}_{e\perp} + m_t\nu_{ta}\mathbf{U}_{a\perp} + m_t\nu_{tr}\mathbf{U}_{r\perp} - \frac{1}{n_t}\nabla_\perp P_t + m_t\mathbf{g}_\perp \tag{2.17}$$

The implicit solution to the momentum equation (Eq. 2.10) give the perpendicular ion velocities in the form

$$\mathbf{V}_{t\perp} = k_{tP}\mathbf{F}_{t\perp} + k_{tH}\mathbf{F}_{t\perp} \times \mathbf{b} \tag{2.18}$$

For any vector $\mathbf{A}_\perp$ we can write $\mathbf{A}_\perp = A_x\mathbf{x} + A_y\mathbf{y}$ and $A_\perp \times \mathbf{b} = A_y\mathbf{x} - A_x\mathbf{y}$. Using these vector relations and upon substitution into the system of perpendicular velocity equations (2.18) we obtain, after some rearrangement, a system of equations with the perpendicular velocity components as unknowns. This system can be written in matrix form as

$$[A]\,[V_t] = [S] \tag{2.19}$$

where

$$\left[\, A \,\right] =$$

$$\begin{bmatrix} 1 & 0 & -k_{r^+P}m_{r^+}\nu_{r^+a^+} & -k_{r^+H}m_{r^+}\nu_{r^+a^+} \\ 0 & 1 & k_{r^+H}m_{r^+}\nu_{r^+a^+} & -k_{r^+P}m_{r^+}\nu_{r^+a^+} \\ -k_{a^+P}m_{a^+}\nu_{a^+r^+} & -k_{a^+H}m_{a^+}\nu_{a^+r^+} & 1 & 0 \\ k_{a^+H}m_{a^+}\nu_{a^+r^+} & -k_{a^+P}m_{a^+}\nu_{a^+r^+} & 0 & 1 \end{bmatrix} \tag{2.20}$$

The unknown velocity vector is

$$[V_t] = (V_{r^+x}, V_{r^+y}, V_{a^+x}, V_{a^+y}) \tag{2.21}$$

and the source term vector is

$$\begin{bmatrix} S_1 \\ S_2 \\ S_2 \\ S_4 \end{bmatrix} = \begin{bmatrix} k_{r^+P}f_{r^+x} + k_{r^+H}f_{r^+y} \\ k_{r^+P}f_{r^+y} - k_{r^+H}f_{r^+x} \\ k_{a^+P}f_{a^+x} + k_{a^+H}f_{a^+y} \\ k_{a^+P}f_{a^+y} - k_{a^+H}f_{a^+x} \end{bmatrix} \tag{2.22}$$

The solution of the system of the ion momentum equations yields the ion velocities. After some manipulation the perpendicular velocity of the ions $V_{t\perp}$ where $t = a^+, r^+$ can be written with the use of transport coefficients in the form

$$\begin{bmatrix} V_{tx} \\ V_{ty} \end{bmatrix} = \begin{bmatrix} \mu_P^t & -\mu_H^t \\ \mu_H^t & \mu_P^t \end{bmatrix} \begin{bmatrix} E_x \\ E_y \end{bmatrix} - \sum_{j=a^+,r^+,e} \left(\begin{bmatrix} D_{jP}^t & -D_{jH}^t \\ D_{jH}^t & D_{jP}^t \end{bmatrix} \begin{bmatrix} \frac{1}{n_j}\frac{\partial n_j}{\partial x} \\ \frac{1}{n_j}\frac{\partial n_j}{\partial y} \end{bmatrix} \right)$$
$$+ \begin{bmatrix} w_{rP}^t & -w_{rH}^t \\ w_{rH}^t & w_{rP}^t \end{bmatrix} \begin{bmatrix} U_{rx} \\ U_{ry} \end{bmatrix} + \begin{bmatrix} w_{aP}^t & -w_{aH}^t \\ w_{aH}^t & w_{aP}^t \end{bmatrix} \begin{bmatrix} U_{ax} \\ U_{ay} \end{bmatrix}$$
$$+ \begin{bmatrix} \beta_P^t & -\beta_H^t \\ \beta_H^t & \beta_P^t \end{bmatrix} \begin{bmatrix} g_x \\ g_y \end{bmatrix} \quad (2.23)$$

These transport coefficients describe the response of the plasma to the external forces. The diffusion coefficients of ions a^+ associated with density gradients of ions a^+ are

$$D_{a^+P}^{a^+} = \left[-m_{a^+} m_{r^+} \nu_{a^+r^+} \nu_{r^+a^+} k_{r^+P} \left(k_{a^+P}^2 + k_{a^+H}^2\right) + k_{a^+P}\right] [kT_{a^+}] / C_\perp \quad (2.24)$$
$$D_{a^+H}^{a^+} = \left[-m_{a^+} m_{r^+} \nu_{a^+r^+} \nu_{r^+a^+} k_{r^+H} \left(k_{a^+P}^2 + k_{a^+H}^2\right) - k_{a^+H}\right] (kT_{a^+}) / C_\perp \quad (2.25)$$

The denominator $C_\perp$ is given by

$$C_\perp = m_{r^+}^2 m_{a^+}^2 \nu_{a^+r^+}^2 \nu_{r^+a^+}^2 (k_{a^+P}^2 + k_{a^+H}^2)(k_{r^+P}^2 + k_{r^+H}^2)$$
$$+2 m_{r^+} m_{a^+} \nu_{a^+r^+} \nu_{r^+a^+} (k_{a^+H} k_{r^+H} - k_{a^+P} k_{r^+P}) + 1 \quad (2.26)$$

The diffusion coefficients of ions a^+ associated with density gradients of ions r^+ are

$$D_{r^+P}^{a^+} = \left[-m_{a^+}^2 m_{r^+} \nu_{a^+r^+}^2 \nu_{r^+a^+} \left(k_{r^+P}^2 + k_{r^+H}^2\right)\left(k_{a^+P}^2 + k_{a^+H}^2\right)\right.$$
$$\left. - m_{a^+} \nu_{a^+r^+} (k_{a^+H} k_{r^+H} - k_{a^+P} k_{r^+P})\right] (kT_{r^+}) / C_\perp \quad (2.27)$$
$$D_{r^+H}^{a^+} = \left[-m_{a^+} \nu_{a^+r^+} (k_{a^+P} k_{r^+H} + k_{r^+P} k_{a^+H})\right] (kT_{r^+}) / C_\perp \quad (2.28)$$

The diffusion coefficients of ions a^+ associated with density gradients of electrons are

$$D_{eP}^{a^+} = \left[m_{a^+}^2 m_{r^+} \nu_{a^+r^+} \nu_{r^+a^+} \nu_{a^+e} k_{r^+H} \left(k_{a^+P}^2 + k_{a^+H}^2\right) + m_{a^+} \nu_{a^+e} k_{a^+H}\right.$$
$$\left. + m_{a^+} m_{r^+} \nu_{a^+r^+} \nu_{r^+e} (k_{r^+P} k_{a^+H} + k_{a^+P} k_{r^+H})\right] (-k_{eH} kT_e) / C_\perp \quad (2.29)$$
$$D_{eH}^{a^+} = \left[-m_{a^+}^2 m_{r^+} \nu_{r^+a^+} \nu_{a^+r^+} \nu_{a^+e} k_{r^+P} \left(k_{a^+P}^2 + k_{a^+H}^2\right) + m_{a^+} \nu_{a^+e} k_{a^+P}\right.$$
$$- m_{a^+}^2 m_{r^+}^2 \nu_{a^+r^+}^2 \nu_{r^+a^+} \nu_{r^+e} \left(k_{r^+P}^2 + k_{r^+H}^2\right)\left(k_{a^+P}^2 + k_{a^+H}^2\right)$$
$$\left. - m_{a^+} m_{r^+} \nu_{r^+a^+} \nu_{a^+e} (k_{r^+H} k_{a^+H} - k_{r^+P} k_{a^+P})\right] (-k_{eH} kT_e) / C_\perp \quad (2.30)$$

The diffusion coefficients of ions r^+ associated with density gradients of ions r^+ are

$$D^{r+}_{r+P} = \left[-m_{a+}m_{r+}\nu_{a+r+}\nu_{r+a+}k_{a+P}\left(k^2_{r+P}+k^2_{r+H}\right)+k_{r+P}\right](kT_{r+})/C_\perp \tag{2.31}$$

$$D^{r+}_{r+H} = \left[-m_{a+}m_{r+}\nu_{a+r+}\nu_{r+a+}k_{a+H}\left(k^2_{r+P}+k^2_{r+H}\right)-k_{r+H}\right](kT_{r+})/C_\perp \tag{2.32}$$

The diffusion coefficients of ions r^+ associated with density gradients of ions a^+ are

$$\begin{aligned} D^{r+}_{a+P} &= \left[-m_{a+}m^2_{r+}\nu_{a+r+}\nu^2_{r+a+}\left(k^2_{r+P}+k^2_{r+H}\right)\left(k^2_{a+P}+k^2_{a+H}\right)\right. \\ &\quad \left.-m_{r+}\nu_{r+a+}\left(k_{a+H}k_{r+H}-k_{a+P}k_{r+P}\right)\right](kT_{a+})/C_\perp \end{aligned} \tag{2.33}$$

$$D^{r+}_{a+H} = \left[-m_{r+}\nu_{r+a+}\left(k_{a+P}k_{r+H}+k_{r+P}k_{a+H}\right)\right](kT_{a+})/C_\perp \tag{2.34}$$

The diffusion coefficients of ions r^+ associated with density gradients of electrons are

$$\begin{aligned} D^{r+}_{eP} = &\left[m_{a+}m^2_{r+}\nu_{a+r+}\nu_{r+a+}\nu_{r+e}k_{a+H}\left(k^2_{r+P}+k^2_{r+H}\right)+m_{r+}\nu_{r+e}k_{r+H}\right. \\ &\left.+m_{a+}m_{r+}\nu_{r+a+}\nu_{a+e}\left(k_{r+P}k_{a+H}+k_{a+P}k_{r+H}\right)\right](-k_{eH}kT_e)/C_\perp \end{aligned} \tag{2.35}$$

$$\begin{aligned} D^{r+}_{eH} = &\left[m_{a+}m^2_{r+}\nu_{a+r+}\nu_{r+a+}\nu_{r+e}k_{a+P}\left(k^2_{r+P}+k^2_{r+H}\right)-m_{r+}\nu_{r+e}k_{r+P}\right. \\ &m^2_{a+}m^2_{r+}\nu_{a+r+}\nu^2_{r+a+}\nu_{a+e}\left(k^2_{r+P}+k^2_{r+H}\right)\left(k^2_{a+P}+k^2_{a+H}\right) \\ &\left.m_{a+}m_{r+}\nu_{r+a+}\nu_{a+e}\left(k_{r+H}k_{a+H}-k_{r+P}k_{a+P}\right)\right](k_{eH}kT_e)/C_\perp \end{aligned} \tag{2.36}$$

A careful examination of these transport coefficients reveals very important and simple relations among them. First, a generalized Einstein relation holds between the mobility μ^t_j of the species t in the direction $j = P$ or H and the diffusion coefficients

$$\mu^t_j = D^t_{r+j}\frac{q_{r+}}{kT_{r+}} + D^t_{a+j}\frac{q_{a+}}{kT_{a+}} + D^t_{ej}\frac{q_e}{kT_e} \tag{2.37}$$

The neutral wind transport coefficients w^t_{nj} of a species t in the direction j due to the neutral wind of the neutrals $n = a$ or r are related to the diffusion coefficients as follows

$$w^t_{nj} = D^t_{r+j}\frac{m_{r+}\nu_{r+n}}{kT_{r+}} + D^t_{a+j}\frac{m_{a+}\nu_{a+n}}{kT_{a+}} \tag{2.38}$$

Finally, the following relationships hold between the diffusion coefficients and the coefficients for gravity β^t_j where $j = P$ or H

$$\beta^t_j = D^t_{r+j}\frac{m_{r+}}{kT_{r+}} + D^t_{a+j}\frac{m_{a+}}{kT_{a+}} + D^t_{ej}\frac{m_e}{kT_e} \tag{2.39}$$

2.4 Parallel Plasma Motion

In the electron momentum equations we write the parallel force terms as

$$\begin{aligned}
\mathbf{F}_{r+\|} &= \mathbf{f}_{r+\|} + m_{r+}\nu_{r+a+}\mathbf{V}_{a+\|} + m_{r+}\nu_{r+e}\mathbf{V}_{e\|} \\
\mathbf{F}_{a+\|} &= \mathbf{f}_{a+\|} + m_{a+}\nu_{a+r+}\mathbf{V}_{r+\|} + m_{r+}\nu_{r+e}\mathbf{V}_{e\|} \\
\mathbf{F}_{e\|} &= \mathbf{f}_{e\|} + m_{e}\nu_{ea+}\mathbf{V}_{a+\|} + m_{e}\nu_{es+}\mathbf{V}_{s+\|}
\end{aligned} \tag{2.40}$$

where the components $\mathbf{f}_{t\|}$ of the force is given by

$$\mathbf{f}_{t\|} = q_t\mathbf{E}_{\|} + m_t\nu_{ta}\mathbf{U}_{a\|} + m_t\nu_{ts}\mathbf{U}_{r\|} - \frac{1}{n_t}\nabla_{\|}P_t + m_t\mathbf{g}_{\|} \tag{2.41}$$

The parallel velocity is given by the implicit solution of the momentum equation in the form

$$\mathbf{V}_{t\|} = \frac{1}{m_t\nu_t}\mathbf{F}_{t\|} \tag{2.42}$$

Using the above relations and after some rearrangement we obtain a system of equations whose unknowns are the three parallel velocity components, V_{a+z}, V_{r+z}, V_{ez} . The system can be written in matrix form as

$$[A]\,[V_t] = [S] \tag{2.43}$$

where

$$\left[\, A \,\right] = \begin{bmatrix} -1 & \frac{\nu_{ea+}}{\nu_e} & \frac{\nu_{er+}}{\nu_e} \\ \frac{\nu_{a+e}}{\nu_{a+}} & -1 & \frac{\nu_{a+r+}}{\nu_{a+}} \\ \frac{\nu_{r+e}}{\nu_{r+}} & \frac{\nu_{r+a+}}{\nu_{r+}} & -1 \end{bmatrix} \tag{2.44}$$

where the unknown vector is

$$[V_t] = (V_{ez}, V_{a+z}, V_{r+z}) \tag{2.45}$$

and the source term vector is

$$\begin{bmatrix} S_1 \\ S_2 \\ S_3 \end{bmatrix} = \begin{bmatrix} -\frac{1}{B}\frac{\Omega_e}{\nu_e}E_z - \frac{\nu_{ea}}{\nu_e}U_{az} - \frac{\nu_{er}}{\nu_e}U_{sz} + \frac{1}{m_e\nu_e n_e}\nabla_z P_e - \frac{1}{\nu_e}g_z \\ -\frac{1}{B}\frac{\Omega_{r+}}{\nu_{r+}}E_z - \frac{\nu_{r+a}}{\nu_{r+}}U_{az} - \frac{\nu_{r+s}}{\nu_{r+}}U_{rz} + \frac{1}{m_{r+}\nu_{r+}n_{r+}}\nabla_z P_{r+} - \frac{1}{\nu_{r+}}g_z \\ -\frac{1}{B}\frac{\Omega_{a+}}{\nu_{a+}}E_z - \frac{\nu_{a+a}}{\nu_{a+}}U_{az} - \frac{\nu_{a+r}}{\nu_{a+}}U_{rz} + \frac{1}{m_{a+}\nu_{a+}n_{a+}}\nabla_z P_{a+} - \frac{1}{\nu_{a+}}g_z \end{bmatrix} \tag{2.46}$$

The solution of the system yields the parallel velocity of a species $t = a^+, r^+, e$ in the form

$$\mathbf{V}_{t\|} = \mu_{\|}^t \mathbf{E}_\| - \sum_{j=a^+,r^+,e} D_{j\|}^t \frac{\nabla_\| n_j}{n_j} + w_{r\|}^t \mathbf{U}_{r\|} + w_{a\|}^t \mathbf{U}_{a\|} + \beta_\|^t \mathbf{g}_\| \tag{2.47}$$

The parallel diffusion coefficients of ambient ions due to density gradients of a^+, r^+ and e are

$$D_{a^+\|}^{a^+} = \frac{\nu_e \nu_{r^+} - \nu_{er^+} \nu_{r^+e}}{C_\|} \frac{kT_{a^+}}{m_{a^+}} \tag{2.48}$$

$$D_{r^+\|}^{a^+} = \frac{\nu_e \nu_{a^+r^+} + \nu_{er^+} \nu_{a^+e}}{C_\|} \frac{kT_{r^+}}{m_{r^+}} \tag{2.49}$$

$$D_{e\|}^{a^+} = \frac{\nu_{a^+r^+} \nu_{r^+e} + \nu_{a^+e} \nu_{r^+}}{C_\|} \frac{kT_e}{m_e} \tag{2.50}$$

The denominator $C_\|$ is given by

$$\begin{aligned} C_\| &= \nu_e \nu_{a^+} \nu_{r^+} - \nu_e \nu_{a^+r^+} \nu_{r^+a^+} - \nu_{ea^+} \nu_{a^+e} \nu_{r^+} \\ &\quad - \nu_{ea^+} \nu_{a^+s} \nu_{r^+e} - \nu_{er^+} \nu_{r^+e} \nu_{a^+} - \nu_{er^+} \nu_{a^+e} \nu_{r^+a^+} \end{aligned} \tag{2.51}$$

The parallel diffusion coefficients of the contaminant ions due to density gradients of a^+, r^+ and e are

$$D_{a^+\|}^{r^+} = \frac{\nu_e \nu_{r^+a^+} + \nu_{ea^+} \nu_{r^+e}}{C_\|} \frac{kT_{a^+}}{m_{a^+}} \tag{2.52}$$

$$D_{r^+\|}^{r^+} = \frac{\nu_e \nu_{a^+} - \nu_{ea^+} \nu_{a^+e}}{C_\|} \frac{kT_{r^+}}{m_{r^+}} \tag{2.53}$$

$$D_{e\|}^{r^+} = \frac{\nu_{r^+a^+} \nu_{a^+e} + \nu_{r^+e} \nu_{a^+}}{C_\|} \frac{kT_e}{m_e} \tag{2.54}$$

The parallel diffusion coefficients of the electrons due to density gradients of a^+, r^+ and e are

$$D_{a^+\|}^{e} = \frac{\nu_{ea^+} \nu_{r^+} + \nu_{er^+} \nu_{r^+a^+}}{C_\|} \frac{kT_{a^+}}{m_{a^+}} \tag{2.55}$$

$$D_{r^+\|}^{e} = \frac{\nu_{er^+} \nu_{a^+} + \nu_{ea^+} \nu_{a^+r^+}}{C_\|} \frac{kT_{r^+}}{m_{r^+}} \tag{2.56}$$

$$D_{e\|}^{e} = \frac{\nu_{a^+} \nu_{r^+} - \nu_{a^+r^+} \nu_{r^+a^+}}{C_\|} \frac{kT_e}{m_e} \tag{2.57}$$

As in the case of the perpendicular transport coefficients, simple relations hold between the parallel transport coefficients as well. A generalized Einstein relation holds between the parallel mobility and the parallel diffusion coefficients

$$\mu_{\|}^{t} = D_{a+\|}^{t}\frac{q_{a+}}{kT_{a+}} + D_{r+\|}^{t}\frac{q_{r+}}{kT_{r+}} + D_{e\|}^{t}\frac{q_{e}}{kT_{e}} \tag{2.58}$$

Also, the following relation holds between the diffusion coefficient and the ambient and contaminant neutral wind coefficients

$$w_{n\|}^{t} = D_{a+\|}^{t}\frac{m_{a+}\nu_{a+n}}{kT_{a+}} + D_{r+\|}^{t}\frac{m_{r+}\nu_{r+n}}{kT_{r+}} + D_{e\|}^{t}\frac{m_{e}\nu_{en}}{kT_{e}} \tag{2.59}$$

Finally, the diffusion coefficients and the gravitational drift coefficient are related as follows

$$\beta_{\|}^{t} = D_{a+\|}^{t}\frac{m_{a+}}{kT_{a+}} + D_{r+\|}^{t}\frac{m_{r+}}{kT_{r+}} + D_{e\|}^{t}\frac{m_{e}}{kT_{e}} \tag{2.60}$$

We will close the discussion with a few comments on the transport coefficients. They have been derived in order to account for an arbitrary degree of ionization of the plasma. In the absence of charged particle collisions, from inspection, we can see that only the self diffusion coefficients are nonzero, i.e., the terms $D_{tP,H,\|}^{t}$ which describe the diffusion of a species t due to density gradients in t. In such a case the diffusion coefficients take the form

$$\begin{aligned} D_{tP}^{t} &= \frac{\nu_t}{\nu_t^2+\Omega_t^2}\frac{kT_t}{m_t} \\ D_{tH}^{t} &= \frac{\Omega_t}{\nu_t^2+\Omega_t^2}\frac{kT_t}{m_t} \\ D_{t\|}^{t} &= \frac{kT_t}{m_t\nu_t} \end{aligned} \tag{2.61}$$

where ν_t is the collision frequency with the neutrals in the plasma. These formulas are identical with the well-known expressions found in the literature [*Bittencourt*, 1986]. Accordingly the generalized Einstein relations give the transport coefficients in a direction $j = P, H$ or $\|$ as

$$\begin{aligned} \mu_{tj} &= D_{tj}^{t}\frac{q_t}{kT_t} \\ w_{nj}^{t} &= D_{tj}^{t}\frac{m_t\nu_{tn}}{kT_t} \\ \beta_{nj}^{t} &= D_{tj}^{t}\frac{m_t}{kT_t} \end{aligned} \tag{2.62}$$

2.5 Collision Processes

2.5.1 Collisions between Charged Particles

The model for charged particle collision is that developed by *Trubnikov* [1961]. Consider the motion of test particles α through field particles β with masses m_α and m_β respectively. For the case where the field particles have infinite mass and are set at rest the momentum equation takes the simple form $d\bar{v}_\alpha/dt = -\nu^o_{\alpha\beta}\bar{v}_\alpha$ The quantity $(\nu^o_{\alpha\beta})^{-1}$ has the dimensions of time and it represents the "longitudinal-slowing time" of the test particles and is called the "basic relaxation time". The collision frequency associated with the momentum transfer process examined above is

$$\nu^o_{\alpha\beta} = \frac{1}{4\pi\epsilon_o^2}\frac{e_\alpha^2 e_\beta^2}{m_\alpha^2 v_\alpha^3}\lambda n_\beta \tag{2.63}$$

where, $e_{\alpha,\beta} = Z_{\alpha,\beta}e$ is the charge of the particles and λ is the Coulomb logarithm. Take as T_a the temperature of the test particle (in eV) and denote by $K_{eV} = 1.602 \times 10^{-19}\ \ J/eV$. The total energy of the test particles (in eV) is $\epsilon_\alpha = m_\alpha v_{o\alpha}^2/2K_{eV} + 3/2T_\alpha$. If we substitude for $m_\alpha = \mu_\alpha m_p$, where $m_p = 1.6726 \times 10^{-27}$ kg, $\epsilon_o = 8.8542 \times 10^{-12}$ Fm^{-1}, the electron charge $e = 1.6022 \times 10^{-19}$ C, then the basic collision frequency for momentum transfer (2.63) becomes

$$\nu^o_{\alpha\beta} = 9.017 \times 10^{-14}\frac{Z_\alpha Z_\beta}{\mu_\alpha^{1/2}\epsilon_\alpha^{3/2}}\lambda n_\beta \tag{2.64}$$

Assume now that both the test and field particles are in motion and described by Maxwellian distributions. Take the temperature of the field particles to be T_β (in eV) and define the parameter $\chi_{\alpha\beta}$ as

$$\chi_{\alpha\beta} = \frac{m_\beta v_\alpha^2}{2K_{ev}T_\beta} = \frac{m_\beta}{m_\alpha}\frac{\frac{1}{2}m_\alpha v_\alpha^2}{K_{eV}T_\beta} = \frac{m_\beta}{m_\alpha}\frac{\epsilon_\alpha}{T_\beta}$$

The momentum transfer collision frequency for the slowing down process is given by

$$\nu_{\alpha\beta} = \left(1 + \frac{m_\alpha}{m_\beta}\right)\Psi(\chi_{\alpha\beta})\nu^o_{\alpha\beta} \tag{2.65}$$

The quantity Ψ is the Maxwell integral defined as

$$\Psi(\chi_{\alpha\beta}) = \frac{2}{\sqrt{\pi}}\int_0^x e^{-t}\sqrt{t}dt \tag{2.66}$$

Substituting the expression for the basic collision frequency from Eq. (2.64) it becomes

$$\nu_{\alpha\beta} = 9.017 \times 10^{-14} \frac{Z_\alpha Z_\beta}{\mu_\alpha^{1/2} \epsilon_\alpha^{3/2}} \lambda \left(1 + \frac{m_\alpha}{m_\beta}\right) \Psi(\chi_{\alpha\beta}) n_\beta \quad (\mathrm{s}^{-1}) \tag{2.67}$$

The formula above takes into account the velocity dependent nature of the collision process. Using this formula we can investigate the magnitude of the collision frequencies in two extreme situations. In the first case the energy of the test particles is thermal, i.e., $\epsilon_\alpha = 3T/2$ where the common temperature of the two species populations is denoted by T. In the second case the kinetic energy of the test particles is so large that $\chi_{\alpha\beta} \gg 1$. The magnitude of the collision frequencies normalized by ν_{ei} are shown in Table 2.3. The order of the charged particle relaxation time is clear; for thermal or very fast electrons such that $\epsilon_e \gg T$, ν_{ee} and ν_{ei} are comparable. However ions behave differently in the two limits. For very fast ions such that $\epsilon_i \gg (\mu_i/\mu_e)T$ the $\nu_{ii} \sim (\mu_e/\mu_i)\nu_{ie}$, that is the ions slow down mainly due to collisions with the electrons. For thermal ions the $\nu_{ii} \sim \sqrt{\mu_i/\mu_e}\nu_{ie}$ which implies that the ions slow down mainly due to collisions with the field ions.

$\alpha\beta$	$\frac{\nu_{\alpha\beta}}{\nu_{ei}}$	
	$\chi_{\alpha\beta} = \frac{3}{2}\frac{\mu_\beta}{\mu_\alpha}$	$\chi_{\alpha\beta} \gg 1$
ei	1	1
ee	1.2	2
ie	$1.4\frac{\mu_e}{\mu_i}$	$2\sqrt{\frac{\mu_i}{\mu_e}}$
ii	$1.2\sqrt{\frac{\mu_e}{\mu_i}}$	$\sqrt{\frac{\mu_e}{\mu_i}}$

Table 2.3: Collision frequency ratio for limiting values of energy of the test particles, ϵ_α.

2.5.2 Ion-Neutral Collisions

There are two types of collisions between the ions and the neutral particles. The non-resonant elastic collisions correspond to a long-range polarization attraction coupled with a short range repulsion. The resonant interactions occur when there is charge transfer during a collision between an ion and a neutral.

Non-Resonant Ion-Neutral Collisions

The model which is adopted here is that developed by *Banks* [1966] based on the work by *Dalgrano et al.* [1959]. This model has been widely used in the past two decades, although more accurate modelling is needed, especially for LEO flight conditions where the species distributions are far from being Maxwellians (Banks, personal communication, 1988).

Consider a two species plasma with ions i and neutrals n, with temperatures T_i and T_n respectively. The relative velocity between two particles is denoted by g, the center of mass scattering angle is θ and the differential scattering cross section is denoted by $\sigma(\theta, g)$. The momentum transfer cross section is defined as

$$Q(g) = 2\pi \int \sigma(\theta, g)(1 - \cos\theta)\sin\theta d\theta \tag{2.68}$$

The velocity dependent momentum transfer collision frequency is then $\nu_{in} = n_n g Q(g)$. To get the average momentum transfer collision frequency one has to integrate over the velocity space, which becomes

$$\nu_{in} = \frac{4}{3} n_n \langle v \rangle_{in} \langle Q \rangle \tag{2.69}$$

where the average relative velocity is

$$\langle v \rangle_{in} = \sqrt{\frac{8k}{\pi}\left(\frac{T_i}{m_i} + \frac{T_n}{m_n}\right)} \tag{2.70}$$

and the average momentum transfer cross section $\langle Q \rangle$ is given by

$$\langle Q \rangle = \frac{1}{c^6} \int g^5 Q(g) exp[-g^2/c^2] dg \tag{2.71}$$

where the constant c is given $c^2 = (\frac{2kT_i}{m_i} + \frac{2kT_n}{m_n})$. *Dalgarno et al.* [1959], evaluated the ion-neutral interaction potential taking into account an attractive polarization potential as well as an elastic sphere repulsive potential. Comparisons of this model with data taken at temperatures below 300 °K appear to give accurate results. However as, *Banks* [1966] notes due to lack of data it is necessary to accept Dalgarno's model over the entire range of temperatures. The ion-neutral momentum transfer cross section is given as

$$Q(g) = 2.21\pi \left(\frac{\alpha e^2}{\mu g^2}\right)^{1/2} \quad (\text{cm}^2) \tag{2.72}$$

In the formula, α is the polarizability of the neutral atom given in units of cm^3 and μ is the ion-neutral reduced mass. With the substitution of (2.72) into (2.71) the average momentum transfer cross section in cm^2 becomes

$$\langle Q\rangle = \frac{3\sqrt{2}}{16}\pi^{3/2}\left(\frac{4.88\alpha e^2}{\mu}\right)\left(\frac{kT_i}{m_i}+\frac{kT_n}{m_n}\right)^{-1/2} \tag{2.73}$$

In the formula above we can express the reduced mass in terms of atomic mass units (amu) $\mu = \frac{m_i m_n}{m_i+m_n} = \mu_A$ and the polarizability as $\alpha = \alpha_o \times 10^{-24}$ cm^3. Using equations (2.70) and (2.73) into (2.69) the average collision frequency becomes

$$\nu_{in} = 2.586 \times 10^{-16}\left(\frac{\alpha_o}{\mu_A}\right)^{1/2} n_n \tag{2.74}$$

where the neutral density is given in m^{-3} and the reduced mass μ_A is in atomic mass units. For the neutrals considered in the present study the polarizabilities are shown in Table 2.4 and taken from *Castellan* [1971] and *Banks* [1966].

Neutral	O	H_e	H	H_2O	CO_2
α_o	0.89	0.21	0.67	1.59	1.26

Table 2.4: Polarizability of neutral gases

Resonant Ion - Neutral Collisions

For temperatures below 500 °K the interactions between ions and neutrals are determined primarily by the induced dipole polarization attraction. The momentum transfer cross section in that case is that given by Eq. (2.72). At higher temperatures the contribution of the polarization diminishes and charge exchange becomes dominant. During charge exchange the particles transfer their charge but they tend to retain their original energy. Charge exchange dominates at temperatures above 500 °K especially between parent particles as well as unlike particles. The reaction is elastic (kinetic energy is conserved) and it can be the source of highly energetic neutrals within the plasma cloud. The charge exchange greatly enhances the momentum transfer cross section. In the plasma cloud conditions it seems that most of the ion-neutral collisions will be charge exchange.

It has been shown by *Dalgarno* [1966] that the charge exchange cross section for particles with relative energy ϵ is

$$Q^M = 2(A - B\log\epsilon)^2 \tag{2.75}$$

The coefficients A and B are given in units of 10^{-8} cm for a particular gas. The average momentum cross section is obtained by integration of the above over the velocity space of the two populations. Assuming Maxwellian populations for the ions and neutrals with temperatures T_i and T_n respectively, the average cross section (in cm^2) becomes

$$\langle Q\rangle^M = 2[(A + 3.96B) - B\log T_r]^2 \times 10^{-16} \tag{2.76}$$

where the temperature $T_r = T_i + T_n$. From the definition of the average momentum transfer collision (Eq. 2.69) frequency we get

$$\nu_{in}^r = \frac{4}{3}\left[\left(\frac{8k}{\pi m}\right)(T_i + T_n)\right]^{1/2}\langle Q\rangle n_n \tag{2.77}$$

In the plasma cloud resonant ion neutral collisions might take place between the ambient O^+ and O and also between the ejected neutrals and the created ions. The calculated collision frequencies are shown in Table 2.5 with cross sections taken from *Banks* [1966], where the temperature T_r is in degrees K, and the density n_n is given in m^{-3}.

2.5.3 Electron-Neutral Elastic Collisions

Electron-neutral collisions in the ionosphere play an important role in the determination of the electric conductivity. Theoretical models for elastic collisions of such

Species	ν_{in}^r, s^{-1}
$O^+ - O$	$4.7 \times 10^{-19}\sqrt{T_r}(10.5 - 0.67\log T_r)^2 N_O$
$CO_2^+ - CO_2$	$2.85 \times 10^{-17}\sqrt{T_r}(1 - 0.083\log T_r)^2 N_{CO_2}$

Table 2.5: Momentum transfer ion-neutral charge exchange collision frequency

kind give poor results, so the models available are based primarily on measurements. Experiments determine the velocity dependent momentum cross section $Q^m(g)$, as it is defined in (2.68). For a mixture of an electron gas (m_e, T_e) and a neutral gas (m_n, T_n), since $m_e \ll m_n$ the average momentum transfer cross section is

$$\langle Q \rangle = \left(\frac{m_e}{2kT_e}\right)^3 \int_0^\infty v^5 Q(u) exp\left[-\frac{m_e v^2}{2kT_e}\right] dv \tag{2.78}$$

where, v is the speed of the electrons and we have used the approximation $g \sim v$. Since we expect that $\frac{T_e}{m_e} \gg \frac{T_n}{m_n}$ the average collision frequency for momentum transfer is given by

$$\nu_{en} = \frac{4}{3}\sqrt{\frac{8kT_e}{\pi m_e}} \langle Q \rangle_D n_n \tag{2.79}$$

Measurements of collisions with neutrals relevant for our study are given by *Itikawa* [1978]. From these data we derived the momentum transfer collision frequency for H_2O; the rest of the fits to the data come from *Schunk and Nagy* [1978]. They are given in Table 2.6 with the density of a neutral n to be denoted by N_n.

2.5.4 Ambient Collision Frequencies

Applying the above formulas for ambient plasma we can derive the ambient collision frequencies shown in Figure 2.2. The ionospheric conditions are at mid-latitude, summer, daytime and average solar activity. The neutrals considered are O, He and H.

Neutrals	ν_{en}, s^{-1}
O	$8.9 \times 10^{-17}(1 + 5.7 \times 10^{-4} T_e) T_e^{1/2} N_O$
He	$4.6 \times 10^{-16} T_e^{1/2} N_{He}$
H	$4.5 \times 10^{-15}(1 - 1.35 \times 10^{-4} T_e) T_e^{1/2} N_H$
H_2O	$6.17 \times 10^{-11} T_e^{-0.731} N_{H_2O}$
CO_2	$3.68 \times 10^{-14}[1 + 4.1 \times 10^{-11} \mid 4500 - T_e \mid^{2.93}] N_{CO_2}$

Table 2.6: Momentum transfer electron-neutral collision frequency.

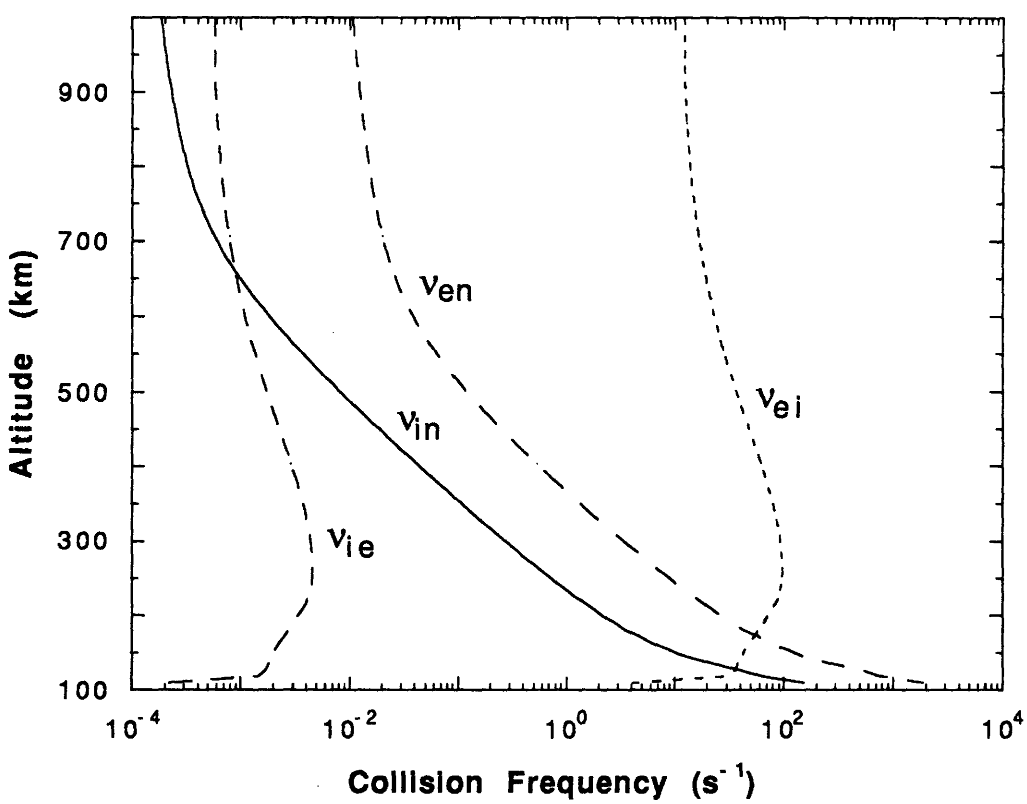

Figure 2.2: Ambient ionospheric collision frequencies. Mid-latitude, summer, daytime, average solar activity conditions.

Chapter 3

Electric Currents

We begin this chapter with Maxwell's equations and the simplifications to them appropriate to our study. Next we derive the currents and the charge conservation equation. We also derive boundary conditions necessary for the solution of the equation of the self-consistent electrostatic electric field. We utilize a layer model to describe the cloud and the background ionosphere and examine the current closure. We discuss the case when closure occurs via Pedersen transverse currents. We present the theory of the Alfvén waves and discuss the conditions under which they are applicable for moving plasma clouds. Next we examine the current closure including both the Pedersen and the Alfvén conductance of the background plasma. We derive the conditions under which Alfvén waves can be neglected. We also address the plasma diffusion with the use of a layer model. Finally we include in the formulation polarization and Alfvén currents and derive a general form of the charge conservation equation.

3.1 Current Balance

The current balance within the plasma cloud is the key to the electrodynamical interactions taking place. The current closure between the plasma cloud and the ambient ionosphere will determine the self-consistent potential of the cloud and, consequently, will determine the dynamical behavior and evolution of the cloud.

To completely describe the plasma flow along with the continuity and momentum equations, presented in Chapter 2, we must include Maxwell's equations. They are given in their full form

$$\nabla \times \mathbf{E} = -\frac{\partial \mathbf{B}}{\partial t} \quad \text{Faraday's law} \tag{3.1}$$

$$\nabla \cdot \mathbf{E} = -\frac{\rho}{\epsilon_o} \quad \text{Poisson's Eqn.} \tag{3.2}$$

$$\nabla \times \mathbf{B} = \mu_o(\mathbf{J} + \epsilon_o \frac{\partial \mathbf{E}}{\partial t}) \quad \text{Ampere's law} \tag{3.3}$$

$$\nabla \cdot \mathbf{B} = 0 \tag{3.4}$$

where ρ is the charge density ($\rho = \sum_j q_j n_j$) and $\mathbf{J} = \sum_j q_j n_j \mathbf{V}_j$ is the current density. From the above equations we can derive the charge conservation equation

$$\nabla \cdot \mathbf{J} = -\frac{\partial \rho}{\partial t} \tag{3.5}$$

Several simplification to the above equations can be made. We begin with the displacement current. If we express in general the current density as $\mathbf{J} = \overline{\overline{\sigma}}\mathbf{E}$, then $J \gg \epsilon_o \partial E/\partial t$ becomes $\omega \ll \sigma/\epsilon_o = 1/\tau$. For typical values for the conductivity $\sigma \sim 10^{-8} - 10^{-4}$ S/m (see Figure 3.1) we obtain $\omega \ll 1.2 \times 10^3 - 1.1 \times 10^6$ rad/s, frequencies which are much greater that the ion gyrofrequency $\Omega_i \simeq 210$ rad/s. Consequently only for time scales shorter than $\tau \sim 10^{-8} - 10^{-3}$ s does the displacement current become important. This is also the time scale required to build the charge density which appears in the charge conservation equation. In general the forces that act on both the ambient and the cloud plasma will create electric fields through the establishment of some charge density. However, the plasma responds quickly to the current divergence through the creation of electric fields which modify the fluid velocities so that charge neutrality is established. Combining the charge conservation with Poisson's equation we can estimate the time scale for establishing charge neutrality in the plasma

$$\tau \sim \frac{\epsilon_o \nabla \cdot \mathbf{E}}{\nabla \cdot \mathbf{J}} \sim \frac{\epsilon_o}{\sigma} \tag{3.6}$$

This is the same time scale derived above for the displacement current. The consequence is that for times $T \gg \tau$ the electric field can be obtained from the solution of

$\nabla \cdot \mathbf{J} \simeq 0$ rather that Poisson's equation. Another issue relates to the induced magnetic field due to currents produced by density variation or motion of the plasma. The effect of the diamagnetic currents is shown by the plasma β given by $\beta = \sum nkT/(B^2/2\mu_o)$. For the plasma densities, temperatures and magnetic fields considered here $\beta \ll 1$ so that diamagnetic effects are neglected. This is not true for plasma clouds released in the magnetosphere. The formation of a diamagnetic cavity due to high β effects has been verified during the AMPTE campaign. We neglect any time variations of the $\mathbf{B}$ field. An approximate condition which implies electrostatic fields has been derived by *Dungey* [1956]. Denote by ω the frequency and L the length scale of the problem, ω_{pe} the electron plasma frequency, $\kappa_i = \Omega_i/\nu_i$; then the field is potential if $c^2/\omega L^2 \gg \omega_{pe}^2/\Omega_e\kappa_i$. Substituting typical parameters $n_e = 10^5$ cm^{-3}, $B = 0.45$ G, and taking the smallest $\kappa_i \simeq 1$ then the above condition becomes $UL \ll 2.3 \times 10^3$ where U is the speed of the cloud (in km/s) and L the length (in km). Finally, we assume that the plasma is quasineutral, i.e., $\sum_j q_j n_j = 0$. This approximation is valid when the length scale under study is much larger than the Debye length $L \gg \lambda_D$. With the definition of $\lambda_D = (\epsilon_o kT_e/ne^2)^{1/2}$ for ionospheric conditions it becomes $\lambda_D \simeq 0.2 - 1$ cm; thus quasineutrality is easily satisfied for the length scales of interest in our study. With the above simplifications Maxwell equations take the following form

$$\nabla \times \mathbf{E} \simeq 0 \tag{3.7}$$

$$\nabla \cdot \mathbf{E} = \rho \simeq 0 \tag{3.8}$$

$$\nabla \times \mathbf{B} = \mu_o \mathbf{J} \tag{3.9}$$

$$\nabla \cdot \mathbf{B} = 0 \tag{3.10}$$

From Faraday's law we deduce that the electric field is electrostatic, i.e, $\mathbf{E} = -\nabla\phi$ where $\phi(\mathbf{r}, t)$ is a potential function. Then, the electric fields are evaluated by the charge conservation equation and Ampere's law serves only as an a posteriori check for the assumption of negligible magnetic field variations. Also, the charge conservation reduces to

$$\nabla \cdot \mathbf{J} = 0 \tag{3.11}$$

The current is given by direct substitution of the velocities of the plasma species equations (2.15), (2.23), and (2.47) into the definition of the current density

$$\mathbf{J} = n_{a^+} q_{a^+} \mathbf{V}_{a^+} + n_{r^+} q_{r^+} \mathbf{V}_{r^+} + n_e q_e \mathbf{V}_{e\perp} \tag{3.12}$$

We can write for the total current density

$$\mathbf{J} = \mathbf{J}^{dir} + \mathbf{J}^{dif}_{r^+} + \mathbf{J}^{dif}_{a^+} + \mathbf{J}^{dif}_{e} + \mathbf{J}^{neu}_{r} + \mathbf{J}^{neu}_{a} + \mathbf{J}^{gra} \tag{3.13}$$

where we have taken into account the direct current, the diffusion current due to density gradients of the contaminant ions, the ambient ions and the electrons, the currents due to the contaminant and ambient neutral winds, and the current due to the gravitational field.

The direct total current density is given by

$$\begin{bmatrix} J_x^{dir} \\ J_y^{dir} \\ J_{\parallel}^{dir} \end{bmatrix} = \begin{bmatrix} \sigma_P & -\sigma_H & 0 \\ \sigma_H & \sigma_P & 0 \\ 0 & 0 & \sigma_{\parallel} \end{bmatrix} \begin{bmatrix} E_x \\ E_y \\ E_{\parallel} \end{bmatrix} \tag{3.14}$$

We define the total direct conductivities in the Pedersen, Hall, and parallel directions, taking into account all the plasma species as

$$\sigma_P = \sigma_P^{r^+} + \sigma_P^{a^+} \tag{3.15}$$

$$\sigma_H = \sigma_H^{r^+} + \sigma_H^{a^+} + \sigma_H^{e} \tag{3.16}$$

$$\sigma_{\parallel} = \sigma_{\parallel}^{r^+} + \sigma_{\parallel}^{a^+} + \sigma_{\parallel}^{e} \tag{3.17}$$

The directional conductivity for any species t is given by $\sigma_j^t = q_t n_t \mu_j^t$ and the directional mobility μ_j^t is given in (2.37) and (2.58). Note also that there is no electron current density in the Pedersen direction, since we assumed that electrons mainly exhibit drifts in the Hall direction.

The total diffusion current density due to gradients of species $t = a^+, r^+, e$ is given by

$$\begin{bmatrix} J_{tx}^{dif} \\ J_{ty}^{dif} \\ J_{t\parallel}^{dir} \end{bmatrix} = -e \begin{bmatrix} D_{tP} & -D_{tH} & 0 \\ D_{tH} & D_{tP} & 0 \\ 0 & 0 & D_{t\parallel} \end{bmatrix} \begin{bmatrix} \frac{1}{n_t}\frac{\partial n_t}{\partial x} \\ \frac{1}{n_t}\frac{\partial n_t}{\partial y} \\ \frac{1}{n_t}\frac{\partial n_t}{\partial z} \end{bmatrix} \tag{3.18}$$

where the total diffusion coefficient tensor due to ions $t = r^+, a^+$ is

$$D_{tP} = n_{r^+} D_{tP}^{r^+} + n_{a^+} D_{tP}^{a^+} \tag{3.19}$$

$$D_{tH} = n_{r^+} D_{tH}^{r^+} + n_{a^+} D_{tH}^{a^+} \tag{3.20}$$

$$D_{t\parallel} = n_{r^+} D_{t\parallel}^{r^+} + n_{a^+} D_{t\parallel}^{a^+} - n_e D_{t\parallel}^{e} \tag{3.21}$$

Note that the units of the so called total diffusion tensor $D_{tP,H,\parallel}$ are (ms^{-1}). The total diffusion coefficient tensor due to electrons

$$D_{eP} = n_{r^+} D_{eP}^{r^+} + n_{a^+} D_{eP}^{a^+} \tag{3.22}$$

$$D_{eH} = n_{r^+} D_{eH}^{r^+} + n_{a^+} D_{eH}^{a^+} + n_e D_{eH}^{e} \tag{3.23}$$

$$D_{e\parallel} = n_{r^+} D_{e\parallel}^{r^+} + n_{a^+} D_{e\parallel}^{a^+} - n_e D_{e\parallel}^{e} \tag{3.24}$$

The current density due to the neutral wind U_n of a species $n = a, r$ is

$$\begin{bmatrix} J_{rx}^{neu} \\ J_{ry}^{neu} \\ J_{r\parallel}^{neu} \end{bmatrix} = e \begin{bmatrix} W_{nP} & -W_{nH} & 0 \\ W_{nH} & W_{nP} & 0 \\ 0 & 0 & W_{r\parallel} \end{bmatrix} \begin{bmatrix} U_{nx} \\ U_{ny} \\ U_{n\parallel} \end{bmatrix} \tag{3.25}$$

where the total neutral wind coefficients are given by

$$W_{nP} = n_{r^+} w_{nP}^{r^+} + n_{a^+} w_{nP}^{a^+} \tag{3.26}$$

$$W_{nH} = n_{r^+} w_{nH}^{r^+} + n_{a^+} w_{nH}^{a^+} \tag{3.27}$$

$$W_{n\parallel} = n_{r^+} w_{n\parallel}^{r^+} + n_{a^+} w_{n\parallel}^{a^+} - n_e w_{n\parallel}^{e} \tag{3.28}$$

Finally, the total current density due to gravitational drifts is

$$\begin{bmatrix} J_{x}^{gra} \\ J_{y}^{gra} \\ J_{\parallel}^{gra} \end{bmatrix} = e \begin{bmatrix} B_{P} & -B_{H} & 0 \\ B_{H} & B_{P} & 0 \\ 0 & 0 & B_{\parallel} \end{bmatrix} \begin{bmatrix} g_{x} \\ g_{y} \\ g_{\parallel} \end{bmatrix} \tag{3.29}$$

where the total coefficients due to gravity are given by

$$B_P = n_{r^+}\beta_P^{r^+} + n_{a^+}\beta_P^{a^+} \tag{3.30}$$

$$B_H = n_{r^+}\beta_H^{r^+} + n_{a^+}\beta_H^{a^+} \tag{3.31}$$

$$B_{\|} = n_{r^+}\beta_{\|}^{r^+} + n_{a^+}\beta_{\|}^{a^+} - n_e\beta_{\|}^{e} \tag{3.32}$$

3.1.1 Equation for the Current Balance

We need now to derive an equation for the electric field within the plasma. In the analysis so far we have denoted $\mathbf{E}$ as the electric field. We take now the electric field to be

$$\mathbf{E}(x,y,z) = \mathbf{E}_o(x,y,z) + \epsilon(x,y,z) + \mathbf{E}_m(x,y,z) \tag{3.33}$$

Here $\mathbf{E}_o$ is the ambient electric field, ϵ is the electric field due to the presence of the plasma cloud. $\mathbf{E}_m$ is the motional electric field used to account for any change of reference frame that we might consider; in such a case the velocities should also be written in the new reference frame.

The current balance will be determined by direct currents, diamagnetic (or diffusion) currents, currents due to both ambient and neutral winds and finally currents due to gravitational drifts. The conditions under which the parallel currents carried by the Alfvén waves can be neglected are discussed in a subsequent section. The equation for charge conservation is

$$\nabla \cdot \mathbf{J}^{dir} + \nabla \cdot \mathbf{J}^{dif}_{a+} + \nabla \cdot \mathbf{J}^{dif}_{r+} + \nabla \cdot \mathbf{J}^{dif}_{e} + \nabla \cdot \mathbf{J}^{neu}_{a} + \nabla \cdot \mathbf{J}^{neu}_{r} + \nabla \cdot \mathbf{J}^{gra} = 0 \tag{3.34}$$

Since we assume that the electric field due to the plasma cloud is electrostatic, then the perturbation potential $\phi(x,y,z)$ is such that $\epsilon = -\nabla\phi$. We will concentrate on the divergence of the direct current, since this is the term which will give the differential dependence of the potential ϕ. It is important to recast the above equation in a form of a steady state advection-diffusion equation for the potential ϕ as follows

$$\nabla \cdot \mathbf{J}^{dir} = \frac{\partial}{\partial x}\left(\sigma_P \frac{\partial \phi}{\partial x}\right) + \frac{\partial}{\partial y}\left(\sigma_P \frac{\partial \phi}{\partial y}\right) + \frac{\partial}{\partial z}\left(\sigma_{\|} \frac{\partial \phi}{\partial z}\right) + \frac{\partial \sigma_H}{\partial y}\frac{\partial \phi}{\partial x} - \frac{\partial \sigma_H}{\partial x}\frac{\partial \phi}{\partial y}$$

$$+\left(\frac{\partial\sigma_P}{\partial x}+\frac{\partial\sigma_H}{\partial y}\right)\tilde{E}_x+\left(\frac{\partial\sigma_P}{\partial y}-\frac{\partial\sigma_H}{\partial x}\right)\tilde{E}_y+\frac{\partial\sigma_{\|}}{\partial z}\tilde{E}_z$$
$$+\sigma_P\left(\frac{\partial\tilde{E}_x}{\partial x}+\frac{\partial\tilde{E}_y}{\partial y}\right)+\sigma_H\left(\frac{\partial\tilde{E}_x}{\partial y}-\frac{\partial\tilde{E}_y}{\partial x}\right)+\sigma_{\|}\frac{\partial\tilde{E}_z}{\partial z} \quad (3.35)$$

where, $\tilde{\mathbf{E}} = \mathbf{E}_o + \mathbf{E}_m$. From inspection we see that all the terms which are not ϕ dependent can be regarded as source terms. Note also that it is only the direct (conductive) current which depends on the potential. Thus we can consider the divergence of all the other current densities in (3.34) as a source term, in a nonself-adjoint elliptic equation for the potential. This can be written as

$$\nabla\cdot\mathbf{J}=\frac{\partial}{\partial x}\left(\sigma_P\frac{\partial\phi}{\partial x}\right)+\frac{\partial}{\partial y}\left(\sigma_P\frac{\partial\phi}{\partial y}\right)+\frac{\partial}{\partial z}\left(\sigma_{\|}\frac{\partial\phi}{\partial z}\right)+\frac{\partial\sigma_H}{\partial y}\frac{\partial\phi}{\partial x}-\frac{\partial\sigma_H}{\partial x}\frac{\partial\phi}{\partial y}+S=0 \quad (3.36)$$

where $\sigma_P, \sigma_H, \sigma_Z$, and S are functions of x, y, z. The source term is given by

$$S(x,y,z)=\nabla\cdot\mathbf{J}^{dif}_{a+}+\nabla\cdot\mathbf{J}^{dif}_{r+}+\nabla\cdot\mathbf{J}^{dif}_{e}+\nabla\cdot\mathbf{J}^{neu}_{a}+\nabla\cdot\mathbf{J}^{neu}_{r}+\nabla\cdot\mathbf{J}^{gra}$$
$$+\left(\frac{\partial\sigma_P}{\partial x}+\frac{\partial\sigma_H}{\partial y}\right)\tilde{E}_x+\left(\frac{\partial\sigma_P}{\partial y}-\frac{\partial\sigma_H}{\partial x}\right)\tilde{E}_y+\frac{\partial\sigma_{\|}}{\partial z}\tilde{E}_z$$
$$+\sigma_P\left(\frac{\partial\tilde{E}_x}{\partial x}+\frac{\partial\tilde{E}_y}{\partial y}\right)+\sigma_H\left(\frac{\partial\tilde{E}_x}{\partial y}-\frac{\partial\tilde{E}_y}{\partial x}\right)+\sigma_{\|}\frac{\partial\tilde{E}_z}{\partial z} \quad (3.37)$$

In general the divergence of a current $\mathbf{J} = [A_{ij}]\mathbf{T}$ is $\nabla\cdot([A_{ij}]\mathbf{T})$ and given by

$$\nabla\cdot\begin{bmatrix}A_P & -A_H & 0\\ A_H & A_P & 0\\ 0 & 0 & A_{\|}\end{bmatrix}\begin{bmatrix}T_x\\ T_y\\ T_z\end{bmatrix}=A_P\left(\frac{\partial T_x}{\partial x}+\frac{\partial T_y}{\partial y}\right)+A_H\left(\frac{\partial T_x}{\partial y}-\frac{\partial T_y}{\partial x}\right)$$
$$+A_{\|}\frac{\partial T_z}{\partial z}+T_x\left(\frac{\partial A_P}{\partial x}+\frac{\partial A_H}{\partial y}\right)+T_y\left(\frac{\partial A_P}{\partial y}-\frac{\partial A_H}{\partial x}\right)+T_z\frac{\partial A_{\|}}{\partial z} \quad (3.38)$$

3.2 Current Closure - Boundary Conditions

To solve the equation for the potential one must supply appropriate boundary conditions. In turn, one needs to discuss the model for current closure. In the beginning we will describe a closure model which is applicable to the ionosphere outside of the equatorial region. The ambient ionosphere , as described in Chapter 2, corresponds to daytime conditions. The conductivities calculated from our model (Eq. (3.15)) are

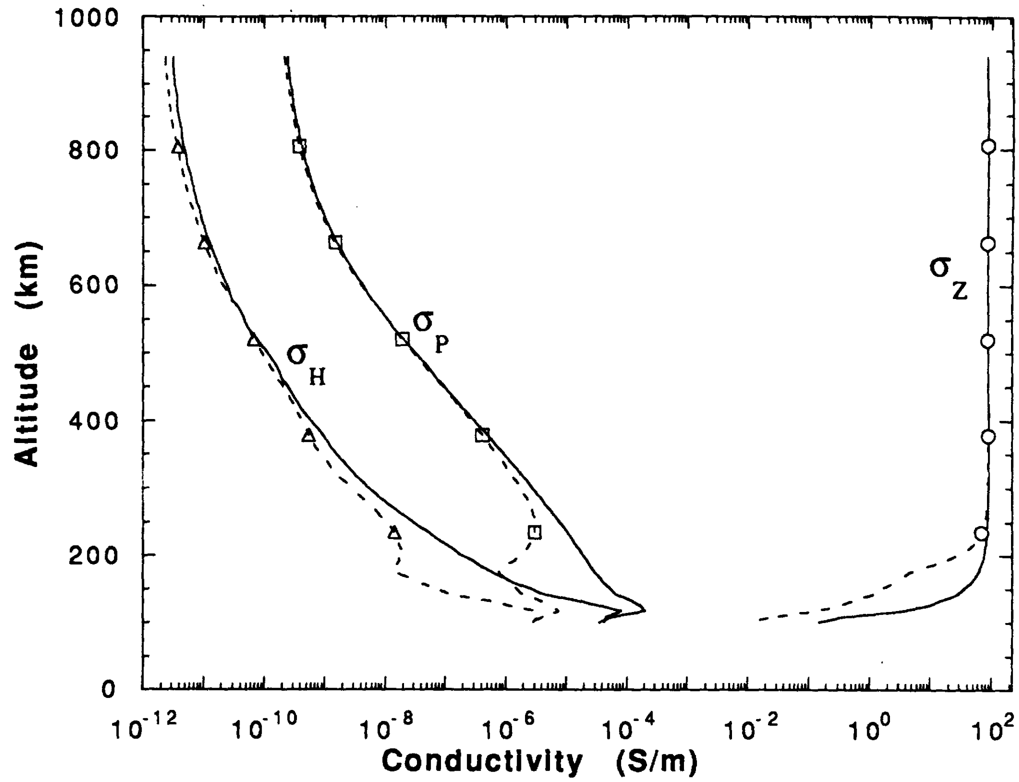

Figure 3.1: Ambient ionospheric conductivites. Mid-latitude, summer, daytime, average solar activity conditions

shown in Figure 3.1. For comparison we calculated conductivities based on the formulas and the ambient conditions given by *Haerendel et al.* [1967]. We can see that the conductivities derived from our model compare well with those presented in Table 3.1, the differences being due to the adopted model ionosphere and the models for collision frequencies. From Figure 3.1 it is shown that the maximum of the transverse conductivities occurs at $\sim$ 130 km. Above and below that altitude both Pedersen and Hall conductivities decrease in magnitude significantly. The parallel conductivity increases with altitude and is between 5 to 12 orders higher than the transverse conductivities. In high latitudes the magnetic field lines will go through the magnetosphere before reaching the conjugate ionosphere. In the absence of currents entering or leaving the topside ionosphere, there will be no perpendicular current flow due to the vanishing transverse conductivity. Thus, one can consider the upper F region, above 1000 km, to be a nonconducting boundary. The lower E region (below 100 km) can be also

	Height, km			
	90	160	160	500
n	1.5×10^{10}	3×10^{10}	5×10^{10}	2×10^{11}
σ_P	6.4×10^{-6}	6.8×10^{-5}	5×10^{-7}	2×10^{-7}
σ_H	6.8×10^{-5}	2.7×10^{-5}	~ 0	~ 0
$\sigma_{\parallel}$	2.8×10^{-2}	9.5×10^{-1}	17.9	5.7×10^{2}

Table 3.1: Ambient conductivities calculated from *Haerendel et al.* [1967]. Conductivities are measured in S/m.

regarded as an insulator. Both the transverse and parallel conductivities vanish and there is no current. This model has been used extensively in previous 2-D models (*Perkins et al.*, 1973). Given that, one can bound the ionospheric plasma between two insulators located at heights h_L and h_U respectively as shown in Figure 3.2.

For the disturbed ionosphere due to the presence of a plasma cloud, we assume that at the upper and lower boundaries the flux will be mainly in the magnetic field direction and that the parallel electron flux will be equal to the parallel ambient ion flux (i.e., the flow will be ambipolar in the parallel direction). On the upper boundary charge conservation can be written as $\nabla_{\perp} \cdot \mathbf{J}_{\perp} + \nabla_{\parallel} \cdot \mathbf{J}_{\parallel} = 0$. The transverse divergence of currents is identically zero due to the vanishing transverse conductivities or homogenous electric fields. Then charge conservation implies that $J_{\parallel} = c$ where c is a constant. This is a more general condition than ambipolar flow. If we further require that there is no coupling between the topside ionosphere and magnetosphere, then the constant is replaced by zero and we can write instead

$$\Gamma_{\parallel e} = \Gamma_{\parallel a+} + \Gamma_{\parallel r+} \quad z = h_L, h_U \tag{3.39}$$

Note that applying the vanishing of parallel current is identical to the notion of a bounding insulator on the two boundaries. We must emphasize here that there is no inherent limitation in the plasma model as to the form of boundary conditions that

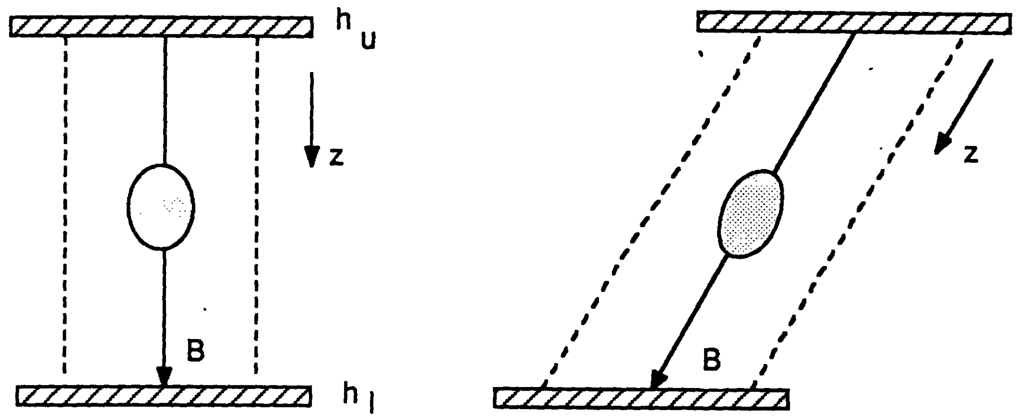

Figure 3.2: The bounding regions for the high latitude (Left), and low latitude (Right) ionosphere.

one can apply. If we substitute for the flux from (2.47), we get

$$\begin{aligned}(n_{a^+}\mu_{\|}^{a^+} + n_{r^+}\mu_{\|}^{r^+} - n_e\mu_{\|}^{e})\frac{\partial \Phi}{\partial z} = &-(n_{a^+}D_{a^+\|}^{a^+} + n_{r^+}D_{a^+\|}^{r^+} - n_eD_{a^+\|}^{e})\frac{1}{n_{a^+}}\frac{\partial n_{a^+}}{\partial z} \\ &-(n_{a^+}D_{r^+\|}^{a^+} + n_{r^+}D_{r^+\|}^{r^+} - n_eD_{r^+\|}^{e})\frac{1}{n_{r^+}}\frac{\partial n_{r^+}}{\partial z} \\ &-(n_{a^+}D_{e\|}^{a^+} + n_{r^+}D_{e\|}^{r^+} - n_eD_{e\|}^{e})\frac{1}{n_e}\frac{\partial n_e}{\partial z} \\ &+(n_{a^+}\beta_{\|}^{a^+} + n_{r^+}\beta_{\|}^{r^+} - n_{e^+}\beta_{\|}^{e})g_{\|} \end{aligned} \tag{3.40}$$

But from the definition of the electric field (3.33) we can write

$$\Phi(x,y,z) = \Phi_o(x,y,z) + \phi(x,y,z) \tag{3.41}$$

In the undisturbed ionosphere the equality of parallel fluxes must hold as well

$$\begin{aligned}(n_{a^+}\mu_{\|}^{a^+} - n_e\mu_{\|}^{e})\frac{\partial \Phi_o}{\partial z} &= -(n_{a^+}D_{a^+\|}^{a^+} - n_eD_{a^+\|}^{e})\frac{1}{n_{a^+}}\frac{\partial n_{a^+}}{\partial z} \\ &\quad -(n_{a^+}D_{e\|}^{a^+} - n_eD_{e\|}^{e})\frac{1}{n_e}\frac{\partial n_e}{\partial z} + (n_{a^+}\beta_{\|}^{a^+} - n_{e^+}\beta_{\|}^{e})g_{\|}\end{aligned} \tag{3.42}$$

If we apply also the condition that

$$n_{r^+} = 0 \quad \text{and } \partial n_{r^+}/\partial z = 0 \text{ at } z = h_L, h_U \tag{3.43}$$

and after some manipulation of the above equations we derive

$$\frac{\partial \phi}{\partial z} = 0 \quad \text{at } z = h_L, h_U \tag{3.44}$$

In other words, we impose the condition that no current will flow perpendicular to the bounding insulators. In the transverse direction the absence of current on these boundaries is enforced by the vanishing of the transverse conductivities, as we explained before. For the transverse direction we require that

$$\phi(x, y, z) = 0 \quad \text{as } (x, y) \rightarrow \infty \tag{3.45}$$

For the equatorial regions the closure occurs between the two conjugate E regions of the ionosphere and the magnetic field lines which cross the perturbation do not necessarily pass through the magnetosphere. The bounding insulators in that case are the E regions of the two hemispheres.

3.3 Current Closure with a Layer Model

3.3.1 Transverse Pedersen Current

We will discuss now the current closure with the use of a layer model as shown in Figure 3.3. We consider a strip of enhanced conductivity, i.e., plasma cloud, in the F region subject to an external electric field $\mathbf{E}_o$. For simplicity we neglect the Hall conductivity and assume a uniform background ionosphere. The applied electric field is shielded by the dielectric polarization property of the plasma so that the field inside the cloud becomes $\mathbf{E} = a\mathbf{E}_o$ where $a \leq 1$. The charge imbalance in the cloud is neutralized by charges which flow along the field lines. Electrons due to their large parallel conductivity easily flow along the $\mathbf{B}$ lines and ions flow most easily in the transverse direction. These ion fluxes arise up to a distance $L_{||}$ along the $\mathbf{B}$ lines. This distance can be derived from a scaling analysis of the current balance equation, $\nabla \cdot \mathbf{J} = 0$. For a perturbation of transverse scale $L_\perp \sim a_\perp$ this equation implies that

$$\frac{\partial J_{||}}{\partial z} \sim \frac{\partial J_\perp}{\partial y} \tag{3.46}$$

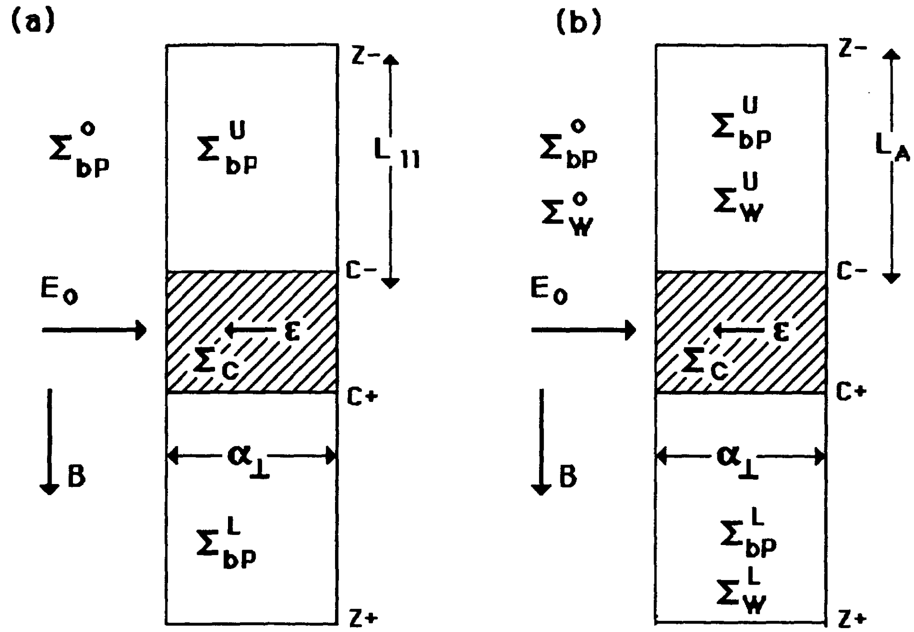

Figure 3.3: Layer model with a plasma cloud in applied electric and magnetic fields.

From the definition of conductivities it can be shown that $\sigma_{e\|} \gg \sigma_{i\|}$ and $\sigma_{e\perp} \ll \sigma_{i\perp}$, where $\sigma_{i\perp}$ is the Pedersen conductivity of the ambient ions and $\sigma_{e\|}$ is the parallel electron conductivity. Under these conditions the currents can be written as $J_\| \simeq \sigma_{e\|}E_\|$ and $J_\perp \simeq \sigma_{i\perp}E_\perp$. The electric field is determined by the potential variation in the transverse and parallel directions with scales $a_\perp$ and $L_\|$ respectively. Substitution of the above into Eq. (3.46) gives

$$\sigma_{i\perp}\frac{\phi}{a_\perp^2} \sim \sigma_{e\|}\frac{\phi}{L_\|^2} \tag{3.47}$$

where ϕ is the perturbation potential. Thus, the perturbation in the background plasma reaches to a distance $L_\|$ given by

$$L_\| \sim a_\perp\sqrt{\frac{\sigma_{e\|}}{\sigma_{i\perp}}} \tag{3.48}$$

For the ionosphere the ratio $\sigma_\|/\sigma_\perp \cdot \sim 10^5 - 10^{12}$. This expression of the parallel interaction length is another statement of the equipotentiality of the magnetic field lines. As a result of the condition $\sigma_\| \gg \sigma_\perp$, the perturbation electric field is mapped at large distances along the magnetic field and results in very small parallel electric fields, thus making the field lines be almost equipotential. The value derived for $L_\|$ is similar to the attenuation length scale for the mapping of electrostatic fields derived in the classic paper by *Farley* [1959]. For a stationary plasma with $\nu \ll \Omega$ the $L_{\|}$ is similar to the extent of the perturbations along $\mathbf{B}$ caused by the presence of a probe [*Sanmartin*, 1970] (Martinez-Sanchez, personal communication, 1991).

An expression for the electric field within the plasma cloud and consequently inside the perturbed region, can be obtained from the conservation of total current. The transverse current, neglecting the Hall contribution in each layer, is given by

$$\begin{aligned}
\mathbf{J}_{\perp}^{U} &= \sigma_{bP}^{U}\mathbf{E}_{\perp} \\
\mathbf{J}_{\perp}^{C} &= \sigma_{bP}^{C}\mathbf{E}_{\perp} + \sigma_{cP}\mathbf{E}_{\perp} \\
\mathbf{J}_{\perp}^{L} &= \sigma_{bP}^{L}\mathbf{E}_{\perp}
\end{aligned} \tag{3.49}$$

The subscript in the Pedersen conductivities denote the species, b for the background ions, c for the cloud ions. Superscripts denote the layer as shown in Figure 3.3. We define the horizontal current within a layer as the integral of the current density along the field lines as $\mathbf{I}_{\perp} = \int \mathbf{J}_{\perp} dz$. The charge conservation $\nabla \cdot \mathbf{J} = 0$ can be written as $\nabla \cdot \mathbf{J}_{\perp} = -\partial J_z / \partial z$. We integrate this equation within each layer along the magnetic field to get

$$\begin{aligned}
\nabla \cdot \mathbf{I}_{\perp}^{U} &= -\int_{Z-}^{C-} dz \frac{\partial J_z}{\partial z} = J_z(Z-) - J_z(C-) \\
\nabla \cdot \mathbf{I}_{\perp}^{C} &= -\int_{C-}^{C+} dz \frac{\partial J_z}{\partial z} = J_z(C-) - J_z(C+) \\
\nabla \cdot \mathbf{I}_{\perp}^{L} &= -\int_{C+}^{Z+} dz \frac{\partial J_z}{\partial z} = J_z(C+) - J_z(Z+)
\end{aligned} \tag{3.50}$$

Assume that there is no current flowing in or out from the boundaries, i.e., $J_z(Z+) = J_z(Z-) = 0$; assume also that the electric field is mapped without attenuation throughout the layers. If $I_{b\perp}^{o}$ is the total current flowing in the unperturbed plasma then from total current conservation it is $I_{b\perp}^{o} = I_{\perp}^{U} + I_{\perp}^{C} + I_{\perp}^{L}$ and the electric field within the perturbation strip is

$$\mathbf{E} = \frac{\Sigma_{bP}^{o}}{\Sigma_{bP} + \Sigma_{cP}} \mathbf{E}_{o} \tag{3.51}$$

In the above expression Σ denotes the field integrated transverse Pedersen conductivity, i.e., $\Sigma = \int \sigma dz$. Specifically, $\Sigma_{bP} = \int \sigma_b^L dz + \int \sigma_b^U dz$ is the Pedersen conductance of the background integrated within the perturbation strip, $\Sigma_{cP} = \int \sigma_c dz$ is the cloud's Pedersen conductance, and Σ_{bP}^o is the Pedersen conductance of the unperturbed ionosphere. The above relation (3.51) shows that if the cloud's conductance is much larger than the ambient, i.e., $\Sigma_{bP} \ll \Sigma_{cP}$, the applied electric field is totally shielded. In such a case $|\mathbf{E}| \ll |\mathbf{E}_o|$ and the plasma cloud is stationary; this property of clouds has been explored in the estimation of the ambient ionospheric electric fields and neutral winds. In the case where the background conductance dominates over the cloud, i.e., $\Sigma_{bP} \gg \Sigma_{cP}$, the cloud drifts with the ambient plasma under the action of the unperturbed field $\mathbf{E}_o$. A picture relevant to our application can be considered as follows. In the contaminant plasma cloud the driving force is the (contaminant) neutral cloud with a velocity $\mathbf{U}_r$. If we transfer to a reference frame moving with the neutral wind, then the force on the plasma cloud is simply that due to the field $\mathbf{E}_r = \mathbf{U}_r \times \mathbf{B}$. If the applied field $\mathbf{E}_r$ is totally shielded in the wind frame the cloud will be stationary, or in the earth's reference frame the cloud will be drifting with the neutral wind. In a situation where the neutral cloud moves with the velocity of the space structure, then total shielding would imply that the plasma cloud drifts with the vehicle.

We can complete now the physical picture of the current closure. The perpendicular background conductivity allows for the parallel (mainly electron) currents to drive current in the transverse direction; this mechanism depolarizes the charge imbalance created by the presence of the cloud. These perpendicular currents, mainly due to ion motion, are driven up to a distance, given by $L_{||}$. Beyond that distance the parallel flux can not drive transverse currents and closure occurs. From the definition of the parallel interaction length we can show that for the altitude range considered in this study, it permeates the E region. In other words, the perturbation field will be mapped down to the E region. This is the region where the conductivity is larger and most of the transverse currents flow and depolarization occurs. The E region contributes the most to the integrated perpendicular conductivity, Σ_{bP}. In the framework of the derivation it is necessary to include the E region in the current closure since otherwise one would reduce the magnitude of the Σ_{bP}. Smaller values of Σ_{bP}, according to Eq. 3.51, result in larger attenuation of the imposed electric fields and, consequently, the cloud drift predicted would be smaller. One clarification is needed here. We concluded that the integrated Pedersen conductivity controls the shielding. Consistent with the above derivation is the assumption of a homogeneous background. In a nonhomogenous background the shielding is determined not only by the integrated conductivity Σ_{bP} but also by the ratio of the conductivities at the point where the cloud connects to the magnetic field lines, σ_{bP}/σ_{cP}. This concept has been confirmed by the numerical simulations presented in this study and is elucidated in Chapter 5.

3.3.2 Transverse Pedersen Currents and Alfvén Waves

We will discuss now the closure of currents by allowing Pedersen and inertia currents to flow in the transverse direction. The latter, as we will see, appear as an Alfvén wave propagating along the **B** lines. We begin first with a review of the theory of Alfvén waves generated by a moving conductor and the conditions of applicability to moving plasma clouds in the ionosphere.

Alfvén Waves from a Moving Conductor

The problem of the wave structure associated with a moving conductor in a magnetic field has been the subject of extended studies since its first treatment by *Drell et al.* [1965] [*Goertz and Boswell*, 1979; *Neubauer*, 1980; *Wright and Southwood*, 1987]. We review the theory applicable to the sub-Alfvénic flow, i.e., $V_o/V_A \ll 1$ where the Alfvén velocity is defined as $V_A = B/\sqrt{\mu_o n_i m_i}$. For the ionosphere $V_A \simeq 600$ km/s and the above condition is easily satisfied since the orbital velocity is $V_o \simeq 8$ km/s.

Take a conductor that is moving at some velocity $\mathbf{V}_o$ perpendicular to the unperturbed magnetic field $\mathbf{B}_o$. The motional electric field seen in the frame moving with the conductor is $\mathbf{E}_o = \mathbf{V}_o \times \mathbf{B}$. This field drives a current in the conductor which then flows into the ambient plasma along specific directions called the Alfvén characteristics, defined by

$$\mathbf{V}_A^{\pm} = \mathbf{V}_o \pm \frac{\mathbf{B}_o}{\sqrt{\mu_o \rho}} = \mathbf{V} \pm \frac{\mathbf{B}}{\sqrt{\mu_o \rho}} \tag{3.52}$$

A schematic of the process is shown in Figure 3.4. The (wave) perturbation mag-

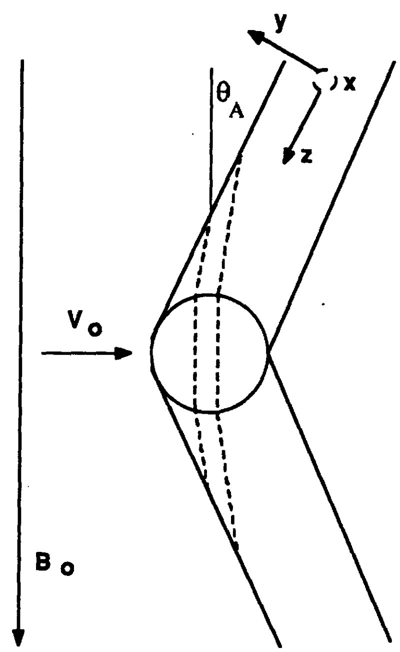

Figure 3.4: The stationary Alfvén waves from a moving conductor. The ambient plasma flow is $\mathbf{V}_o$.

netic field $\delta\mathbf{B}$ and perturbation velocity $\delta\mathbf{V}$ are associated with the motion of the background plasma are given by the Alfvén relation as

$$\delta\mathbf{B} = \pm\delta\mathbf{V}\sqrt{\mu_o\rho} \tag{3.53}$$

For stationary conditions the wave electric field can be derived from a potential and does not vary along the characteristic, i.e., $\delta\mathbf{E} = -\nabla\phi(x, y)$. An important relation, obtained after manipulating Maxwell's equations, gives the current density in the direction of the Alfvén characteristic as

$$\nabla\cdot\mathbf{E} = \mu_o(\mathbf{V}_o \pm \mathbf{V}_A)\cdot\mathbf{J} = \mu_o(\mathbf{V}_A^{\pm})\cdot\mathbf{J} \quad \text{or} \tag{3.54}$$
$$\nabla^2\phi = -\mu_o V_A^{\pm} J_z$$

Hence the wave propagates along the characteristic and the solution is independent of $\mathbf{z}$. To satisfy Amperes's law there must be a component of the current flowing perpendicular to the characteristics ; it is given by $\mathbf{J}_\perp = \frac{1}{\mu_o}\nabla\mathbf{B}_z \times \mathbf{z}$. A general solution to the problem can be obtained given the distribution of the current $J_z(x, y)$. Then the electric field can be determined and, consequently, the plasma flow and magnetic field perturbation.

An example is a moving conductor with a cylindrical flux tube of radius R and with the surface charge of an electrostatic dipole. Assume that the field inside the tube is constant and dipolar outside. The motional electric field is reduced by a fraction in the conductor and becomes $\mathbf{E} = \mathbf{E}_o + \delta\mathbf{E}$. If the conductivity of the moving body is σ_c then the steady current density inside the conductor is given by $\mathbf{J}_c = \sigma_c\mathbf{E}$. This current closes in the surroundings by the Alfvén waves with a current pattern that is stationary in the moving frame of the conductor. If we apply total current conservation we can evaluate the perturbation field as

$$\delta\mathbf{E} = -\frac{\Sigma_C}{\Sigma_C + (\Sigma_A^+ + \Sigma_A^-)}\mathbf{E_o} \quad \text{for } r < R \tag{3.55}$$

Here Σ_C is the integrated along $\mathbf{z}$ conductivity of the conductor and $\Sigma_A^\pm$ is the background wave conductance in the upper and lower leg of the wing. The surface charge on the surface of the flux tube induces a field inside given by the above relation. Outside of the flux tube this surface charge induce a dipole field given by

$$\delta\mathbf{E} = \left(\frac{R}{r}\right)^2 (\cos\theta\mathbf{e_r} + \sin\theta\mathbf{e}_\phi)\frac{\Sigma_C}{\Sigma_C + (\Sigma_A^+ + \Sigma_A^-)}\mathbf{E}_o \quad \text{for } r > R \tag{3.56}$$

where $\theta = \tan^{-1}(y/x)$. It is an easy exercise to show that the $\delta\mathbf{B}$ obtained is that due to a magnetostatic dipole with a surface current on the surface of the flux tube. The plasma velocity induced by this field, in the frame of the moving conductor, is $\mathbf{V} = \delta\mathbf{B}/\sqrt{\mu_o\rho} + \mathbf{V}_o$ or

$$\mathbf{V} = \begin{cases} \frac{\Sigma_A^+ + \Sigma_A^-}{\Sigma_C + \Sigma_A^+ + \Sigma_A^-}\mathbf{V}_o & \text{for } r < R \\ \left\{\left(\frac{R}{r}\right)^2 \sin 2\theta\mathbf{x} - \left[\left(\frac{R}{r}\right)^2 \cos 2\theta + 1\right]\mathbf{y}\right\}\frac{\Sigma_A^+ + \Sigma_A^-}{\Sigma_C + \Sigma_A^+ + \Sigma_A^-}\mathbf{V}_o & \text{for } r > R \end{cases} \tag{3.57}$$

In the limit $\Sigma_C \gg \Sigma_A = \Sigma_A^+ + \Sigma_A^-$ the perturbation field inside the flux tube is $\delta\mathbf{E} \simeq -\mathbf{E}_o$, thus the total field inside becomes $\mathbf{E}_c \simeq 0$. From Eq. (3.57) we see that the plasma inside the flux tube is at rest, i.e., $\mathbf{V} \simeq 0$. The plasma flow pattern then is similar to the incompressible flow about a body. The current pattern however is more complex. In general the perpendicular (to the characteristics) currents form closed loops and are connected with surface parallel currents [*Neubauer*, 1980]. The mechanical analogy of the flow picture in the stationary plasma frame is as follows.

The currents flowing in the conductor result in a $\mathbf{J} \times \mathbf{B}$ force which slows it down, in the $-\mathbf{V}_o$ direction. The momentum loss is transferred to the plasma by the Alfvén wave and speeds it up. In the moving frame the plasma flowing above or below the conductor encounters the front edge of the Alfvén tube and thus the currents which slow it down.

Let us now consider the conditions of applicability of the above theory in the case of a moving cloud. The necessary condition in the derivation of Alfvén waves is that the perturbations do not compress the plasma which is achieved in a plasma with $\beta \ll 1$. This condition is satisfied in our study as we stated in the beginning of this chapter. The other condition for the existence of (shear) Alfvén waves is that $\omega \ll \Omega_i$. Take $k_{||}$ and $k_{\perp}$ as the wavenumbers associated with the parallel and transverse length of disturbance given by $L_{\perp,||} \sim 2\pi k_{\perp,||}$. Substitution for $\omega = k_{||}/V_A$ and using $k_{||} \sim k_{\perp} V_c/V_A$ we can estimate the limit of the transverse length of the perturbation, i.e., $L_{\perp} \gg 2\pi V_o/\Omega_i$. With the maximum cloud velocity of $V_c \simeq 8$ km/s this requires that $L_{\perp} \gg 240$ m which is also satisfied in our study.

Closure Model

We apply now the concepts of the two previous sections and develop a simple model for current closure including both the wave conductivity and the perpendicular conductivity of the background plasma. The moving density perturbation generates an electric field which propagates along the **B** lines in the form of an Alfvén wave. At the same time, inertia currents flow perpendicular to the **B** lines [*Mitchell et al.*, 1985; *Nalesso and Jacobson*, 1988]. The issue is that of the field-aligned propagation of transverse fields and the associated currents, and is similar to that studied by many authors in ionospheric-magnetospheric coupling phenomena [*Mallinckrodt and Carlson*, 1978; *Goertz and Boswell*, 1979; *Pudovkin et al.*, 1987]. The perpendicular, mainly ion, current can be written as

$$\mathbf{J}_{\perp} = \frac{\Sigma_W}{V_A}\frac{d\mathbf{E}_{\perp}}{dt} + \sigma_P \mathbf{E}_{\perp} \tag{3.58}$$

where $\Sigma_W = 1/\mu_o V_A$ is the wave conductance of the ambient plasma, V_A is the Alfvén velocity and σ_P the Pedersen conductivity. We apply now the current balance in the ambient plasma assuming that the cloud is located at $z = Z_C$ and the upper and lower wave fronts at $z = Z_+$ and $z = Z_-$ respectively. Integrating from $Z_\pm$ up to the height of the cloud we get the parallel current density given by

$$J_{||}(Z_+) - J_{||}(Z_C) = \int_{Z_+}^{Z_C} dz \nabla_\perp \cdot (\frac{\Sigma_W}{V_A}\frac{dE_\perp}{dt} + \sigma_{bP}\mathbf{E}_\perp) \tag{3.59}$$

$$J_{||}(Z_C) - J_{||}(Z_-) = \int_{Z_-}^{Z_C} dz \nabla_\perp \cdot (\frac{\Sigma_W}{V_A}\frac{dE_\perp}{dt} + \sigma_{bP}\mathbf{E}_\perp) \tag{3.60}$$

If we set the currents $J_{||}(Z_+) = J_{||}(Z_-) = 0$ and assume that $\mathbf{E}_\perp$ is independent of z then the integral can be moved into the divergence to yield

$$J_{||} = \pm\nabla \cdot [(\Sigma_W + \Sigma_{bP})\mathbf{E}_\perp] \tag{3.61}$$

where Σ_{bP} and Σ_W are integrated within the strip where the electric field is disturbed (Figure 3.3b). Note that this expression is similar to that given by Eq. (3.54). Applying total current conservation within the perturbation region, i.e., the strip bounded by the $\mathbf{B}$ lines which pass from the edges of the cloud, we get for the electric field

$$\mathbf{E}_\perp = \frac{\Sigma_W^o + \Sigma_{bP}^o}{\Sigma_W + \Sigma_{bP} + \Sigma_{cP}}\mathbf{E}_o \tag{3.62}$$

Σ_{cP} is the height integrated Pedersen conductivity of the plasma cloud and $\mathbf{E}_\perp = \mathbf{E}_o + \epsilon_\perp$ where ϵ is the perturbation electric field. In the absence of the wave conductivity the above expression is reduced to that given in Eq. (3.51). Clearly, the wave conductivity can be neglected if $\Sigma_{bP} \gg \Sigma_W$. By introducing the wave conductivity, additional parallel currents appear as (3.61) shows. It is important to define the length of integration used to evaluate the integrated conductivities appearing in the above formula. Clearly, for an altitude varying ionosphere the magnitude of the conductances will depend on this integration length.

We begin the evaluation of the conductances for a case where the plasma cloud with a transverse length $\alpha_\perp$ appears at time $t = 0$ moving at velocity $\mathbf{V}_c$ perpendicular to the magnetic field lines. The analysis is kept general and one should distinguish between the cloud velocity V_c and the orbital velocity denoted by $V_o \simeq 8$ km/s. The orbital velocity represents the upper limit to the cloud's velocity and as we explain in the analysis below is practically not attainable. The time that it takes to travel the cloud diameter with speed V_c is given by $\tau = \alpha_\perp / V_c$. During the time τ the Alfvén front has travelled a distance $L_A = a_\perp V_A / V_c$ along the characteristics. Thus, for time scales which are shorter than the cloud characteristic time, i.e., $T \leq \tau$ we can determine the mechanism which controls the shielding of the imposed electric field $\mathbf{E}_o$, by comparing the magnitudes of the conductances according to Eq. (3.62). In Figure 3.5 we plot the integration length, L_A versus the altitude of the location of the cloud for three different characteristic times, $\tau = 0.125, 0.25, 0.375$ s respectively. It has been evaluated for a mid-latitude,summer, day time ionosphere. The variation in L_A is due to the change that the Alfvén velocity exhibits in the ionosphere. For a given cloud altitude and with L_A known we can evaluate the conductances. For three typical cloud altitudes -250, 450 and 600 km- we have evaluated the ratio Σ^o_{bP}/Σ^o_W. This is shown in Figure 3.6. Larger cloud times, i.e. slower clouds, result in larger L_A and consequently larger Σ^o_{bP}/Σ^o_W ratios. For a fixed cloud radius we can find the upper bound of the initially cloud velocity in order for the wave conductance to be neglected. These are shown in Table 3.2. Some clarifications are needed at this point.

$a_\perp$(km)	V_c^{max} (km/s)	
	h$= 250 - 450$km	h$=$ 600km
0.5	1.3	2
1	2.7	4
2	5.3	8
3	8	12

Table 3.2: Cloud radius and the upper bound of the velocity for which wave conductance can be neglected.

First, the notion of the "initial" cloud velocity V_c should be understood as the fluid

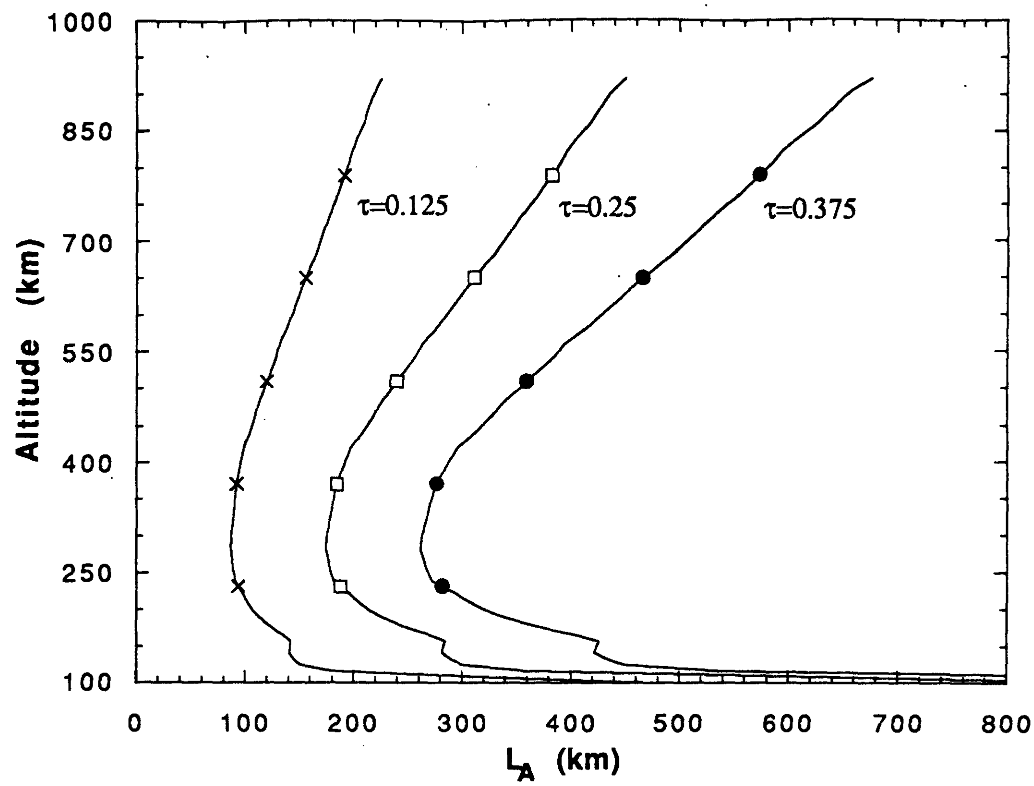

Figure 3.5: The Alfvén parallel interaction length for different cloud time scales $\tau = a_\perp/V_c$.

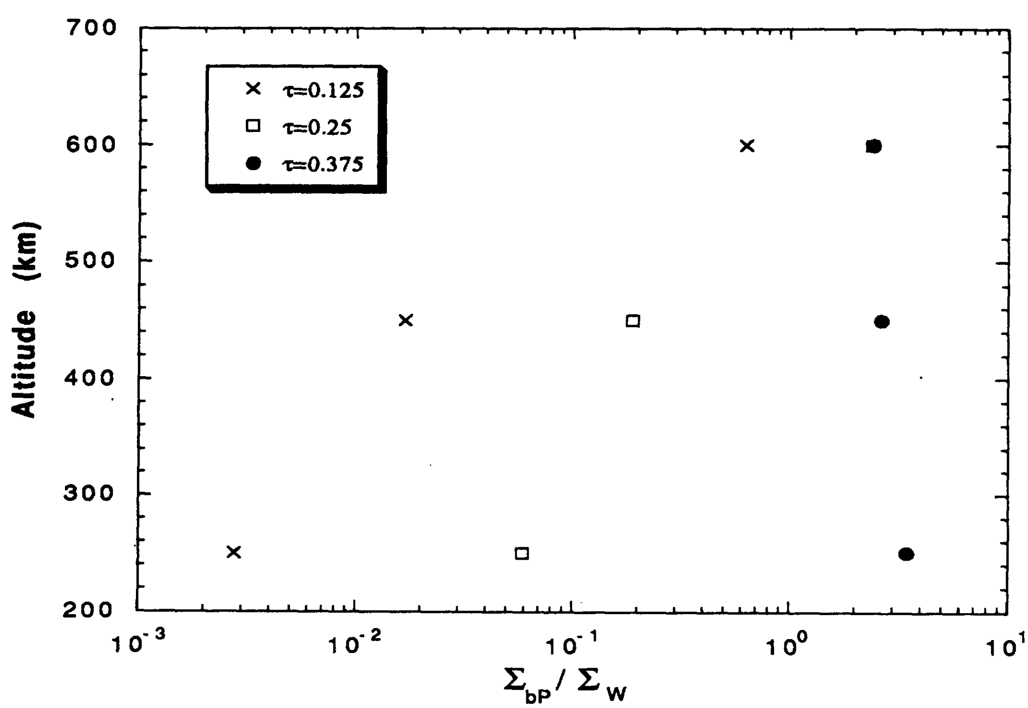

Figure 3.6: The ratio of $\Sigma^{o}_{bP}/\Sigma^{o}_{W}$ for different cloud times scales, $\tau = a_\perp/V_c$.

velocity of the cloud; it is not the individual velocity of a released ion. The physics can be clarified with the aid of both equations (3.51) and (3.55). Assume that we are sitting on the frame of the space system moving with V_o ; the applied electric field is the motional electric field. For the cloud to drift with $V_c = V_o$ it would be required that the motional field be totally shielded. Since there will always be a finite ratio of the cloud conductance to the background, whether it is wave or Pedersen is not relevant, the cloud drift will be always less than the motional, i.e., $V_c \leq V_o$. In other words, there will be transverse leakage of the parallel current allowing for the partial shielding of the motional field. This collective behavior of the plasma is seen in the cloud bulk velocity, V_c. Thus a stationary cloud, measured in the moving frame, or a drift of $V_c = 8$ km/s, measured in the stationary earth frame, is practically not attainable. This is one of the major differences of the plasma cloud compared to a moving conductor. The latter, always moves with V_o speeding up the plasma near it in expense of its own energy, as we discussed in the previous section.

Next we discuss the steady state Alfvénic waves associated with a moving cloud. Even in the case where initially the wave conductance establishes the electric field, at later times the Alfvén front moving along the characteristics with V_A clearly will reach the lower E region of the ionosphere. We neglect here the problem of attenuation of the waves in the altitude varying ionosphere as well as the possible reflection from the E region. Even for $\tau = 0.125$ it will take $T \sim 0.5$ s for a pulse originating at 800 km to reach the low E region. In order to determine the electric field from Eq. (3.62) one has to evaluate the conductances. For times larger than the characteristic time τ the conductances have to be evaluated over the entire ionosphere since currents will flow throughout it. The integration length L_A permeates the low F region which contributes the most to the conductance Σ^o_{bP}. In Table 3.3 we show the ionospheric conductances for day and nighttime conditions both at high and mid-latitudes. All values were obtained by integrating from a height of 150 km up to 1000 km. Above that height the contribution of σ^o_{bP} to the Σ^o_{bP} is negligible, while the contribution of the wave conductance would make the average value of Σ^o_W smaller. From Table 3.3 we see that at high latitudes the Pedersen conductance dominates for both day and

	Mid-latitude		High latitude	
	Σ_W^o(S)	Σ_{bP}^o(S)	Σ_W^o(S)	Σ_{bP}^o (S)
Daytime	1.7	6.66	1.52	3.91
Nighttime	1.37	0.7	1.52	3.48

Table 3.3: Integrated Conductances for different ionospheric conditions.

nigh-time conditions. However, at low latitudes the substantially depleted nighttime ionosphere does not satisfy $\Sigma_{bP}^o > \Sigma_W^o$; in such a case, Alfvén waves play an important role in the current closure circuit.

The physical picture can also be illustrated by assuming $\Sigma^o \sim \Sigma$; then the perturbation electric field can be written as

$$\epsilon_\perp = -\frac{1}{1+\frac{\Sigma_W}{\Sigma_{cP}}+\frac{\Sigma_{bP}}{\Sigma_{cP}}}\mathbf{E}_o \tag{3.63}$$

Thus, inclusion of Alfvén waves would lead to smaller perturbation fields within the plasma perturbation. Larger parallel electron currents are allowed to flow, thus depolarizing the charge accumulation which has benn formed at the height of the plasma perturbation. From the above formula we can see that if $\Sigma_B = \Sigma_W + \Sigma_{bP}$ in the limit $\Sigma_B/\Sigma_{cP} \to 0$, then $\epsilon_\perp \to -\mathbf{E}_o$, i.e., the applied electric field is totally shielded in the case where the cloud's conductance is much larger than the ionospheric. In the opposite limit, $\Sigma_B/\Sigma_{cP} \to \infty$ and $\epsilon_\perp \to 0$, i.e., in the case of a very rarefied cloud the perturbation field is negligible. In this work we have neglected the wave contribution to the conductivity and discuss the implications in the last section of this chapter. From the discussion above it is clear that for nighttime low-latitude conditions our model will underestimate the drift of a plasma cloud.

3.3.3 Pedersen and Diffusion Currents

We will utilize a layer model to discuss some of the properties of current closure with diffusion included. Assume that the one-dimensional plasma perturbation is

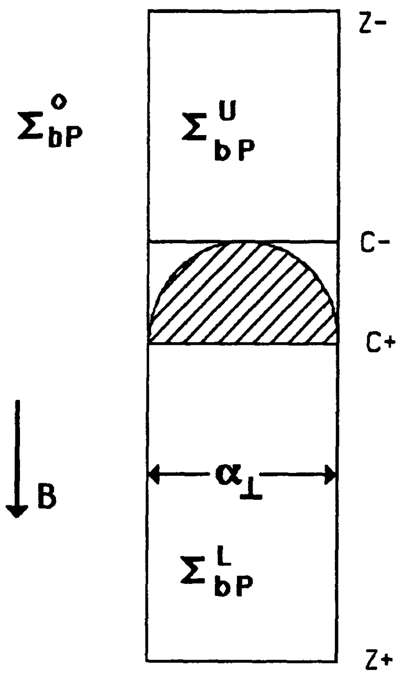

Figure 3.7: Layer model for a plasma perturbation under diffusion.

imbedded in the background ionosphere as shown in Figure 3.7. Assuming that there is no transverse external electric field the transverse current in each layer is given by

$$J_C = \sigma^C_{bP}E_\perp + \sigma_{cP}E_\perp - eD^C_b\frac{\partial n_b}{\partial x} - eD_c\frac{\partial n_c}{\partial x} - eD^C_e\frac{\partial n_e}{\partial x} \tag{3.64}$$

$$J_U = \sigma^U_{bP}E_\perp - eD^U_b\frac{\partial n^U_b}{\partial x} - eD^U_e\frac{\partial n^U_e}{\partial x} \tag{3.65}$$

$$J_L = \sigma^L_{bP}E_\perp - eD^L_b\frac{\partial n^L_b}{\partial x} - eD^L_e\frac{\partial n^L_e}{\partial x} \tag{3.66}$$

$$\tag{3.67}$$

We have neglected the Hall contributions. The subscript in the quantities denote the species, b for the background ions, c for the cloud ions and e for the electrons. Superscripts denote the layer as shown in Figure 3.7. We apply charge conservation $\nabla\cdot\mathbf{J} = 0$ and integrate along the magnetic field lines, as we did earlier in the case of Pedersen current closure. Assume that there is no current flowing in or out from the boundaries, i.e., $J_z(Z+) = J_z(Z-) = 0$; assume also that the electric field is mapped without attenuation throughout the layers. Then total current conservation leads to

$$E_\perp = \frac{eD^c_b\frac{\partial N^c_b}{\partial x} + eD^c_e\frac{\partial N^c_e}{\partial x} + eD^c_c\frac{\partial N^c_c}{\partial x} + e(D^U_b + D^U_e)\frac{\partial N^U}{\partial x} + e(D^L_b + D^L_e)\frac{\partial N^U}{\partial x}}{\Sigma^U_{bP} + \Sigma^L_{bP} + \Sigma_{cP}} \tag{3.68}$$

where N is the height integrated density within a layer $N_t = \int n_t dz$. The above relation also expresses the mechanism of coupling between the cloud and the background ionosphere. Similar expressions for the coupling between the F and E regions have been developed by *Heelis et al.* [1985]. It is of interest to examine two extreme situations. Suppose that due to the absence of the background conductivity there are no currents driven in the ambient plasma, i.e., $\Sigma_{bP}^L + \Sigma_{bP}^U \ll \Sigma_{cP}$. Then the electric field reduces to

$$E_\perp \simeq \frac{eD_c \frac{\partial N_c}{\partial x}}{\Sigma_{cP}} = \frac{kT_c}{e} \frac{1}{n_c} \frac{\partial n_c}{\partial x} \tag{3.69}$$

This is the ambipolar electric field which develops due to the fast transverse diffusion of ions. It is a simple exercise to show that in that case the plasma diffuses with the slow rate of electrons. In the other limiting case large transverse currents are allowed to flow in the ambient plasma, due to the large integrated conductivity of the background plasma, i.e., $\Sigma_{bP}^U + \Sigma_{bP}^L \gg \Sigma_{cP}$. In such a case the electric field becomes

$$E_\perp \simeq \frac{kT}{e} \frac{\mu_c}{\mu_b} \frac{1}{N_b} \frac{\partial N_c}{\partial x} \tag{3.70}$$

For the background conductance to dominate it is necessary that $N_c \ll N_b$. The electric field $E_\perp \to 0$ and, therefore, it is short-circuited very effectively. In this case diffusion proceeds -in the transverse direction- with the fast ion diffusion rate D_i. One limitation of the layer model is that it does not address for the parallel diffusion of species. Another limitation is that it does not account for the attenuation of the electric field as it is mapped along the magnetic field lines. Phenomena associated with 3-D diffusion can only be illustrated in numerical simulations where few simplifications of the underlying physics are made. Such simulations are presented in Chapter 5.

3.4 Generalized Charge Conservation Equation

We return now to derive a general form of charge conservation equation taking into account the unsteady and inertia effects. They could arise in situations where there are slowly varying forces acting on the plasma such as electric fields or neutral winds.

We can derive the currents driven by these time dependent forces utilizing the analysis from Chapter 2. The correction to the velocity due to the assumption that the terms $d\mathbf{V}_t/dt \simeq 0$ has been derived in Eq. (2.12). We restrict the analysis to the condition $\nu \ll \Omega_i$ which is always satisfied in the ambient plasma. This assumption does not limit the analysis because most of the currents flow in the background plasma. Under these conditions the velocity correction from Eq. (2.12) is given by

$$\widetilde{\mathbf{V}}_{t\perp}^{(iner)} = k_{tp}\frac{d\mathbf{V}_t}{dt} \tag{3.71}$$

The approximate velocity is given from Eq. (2.10)

$$\begin{aligned} V_t &\simeq \left[\frac{\mathbf{E}}{B} + \Sigma_n\left(\frac{\nu_{tn}}{\Omega_t}\right)\mathbf{V}_n + \Sigma_j\left(\frac{\nu_{tj}}{\Omega_t}\right)\mathbf{V}_j - \frac{kT}{qB}\frac{\nabla n_t}{n_t} + \frac{1}{\Omega_t}\mathbf{g}\right]\times\mathbf{b} \\ &\simeq \left[\frac{\mathbf{E}}{B} - \frac{kT}{qB}\frac{\nabla n_t}{n_t}\right]\times\mathbf{b} \end{aligned} \tag{3.72}$$

If we further assume that $E_\perp a_\perp \gg kT_t/q_t$ then the correction to the drift becomes

$$\widetilde{\mathbf{V}}_{t\perp}^{(iner)} = \frac{m}{q_t B^2}\frac{d\mathbf{E}}{dt} \equiv \mathbf{V}_t^{pol} \tag{3.73}$$

This is exactly the polarization drift due to slowly varying electric fields. The current density due to the polarization drift is

$$\mathbf{J}_t^{pol} = \frac{n_t m_t}{B^2}\frac{d\mathbf{E}_\perp}{dt} = \frac{\Sigma_W}{V_A}\frac{d\mathbf{E}_\perp}{dt} \tag{3.74}$$

The total current density due to the polarization drift of all species can be formally written as

$$\mathbf{J}^{pol} = \sum_{t=j}\frac{n_t m_t}{B^2}\frac{d\mathbf{E}_\perp}{dt} \tag{3.75}$$

To complete the current balance we must add the currents carried by the Alfvén waves along the characteristics [*Goertz*, 1980]. They are given by

$$\mathbf{J}^{Alf} = \frac{1}{\mu_o V_A}\nabla\cdot\mathbf{E}\frac{\mathbf{B}}{B} \tag{3.76}$$

The total current density is simply $\mathbf{J}^{tot} = \mathbf{J}^{pol} + \mathbf{J}^{Alf} + \mathbf{J}$ where and $\mathbf{J}$ is given by Eq. (3.13). If we substitute into the charge conservation equation it becomes

$$\nabla\cdot\left(\frac{1}{\mu_o V_A^2}\frac{d\mathbf{E}}{dt} \pm \frac{1}{\mu_o V_A}\nabla\cdot\mathbf{E}\frac{\mathbf{B}}{B} + \mathbf{J}\right) = 0 \tag{3.77}$$

The first two terms can be combined to give the gradient of $\nabla \cdot \mathbf{E}_\perp$ along the Alfvén characteristics. This equation determines the self-consistent electric field $\mathbf{E}$. In addition to the steady currents arising in a plasma, this formulation includes those driven by slowly varying electric fields. These are polarization currents that flow in the background plasma transverse to the magnetic field lines. The transverse currents close with steady field aligned currents and additional Alfvén currents carried along the characteristics. Note that we are within the electrostatic formulation but one can include a vector potential for completeness. A 2-D analysis in the framework of Eq. (3.77) has been presented in *Hastings and Gatsonis* [1989]. The wave phenomena that are associated with the 3-D equation along with the boundary conditions make the numerical solution in this form very difficult. In this study we include perturbatively the effects arising from polarization currents, by adding the correction term to the velocity and evaluating numerically the associated divergence term in the charge conservation equation.

The nature of the excited electric field perturbations is related to the propagation of the disturbance. It is expected that both electrostatic and electromagnetic disturbances arise from a moving plasma cloud. In a pure electrostatic problem with steady electric fields the equation for the potential is of elliptic type. It implies that fields are transferred to distances given by the attenuation length $L_{\|} \sim a_\perp \sqrt{\sigma_{\|}/\sigma_\perp}$. With the introduction of unsteady electric fields and ion inertia, the propagation of fields occurs at the Alfvén speed. We considered here transverse Alfvén waves due to the ion inertia. From simple layer models we derived relations that give the relative contribution to the current closure by the Pedersen and the Alfvén waves. The critical parameter in determining this contribution is the ratio of the conductances Σ_{bP}/Σ_W. For clouds that stay long enough on the same flux tube transverse Pedersen current leakage depolarizes the charge imbalance generated at the height of the cloud. Whether or not transverse currents will flow all the way down to the E region depends on the time that the cloud stays on the same flux tube and the speed of the propagation of the generated electric field. From the simple layer models it was deduced that Alfvén waves are important in cases of small clouds drifting with high speeds. Note that there will always be transverse leakage due to Pedersen and polarization currents. These currents short-circuit the perturbation electric field and slow down the cloud. Thus, neglecting the Alfvén waves results in faster drift for the plasma clouds. In a realistic situation cloud drifts of the order of the orbital velocity can only be attained with very high cloud densities and at very early times. Once leakage occurs, regardless of the mechanism, the cloud slows down. Also, large cloud velocities are confined to the cloud's dense regions while the bulk of the cloud drifts with much smaller speeds thus allowing Pedersen currents to depolarize more effectively.

There are several problems still to be addressed. The most important is the investigation of the entire spectrum of the electrostatic and electromagnetic waves emitted by the moving cloud. Such an approach should clearly examine also the attenuation or reflection of the emitted waves on the low altitude ionosphere, as well as the interaction with the magnetosphere. In this study wave effects have been introduced perturbatively with the introduction of polarization currents into the current balance equation. Clearly, a complete formulation of the problem would require the solution of the 3-D fluid plasma equations along with the the full Maxwell equations. Given the theoretical and numerical complexity of such an approach, the simplifications undertaken in this and previous studies of wave radiation from moving plasma clouds are justified.

Chapter 4

Numerical Methods

One of the efforts in this study was the development and implementation of appropriate numerical schemes. In this chapter we present the numerical methods used in the solution of the 3-D model equations. We begin with the analysis of hyperbolic systems. We develop an extension of the original Flux Corrected Transport (FCT) algorithm in three dimensions (3D-FCT). We discuss the numerical properties of the high and low-order scheme used in the construction of the 3D-FCT. We present numerical results of a 3-D wave problem. Next we discuss the solution of three-dimensional nonself-ajoint elliptic equations. We present the discrete form of the equation and the storage schemes. We discuss methods for solving the large, sparse, asymmetric system of equations that are derived.

4.1 Numerical Solution of 3-D Hyperbolic Systems

In Chapter 2 we presented the continuity equations for the plasma species. The continuity equations are of hyperbolic type and are one example of *conservation laws.* The discussion that follows can be applied to any system of conservation laws which can be written in the form

$$\frac{\partial U}{\partial t} + \frac{\partial f}{\partial x} + \frac{\partial g}{\partial y} + \frac{\partial h}{\partial z} = 0 \tag{4.1}$$

Here U is the state vector and f, g and h are the flux vectors. An example of such a system is the 3-D inviscid Euler equations in fluid mechanics. The discussion on the behavior of hyperbolic systems and methods for their numerical solution has been presented by *Lax* [1954]. The most important property of hyperbolic systems is that they admit *genuine* and *weak* solutions. The state vector U may have bounded discontinuities in its derivatives (genuine solution) or might be discontinuous along a surface (weak). Conservation laws in fluid mechanics, allow the formation of shocks. The challenge to the numerical solution is the accurate representation of these discontinuities, where most of schemes break down as we will explain in what follows.

We discretize our equations on a 3-D cartesian grid with $\Delta x_i, \Delta y_j$ and Δz_k the mesh spacings given by $\Delta x_i = \frac{1}{2}(x_{i+1} - x_{i-1}), \Delta y_j = \frac{1}{2}(y_{j+1} - y_{i-1})$, and $\Delta z_k = \frac{1}{2}(z_{k+1} - z_{k-1})$. On a grid point (i,j,k) as shown in Figure 4.1 a finite difference (FD) approximation of Eq. (4.1) in conservation or "flux" can be written as

$$U^{n+1}_{i,j,k} = U^n_{i,j,k} - \frac{1}{V_{i,j,k}}\Big[\Big(F_{i+\frac{1}{2},j,k} - F_{i-\frac{1}{2},j,k}\Big) + \Big(G_{i,j+\frac{1}{2},k} - G_{i,j-\frac{1}{2},k}\Big) + \Big(H_{i,j,k+\frac{1}{2}} - H_{i,j,k-\frac{1}{2}}\Big)\Big] \tag{4.2}$$

The volume element around (i,j,k) is $V_{i,j,k} = \Delta x_i \Delta y_j \Delta z_k$. Superscripts show a temporal grid point at a given time $t^n = n\Delta t$, with Δt the time step for the explicit numerical integration. The quantities $F_{i\pm\frac{1}{2},j,k}$ at the interface of the cells in the i direction are called transportive fluxes and are also given at time t^n. They are in general functions of the fluxes, i.e., $F = F(f)$; this functional dependence defines the specific numerical scheme. Similar arguments hold for the interface transportive fluxes in the other directions, i.e, $G_{i,j\pm\frac{1}{2},k}, H_{i,j,k\pm\frac{1}{2}}$. The numerical solution of hyperbolic systems suffers from dispersion and dissipation. These errors appear in regions of discontinuities or large gradients. Dispersive errors appear as ripples with overshoots and undershoots. An analysis of the truncation error of the numerical schemes exhibiting ripples reveals odd derivatives as the leading term. The result is that the phase relation between waves is distorted. Second or higher order methods exhibit usually dispersive errors. Another form of numerical error is dissipation due to the presence of even derivative terms in the truncation error. These terms act as an im-

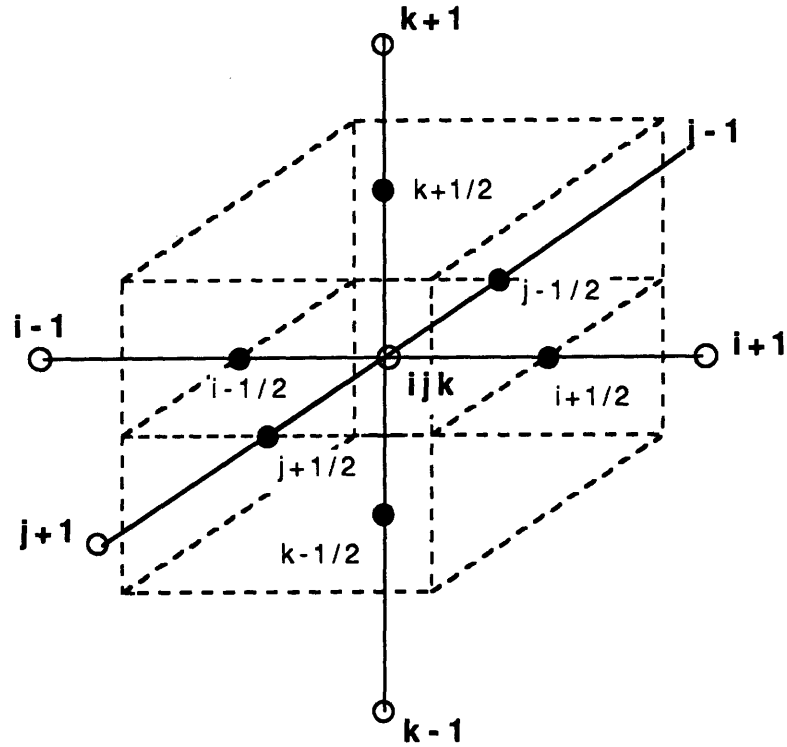

Figure 4.1: Grid configuration used in the finite-difference of hyperbolic equations

plicit artificial viscocity which reduces the gradients in the solution. This error is a common characteristic of low order schemes.

The solution to the problems of dispersion has been the addition of artificial viscocity, i.e., terms which contain even derivatives of U. The problem with artificial viscocity is in determining how much and where to be added. There are heuristic arguments for such an approach but one is always faced with the problem of either reoccurring ripples or smearing out the gradients.

The Flux Corrected Transport (FCT) method developed originally by *Boris and Book* [1973, 1975, 1976] successfully addressed the problems of dispersion and dissipation. The idea behind FCT is to preserve as much of a high order scheme in terms of accuracy as possible; at the same time preserve the most important property of low order schemes, i.e., the lack of ripples and the enforcement of positivity. There has been numerous applications of FCT in both fluid and plasma problems. The original algorithm was implemented in two-dimensions in another formulation of FCT by *Za-*

lesak [1979]. After its appearance Zalesak's formulation received wide attention for its superior performance over the original FCT: it does not result in time splitting, it corrects the clipping phenomena, and it can be applied as a filter with any CFD scheme [*Lohner et al.*,1987; *Zalesak*, 1987].

4.1.1 3-D Flux-Corrected Transport

We consider the flux FD form of the three-dimensional equations as given in Eq. (4.2). We apply the FCT algorithm as it is described by *Zalesak* [1979] in the following steps.

(1) Compute $F^L_{i\pm\frac{1}{2},j,k}$, $G^L_{i,j\pm\frac{1}{2},k}$, and $H^L_{i,j,k\pm\frac{1}{2}}$ by a low order scheme.

(2) Compute $F^H_{i\pm\frac{1}{2},j,k}$and $G^H_{i,j\pm\frac{1}{2},k}$, and $H^L_{i,j,k\pm\frac{1}{2}}$ by a high order scheme.

(3) Compute the "antidiffusive fluxes"

$$\begin{aligned} A_{i\pm\frac{1}{2},j,k} &\equiv F^H_{i\pm\frac{1}{2},j,k} - F^L_{i\pm\frac{1}{2},j,k} \\ A_{i,j\pm\frac{1}{2},k} &\equiv G^H_{i,j\pm\frac{1}{2},k} - G^L_{i,j\pm\frac{1}{2},k} \\ A_{i,j,k\pm\frac{1}{2}} &\equiv H^H_{i,j,k\pm\frac{1}{2}} - H^L_{i,j,k\pm\frac{1}{2}} \end{aligned} \tag{4.3}$$

(4) Compute the low order time advanced ("transported and diffused") solution

$$\begin{aligned} U^{td}_{i,j,k} = U^n_{i,j,k} - \frac{1}{V_{ijk}} \Big[\left(F^L_{i+\frac{1}{2},j,k} - F^L_{i-\frac{1}{2},j,k}\right) + \left(G^L_{i,j+\frac{1}{2},k} - G^L_{i,j-\frac{1}{2},k}\right) \\ + \left(H^L_{i,j,k+\frac{1}{2}} - H^L_{i,j,k-\frac{1}{2}}\right)\Big] \end{aligned} \tag{4.4}$$

(5) Apply the FCT limiter to the antidiffusive fluxes so that U^{n+1}, as computed in step (6),is bounded by the extrema in U^{td} or U^n.

$$\begin{aligned} A^C_{i\pm\frac{1}{2},j,k} &= A_{i\pm\frac{1}{2},k} C_{i\pm\frac{1}{2},j,k} \quad 0 \le C_{i\pm\frac{1}{2},j} \le 1 \\ A^C_{i,j\pm\frac{1}{2},k} &= A_{i,j\pm\frac{1}{2},k} C_{i,j\pm\frac{1}{2},k} \quad 0 \le C_{i,j\pm\frac{1}{2},k} \le 1 \\ A^C_{i,j,k\pm\frac{1}{2}} &= A_{i,j,k\pm\frac{1}{2}} C_{i,j,k\pm\frac{1}{2}} \quad 0 \le C_{i,j,k\pm\frac{1}{2}} \le 1 \end{aligned} \tag{4.5}$$

(6) Apply the corrected antidiffusive fluxes

$$\begin{aligned} U^{n+1}_{i,j,k} = U^{td}_{i,j,k} - \frac{1}{V_{i,j,k}} \Big[\left(A^C_{i+\frac{1}{2},j,k} - A^C_{i-\frac{1}{2},j,k}\right) + \left(A^C_{i,j+\frac{1}{2},k} - A^C_{i,j-\frac{1}{2},k}\right) \\ + \left(A^C_{i,j,k+\frac{1}{2}} - A^C_{i,j,k-\frac{1}{2}}\right)\Big] \end{aligned} \tag{4.6}$$

The FCT limiter gives the weighting coefficients C in step (5) by which we multiply the antidiffusive fluxes. For $C = 0$ the corrected flux is set to zero and the obtained solution is the low-order while for $C = 1$ the solution is the high-order. The 3-D limiter developed here is an extension of the 2-D one presented by *Zalesak* [1979]. We compute the following quantities

$$\begin{aligned}
P^+_{i,j,k} &= \max(0, A_{i-\frac{1}{2},j,k}) - \min(0, A_{i+\frac{1}{2},j,k}) \\
&+ \max(0, A_{i,j-\frac{1}{2},k}) - \min(0, A_{i,j+\frac{1}{2},k}) \\
&+ \max(0, A_{i,j,k-\frac{1}{2}}) - \min(0, A_{i,j,k+\frac{1}{2}}) \\
Q^+_{i,j,k} &= (U^{\max}_{i,j,k} - U^{td}_{i,j,k})\Delta V_{i,j,k} \\
R^+_{i,j,k} &= \begin{cases} \min(1, \frac{Q^+_{i,j,k}}{P^+_{i,j,k}}) & \text{if } P^+_{i,j,k} > 0 \\ 0 & \text{if } P^+_{i,j,k} = 0 \end{cases}
\end{aligned} \tag{4.7}$$

and similarly

$$\begin{aligned}
P^-_{i,j,k} &= \max(0, A_{i+\frac{1}{2},j,k}) - \min(0, A_{i-\frac{1}{2},j,k}) \\
&+ \max(0, A_{i,j+\frac{1}{2},k}) - \min(0, A_{i,j-\frac{1}{2},k}) \\
&+ \max(0, A_{i,j,k+\frac{1}{2}}) - \min(0, A_{i,j,k-\frac{1}{2}}) \\
Q^-_{i,j,k} &= (U^{td}_{i,j,k} - U^{\min}_{i,j,k})\Delta V_{i,j,k} \\
R^-_{i,j,k} &= \begin{cases} \min(1, \frac{Q^-_{i,j,k}}{P^-_{i,j,k}}) & \text{if } P^-_{i,j,k} > 0 \\ 0 & \text{if } P^-_{i,j,k} = 0 \end{cases}
\end{aligned} \tag{4.8}$$

The weighting coefficients are given by

$$\begin{aligned}
C_{i+\frac{1}{2},j,k} &= \begin{cases} \min(R^+_{i+1,j,k}, R^-_{i,j,k}) & \text{if } A_{i+\frac{1}{2},j,k} \geq 0 \\ \min(R^+_{i,j,k}, R^-_{i+1,j,k}) & \text{if } A_{i+\frac{1}{2},j,k} < 0 \end{cases} \\
C_{i,j+\frac{1}{2},k} &= \begin{cases} \min(R^+_{i,j+1,k}, R^-_{i,j,k}) & \text{if } A_{i,j+\frac{1}{2},k} \geq 0 \\ \min(R^+_{i,j,k}, R^-_{i,j+1,k}) & \text{if } A_{i,j+\frac{1}{2},k} < 0 \end{cases} \\
C_{i,j,k+\frac{1}{2}} &= \begin{cases} \min(R^+_{i,j,k+1}, R^-_{i,j,k}) & \text{if } A_{i,j,k+\frac{1}{2}} \geq 0 \\ \min(R^+_{i,j,k}, R^-_{i,j,k+1}) & \text{if } A_{i,j,k+\frac{1}{2}} < 0 \end{cases}
\end{aligned} \tag{4.9}$$

The search for bounds in the solution is extended in all three coordinate dimensions and given by

$$
\begin{aligned}
U^{a}_{i,j,k} &= \max(U^{n}_{i,j,k}, U^{td}_{i,j,k}) \\
U^{\max}_{i,j,k} &= \max(U^{a}_{i-1,j,k}, U^{a}_{i,j}, U^{a}_{i+1,j}, U^{a}_{i,j-1,k}, U^{a}_{i,j+1,k}, U^{a}_{i,j,k-1}, U^{a}_{i,j,k+1}) \\
U^{b}_{i,j,k} &= \min(U^{n}_{i,j,k}, U^{td}_{i,j,k}) \\
U^{\min}_{i,j,k} &= \min(U^{b}_{i-1,j,k}, U^{b}_{i,j,k}, U^{b}_{i+1,j,k}, U^{b}_{i,j-1,k}, U^{b}_{i,j+1,k}, U^{b}_{i,j,k-1}, U^{b}_{i,j,k+1})
\end{aligned}
\tag{4.10}
$$

The above algorithm is sufficient to prevent the occurrence of ripples; there have been various improvements with regard to the clipping problem, i.e, the disability to restore existing maxima once diffusion is added.

4.1.2 High Order Scheme

The high order scheme of the 3D-FCT is a predictor-corrector type, with the leapfrog as the predictor step and the trapezoidal as the corrector step. These schemes have been introduced by *Kurihara* [1965].

The predictor step is given by

$$
\begin{aligned}
U'_{i,j,k} = U^{n-1}_{i,j,k} - \frac{2\Delta t}{\Delta x_i}\left(F^{n}_{i+\frac{1}{2},j,k} - F^{n}_{i-\frac{1}{2},j,k}\right) - \frac{2\Delta t}{\Delta y_j}\left(G^{n}_{i,j+\frac{1}{2},k} - G^{n}_{i,j-\frac{1}{2},k}\right) \\
-\frac{2\Delta t}{\Delta z_k}\left(H^{n}_{i,j,k+\frac{1}{2}} - H^{n}_{i,j,k-\frac{1}{2}}\right)
\end{aligned}
\tag{4.11}
$$

The U' is at a provisional time step and the fluxes at the interface of the cells will be defined below. Note that these fluxes are different from the ones in Eq. (4.2) by the factor $\Delta t S$ where S is the area at the interface of the cell.

The values of U' at the leapfrog time step are then corrected by the trapezoidal step. First we evaluate the fluxes

$$
\begin{aligned}
f^{*}_{i,j,k} &= \frac{1}{2}(f^{n}_{i,j,k} + f'_{i,j,k}) \\
g^{*}_{i,j,k} &= \frac{1}{2}(g^{n}_{i,j,k} + g'_{i,j,k}) \\
h^{*}_{i,j,k} &= \frac{1}{2}(h^{n}_{i,j,k} + h'_{i,j,k})
\end{aligned}
\tag{4.12}
$$

Then we obtain

$$
F^{*}_{i,j,k} = F(f^{*}_{i,j,k}) \text{ and } G^{*}_{i,j,k} = G(g^{*}_{i,j,k}) \text{ and } H^{*}_{i,j,k} = H(h^{*}_{i,j,k}) \tag{4.13}
$$

Finally we perform the correction step which is

$$U^{n+1}_{i,j,k} = U^{n}_{i,j,k} - \frac{\Delta t}{\Delta x_i}\left(F^{*}_{i+\frac{1}{2},j,k} - F^{*}_{i-\frac{1}{2},j,k}\right) - \frac{\Delta t}{\Delta y_j}\left(G^{*}_{i,j+\frac{1}{2},k} - G^{*}_{i,j-\frac{1}{2},k}\right) \\ -\frac{\Delta t}{\Delta y_j}\left(H^{*}_{i,j,k+\frac{1}{2}} - H^{*}_{i,j,k-\frac{1}{2}}\right) \qquad (4.14)$$

To conform with the flux form as given in the FCT we define the high-order fluxes as

$$\begin{aligned} F^{H}_{i+\frac{1}{2},j,k} &= F^{*}_{i+\frac{1}{2},j,k}\Delta t \Delta y_j \Delta z_k \\ G^{H}_{i,j+\frac{1}{2},k} &= G^{*}_{i,j+\frac{1}{2},k}\Delta t \Delta x_i \Delta z_k \\ H^{H}_{i,j,k+\frac{1}{2}} &= H^{*}_{i,j,k+\frac{1}{2}}\Delta t \Delta x_i \Delta y_j \end{aligned} \qquad (4.15)$$

Properties of the High Order Scheme

We will examine the accuracy and stability of the leapfrog-trapezoidal scheme. The spatial accuracy of the scheme is defined by the functional dependence of the interface fluxes $F_{i\pm1/2,j,k}$ on f and similarly for the fluxes in the other directions. *Zalesak* [1979] developed such expressions for any order of accuracy. On a uniform grid they are given for second order accuracy as follows

$$\begin{aligned} F_{i+\frac{1}{2}i,j,k} &= \frac{1}{2}(f_{i,j} + f_{i+1,j,k}) \\ G_{i,j+\frac{1}{2},k} &= \frac{1}{2}(g_{i,j,k} + g_{i,j+1,k}) \\ H_{i,j,k+\frac{1}{2}} &= \frac{1}{2}(h_{i,j,k} + h_{i,j,k+1}) \end{aligned} \qquad (4.16)$$

For fourth order of accuracy the expressions are

$$\begin{aligned} F_{i+\frac{1}{2},j,k} &= \frac{7}{12}(f_{i,j,k} + f_{i+1,j,k}) - \frac{1}{12}(f_{i-1,j,k} + f_{i+2,j,k}) \\ G_{i,j+\frac{1}{2},k} &= \frac{7}{12}(g_{i,j,k} + g_{i,j+1,k}) - \frac{1}{12}(g_{i,j-1,k} + g_{i,j+2,k}) \\ H_{i,j,k+\frac{1}{2}} &= \frac{7}{12}(h_{i,j,k} + h_{i,j,k+1}) - \frac{1}{12}(h_{i,j,k-1} + h_{i,j,k+2}) \end{aligned} \qquad (4.17)$$

An interpretation of these so called "flux formulae" is given by *Zalesak* [1984].

We will proceed now with the stability analysis of the high-order scheme. The predictor step is the familiar leapfrog method. We consider the linear case of the 3-D wave equation where the convective velocities are constant.

$$\frac{\partial U}{\partial t} + u\frac{\partial U}{\partial x} + v\frac{\partial U}{\partial y} + w\frac{\partial U}{\partial z} = 0 \tag{4.18}$$

Substitute in the leapfrog finite difference equation (FDE) (4.11) a Fourier mode of the form $U^n_{ijk} = A^n \exp[\imath(i\theta_x + j\theta_y + k\theta_z)]$. The amplitude of the mode is A, the wavenumbers k_x, k_y and k_z, and $\imath = \sqrt{-1}$. The phase angles are $\theta_x = k_x\Delta x$, $\theta_y = k_y\Delta y$ and $\theta_z = k_z\Delta z$ respectively. The amplification matrix of the leapfrog mode is given by

$$A' = A^{n-1} - 2\imath A^n(c_x \sin\theta_x + c_y \sin\theta_y + c_z \sin\theta_z) \tag{4.19}$$

where the CFL numbers are given by $c_x = u\Delta t/\Delta x$, $c_y = v\Delta t/\Delta y$ and $c_z = w\Delta t/\Delta z$ in the x,y and z direction respectively. The eigenvalues of the amplification matrix, i.e, the amplification factors λ are obtained from $det|A - \lambda I| = 0$.

$$\lambda^{\pm} = -\imath(c_x sin\theta_x + c_y \sin\theta_y + c_z \sin\theta_z) \pm \sqrt{1 - (c_x \sin\theta_x + c_y \sin\theta_y + c_z \sin\theta_z)^2} \tag{4.20}$$

For stability it is required that

$$c_x \sin\theta_x + c_y \sin\theta_y + c_z \sin\theta_z \leq 1 \tag{4.21}$$

This same condition also provides the maximum time step for stability as

$$\Delta t \leq 1/\left(\frac{|u|}{\Delta x} + \frac{|v|}{\Delta y} + \frac{|w|}{\Delta z}\right) \tag{4.22}$$

Note that if the stability condition is satisfied, then $|\lambda| = 1$, so there is no dissipation in the numerical solution.

The phase angle of the numerical solution is given by the amplification factor as $\phi = \tan^{-1}[Im(\lambda)/Re(\lambda)]$. The phase angle of the exact solution is ϕ_e so the relative phase error is

$$\frac{\phi}{\phi_e} = \frac{\tan^{-1}\left(-C_s \pm \sqrt{1 - C_s^2}\right)}{c_x\theta_x + c_y\theta_y + c_z\theta_z} \tag{4.23}$$

where $C_s = c_x \sin\theta_x + c_y \sin\theta_y + c_z \sin\theta_z$. If stability conditions are satisfied, then the wave speed will always be less than the exact, i.e., the solution will suffer from lagging phase error. The above conclusions can also be achieved by examining the modified equation obtained by Taylor expansion of the various terms in the leapfrog FDE.

$$\frac{\partial U}{\partial t}+u\frac{\partial U}{\partial x}+v\frac{\partial U}{\partial y}+\frac{\partial U}{\partial z}=u\frac{\Delta x^2}{6}(c_x^2-1)\frac{\partial^3 U}{\partial x^3}+v\frac{\Delta y^2}{6}(c_y^2-1)\frac{\partial^3 U}{\partial y^3}$$
$$+w\frac{\Delta z^2}{6}(c_z^2-1)\frac{\partial^3 U}{\partial z^3}-O\left(\frac{\partial^5 U}{\partial x^5}\right)-\ldots.. \tag{4.24}$$

In the truncation error the leading term has odd derivatives of U so the scheme is dispersive. There are no dissipative terms so the algorithm is neutrally stable.

For the nonlinear equation the above simple Fourier analysis is not strictly valid. *Hirt* [1968], in his classical paper offered a heuristic stability analysis for nonlinear equations. Using the concepts of this analysis it can be shown that the odd term in the truncation error contains terms which will destabilize the numerical solution.

We can apply the Von Neumann stability analysis for the corrector step of the high-order scheme. Using the second order flux formula substitution of the Fourier mode into Eq. (4.14) gives the amplification for the trapezoidal step as

$$A^{n+1}=A^n-\frac{1}{2}\imath(c_x\sin\theta_x+c_y\sin\theta_y+c_z\sin\theta_z)(A'+A^n) \tag{4.25}$$

Substitude in the above from Eq.(4.19) we obtain the amplification factors for the leapfrog-trapezoidal method.

$$\lambda^{\pm}=\frac{1}{2}\left[1-C_s^2-\frac{1}{2}\imath C_s\right]\pm\frac{1}{2}\sqrt{\left[1-C_s-\frac{1}{2}\imath C_s\right]^2-2\imath C_s} \tag{4.26}$$

Stability requires that $|\lambda|\leq 1$ which is enforced under the condition $c_x+c_y+c_z\leq\sqrt{2}$. This relation gives also the maximum time step as

$$\Delta t\leq\sqrt{2}/\left(\frac{|u|}{\Delta x}+\frac{|v|}{\Delta y}+\frac{|w|}{\Delta z}\right) \tag{4.27}$$

To conclude, the high order scheme is second order in time while the spatial order depends on the specific flux formula used. It is also conservative in both steps *Gatsonis* [1987].

4.1.3 Low Order Algorithm: Donor Cell

We will complete the 3D-FCT algorithm with the low order algorithm. We will implement in 3-D the "Donor Cell" algorithm, originally derived by *Gentry et al.*

[1966]. This scheme belongs to the upwinding class of algorithms and uses average velocities defined at the interface of a cell. The algorithm is given as

$$U^{n+1}_{i,j,k} = U^{n}_{i,j,k} - \frac{\Delta t}{\Delta x_i}\left(F^{DC}_{i+\frac{1}{2},j,k} - F^{DC}_{i-\frac{1}{2},j,k}\right) - \frac{\Delta t}{\Delta y_j}\left(G^{DC}_{i,j+\frac{1}{2},k} - G^{DC}_{i,j-\frac{1}{2},k}\right)$$
$$-\frac{\Delta t}{\Delta z_k}\left(H^{DC}_{i,j,k+\frac{1}{2}} - H^{DC}_{i,j,k-\frac{1}{2}}\right) \qquad (4.28)$$

The fluxes at the interface of a cell are given by

$$F^{DC}_{i+\frac{1}{2},j,k} = \frac{1}{2}(u_{i,j,k} + u_{i+1,j,k})U_{i+\frac{1}{2},j,k} = u_{i+\frac{1}{2},j,k}U_{i+\frac{1}{2},j,k}$$
$$G^{DC}_{i,j+\frac{1}{2},k} = \frac{1}{2}(v_{i,j,k} + v_{i,j+1,k})U_{i,j+\frac{1}{2},k} = v_{i,j+\frac{1}{2},k}U_{i,j+\frac{1}{2},k}$$
$$H^{DC}_{i,j,k+\frac{1}{2}} = \frac{1}{2}(w_{i,j,k} + w_{i,j,k+1})U_{i,j,k+\frac{1}{2}} = w_{i,j,k+\frac{1}{2}}U_{i,j,k+\frac{1}{2}} \qquad (4.29)$$

The choice of the U at the interfaces of a cell depends upon the sign of the interface velocities (upwind).

$$U_{i+\frac{1}{2},j,k} = U^{n-1}_{i,j,k} \quad \text{if } u_{i+\frac{1}{2},j,k} \geq 0$$
$$U_{i+\frac{1}{2},j,k} = U^{n-1}_{i+1,j,k} \quad \text{if } u_{i+\frac{1}{2},j,k} < 0 \qquad (4.30)$$

Similar expressions hold for the interfacial quantities in the other directions.

The low order fluxes used in the flux formulation of 3D-FCT are given by

$$F^{L}_{i+\frac{1}{2},j,k} = F^{DC}_{i+\frac{1}{2},j,k}\Delta t\Delta y_j\Delta z_k$$
$$G^{L}_{i,j+\frac{1}{2},k} = G^{DC}_{i,j+\frac{1}{2},k}\Delta t\Delta x_i\Delta z_k$$
$$H^{L}_{i,j,k+\frac{1}{2}} = H^{DC}_{i,j,k+\frac{1}{2}}\Delta t\Delta x_i\Delta y_j \qquad (4.31)$$

To examine the stability of the method we consider the linear hyperbolic wave equation as before. Applying the Von Neumann stability analysis we obtain the amplification factor.

$$\lambda = [1 - (c_x + c_y + c_z) + (c_x \cos\theta_x + c_y \cos\theta_y + c_z \cos\theta_z)]$$
$$-\imath(c_x \sin\theta_x + c_y \sin\theta_y + c_z \sin\theta_z) \qquad (4.32)$$

For stability it is required that $|\lambda| \leq 1$ which is satisfied under the condition that $c_x + c_y + c_z \leq 1$. The method is dissipative, first order in time, stable and conservative. In the nonlinear case the accuracy is more than first order, since it retains some of the characteristics of the centered schemes (*Roach*, 1972).

4.1.4 A 3-D Computational Example

To test the 3D-FCT algorithm developed, we choose a 3-D wave propagation example. We consider the solid body rotation along with a relative motion. The equations which describe the motion are

$$\frac{\partial \rho}{\partial t} + \frac{\partial f}{\partial x} + \frac{\partial g}{\partial y} + \frac{\partial h}{\partial z} = 0 \tag{4.33}$$

with $f = \rho u$, $g = \rho v$, and $h = \rho w$. Assume that the cylinder is located initially at x_o, y_o, z_o and rotates counterclockwise with a constant angular velocity Ω. The velocities are given by

$$u = -\Omega(y - y_0) \quad v = \Omega(x - x_0) \quad w = W \tag{4.34}$$

The computational grid is a $53 \times 53 \times 53$ cartesian with $\Delta x = \Delta y = \Delta z$. The cylinder rotates around the center of the domain, its radius spans 12 grid cells, has a length of 16 grid points and a width cut of 6 points. The density is taken to be $\rho = 3$ in the cylinder and $\rho = 1$ everywhere outside. The time step is taken so that the cylinder completes a revolution in 628 time steps, i.e., for $\Omega = 1$ the time-step is $\Delta t = 0.01$. The velocity along z is $W = 3$. With the parameters of the problem the stability condition 4.22 becomes

$$\Delta t^{max} \leq 1/\left(\frac{u_{max}}{\Delta x} + \frac{v_{max}}{\Delta y} + \frac{w_{max}}{\Delta z}\right) = 0.02 \tag{4.35}$$

The 3D-FCT algorithm developed previously applied to the problem. Complete multidimensional limiting was applied at each time step. In Figure 4.2 we show in perspective two planes of the cylinder. The top picture shows the plane through the center perpendicular to the axis of rotation and the bottom picture shows a plane along the axis of rotation through the center of the cylinder. In Figure 4.3 the low order (donor cell) solution is shown after 157 iterations- a quarter of rotation. The filling of the gap and the smoothing of the sharp density gradients are the effects of the dissipative character of the scheme. The higher order solution shown in Figure 4.4 at the 157th iteration, depicts its dispersive character. The gap is captured accurately as well as the location of the step functions in the z direction, but "ripples"

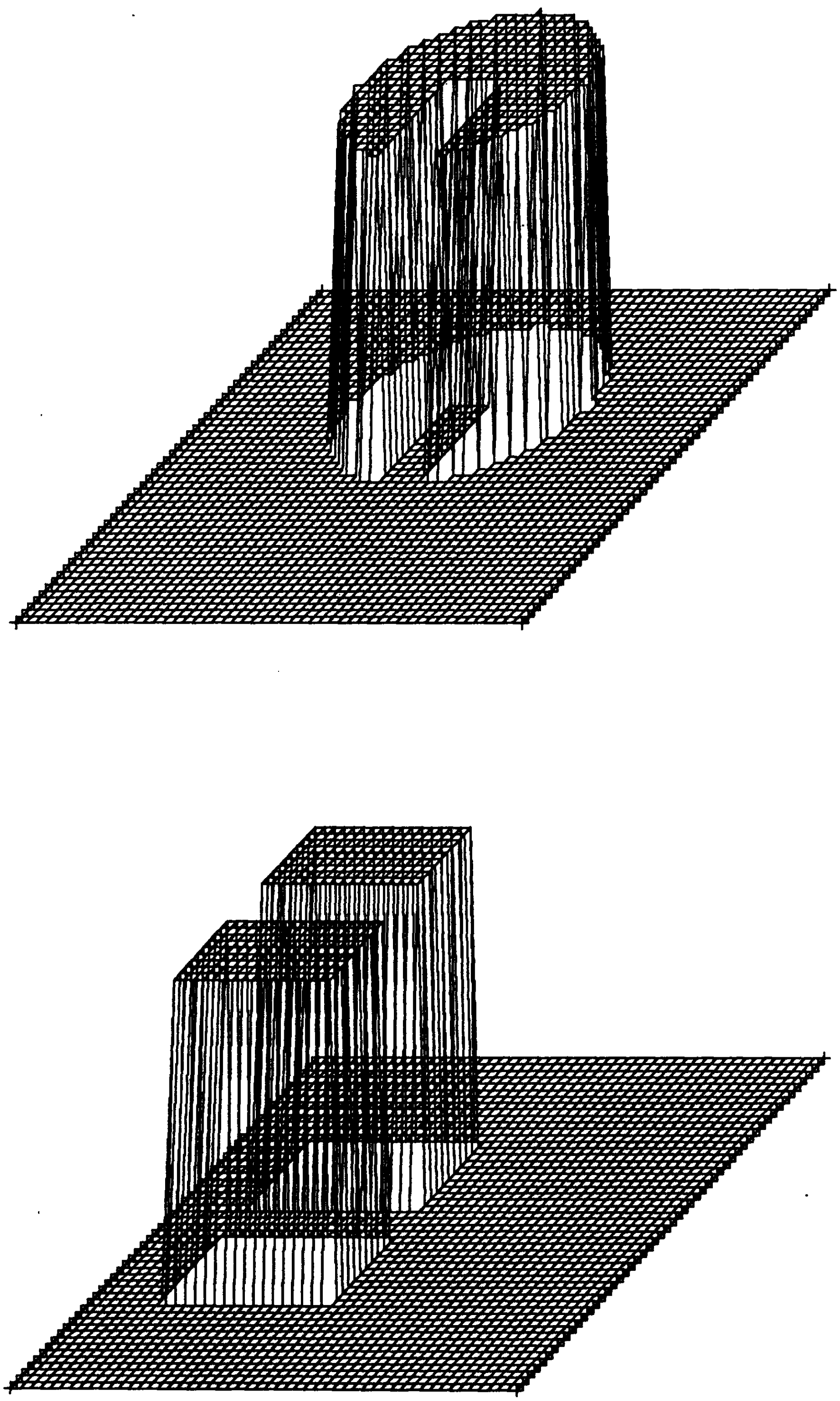

Figure 4.2: Prespective view of the initial conditions. Two central planes of the cylinder; (Top) Perpendicular to the axis of rotation. (Bottom) Parallel to the axis of rotation.

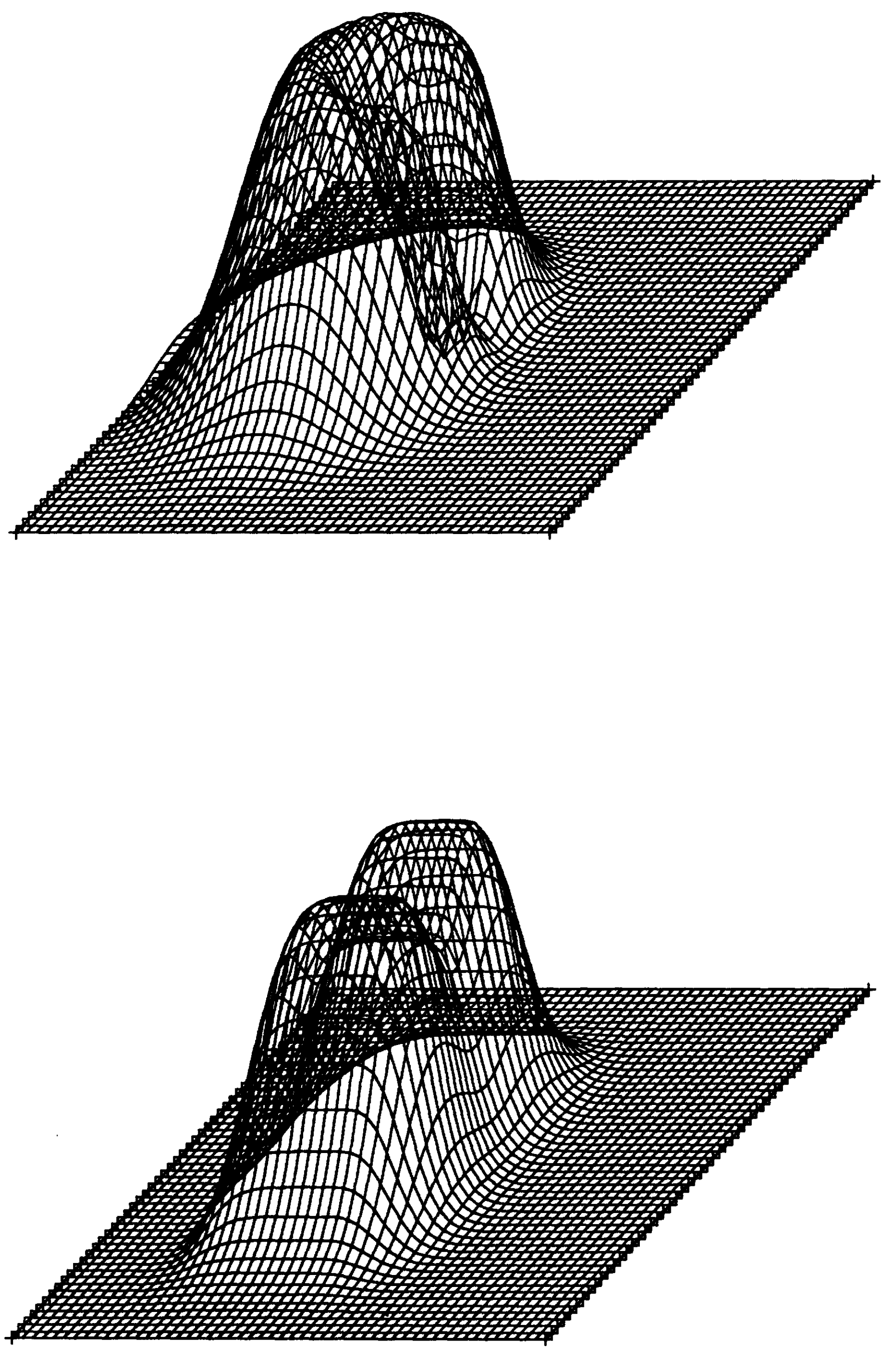

Figure 4.3: Prespective view of two central planes of the cylinder. The solution is shown after 157 iterations using the low-order scheme (Donor Cell).(Top) Plane perpendicular to the axis of rotation. (Bottom) Plane along the axis of rotation

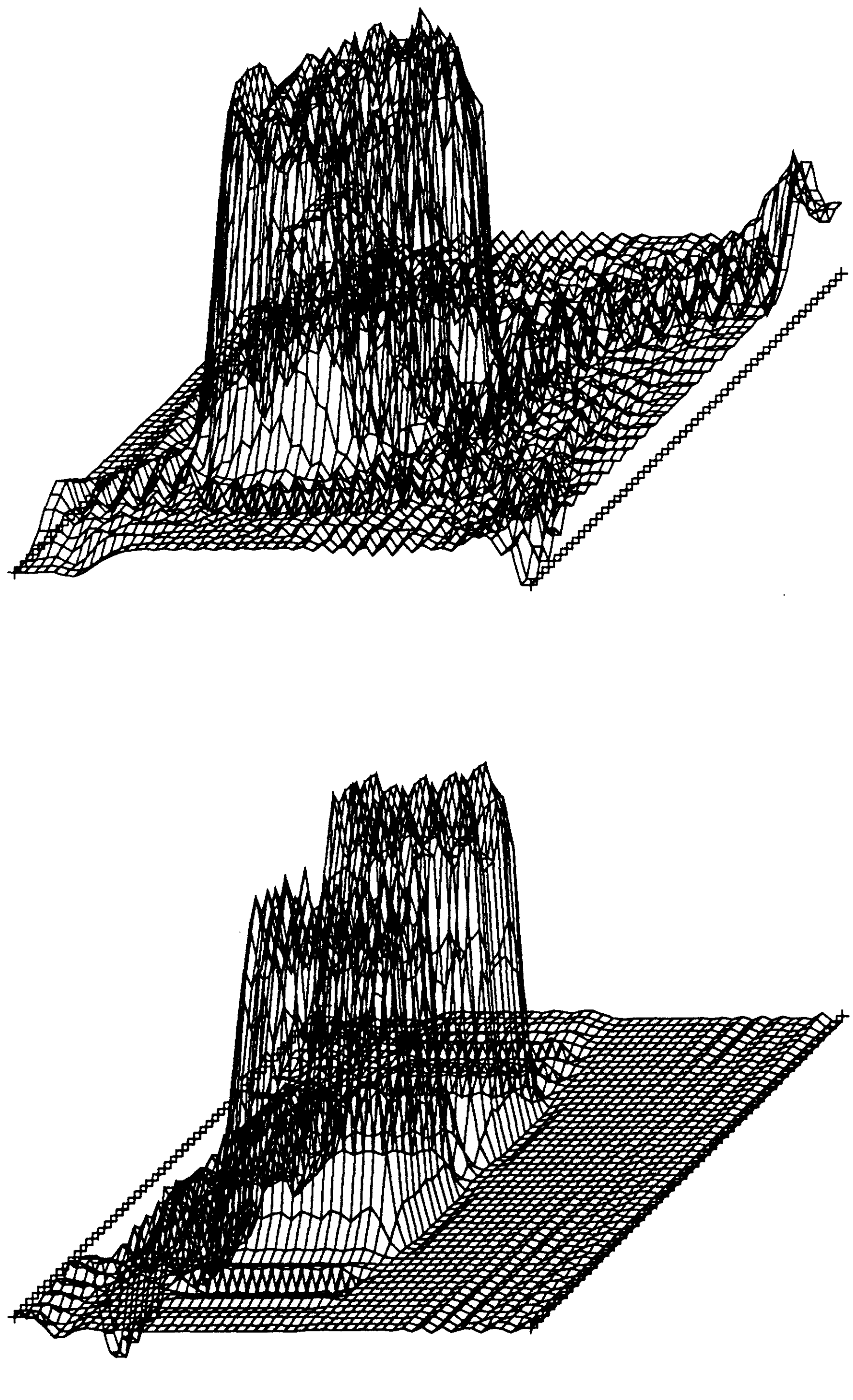

Figure 4.4: Prespective view of the solution on two planes of the cylinder after 157 iterations using the high-order scheme (Leapfrog-Trapezoidal).(Top) On a plane perpendicular to the axis of rotation. (Bottom) Plane along the axis of rotation

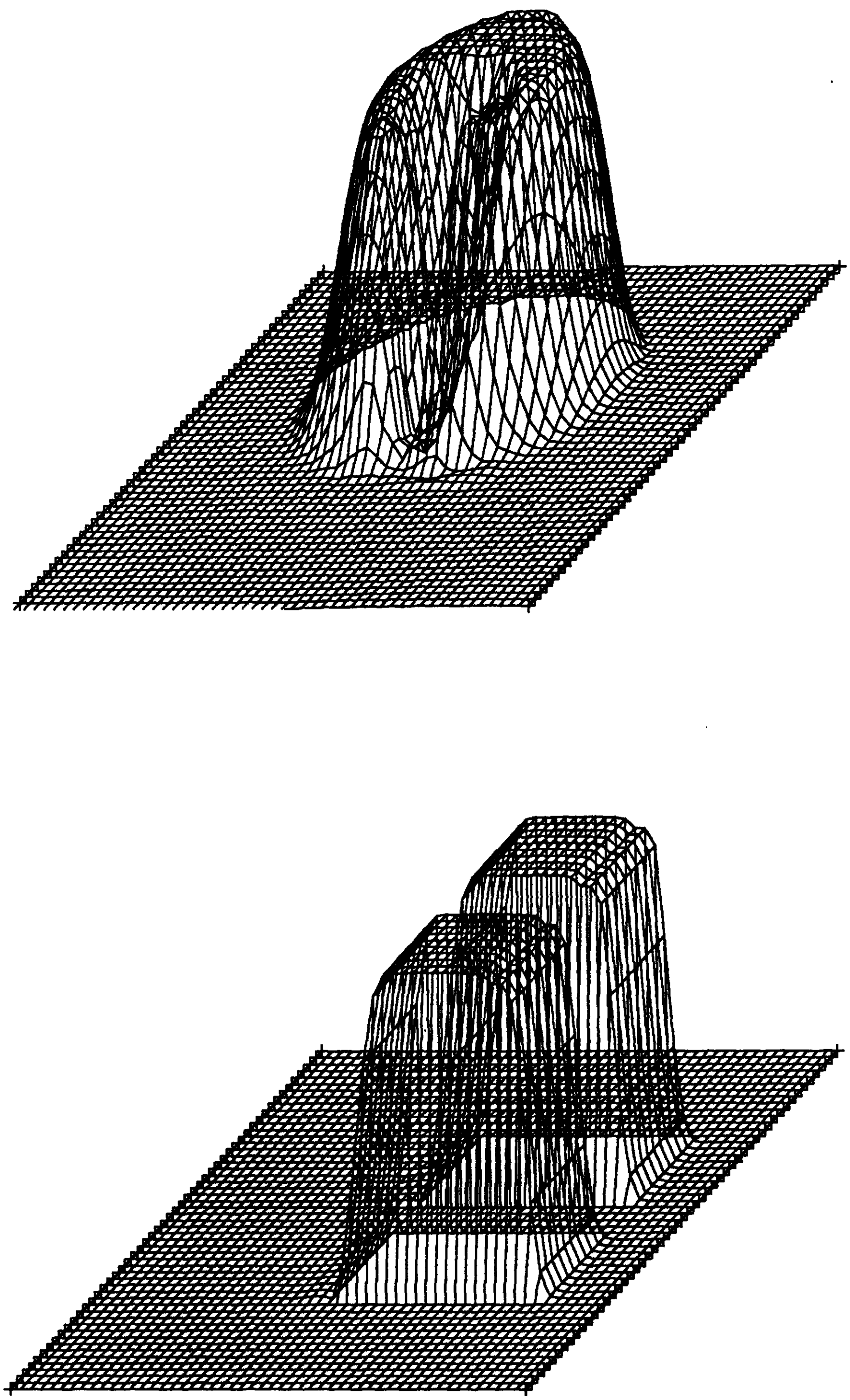

Figure 4.5: Prespective view of the solution at two planes of the cylinder. The solution is shown after 620 iterations using the 3D-FCT scheme. (Top) On a plane perpendicular to the axis of rotation. (Bottom) Plane along the axis of rotation.

have appeared in the location of the steep gradients exist. In Figure 4.5 we show the results from the 3D-FCT solution after a complete revolution. The filling of the gap is minimal. The ripples have disappeared from the cylinders surface and only some dissipation is left.

4.2 Numerical Solution of 3-D Elliptic Equations

The equation for the potential (3.36) is a nonself-adjoint elliptic equation, three dimensional, with highly dissimilar coefficients. It is this inherent difficulty that prohibited the solution of the fully three-dimensional problem in the past. The difficulties can be revealed further if one recasts the potential equation in the form of a steady state advection-diffusion equation. From a physical and consequently numerical point of view, one has to deal with time scales which are very dissimilar, in the transverse and parallel directions. One more source of difficulty lies in the Neumann condition which is applied in the parallel direction, which is the direction of the highest conductivity, thus making convergence very difficult to achieve.

4.2.1 Discrete Potential Equation

We discretize the potential equation on a non-uniform rectangular grid with Δx_i, Δy_j, and Δz_k being the grid sizes in the x, y, and z directions respectively. In the discrete space the indices i, j, k refer to the computational coordinates, aligned with the x, y, and z directions and such that $\Delta x_i = x_{i+1} - x_i$, $\Delta y_j = y_{j+1} - y_j$, and $\Delta z_k = z_{k+1} - z_k$. For a grid point (i, j, k) as shown in Figure 4.6 the following finite difference operator is used:

$$\frac{\partial}{\partial x}\left(A\frac{\partial F}{\partial x}\right) = \frac{A_{i+\frac{1}{2},j,k}(F_{i+1,j,k} - F_{i,j,k})}{\Delta x_i(\Delta x_i + \Delta x_{i-1})/2} - \frac{A_{i-\frac{1}{2},j,k}(F_{i,j,k} - F_{i-1,j,k})}{\Delta x_{i-1}(\Delta x_i + \Delta x_{i+1})/2} \tag{4.36}$$

Both A and F are functions of x, y, z. The quantity at the interfaces of a cell is defined as

$$A_{i+1/2,j,k} = \frac{A_{i+1,j,k} + A_{i,j,k}}{2} \tag{4.37}$$

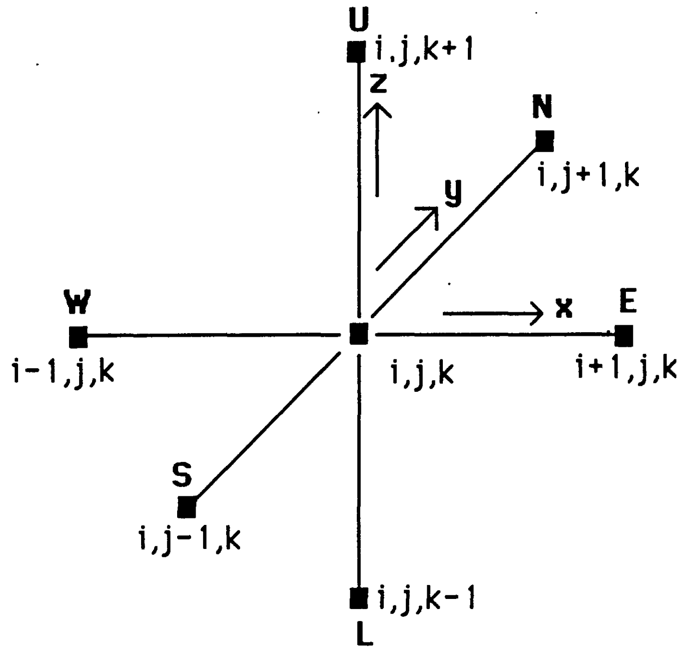

Figure 4.6: Grid configuration used in the finite difference of the elliptic type of equation.

Similar operators were applied in the j and k directions. Using the above and expanding in all three directions we derive the finite difference equation for the potential $\phi_{i,j,k}$ at the grid point (i,j,k). Furthermore, we denote as the east, west, north, and south grid points as shown in Figure 4.6. Then the FDE can be written in the form

$$A^C_{i,j,k}\phi_{i,j,k} + A^E_{i,j,k}\phi_{i+1,j,k} + A^N_{i,j,k}\phi_{i,j+1,k} + A^W_{i,j,k}\phi_{i-1,j,k} + A^S_{i,j,k}\phi_{i,j-1,k}$$
$$+A^U_{i,j,k}\phi_{i,j,k+1} + A^L_{i,j,k}\phi_{i,j,k-1} = S_{i,j,k} \qquad (4.38)$$

where S_{ijk} is the discrete source term obtained through the finite difference of all the source terms in the potential equation. The coefficients at each (i,j,k) with $a = \Delta x_i/\Delta x_{i-1}$ and $b = \Delta y_j/\Delta y_{j-1}$ are given by

$$\begin{aligned} A^C_{ijk} = \Bigg(& -\frac{\sigma^P_{i+\frac{1}{2},j,k}}{\Delta x_i(\Delta x_i + \Delta x_{i-1})/2} - \frac{\sigma^P_{i-\frac{1}{2},j,k}}{\Delta x_{i-1}(\Delta x_i + \Delta x_{i+1})/2} \\ & - \frac{\sigma^H_{i,j+\frac{1}{2},k}}{\Delta y_j(\Delta y_j + \Delta y_{j-1})/2} - \frac{\sigma^H_{i,j-\frac{1}{2},k}}{\Delta y_{j-1}(\Delta y_j + \Delta y_{j+1})/2} \\ & - \frac{\sigma^Z_{i,j,k+\frac{1}{2}}}{\Delta z_k(\Delta z_k + \Delta z_{k-1})/2} - \frac{\sigma^Z_{i,j,k-\frac{1}{2}}}{\Delta z_{k-1}(\Delta z_k + \Delta z_{k+1})/2} \Bigg) \end{aligned}$$

$$
\begin{aligned}
A^E_{ijk} &= \left[\frac{\sigma^P_{i+\frac{1}{2},j,k}}{\Delta x_i(\Delta x_i + \Delta x_{i-1})/2} + \frac{\left(\frac{\partial\sigma^H}{\partial y}\right)_{i,j,k}}{a(a+1)\Delta x_{i-1}}\right] \\
A^W_{ijk} &= \left[\frac{\sigma^P_{i-\frac{1}{2},j,k}}{\Delta x_{i-1}(\Delta x_i + \Delta x_{i+1})/2} - \frac{\left(\frac{\partial\sigma^H}{\partial y}\right)_{i,j,k}}{a(a+1)\Delta x_{i-1}}\right] \\
A^N_{ijk} &= \left[\frac{\sigma^P_{i,j+\frac{1}{2},k}}{\Delta y_j(\Delta y_j + \Delta y_{j-1})/2} - \frac{\left(\frac{\partial\sigma^H}{\partial x}\right)_{i,j,k}}{b(b+1)\Delta y_{j-1}}\right] \\
A^S_{ijk} &= \left[\frac{\sigma^P_{i,j-\frac{1}{2},k}}{\Delta y_{j-1}(\Delta y_j + \Delta y_{j+1})/2} + \frac{\left(\frac{\partial\sigma^H}{\partial x}\right)_{i,j,k}}{b(b+1)\Delta y_{i-1}}\right] \\
A^U_{ijk} &= \left[\frac{\sigma^z_{i,j,k+\frac{1}{2}}}{\Delta z_k(\Delta z_k + \Delta z_{k-1})/2}\right] \\
A^L_{ijk} &= \left[\frac{\sigma^z_{i,j,k-\frac{1}{2}}}{\Delta z_{k-1}(\Delta z_i + \Delta z_{k+1})/2}\right]
\end{aligned} \tag{4.39}
$$

If we work on a grid with nx, ny, and nz grid points in the x, y, and z direction, respectively, and apply the above discretization to all the interior grid points, we end up with a matrix equation of the form

$$
\begin{bmatrix} a_{11} & \dots & a_{1N} \\ \vdots & \vdots & \vdots \\ a_{N1} & \dots & a_{NN} \end{bmatrix}
\begin{bmatrix} \phi_{222} \\ \vdots \\ \phi_{nx-1,ny-1,nz-1} \end{bmatrix}
=
\begin{bmatrix} S_{222} \\ \vdots \\ S_{nx-1,ny-1,nz-1} \end{bmatrix} \tag{4.40}
$$

The matrix $[a_{NN}]$ is an $N \times N$ sparse matrix, where $N = (nx-2) \times (ny-2) \times (nz-2)$, with only seven nonzero elements in each row. For example, on a typical grid configuration with $32 \times 32 \times 64$ the matrix is 55800×55800. In order to make the problem computationally tractable we have developed a special storage system. We begin first by mapping the ϕ_{ijk} into a 1-D vector using the following ordering scheme

$$
p(i,j,k) = (k-2)(nx-2)(ny-2) + (j-2)(nx-2) + (i-1) \tag{4.41}
$$

$$
\begin{bmatrix} \phi_{222} \\ \vdots \\ \phi_{ijk} \\ \vdots \\ \phi_{nx-1,ny-1,nz-1} \end{bmatrix}
\longleftrightarrow
\begin{bmatrix} \phi_1 \\ \vdots \\ \phi_p \\ \vdots \\ \phi_N \end{bmatrix} \tag{4.42}
$$

Also for each grid point (i, j, k) we store only the seven elements of the array a_{NN}. In this way we can compress then the $(N \times N)$ array into a new $(N \times 7)$ array denoted by A_{N7}.

$$\begin{bmatrix} A_{11} & \dots & A_{17} \\ \vdots & \vdots & \vdots \\ A_{irow,1} & \dots & A_{irow,7} \\ \vdots & \vdots & \vdots \\ A_{N1} & \dots & A_{N7} \end{bmatrix} \tag{4.43}$$

For every grid point (i, j, k) the elements of the new array are given by

$$\begin{aligned} irow &= p(i,j,k) && (4.44) \\ A(irow,1) &= A^C_{i,j,k} \\ A(irow,2) &= A^E_{i,j,k} \\ A(irow,3) &= A^N_{i,j,k} \\ A(irow,4) &= A^W_{i,j,k} \\ A(irow,5) &= A^S_{i,j,k} \\ A(irow,6) &= A^U_{i,j,k} \\ A(irow,7) &= A^L_{i,j,k} && (4.45) \end{aligned}$$

We need also to store a pointer array with the column destination for the nonzero elements of the uncompressed array $[a_{N,N}]$ for each $[A_{N,7}]$. This is done with the following scheme

$$\begin{aligned} IFLAGA(irow,1) &= p(i,j,k) \\ IFLAGA(irow,2) &= p(i+1,j,k) \\ IFLAGA(irow,3) &= p(i,j+1,k) \\ IFLAGA(irow,4) &= p(i-1,j,k) \\ IFLAGA(irow,5) &= p(i,j-1,k) \\ IFLAGA(irow,6) &= p(i,j,k-1) \\ IFLAGA(irow,7) &= p(i,j,k+1) && (4.46) \end{aligned}$$

Implementation of Boundary Conditions

There are two types of boundary conditions that we are concerned with: Dirichlet and Neumann. We will examine how they modify the structure of the matrix equation.

Suppose that the unknown ϕ is specified on a surface as $\phi_{1,j,k} = \phi_o$ (see Figure 4.7). Then the FDE (4.38) at the point $(2, j, k)$ becomes

$$\begin{aligned} A^C_{2,j,k}\phi_{2,j,k} + A^E_{2,j,k}\phi_{3,j,k} + A^N_{2,j,k}\phi_{2,j+1,k} & \\ +A^S_{2,j,k}\phi_{2,j-1,k} + A^U_{i,j,k}\phi_{i,j,k+1} + A^L_{2,j,k}\phi_{2,j,k-1} &= S_{i,j,k} - A^W_{2,j,k}\phi_o \end{aligned} \tag{4.47}$$

Similarly, for Dirichlet b.c. on the other surfaces we transfer the appropriate terms

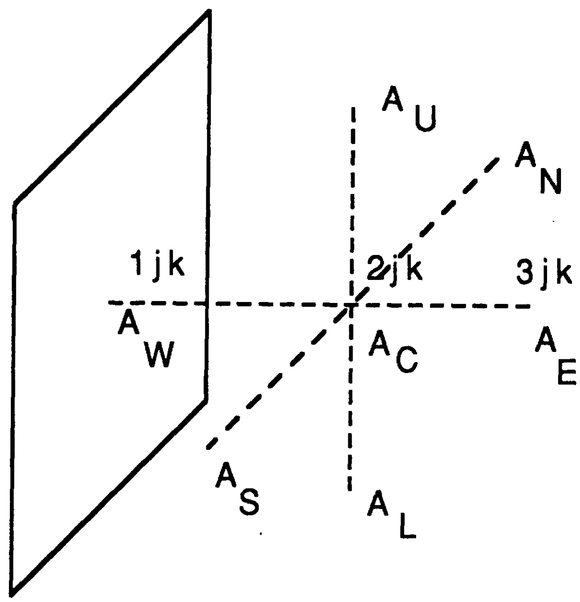

Figure 4.7: Grid configuration near a boundary.

to the right hand side of the equation.

Consider next that Neumann conditions are specified on the surface $(1, j, k)$. Then we can write for the boundary value $\phi_{1,j,k}$ using second order differencing as follows

$$\phi_{1,j,k} = -\frac{2}{3}\beta\Delta x + \frac{4}{3}\phi_{2,j,k} - \frac{1}{3}\phi_{3,j,k} \tag{4.48}$$

Accordingly the FDE (4.38) for the point $(2, j, k)$ is modified and becomes

$$\frac{\partial\phi_{1jk}}{\partial x} = \beta$$

$$\left(A^C_{2,j,k} + \frac{4}{3}A^W_{2,j,k}\right)\phi_{2,j,k} + \left(A^E_{2,j,k} - \frac{1}{3}A^W_{2,j,k}\right)\phi_{3,j,k} + A^N_{2,j,k}\phi_{2,j+1,k}$$
$$+A^S_{2,j,k}\phi_{2,j-1,k} + A^U_{i,j,k}\phi_{i,j,k+1} + A^L_{2,j,k}\phi_{2,j,k-1} = S_{i,j,k} + \frac{2}{3}\beta\Delta x A^W_{2,j,k} \qquad (4.49)$$

The extension of the above to any other surfaces with Neumann conditions is trivial.

4.2.2 Solution of Sparse, Asymmetric Systems

Thus far we have reduced the problem into a linear system of equations (4.40). We will discuss now the methods used in the solution of the system $A\mathbf{x} = \mathbf{b}$. Most boundary value problems (elliptic equations for example) reduce to solving sparse systems of that form. There are two general methods of solution: Direct and iterative.

Direct methods usually employ some kind of decomposition of the matrix and have been extensively used (see the books by *Ortega* [1972], and *George and Liu* [1981]). One of the most common direct methods is the Gaussian elimination. For a matrix of $O(n)$ it would require $O(n^3/3)$ multiplications/divisions and $O(n^3/3)$ additions/subtractions. For a sparse matrix, such as ours, pivoting would be necessary, a procedure that would add to the number of operations considerably. The Fast Fourier Transform (FFT) method requires equations which have constant coefficients in space. The Cyclic Reduction Methods are more general but require that the equations be separable. Other forms of matrix decomposition are discussed bellow.

The literature in iterative methods is also vast and we anly need to reference here the books by *Varga* [1962] and *Hageman and Young* [1981]. One of the basic iterative methods is the Conjugate Gradient (CG) given by *Hestenes and Stiefel*, [1952]. Let us set $r_o = b - Ax_o$ and $p_o = r_o$. The CG algorithm is then

$$\begin{aligned} \alpha_i &= (r_i^T r_i)/(p_i^T, Ap_i) \\ x_{i+1} &= x_i + \alpha_i p_i \\ r_{i+1} &= r_i - \alpha_i Ap_i \\ b_i &= (r_{i+1}^T r_{i+1})/(r_i^T r_i) \\ p_{i+1} &= r_{i+1} + b_{i+1} p_i \end{aligned} \qquad (4.50)$$

The convergence of CG -and any iterative method- depends on the conditioning and the rank of the matrix [*Golub and Van Loan*, 1989]. One way of accelerating the convergence of an iterative procedure is to apply preconditioning. This is of extreme importance for matrices with unclustered eigenvalues. The idea is that we want to find a preconditioner matrix Q so that the system $Q^{-1}A\mathbf{x} = Q^{-1}\mathbf{b}$ is better conditioned than the original system. One of the most important preconditioning strategies involves matrix decomposition. The method is often applied in the solution of systems of equations $A\mathbf{x} = \mathbf{b}$. If the matrix is symmetric and positive definite the factorization takes the form $A = LL^T$ where L is the lower triangular. Then the solution is calculated by $\mathbf{x} = (L^T)^{-1}(L^{-1})\mathbf{b}$. The steps in determining the elements of L are

$$L_{i,j} = \left[a_{ij} - \sum_{k=1}^{i-1} L_{ik}^2\right]^{1/2}$$

$$\text{for} \quad j = i+1, .., n$$

$$L_{j,i} = \frac{1}{L_{ii}}\left[a_{ji} - \sum_{k=1}^{i-1} L_{jk}L_{ik}\right] \tag{4.51}$$

It is a simple exercise to show that a positive definite $n \times n$ matrix requires n square roots, $n^3 + 9n^2 + 2n/6$ multiplications/divisions and $n^3 + 9n^2 - 7n/6$ additions/subtractions almost half of those needed in Gaussian elimination. Additional savings can be obtained if we avoid square roots and instead factorize $A = LDL^T$. The off diagonal elements of D are zero and the elements of L and D are

$$\text{for} \quad j = i, i+1, .., n$$

$$L_{i,j} = A_{i,j} - \sum_{k}^{i-1} L_{jk}L_{ik}D_{kk}$$

$$D_{ii} = (L_{ii})^{-1} \tag{4.52}$$

The problem with this form of decomposition starts with large sparse matrices. In such a case storage and operation requirements become enormous. The alternative is the Incomplete Cholesky decomposition (ICD). In this variation one defines a set of elements of L to be zero for those elements i, j which lie in a set P. One choice of P which would make L to have the same sparsity pattern as A is $L_{i,j} = 0$ for i, j such that $A_{i,j} = 0$. The approximate matrix for A is then

$$A = LDL^T + E \tag{4.53}$$

where E is a small error matrix whose entries are in the set P. Then the exact solution is given by

$$[L^{-1}A(L^T)^{-1}](L^Tx) = L^{-1}y \tag{4.54}$$

The above algorithm has been generalized by *Kershaw*, [1978] for cases where A is neither symmetric or positive . We proceed in the LU decomposition as before and obtain an approximate inverse for A so that the original system is written in the form

$$L^{-1}AU^{-1}(Ux) = L^{-1}b \tag{4.55}$$

Here $(LL^T)^{-1}$ is an approximate inverse of A; then applying regular conjugate gradient (4.50) to the preconditioned system, i.e., to the matrix $L^{-1}A(L^T)^{-1}$ convergence will be very rapid [*Golub and Van Loan*, 1989]. The ICCG was the starting algorithm for our computations but had the potential to break down in certain applications.

Several improvements to the above ICCG algorithm have been developed. The Generalized Minimal Residual (GMRES) method developed in particular for nonsymmetric linear systems by [*Saad and Schultz*, 1984]. GMRES accelerates and stabilizes iterative solutions. The strategy of preconditioning followed by acceleration has been implemented in a computer package, the NSPCG (for Nonsymmetric Preconditioned Conjugate Gradient). It is written by *Oppe, Joubert and Kincaid* and is a part of the ITPACK. We used an experimental version of the package that is available in the public domain. There are several options of preconditioners and accelerators in NSPCG. This feature of NSPCG gives the opportunity to choose the most appropriate combination for a specific matrix. We found that for the problem at hand the successful combination was that of ICD as a preconditioner with GMRES as the accelerator. A computational example of the potential equation solver is reserved for Chapter 5.

Chapter 5

3-D Current Closure: Initial Time Simulations

In this chapter we examine the 3-D current closure between a plasma cloud and the background plasma in a variety of conditions. The objective here is to simulate and characterize the initial development of the self-consistent electric fields due to the different driving mechanisms, i.e., electric fields, diffusion, and neutral winds. We begin with a discussion of a uniform spherical plasma cloud imbedded in a uniform background plasma with an applied electric and magnetic field. In the absence of magnetic field we compare the numerical solution with the derived analytic solution. In the presence of the magnetic field we examine the role of the increased parallel conductivity and verify the electric field mapping process as it was discussed in the layer model of Chapter 3. Next we examine the current closure in the case where a non-uniform Gaussian plasma cloud is released in an altitude varying ionosphere. We discuss the problem of 3-D diffusion in the absence of a neutral wind. It is shown that the cloud rotates around the **B** field while it expands rapidly along the **B** lines. We allow then for a unidirectional neutral wind simulating the conditions of an orbital release of a gas. We examine the role of the density of the released material and the altitude of the release on the initial structure of the electric field. It is shown that along with the diffusion fields a dipole field develops associated with the applied neutral wind. The results of this chapter elucidate important electrodynamic processes, are compared with the analytical closure models derived in Chapter 2, and are used in the simulations presented in subsequent chapters.

5.1 Grid Configuration - Frames of Reference

We study numerically the release of neutrals and ions at various altitudes between 200 and 700 km. The computational frame is centered at the altitude of the release and is shown for a typical case in Figure 5.1. The positive **z** direction points towards lower altitudes, the positive **y** direction points to the east and the negative **x** direction points to the south. The computational grid is orthogonal and uniform on the (x,y) planes, with $\Delta x = \Delta y$. The grid along **z** is nested; the inner grid has $\Delta x \simeq \Delta z_i$ while the outer grid has $\Delta z_o > \Delta z_i$. A typical domain has $21 \times 21 \times 61$ grid points. The number of grid points in the inner grid depends on the specific application. In all the simulations the lower boundary was located at $h_L = 100$ km. That was necessary in order to account for the large currents that flow in the E region where the transverse conductivity peaks. The upper boundary was located appropriately so that there would be no effect on the obtained numerical solution. The model for the ambient ionosphere is that presented in Chapter 2.

There are two reference frames of interest in the problem, and we will discuss briefly the physical processes associated with each one. The first reference frame is moving with the space structure and is shown in Figure 5.2*a*. This frame is important in the case of contaminant clouds about space vehicles, since it gives directly the picture that the moving observer would see. In the moving frame under the assumption that the orbital velocity is $\mathbf{V}_m$ in the $-\mathbf{x}$ direction there is a motional electric field acting on the plasma $\mathbf{E}_m = \mathbf{V}_m \times \mathbf{B}$ in the **y** direction. For LEO conditions the magnitude of the motional electric field is $E_m \simeq 0.28$ V/m. There is also the ambient neutral wind $\mathbf{U}_a = -\mathbf{V}_m$ which acts on the plasma in the **x** direction. In general, there is also the force due to the relative motion of the contaminant neutrals, $\mathbf{U}_r$. For completeness, one has to add the forces due to the ambient electric field $\mathbf{E}_o$. It is the balance of all these forces that will determine the electrodynamical behavior of the plasma cloud. The second reference frame is stationary with the Earth observer and is shown in Figure 5.2*b*. In the stationary frame, besides the ambient electric field and neutral wind, the only force acting on the ion cloud is due to the contaminant neutrals, referred to here as the contaminant neutral wind $\mathbf{U}_r$. We found it computationally more tractable to use the stationary frame. However, in some occasions we discuss the results in both frames.

5.2 Uniform Plasma Cloud

First, we examine a uniform plasma cloud with sharp boundaries, water-bag model, moving with $\mathbf{V}_m = -V_o\mathbf{x}$ in a uniform background plasma. Assume that the ambient neutrals co-move with the plasma cloud. Then, in the moving frame the only force acting on the plasma is the motional electric field, $\mathbf{E}_m = E_o\mathbf{y}$. Thus, this problem is identical with that of a dielectric sphere immersed in a uniform electric and magnetic fields, as shown in Figure 5.3. The purpose of this computational example is twofold. The first is to test the numerical algorithm and compare it with a known analytical solution. The second is to get insight on the effect of an applied electric field on a plasma cloud and see the effects of the increased parallel conductivity in the case of an applied magnetic field.

We assume that this plasma sphere of radius R consists of species r^+ while the plasma medium of species a^+ and neutrals a. The densities are n_{r^+}, n_{a^+}, and n_a respectively. If we neglect the diffusion currents then the equation for the potential, (3.36) is given by

$$\nabla \cdot \mathbf{J} = \frac{\partial}{\partial x}\left(\sigma_p \frac{\partial \Phi}{\partial x}\right) + \frac{\partial}{\partial y}\left(\sigma_p \frac{\partial \Phi}{\partial y}\right) + \frac{\partial}{\partial z}\left(\sigma_{\|} \frac{\partial \Phi}{\partial z}\right) + \frac{\partial \sigma_H}{\partial y}\frac{\partial \Phi}{\partial x} - \frac{\partial \sigma_H}{\partial x}\frac{\partial \Phi}{\partial y} = 0 \quad (5.1)$$

where $\Phi = \phi + \phi_o$ is the total electrostatic potential, ϕ the perturbation, and $\mathbf{E}_o = -\nabla\phi_o$. We can further simplify the problem by setting the Hall conductivity to zero and also equating the parallel conductivity to that of the Pedersen. In that way, the problem is isotropic and is reduced to that of a sphere with conductivity σ_c immersed

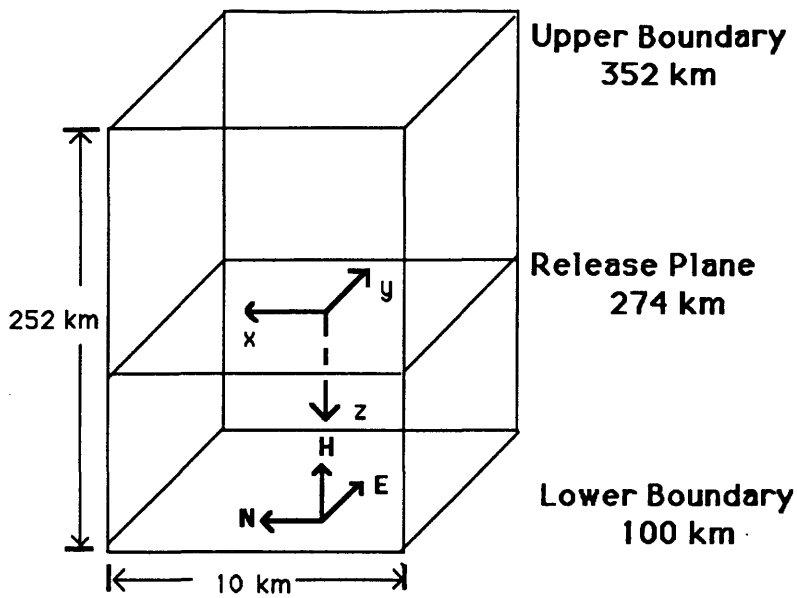

Figure 5.1: Computational domain for a typical simulation.

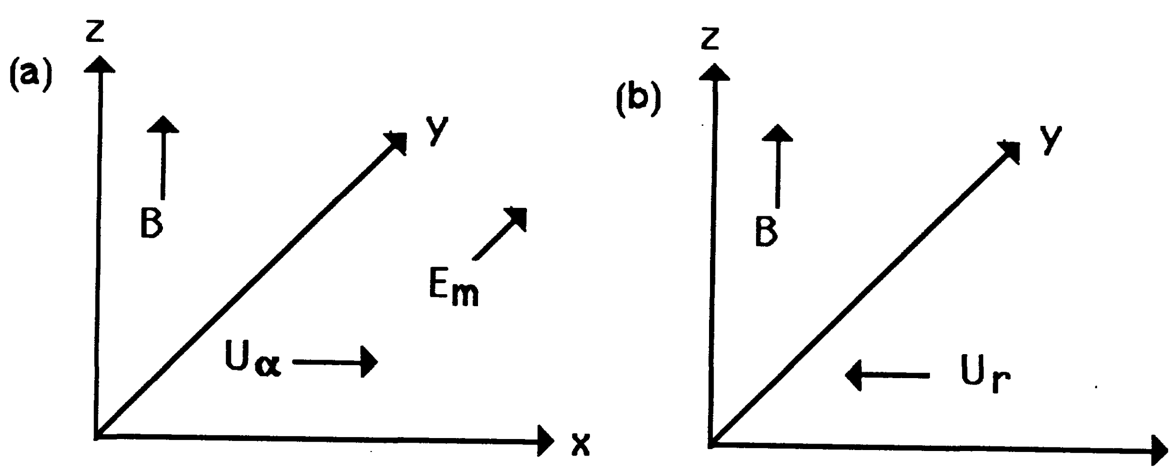

Figure 5.2: (a)Moving and (b) Stationary frame.

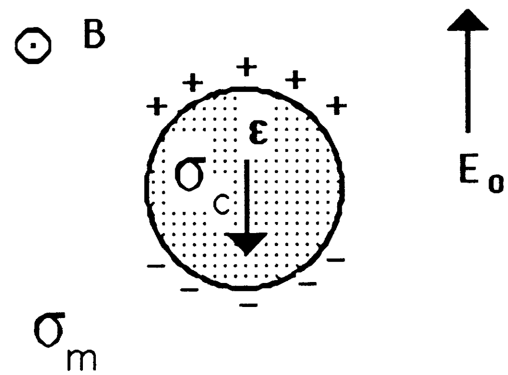

Figure 5.3: Conducting plasma sphere in applied $\mathbf{E_o}$ and $\mathbf{B}$ fields.

in a medium with conductivity σ_m. An analytic solution can be found if we write the equations describing this problem along with the appropriate boundary conditions as follows

$$\nabla^2\phi = 0$$
$$\phi_c = \phi_m$$
$$\mathbf{n}\cdot\mathbf{J_c} = \mathbf{n}\cdot\mathbf{J_m} \quad \text{at } r = R \tag{5.2}$$

The boundary conditions require that the normal current density and the tangential electric field to be continuous. From the solution of the above equations the perturbation electric field inside the cloud is given by

$$\epsilon_c = -\frac{\sigma_c - \sigma_m}{\sigma_c + 2\sigma_m}\mathbf{E}_o = \alpha\mathbf{E}_o \tag{5.3}$$

where α is the shielding factor. The perturbation field outside the cloud is

$$\epsilon_m = -\frac{2(\sigma_c - \sigma_m)}{\sigma_c + 2\sigma_m}E_o\frac{R^3}{r^3}\cos\theta\hat{r} + \frac{\sigma_c - \sigma_m}{\sigma_c + 2\sigma_m}E_o\frac{R^3}{r^3}\sin\theta\hat{\theta} \tag{5.4}$$

This perturbation field is of a dipole type and is caused by the charge accumulation as it is shown in Figure 5.4a. As (5.3) shows the shielding factor, α depends on the conductivity ratio σ_c/σ_m. We have solved numerically the above problem by varying

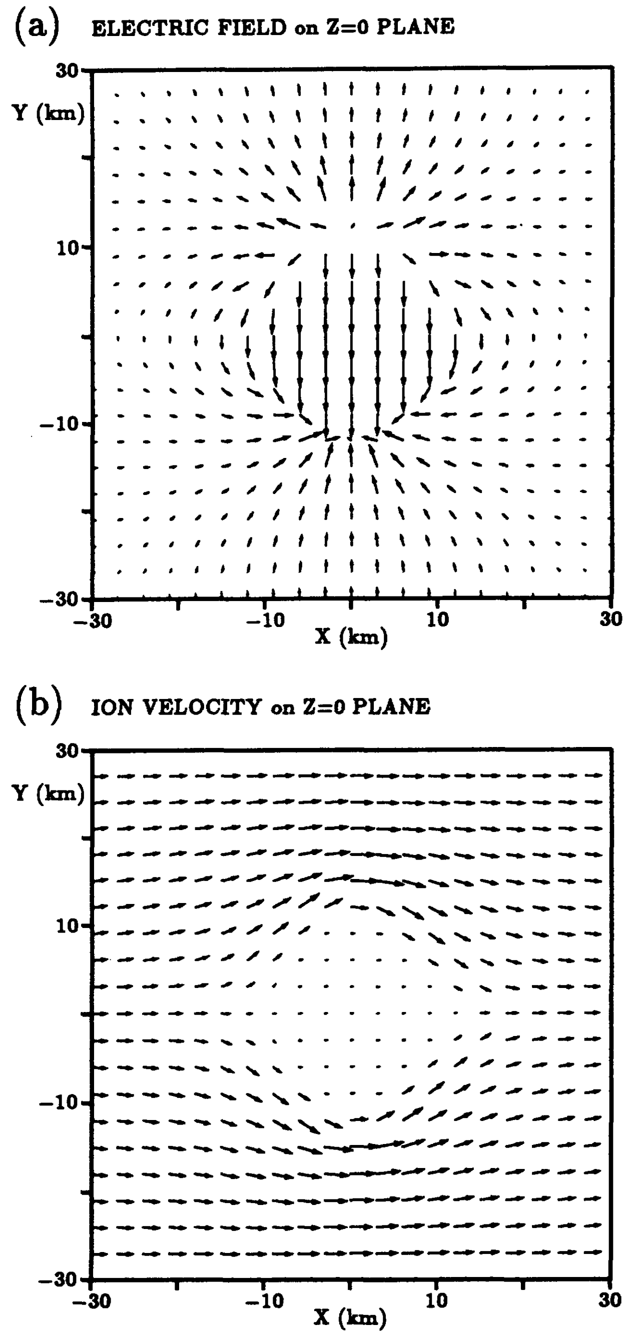

Figure 5.4: Conducting plasma sphere in an applied electric field. (a)Perturbation electric field (b) The velocity vector field of the ions

n_{r+}, Cloud	n_{a+}		σ_c	σ_m	σ_c/σ_m	α
	Cloud	Medium				
10^9	10^9	10^{11}	1.358×10^{-7}	5.347×10^{-6}	2.54×10^{-3}	0.492
10^{10}	10^{10}	10^{11}	1.358×10^{-6}	5.347×10^{-6}	2.54×10^{-1}	0.328
0	10^{11}	10^{11}	5.347×10^{-6}	5.347×10^{-6}	1	0
10^{11}	10^{11}	10^{11}	1.35×10^{-5}	5.347×10^{-6}	2.53	-0.337
10^{12}	10^{11}	10^{11}	8.779×10^{-5}	5.347×10^{-6}	16.04	-0.833
10^{13}	10^{11}	10^{11}	8.322×10^{-4}	5.347×10^{-6}	155.8	-0.98

Table 5.1: Densities, conductivities and the shielding Factor (numerical) for a plasma sphere in an electric field

the densities of the cloud and medium. The densities and the appropriate values of the conductivities used in the simulations are shown in Table 5.1

In Figure 5.5 we plot the shielding factor α and we show that the numerical results are identical with the analytic solution. For large conductivity ratios $\sigma_c/\sigma_m \gg 1$ the perturbed electric field shields out the imposed field so that the total field inside the cloud is almost zero, i.e., $\mathbf{E} = \epsilon + \mathbf{E}_o \simeq 0$. In the opposite extreme of conductivity ratios $\sigma_c/\sigma_m \ll 1$ the perturbation field acts with the external enhancing the total field within the cloud, i.e., $\mathbf{E} > \mathbf{E}_o$. This is the case of a "hole", a cloud with plasma content lower than its surroundings. This situation is of interest since it often arises in artificial cloud releases.

The assumption of uniform directional conductivities has eliminated the effect of the magnetic field. If we allow now for the parallel conductivity to take a finite value, then the potential distribution is greatly altered. In Figure 5.6 we show the potential on a plane along the **B** lines and passing through the density maximum. In the isotropic case, $\sigma_{||} = \sigma_\perp$ and the perturbation potential has the form of a dipole as Figure 5.6*a* shows. The calculated parallel and transverse perturbation length scales, $L_\perp andL_{||}$ repsectively, evaluated at the distance where the potential takes 10% of its maximum value are $L_{||} \sim L_\perp \sim 15$ km. For $\sigma_{||}/\sigma_\perp = 100$ the potential perturbation spreads at larger distances as Figure 5.6*b* shows. The parallel scale is

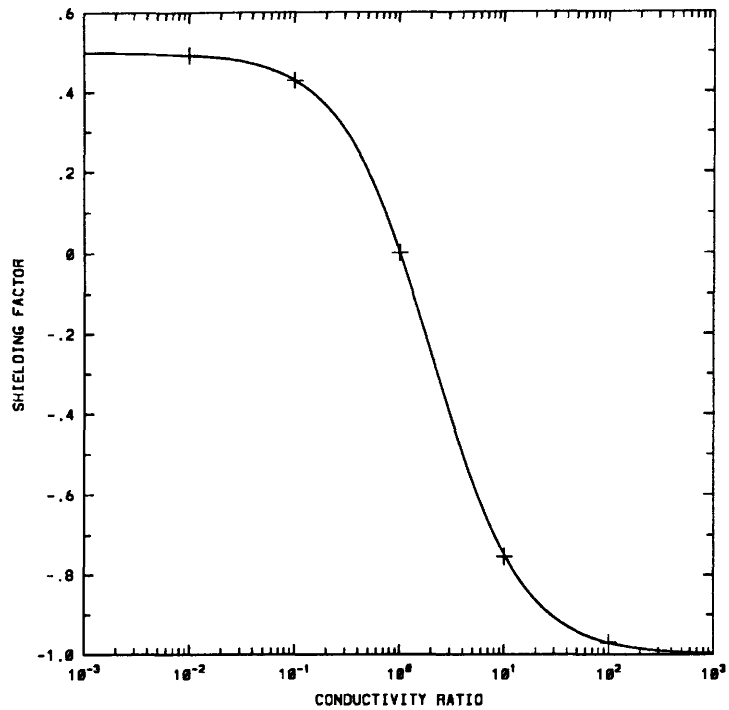

Figure 5.5: The shielding factor inside a plasma sphere plotted against the conductivity ratio. Analytical solution (solid) and numerical solution (symbols).

$L_{\|} \sim 70$ km which compares well with the analytic estimate given in (3.48). For the case where $\sigma_{\|}/\sigma_{\perp} = 10^6$, which corresponds to the ratio of ionospheric conductivities, the magnetic field lines are almost equipotential lines as depicted in Figure 5.6*c*. Charges easily flow along the magnetic field lines mapping the transverse field that is set up at the height of the cloud throughout the computational region. A three-dimensional picture of the potential is shown in Figure 5.7. The effect on the motion of the plasma is also important. The plasma inside the entire flux tube which encircles the cloud is almost stationary in the moving frame as Figure 5.4*b* shows. The plasma outside drifts around the flux tube with a drift which in the far field regions is the $\mathbf{E}_o \times \mathbf{B}/B^2$ velocity.

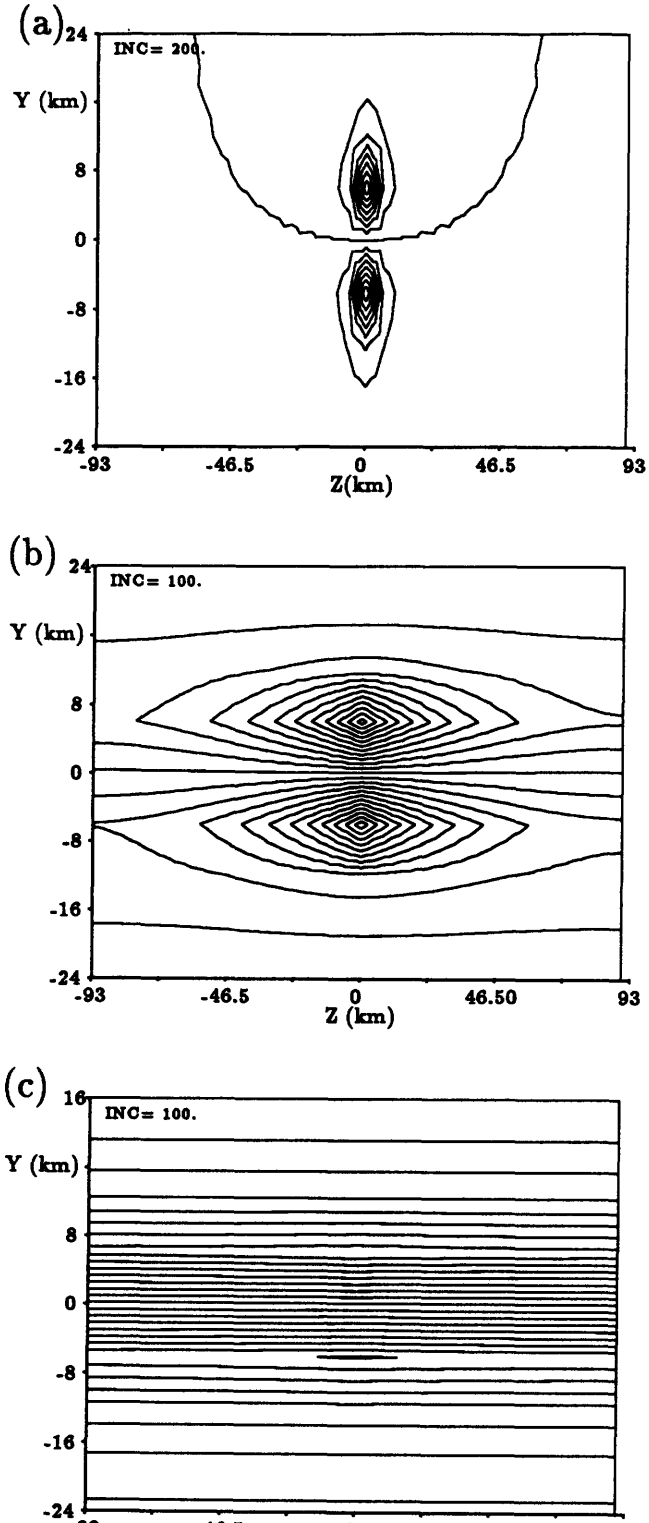

Figure 5.6: The potential distribution of a plasma sphere on the (x=0,y,z) plane for (a) uniform conductivities $\sigma_{||}/\sigma_{\perp} = 1$, ($b$) $\sigma_{||}/\sigma_{\perp} = 100$, and ($c$) $\sigma_{||}/\sigma_{\perp} = 10^6$.

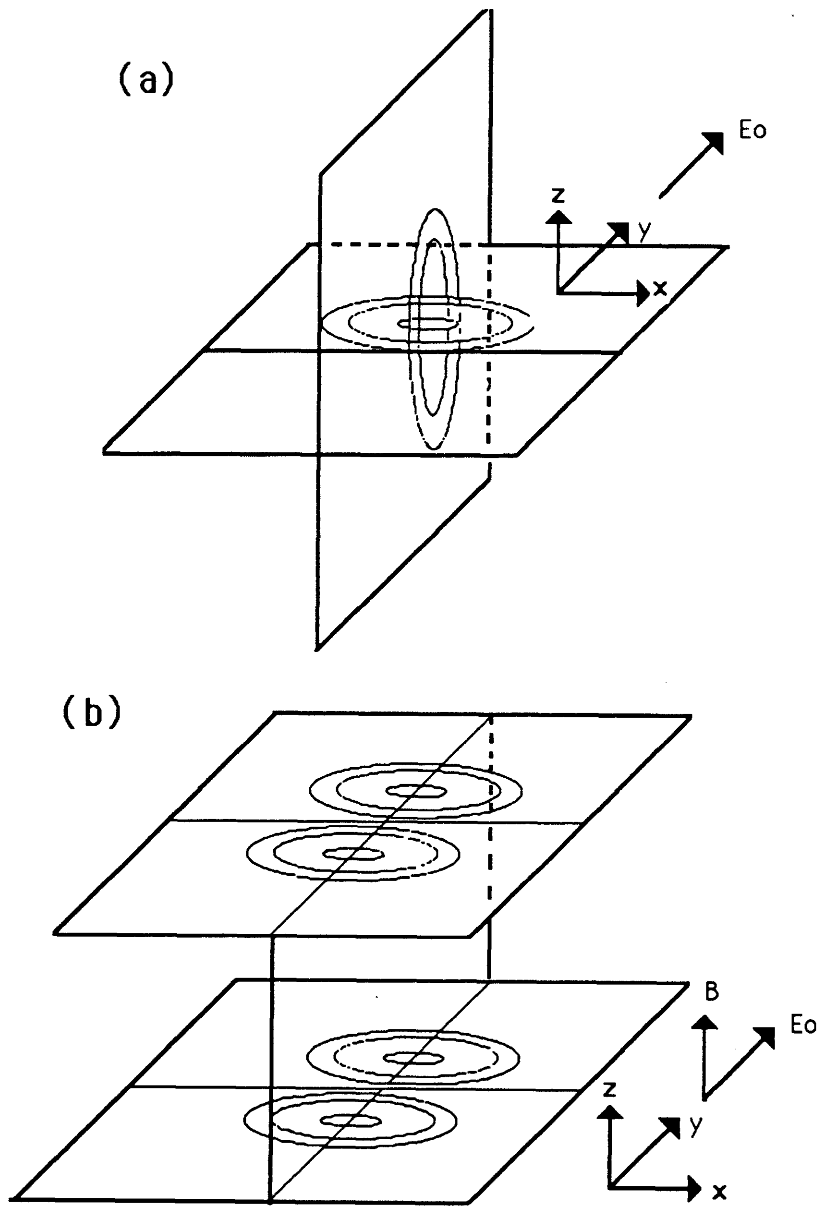

Figure 5.7: The three-dimensional potential distribution of a plasma sphere in an applied electric and magnetic field. (*a*) uniform conductivities, and (*b*) nonuniform conductivities.

5.3 Nonuniform Plasma Cloud

5.3.1 Initial Conditions

We assume that the ion cloud can be described initially by a Gaussian profile given by

$$n_{r+}(\mathbf{r}, t=0) = n^{\circ}_{r+} \exp\left[-\left(\frac{x^2+y^2}{r_\perp^2}\right)\right] \exp\left[-\left(\frac{z^2}{r_\parallel^2}\right)\right] \tag{5.5}$$

where x, y, z are the distance from the point of release and n°_{r+} is the density at the center of the cloud. With this model the mass of the released material is given by $M_{r+} = \pi^{3/2} n^{\circ}_{r+} r_\perp^2 r_\parallel m_{r+}$.

In most cases of artificial ion clouds a neutral cloud in present. For the neutral cloud we assume initially a profile given by a similar Gaussian distribution. The other parameter which describes the neutral cloud is the velocity of the neutrals (wind). For both the ion and neutral central densities we can write $n^{\circ}_{r+} = A_I n_{a+}$ and $n^{\circ}_{r} = A_N n_a$, where n_{a+} and n_a are the ambient densities at the plane of the release. The parameters A_I and A_N define the degree of the perturbation that the plasma cloud represents with respect to the local ambient environment. For both the neutral and ion clouds, the e-folding distances in the assumed Gaussian distributions are $r_\perp = 0.6$ km and $r_\parallel = 0.6$ km, thus simulating spherical clouds. The grid is such that $\Delta x = \Delta y = r_\perp$ and $\Delta z_i = r_\parallel$. We consider water ions and neutrals since water was found to be the major contaminant about the shuttle. We assume the contaminant ions to be isothermal with $T_{H_2O^+} = 0.025$ eV. We neglect ambient transverse electric fields and ambient neutral winds.

5.3.2 The Unperturbed Electric Fields

In all the simulations of this and of subsequent chapters the background ionosphere is altitude dependent. The plasma model developed here can be applied to describe the motion of the ionospheric plasma with care taken for the boundary conditions. The electrodynamics and motion of the background ionosphere are *not* the focus of this study (for extensive coverage of the subject see the book by *M. Kelley*, 1989). Due to the small time scales of interest we require that in the absence of a plasma perturbation a given ambient density profile is in steady state. In order to obtain the equilibrium electric fields we solve (3.34) with appropriate boundary conditions.

For the high latitude ionosphere an analytic approximation to the unperturbed electric field can be obtained by assuming steady state ion and electron continuity equations. It is required that

$$\nabla \cdot \mathbf{\Gamma}_i = \nabla \cdot \mathbf{\Gamma}_e = 0 \tag{5.6}$$

If we neglect the ambient neutral wind under the assumption that there is no shear in the perpendicular electric field, the relations above become

$$\begin{aligned}
\nabla \cdot \mathbf{\Gamma}_i &= \frac{\partial}{\partial z}\left(n\mu_{\|}^{a^+}E_{o\|}\right) - \frac{\partial}{\partial z}\left[\left(D_{a+\|}^{a^+} + D_{e\|}^{a^+}\right)\frac{\partial n}{\partial z}\right] + \frac{\partial}{\partial z}\left(n\beta_{\|}^{a^+}g_{o\|}\right) \\
\nabla \cdot \mathbf{\Gamma}_e &= \frac{\partial}{\partial z}\left(n\mu_{\|}^{e}E_{o\|}\right) - \frac{\partial}{\partial z}\left[\left(D_{e\|}^{e} + D_{a+\|}^{e}\right)\frac{\partial n}{\partial z}\right] + \frac{\partial}{\partial z}\left(n\beta_{\|}^{e}g_{\|}\right)
\end{aligned} \tag{5.7}$$

Note that at the high-latitude ionosphere the divergence of the perpendicular flux vanishes, since both the density and the ambient perpendicular electric field are spatially uniform. With some manipulation and applying the condition of equal fluxes of ions and electrons at the upper and lower boundaries we get

$$E_{o\|} = \frac{D_{a+\|}^{e} + D_{e\|}^{e} - D_{a+\|}^{a^+} - D_{e\|}^{a^+}}{n(\mu_{e\|} - \mu_{a+\|})}\frac{\partial n}{\partial z} + \frac{\beta_{e\|} - \beta_{a+\|}}{(\mu_{e\|} - \mu_{a+\|})}g_{\|} \tag{5.8}$$

The numerical solution is shown in Figure 5.8 in comparison with the analytic Boltzmann potential derived from (5.8).

In the middle and low latitude ionosphere the equation resulting from setting $\nabla \cdot \mathbf{\Gamma}_i = \nabla \cdot \mathbf{\Gamma}_e$ cannot be separated into one-dimensional equations and analytic solutions are not generally available; the numerical solution of $\nabla \cdot \mathbf{J} = 0$ with the appropriate boundary conditions gives the equilibrium ambient electric fields. One possible analytic solution is obtained by requiring that the electron and ion fluxes be equal individually in each direction. For a certain class of problems addressing large scale plasma transport phenomena, for instance the equatorial irregularities or spread

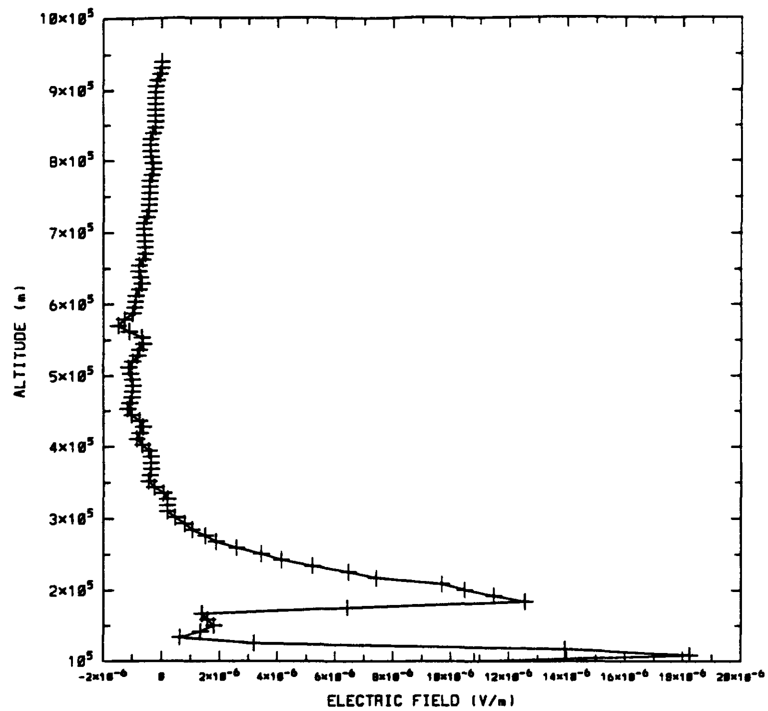

Figure 5.8: Ambient electric fields in the high latitude ionosphere. Numerical solution (solid line) and analytical solution (symbols).

F, special care should be taken for the implementation of boundary conditions and current closure.

Some comments on the role of the ambient electric fields are necessary to clarify the simulation results presented here and in subsequent chapters. In the course of this study we are given an ambient density profile and we solve the current balance equation in order to obtain the self-consistent ambient electric field. This field in turn will develop drifts in the ambient plasma. For example in the high latitude ionosphere there will be plasma flow along the **B** lines. The loss of ambient plasma is replenished by some artificial source-sink term in the ambient ion continuity equation. This is equivalent to adding ionization-recombination terms in the continuity equation [*Heelis and Vickrey* , 1990]. The parallel drift becomes larger as the altitude increases due to the increasing parallel conductivity; in fact high speed flows in the upper ionosphere are still an area of active research. For altitudes of about 500 km and above a different implementation of equilibrium closure should be applied. There is no inherent limitation of our plasma model on the boundary conditions one can supply it with. Such an alternative implementation could be to require diffusive equilibrium for the plasma by setting both the ion and electron velocities to zero. *Risbeth and Garriott* [1969] discuss in detail the derivation of the various ionospheric layers based on diffusive equilibrium, photoionization, recombination, charge exchange and neglect of horizontal transport. For the purpose of this study, especially as we are interested in evolution of clouds in time scales of seconds, it is not necessary to account for the chemistry of the ambient plasma. Our treatment is sufficient to account for the coupling between the cloud and the altitude varying ionosphere as well as the developing of image clouds in the background. To summarize, the developed potential and density perturbations due to the presence of the plasma cloud are perturbations on the underlying otherwise steady state ambient plasma.

5.3.3 3-D Diffusion in the Absence of Neutral Wind

We examine a situation where the cloud is initialized without relative drift of the released neutrals. This is the problem of 3-D diffusion in a magnetic field. It is a very anisotropic process due to the structure of the diffusion coefficient matrix $[D^t_{ik}]$. These coefficients were derived in Chapter 2 for an arbitrary degree of ionization; for ionospheric conditions $D_{e||} \gg D_{i||}$ and $D_{i\perp} \gg D_{e\perp}$. This difference makes the ions diffuse much faster than the electrons in a transverse (to the magnetic field) density gradient. Similarly, electrons diffuse much faster than the ions in a density gradient along the magnetic field. In both cases of diffusion an electric field builds-up parallel to ∇n so that it retards the motion of the faster diffusing species. The result is an overall diffusion process with altered diffusion coefficients. For example, for diffusion parallel to the magnetic field the species diffuse with the ion (low) diffusion coefficient. This is the case of ambipolar diffusion where the current densities for the ions and electrons satisfy the condition $\mathbf{J_i} + \mathbf{J_e} = c$. However, in a situation of a 3-D density perturbation the problem of diffusion cannot be separated in simple one-dimensional ambipolar flows and depends greatly on the imposed boundary conditions [*Zhiliskii and Tsendin*, 1980]. We showed in Chapter 3 using a layer model that if the density perturbation is imbedded in an insulator, then the electric field is the ambipolar one and diffusion takes place with the ion rate. If instead the density perturbation is surrounded by conductors, the field is short-circuited by electrons which flow along the field lines. In what follows we investigate the role of the electric fields established for a typical case of a plasma cloud. We are only interested in the initial time characteristics; the evolution of the density perturbation will be addressed in a subsequent chapter.

We consider an ion density perturbation given by a Gaussian distribution in a magnetic field. We assume that there exists only a parallel component of the ambient electric field, E_{oz}. We begin our discussion by examining the potential structure. Figure 5.9 shows the potential on a midplane in the parallel direction. The Boltzmann diffusion potential necessary to establish ambipolar flow is given by

$$\phi \simeq \frac{kT_e}{e} \ln \left(1 + \frac{n_{s+}}{n_{a+}}\right) \tag{5.9}$$

For comparison we plot in Figure 5.10 the analytical potential obtained through the above formula and the numerical potential obtained from the simulation. This figure shows that parallel diffusion within the region of the density perturbation is ambipolar and thus proceeds with the ion (slow) diffusion rate. The overall structure of the potential shown in Figure 5.9 resembles that of a quadrupole [*Voskoboynikov et al.*, 1986; *Drake et al.*, 1988]. In the transverse direction an ambipolar potential is established in order to inhibit the fast transverse ion diffusion rate. This corresponds to a potential well, i.e., the transverse electric field points inward, and is partially short-circuited. This picture is in accordance with the concepts of current closure outlined with the use of a layer model in Chapter 3. This potential well is mapped along the **B** lines and can be seen clearly outside the density perturbation. However, within the density perturbation the potential is dominated by the parallel ambipolar flow and corresponds to a Botzmann potential hill, i.e., the electric field points outward.

The motion of the plasma cloud is shown in Figure (5.11). The released ions exhibit a clockwise rotation which decreases in magnitude as we move away from the midplane. The transverse velocity of the ions is due to the contribution of both the radial electric field and the diamagnetic drift due to the density gradient. This velocity is given by Eq. 2.23

$$V_{t\perp} = [\mu]_{t\perp} E_\perp + [D]^t_{s+\perp} \frac{\nabla_\perp n_{s+}}{n_{s+}} + [D]^t_{a+\perp} \frac{\nabla_\perp n_{a+}}{n_{a+}} + [D]^t_{e\perp} \frac{\nabla_\perp n_e}{n_e} \tag{5.10}$$

For comparison we plot the velocity of the ambient ions (see Figure 5.12). They rotate in the same clockwise direction as the released ions do but with reduced speeds. Since the mobilities of the two ion species are not very different this implies that the diamagnetic drift is comparable with the drift due to the electric field. The difference in the transverse flow pattern of the ions can be explained by examining equation (5.10). The contribution to the velocity of the species $t = a^+, s^+$ due to the density gradient of s^+ comes through the diffusion coefficient $[D]^t_{s+\perp}$. In general, $[D]^{s+}_{s+\perp} > [D]^{a+}_{s+\perp}$ which in turn makes the diamagnetic drift of the released ions to be greater than the ambient ones. In the parallel direction the drifts of the ions and electrons are shown in Figure 5.13. The parallel drifts are much greater in magnitude than the transverse drifts. On the midplane along **B** the maximum speed of the ions reaches 2560 m/s. This implies that the cloud will mainly diffuse along the **B** lines so that it will develop a "cigar" looking shape while it will spin slowly around the **B** axis. The flow field of the electrons shown in Figure 5.13 is similar to that of the ambient ions. This flow pattern can be explained by applying equality of the parallel electron and ion fluxes due to the ambipolar flow. The velocity of the electrons is then

$$V_{ez} \simeq \frac{1}{1 + n_{s+}/n_{a+}} V_{a+z} + \frac{1}{1 + n_{a+}/n_{s+}} V_{s+z} \tag{5.11}$$

In regions where $n_{a+} \gg n_{s+}$ the electrons drift with the ambient ions, since the ambipolar electric field balances the ambient pressure mainly. In the central cloud region however, $n_{a+} < n_{s+}$ and $V_{ez} \sim V_{s+z}$. From the flow picture we can examine the current balance. It seems that $\nabla \cdot \mathbf{J} = 0$ is independently satisfied in the two directions. In the parallel direction the flow is ambipolar as we have shown. In the transverse direction the divergence of the diamagnetic currents is identically zero since it is independent of the translation of the guiding centers.

Density, m^{-3}		
10^{14}	10^{16}	10^{18}
0.36	3.61	36.1

Table 5.2: The contaminant mass of water with the corresponding central density, $N^{\circ}_{H_2O}$ or $N^{\circ}_{H_2O+}$. Mass measured in kilograms.

5.3.4 3-D Diffusion with Unidirectional Neutral Wind

We examine the case of a plasma cloud with an applied unidirectional neutral wind with velocity $\mathbf{U}_r$. In the frame of the moving neutrals the problem is that of applying an electric field $\mathbf{E}_r = \mathbf{U}_r \times \mathbf{B}$. We present below results from simulations using Gaussian-like neutral and ion clouds placed in an altitude varying ionosphere. The central densities of the water neutrals and ions were varied so that they span the entire range of applications of interest. The corresponding masses of the released water ions or neutrals are shown on Table 5.2. The initial velocity of the neutral cloud is $\mathbf{U}_r = \mathbf{U}_{H_2O} = -8000\mathbf{x}$ m/s, simulating thus an orbital release.

We begin with the discussion of results of a low-density plasma cloud with densities $N^{\circ}_{H_2O+} = 10^{11}$ m^{-3} and $N^{\circ}_{H_2O} = 10^{14}$ m^{-3}. This cloud represents a small perturbation with $A_I = 0.5$ and $A_N = 10^{-3}$. The perturbation potential is shown in Figure 5.14 on three perpendicular planes. On the plane of the release the potential is the result of the superposition of the dipole field caused by the action of the contaminant neutral wind and the diffusion potential due to the density gradients of the ion cloud (Figure 5.14). Similar results were obtained by *Voskoboynikov et al.* [1987]. The contaminant ion drift velocities are shown on three perpendicular planes. At the release plane the drift is due to the diffusion giving rise to the clockwise rotation of the ions as Figure 5.15 shows. The magnitudes of those velocities are small, in the order of meters. This low-density cloud is almost stationary with its ions spinning around the **B** field. In the moving frame of the spacecraft this cloud would drift away with ~ 8 km/s, and the shielding of the motional electric field would be negligible. Note that in this case the action of the ambient electric field has to be taken into account. We will discuss several 3-D effects present in our calculations. In Figure 5.14 is shown that the perturbation potential exhibits a different behavior, depending on the distance from the release plane along the magnetic field lines. The dipole and the diffusion (due to electrons) field are present at the height of the release as Figure 5.14(Bottom) shows. The (electron) diffusion field is confined to the cloud region and corresponds to a Boltzmann potential with a diffusion length scale of $L_\perp^D \sim a_\perp$ and $L_\parallel^D \sim a_\parallel$, as we explained in the previous section. However, the dipole field (Figure 5.14(top)) is easily mapped along the magnetic field lines due to the large parallel conductivity (in general, $\sigma_\parallel/\sigma_{p,h} \gg 1$). As we derived in section 5.2, its length scales are very different in the transverse and parallel directions, i.e., $L_\perp^E \sim a_\perp$ and $L_\parallel^E \sim a_\perp\sqrt{\sigma_\parallel/\sigma_\perp}$. Figure 5.16(Top) agrees with these theoretical estimates. The **B** lines are nonequipotentials only within the region dominated by the diffusion field.

The contaminant ion flow field shows in Figure 5.15 the response of the plasma to the different forcing mechanisms. At the plane of the release the drift is due to diffusion mainly as shown in Figure 5.15(Bottom). On a plane 1.8 km away from the cloud's midplane the diamagnetic drift dominates although the potential structure is of a dipole type. On this plane the radial electric field is very small and the only remaining contribution to the drift is due to the density gradient (diamagnetic drift). Note that the maximum velocity is $\sim$ 12 m/s on the release plane and $\sim$ 10 m/s 1.8 km away from it. Given also that the plasma cloud has a Gaussian e-folding distance of 600 m implies that the diamagnetic drift dominates the plasma velocity. On a plane which is located 4.2 km away from the release plane the velocity field becomes purely a drift due to the action of the dipole field as Figure 5.15(Top) shows. This plane is located practically outside of the density perturbation and the drifts on this layer are much smaller compared with those inside the cloud (less than 0.1 m/s). The ion velocities on a plane along the magnetic field lines passing through the center of the cloud are shown in Figure 5.16(Bottom). The drift is mainly due to ambipolar diffusion. The velocity is parallel to the magnetic field lines due to the fact that the cloud expands along the magnetic field lines with much higher speeds than it rotates in the transverse direction (the maximum speed is ~ 660 m/s). Qualitatively the results of the low density plasma cloud are similar with those presented in the previous section. The neutral wind has a very small effect in the plasma cloud dynamics.

We discuss next results of a very dense cloud with $A_I = 50$ and $A_N = 10$. The central densities are $N^{\circ}_{H_2O+} = 10^{13}$ m^{-3} and $n^{\circ}_{\mathrm{H_2O}} = 10^{18}$ m^{-3}, a case which represents a massive release. The potential shown in Figure 5.17 at the height of the release is dominated by the dipole field due to the action of the contaminant neutral wind. This dipole potential is mapped very effectively along the field lines as Figure 5.17 shows. The potential field shows substantial rotation which is a direct effect of the increased Hall conductivity. The transverse ion velocities are shown in Figure 5.18. On the release plane the drift is due to the dipole and radial electric field, plus the diamagnetic drift due to the density gradient. On the release plane the clockwise rotation due to the diamagnetic effects cancels the counter-clockwise rotation due to the Hall effect of dipole electric field. Outside of the cloud the drift is due to the dipole primarily. On the plane (x,y,z=4.2) km the rotation is significant due to the absence of the clockwise component of the diamagnetic drift. The physical picture can be further elucidated by looking at the velocity vectors parallel to the field lines. Figure 5.19 shows the velocity vector on the (x=0,y,z) plane. Two effects are apparent. The rotation of the electric field which gives the directional component in the y direction. A dipole without rotation should not have any component in that direction. The effects of the parallel expansion of the cloud are also present. Almost 4 km away from the clouds center diffusion no longer affects the dynamics, as it is the case for the low density cloud that we examined earlier. In Figure 5.19(Top) the ion velocity on the (x,y=0,z) plane is shown. The drift is mainly along the direction of the neutral wind which shows that the expansion along the field lines is smaller than the transverse drift, opposite with what happens in the case of the low density cloud. The maximum expansion velocity is in this case ~ 1.1 km/s. The parallel velocity field of the contaminant ions in Figure 5.19(Bottom) shows the effects of diffusion to be confined within the density perturbation. The asymmetry between the velocity vectors is caused by the y component of the ion flow due to Hall effects. The electric field at the cloud's center is ~ 0.23 V/m and the drift is ~ 7.4 km/s in the direction of the contaminant neutral wind. Previous two-dimensional models anticipated high-speed ion drifts in case of neutral releases at orbital speeds [*Mitchell et al.*, 1985]. The action of the large neutral wind force and the presence of a dense ion cloud contributes to the generation of a large perturbation field. In the moving frame of the spacecraft this situation corresponds to a highly shielded cloud which drifts almost with it.

In general both diffusion and neutral drag dictate the electric fields and, consequently the drift of the ion cloud. The effects of the unidirectional wind appear to relate with the transverse drift of the ion cloud while diffusion dominates the motion along the **B** lines. The effects of the central densities of ions and neutrals are shown in Figure 5.20. For a given contaminant neutral density, increase of the ion density increases both the perturbation field and the drift. The action of the force of the neutrals increases as the ion density increases. Also, for a given ion density the drift increases with increasing contaminant neutral densities since the neutral force becomes in effect larger. It is only for neutral densities of 10^{18} m^{-3} that the transverse central drift is of the order of the orbital velocity.

Another important aspect is the motion of the ambient plasma. The induced drifts on the ambient ions are similar in magnitude and direction to those shown for the contaminant ions. For the case of the low-density cloud these drifts are dominated by diffusion mechanisms. Thus, the ambient ions trapped in the electric fields of the density perturbation rotate and at the same time drift along the axis of the **B** field. For the case of the high-density cloud the entire flux tube that confines the ion cloud develops a drift and speeds up. The contaminant neutral cloud imparts its momentum and speeds up the ambient plasma. Due to the developed drifts the ambient plasma is expected to develop nonuniformities, called "image-clouds." These effects are shown in Chapter 7. By examining the ambient ion drifts we can deduce the different response of the ionospheric layers. In Figure 5.21 we show the angle of rotation, measured with respect to the contaminant neutral wind. From Figure 5.21a we see that the rotation on the upper F layer is between 2° and 12° while in the E layer (Figure 5.21b) increases and becomes 15°-30°. This is a direct effect of the increased Hall conductivity in the lower ionospheric regions. This differential rotation between the various ionospheric layers will, consequently, rotate the entire flux tube and in subsequent times will rotate the potential structure.

Notice also that in all cases the velocity field is spatially nonuniform; the cloud's center drifts with speeds higher than those at the edges of the cloud. This will result in the pile-up of the density and will develop structure in both the cloud and the ambient plasma. All these phenomena are shown in Chapter 7.

Another set of simulations examined the effect of the altitude of the release on the motion of the ion cloud. We examined a large cloud, the worst scenario for contamination, with central densities of $N^{o}_{\mathrm{H_2O^+}} = 10^{13}$ m^{-3} and $N^{o}_{\mathrm{H_2O}} = 10^{18}$ m^{-3} between altitudes of 200 – 600 km. In Figure 5.22 we plot the velocity component of the contaminant ions at the cloud's center. As the altitude of the release increases, the central speed increases. This can be attributed directly to the ratio of the perpendicular conductivities $\sigma_{c\perp}/\sigma_{a\perp}$ at the height of the cloud. At higher altitudes this becomes larger since the ambient conductivity reduces with height. The higher the ratio the larger the perturbation field and, consequently, the drift, as we have shown in the previous example of the plasma sphere.

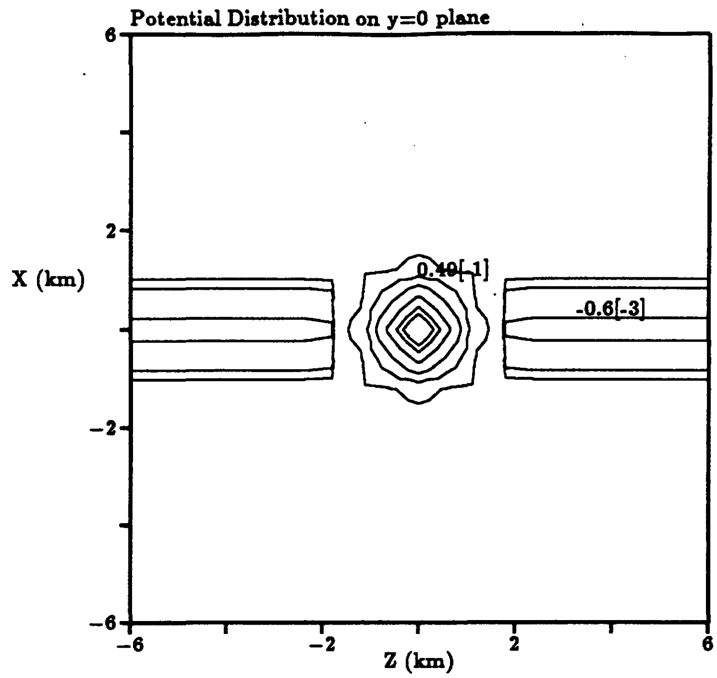

Figure 5.9: Potential distribution on the plane (x,y=0,z). Countours are plotted at arbitrary potential levels for clarity. The ion cloud is initialized at 256 km with a Gaussian profile and central density of $N^{o}_{H_2O^+} = 10^{12}$ m^{-3}. There is no applied neutral wind.

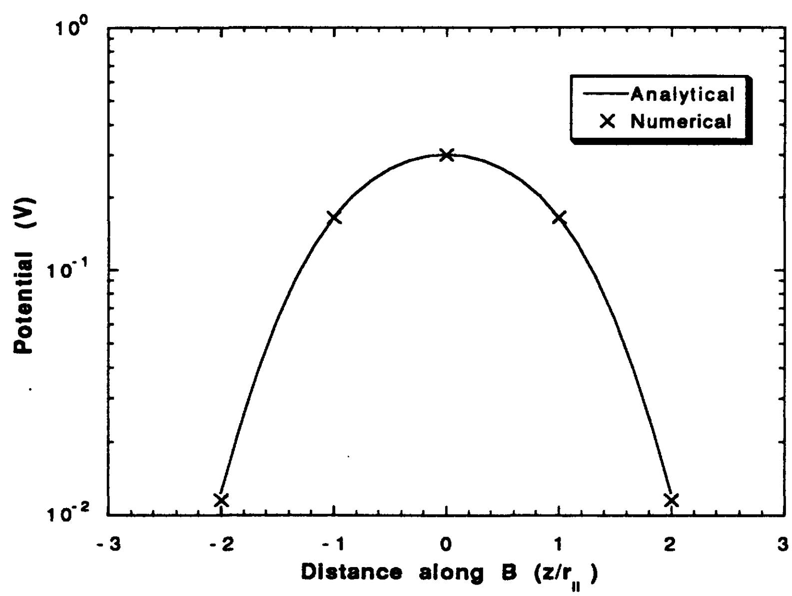

Figure 5.10: Potential along **B** through the center of the plasma cloud. Analytical Boltzmann (solid) and numerical (symbols). Conditions are the same as in Figure 5.9.

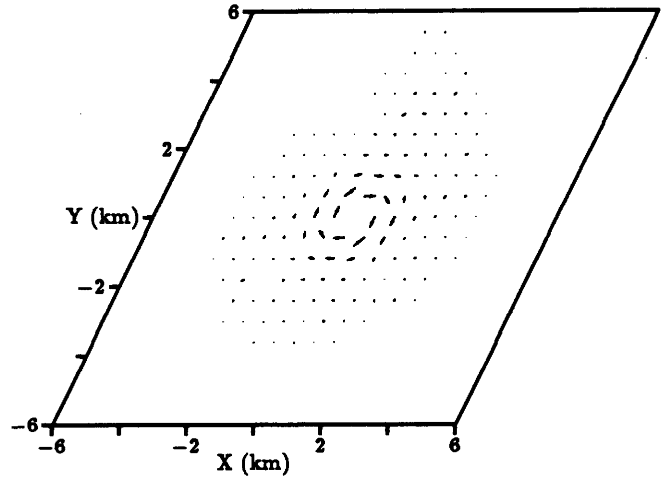

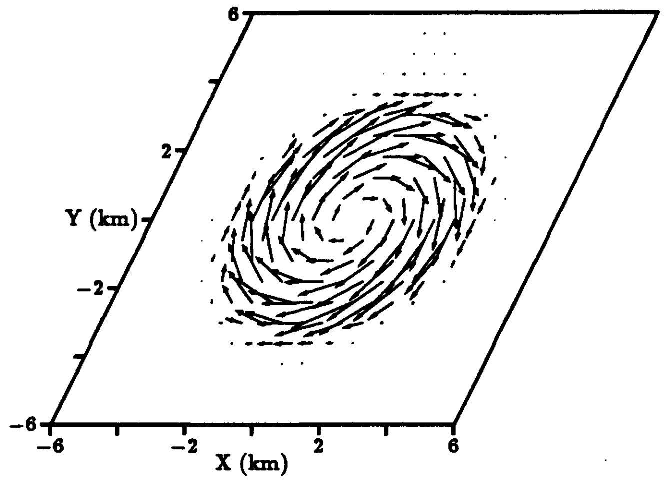

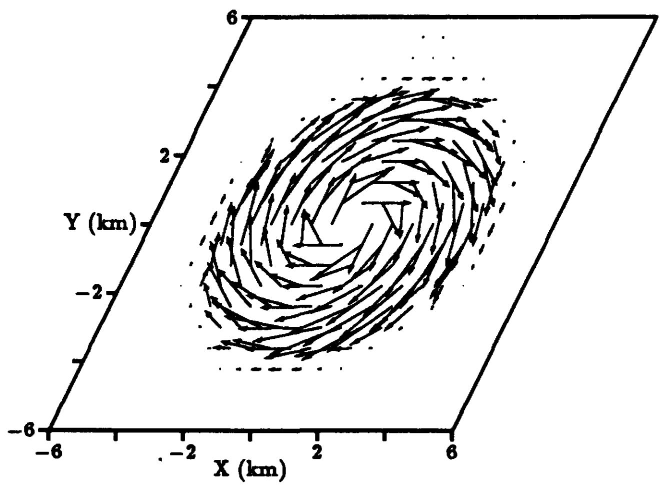

Figure 5.11: Velocity of released ions. (Top) On the (x,y,z=3.6) km plane; maximum velocity is 1.8 m/s. (Middle) On the (x,y,z=1.8) km plane; maximum velocity is 10.5 m/s. (Bottom) On the (x,y,z=0) release plane; maximum velocity is 12.2 m/s. The ion cloud is initialized at h =256 km with a Gaussian profile and central density of $N^{o}_{H_2O+} = 10^{12}$ m^{-3}. There is no applied neutral wind.

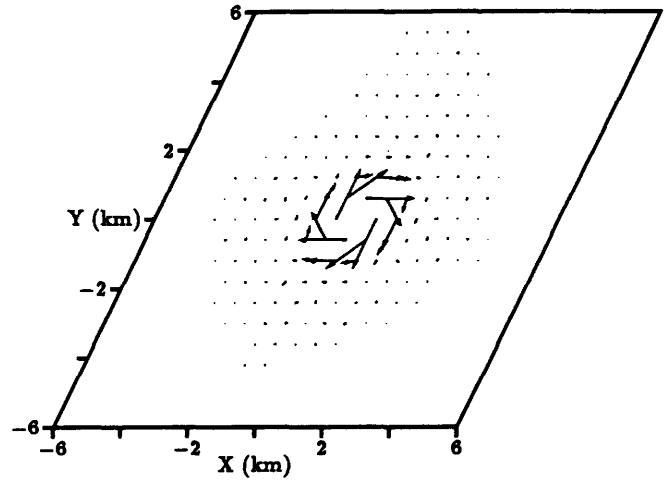

Figure 5.12: Velocity of ambient ions on the (x,y,z=0) midplane. Maximum velocity is 6.8 m/s. The ion cloud is initialized at h =256 km with a Gaussian profile and central density of $N^{\circ}_{H_2O+} = 10^{12}$ m^{-3}. There is no applied neutral wind.

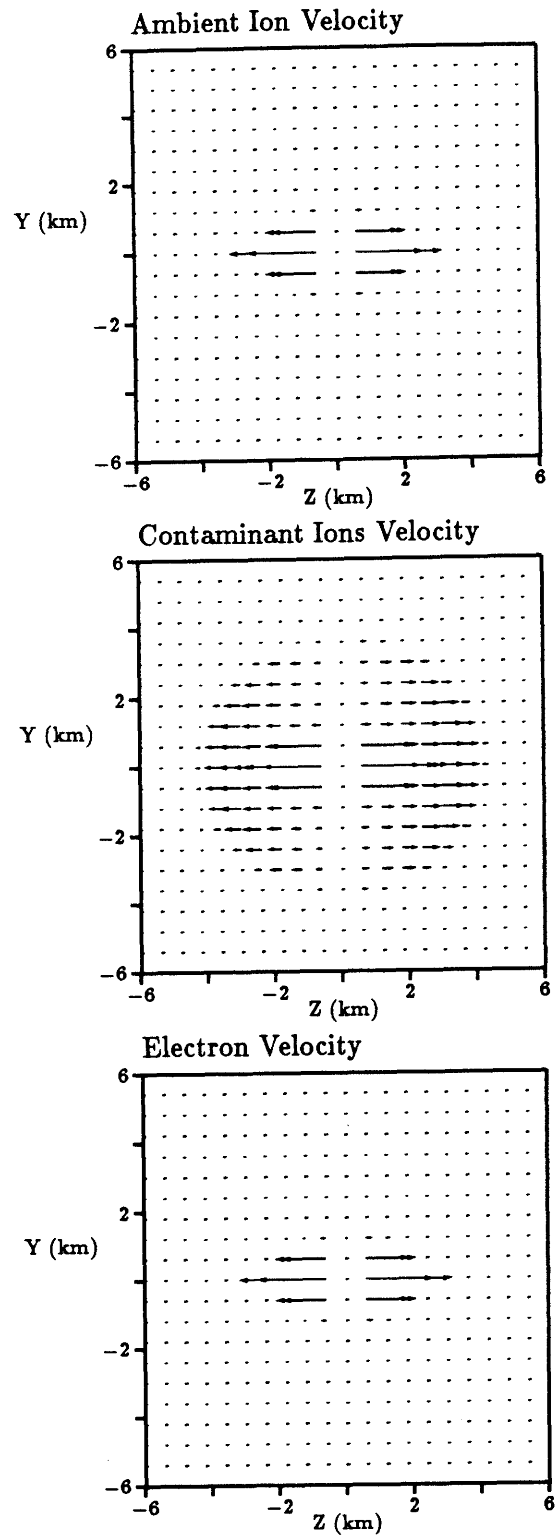

Figure 5.13: Velocity at the (x=0,y,z) plane (Top) Ambient ions; maximum velocity is 2560 m/s. (Middle) Released ions; maximum velocity is 2515 m/s. (Bottom) Electrons; maximum velocity is 2560 m/s. The ion cloud is initialized at h = 256 km and has a Gaussian profile with central density of $N^{o}_{H_2O^+} = 10^{12}$ m^{-3} without a neutral wind.

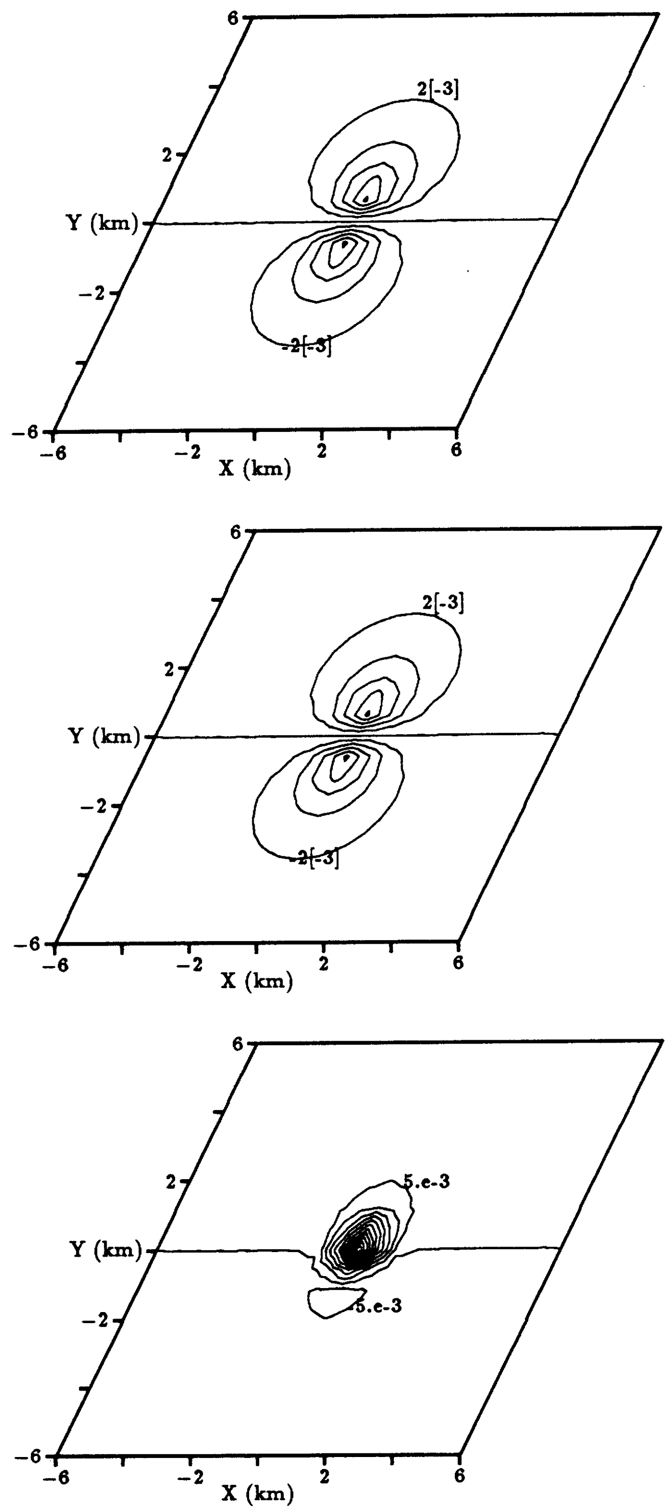

Figure 5.14: Perturbation potential. (Top) On the (x,y,z=4.2) km plane; contour separation is 2×10^{-3} V. (Middle) On the (x,y,z=1.8) km plane; contour separation is 2×10^{-3} V. (Bottom) On the (x,y,z=0) release plane; contour separation is 5×10^{-3} V. The neutral-ion cloud is initialized at h =256 km with a Gaussian profile and central density of $N^{o}_{H_2O} = 10^{14}$ m^{-3} and $N^{o}_{H_2O+} = 10^{11}$ m^{-3}. The neutral wind is $\mathbf{U}_{H_2O} = -8000\mathbf{x}$ m/s.

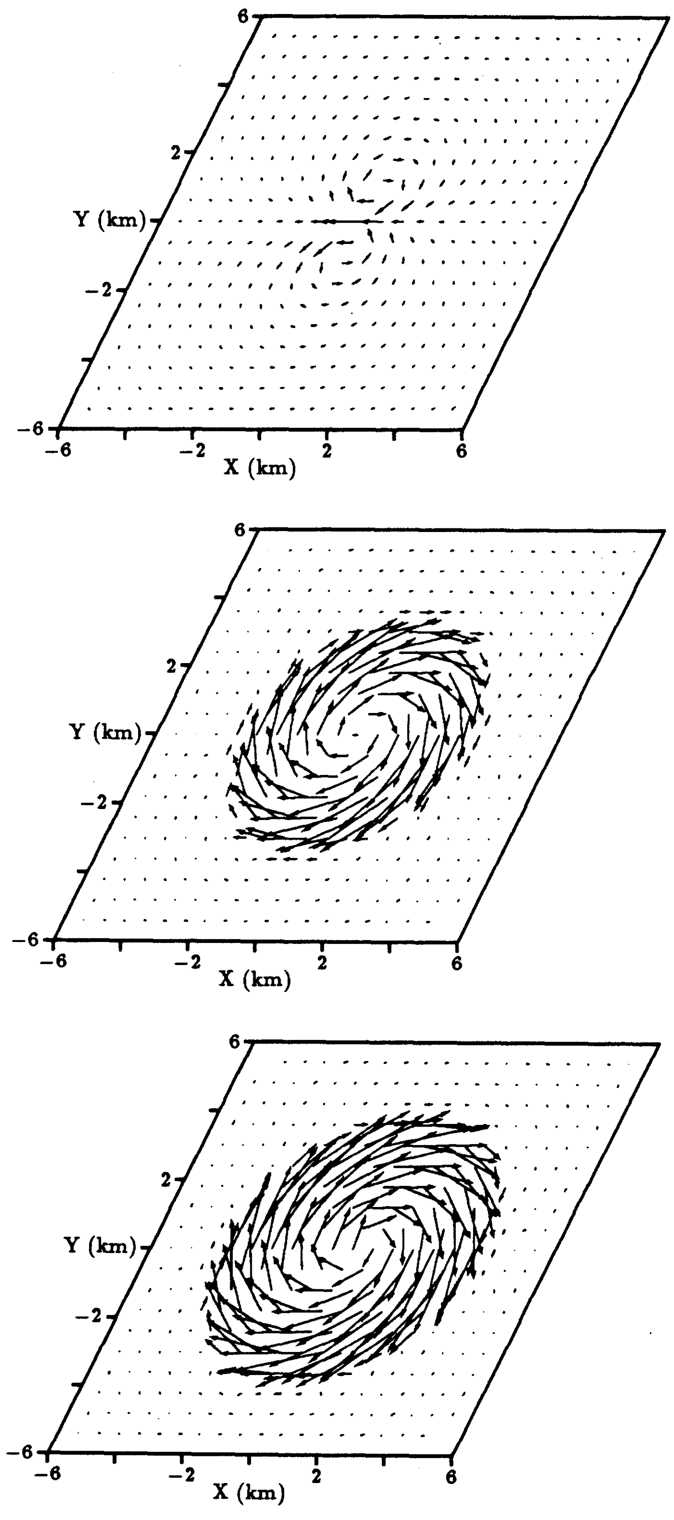

Figure 5.15: Velocity of released ions. (Top) On the (x,y,z=4.2) km plane; maximum velocity is 0.49 m/s. (Middle) On the (x,y,z=1.8) km plane; maximum velocity is 10 m/s. (Bottom) On the (x,y,z=0) release plane; maximum velocity is 11.9 m/s. The neutral-ion cloud is inititalized at h =256 km with a Gaussian profile and central density of $N^{\circ}_{\mathrm{H_2O}} = 10^{14}$ m^{-3} and $N^{\circ}_{\mathrm{H_2O^+}} = 10^{11}$ m^{-3}. The neutral wind is $\mathbf{U}_{\mathrm{H_2O}} = -8000\mathbf{x}$ m/s.

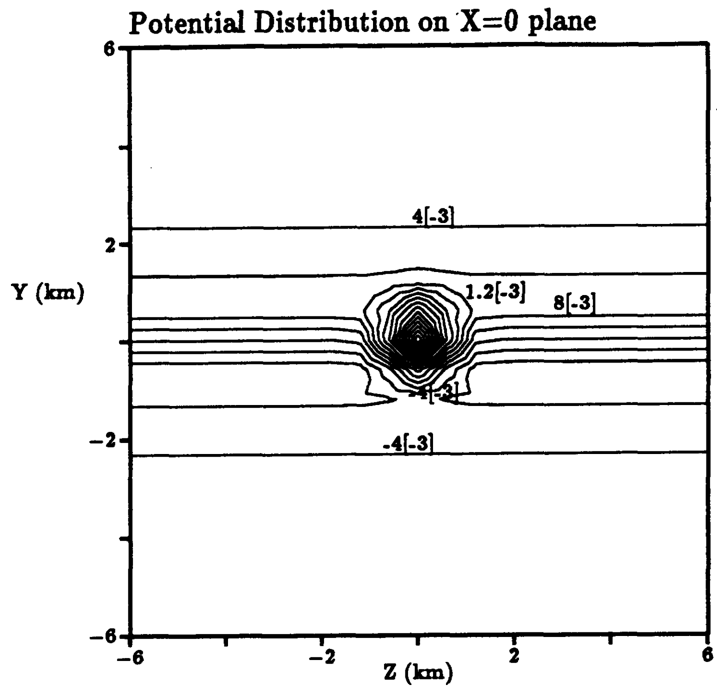

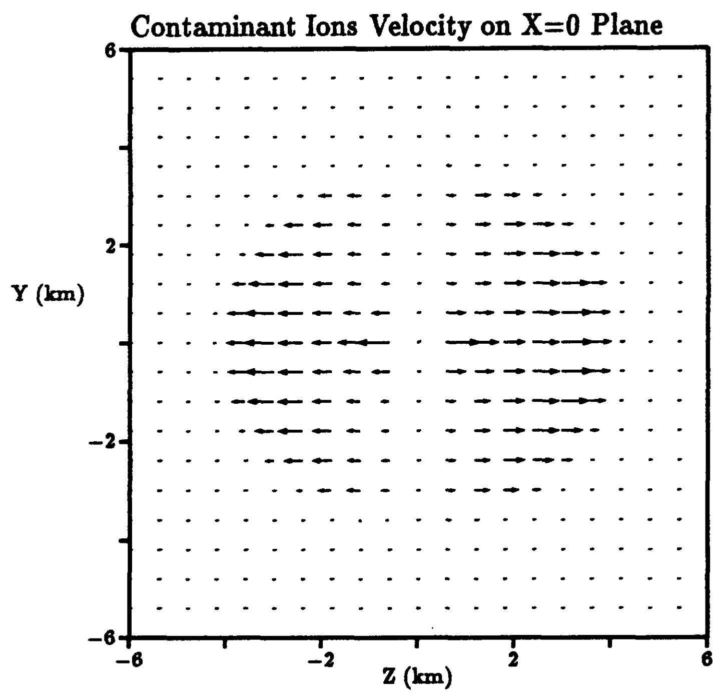

Figure 5.16: (Top) Perturbation potential; contour separation is 4×10^{-3} V. (Bottom) The released ion velocity; the maximum velocity vector is 664 m/s. Quantities are shown on the (x=0,y,z) plane. The neutral-ion cloud is initialized at $h = 256$ km with a Gaussian profile and central density of $N^o_{H_2O} = 10^{14}$ m^{-3} and $N^o_{H_2O+} = 10^{11}$ m^{-3}. The neutral wind is $\mathbf{U}_{H_2O} = -8000\mathbf{x}$ m/s.

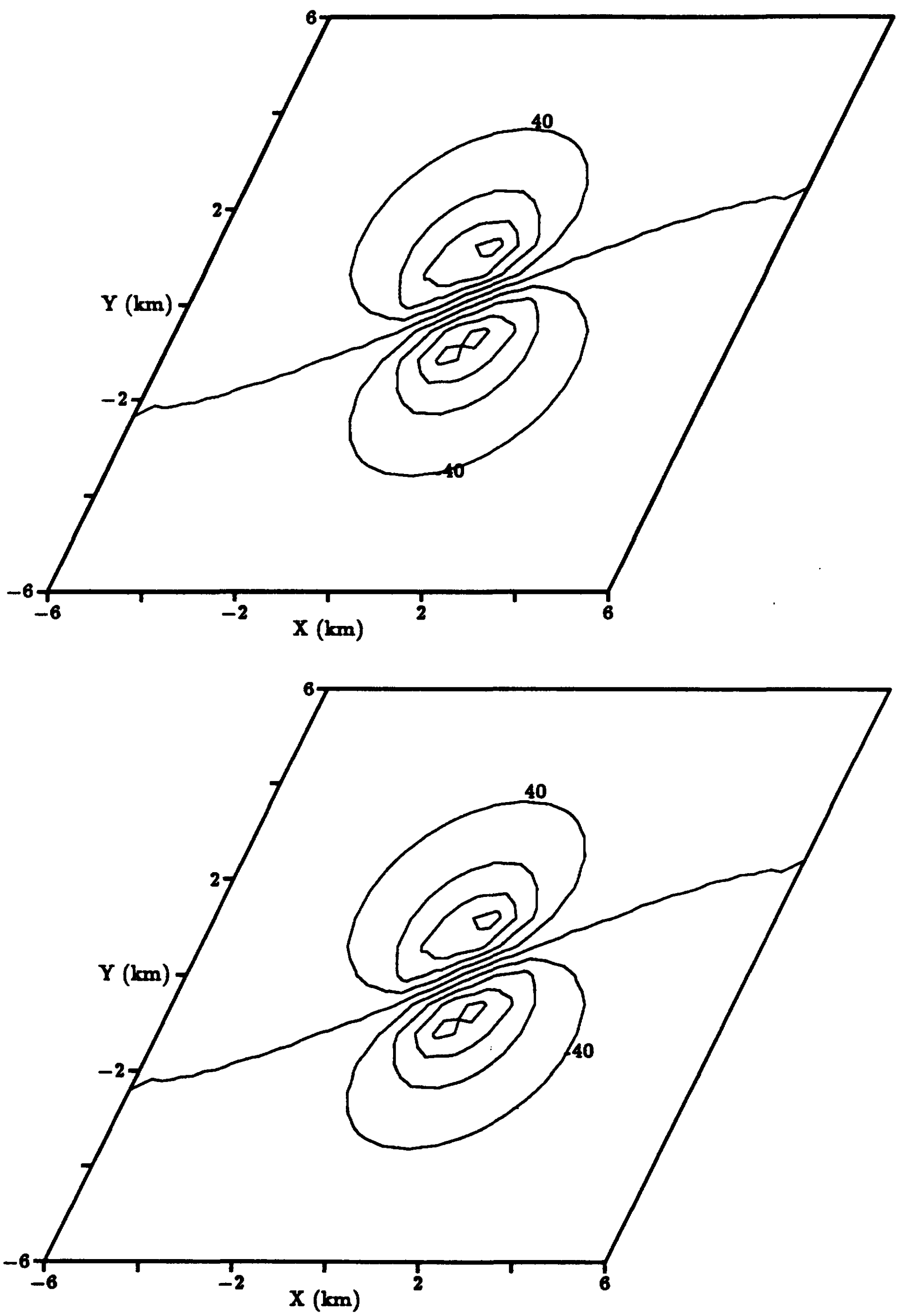

Figure 5.17: Perturbation potential. (Top) On the (x,y,z=4.2) km plane; contour separation is 40 V. (Bottom) On the release plane (x,y,z=0); contour separation is 40 V. The neutral-ion cloud is initialized at $h = 256$ km with a Gaussian profile and central density of $N^{\circ}_{H_2O} = 10^{18}$ m^{-3} and $N^{\circ}_{H_2O+} = 10^{13}$ m^{-3}. The neutral wind is $\mathbf{U}_{H_2O} = -8000\mathbf{x}$ m/s.

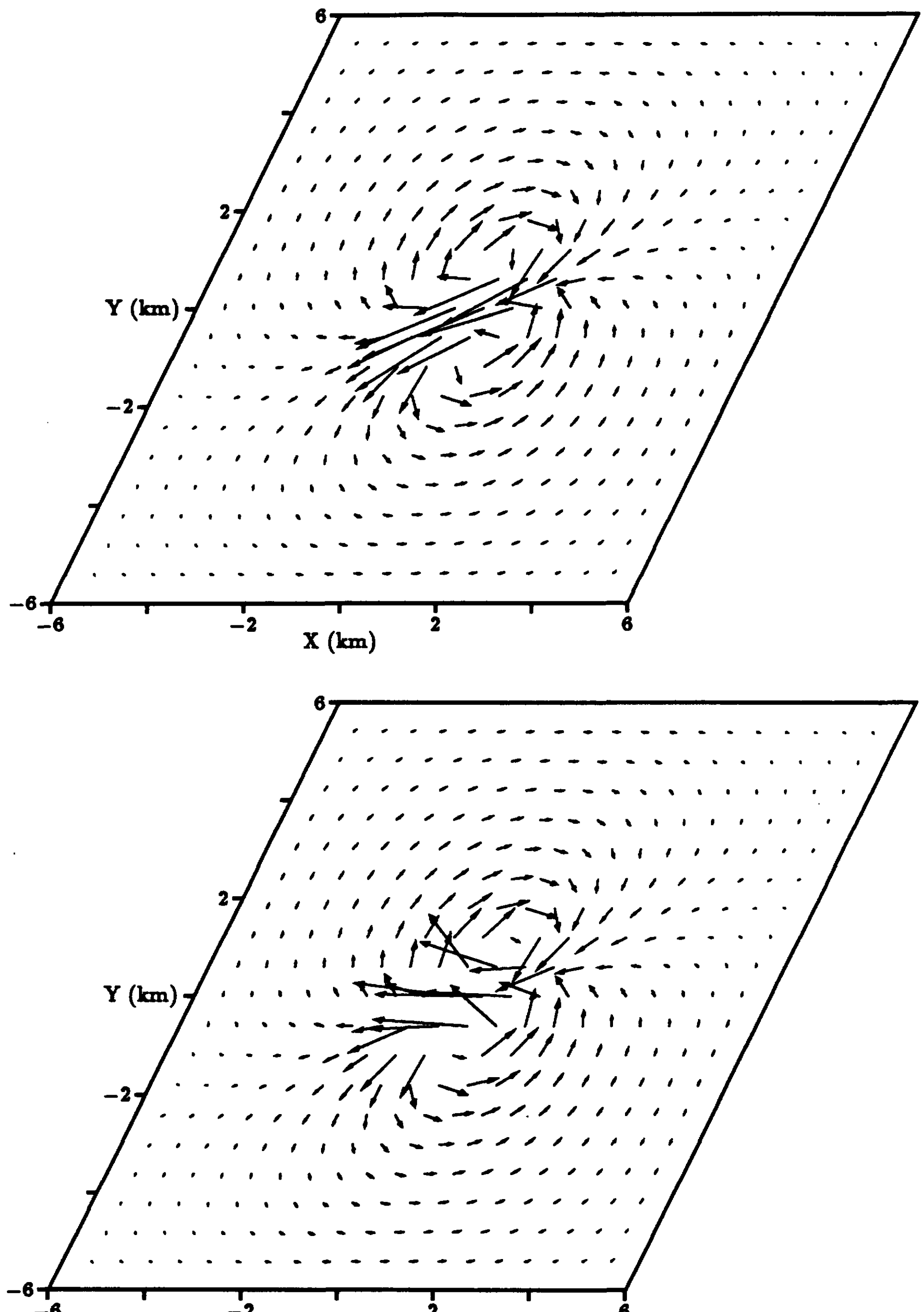

Figure 5.18: Velocity of released ions. (Top) On the (x,y,z=4.2) km plane; maximum velocity is 7413 m/s. (Bottom) On the release plane (x,y,z=0); maximum velocity is 7399 m/s. The neutral-ion cloud is initialized at h = 256 km with a Gaussian profile and central density of $N^{o}_{H_2O} = 10^{18}$ m^{-3} and $N^{o}_{H_2O+} = 10^{13}$ m^{-3}. The neutral wind is $U_{H_2O} = -8000$x m/s.

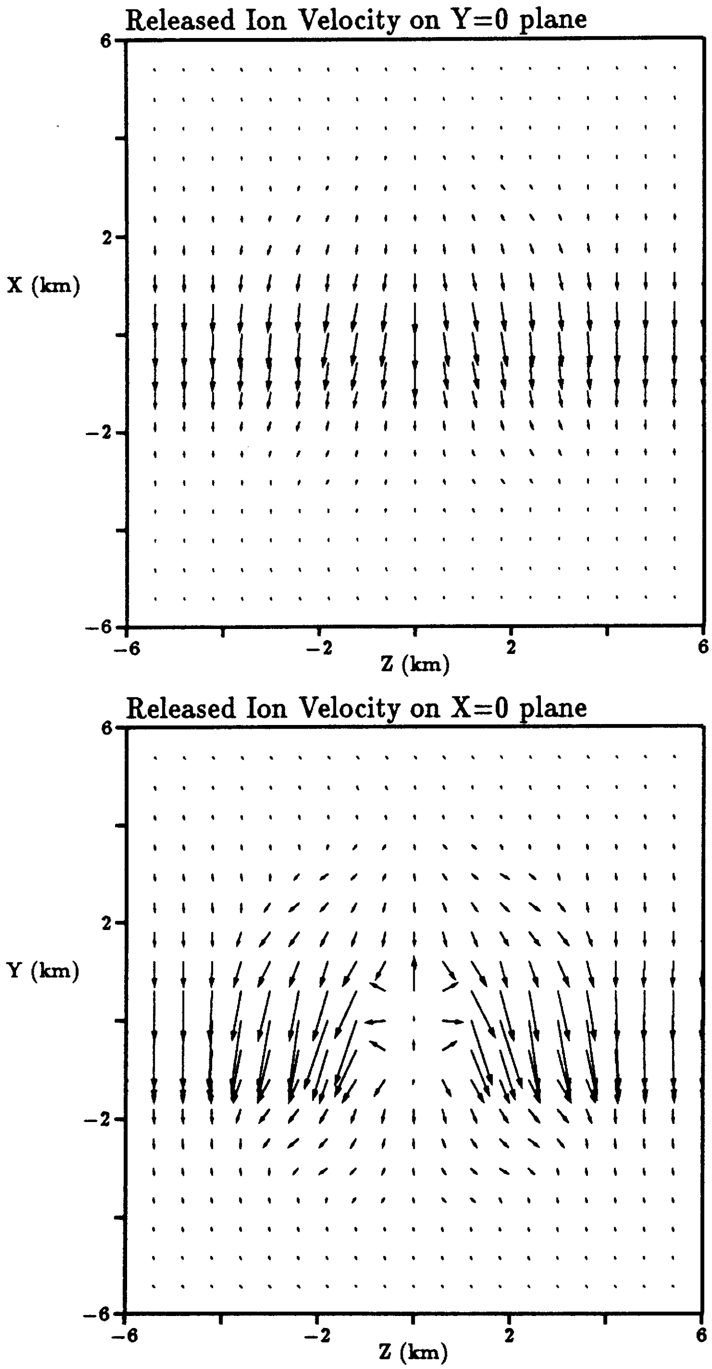

Figure 5.19: Velocity of released ions. (Top) On the (x=0,y,z) plane; maximum velocity is 4426 m/s. (Bottom) On the (x,y=0,z) plane; maximum velocity is 7399 m/s. The neutral-ion cloud is initialized at h = 256 km with a Gaussian profile and central density of $N^{o}_{H_2O} = 10^{18}$ m^{-3} and $N^{o}_{H_2O+} = 10^{13}$ m^{-3}. The neutral wind is $\mathbf{U}_{H_2O} = -8000\mathbf{x}$ m/s.

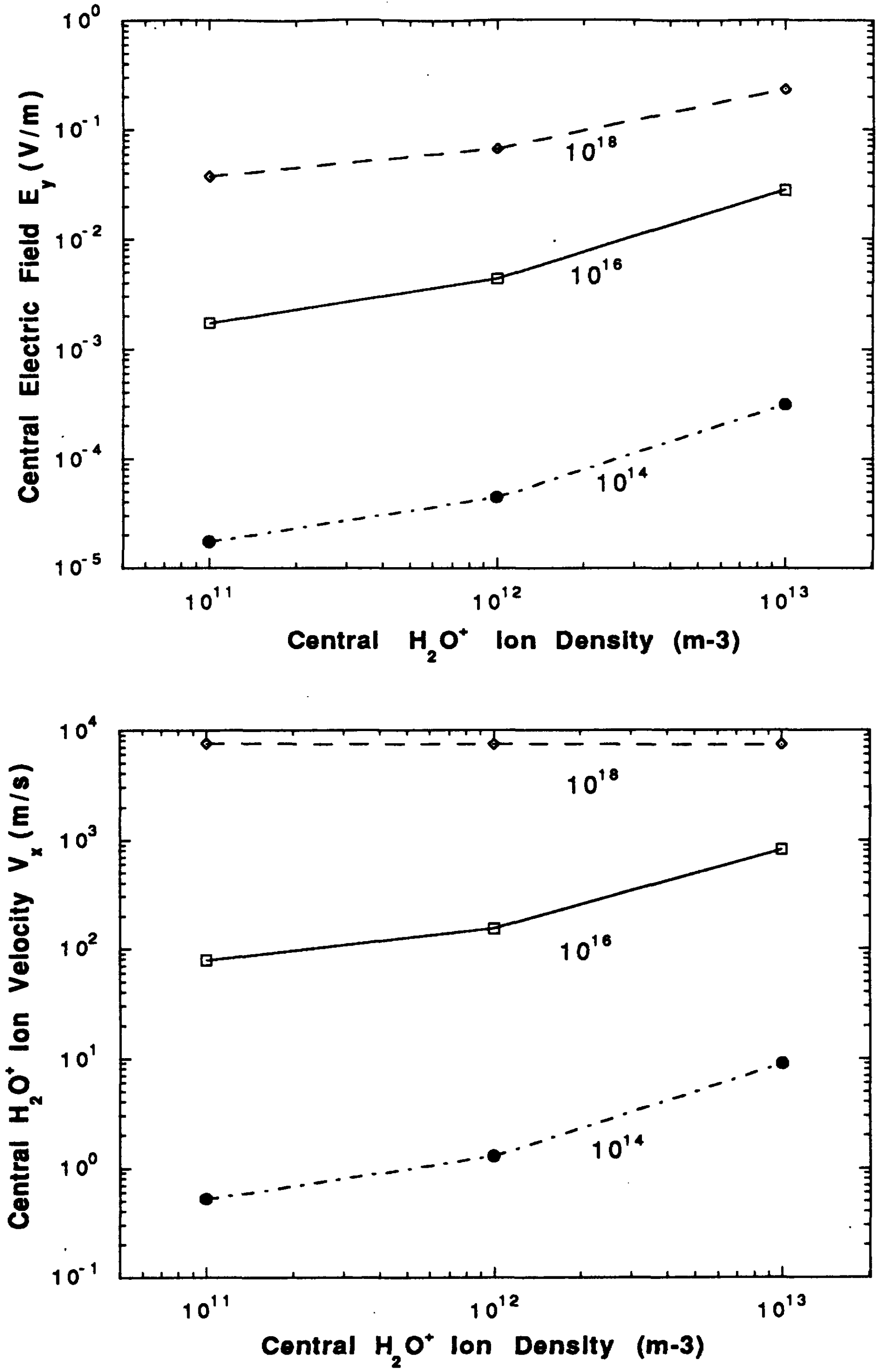

Figure 5.20: (Top) The electric field $|\epsilon_y|$ (V/m) at the center of the cloud plotted against the central H_2O^+ density. (Bottom) The H_2O^+ velocity V_x at the cloud's center (m/s). The central neutral density is $N^o_{H_2O} = 10^{14}$ m^{-3} (dot-broken), $N^o_{H_2O} = 10^{16}$ m^{-3} (solid) and $N^o_{H_2O} = 10^{18}$ m^{-3} (broken). The neutral cloud velocity is $U_{H_2O} = -8$x km/s.

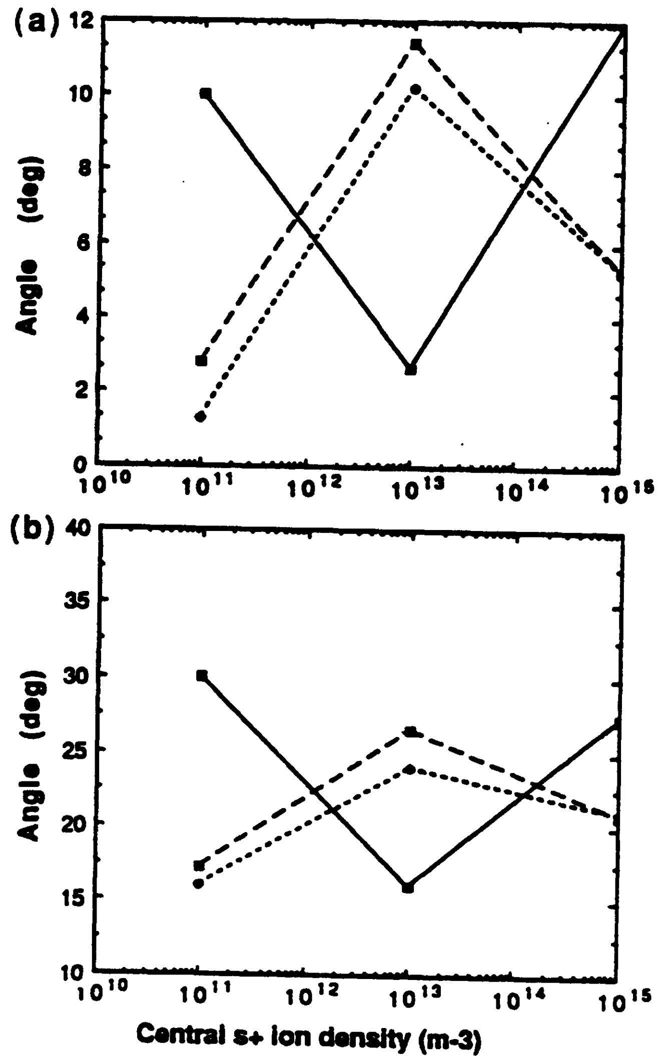

Figure 5.21: The angle between the ambient ion velocity and the neutral wind (in deg) plotted against the central H_2O^+ ion density (m^{-3}). (*a*) On a plane located at 378 km. (*b*) On a plane located at 130 km. The central neutral density is $N^o_{H_2O} = 10^{14}$ m^{-3} (solid), $N^o_{H_2O} = 10^{16}$ m^{-3} (dotted), $N^o_{H_2O} = 10^{18}$ m^{-3}(broken). The neutral cloud velocity is $\mathbf{U}_{H_2O} = -8000\mathbf{x}$ m/s.

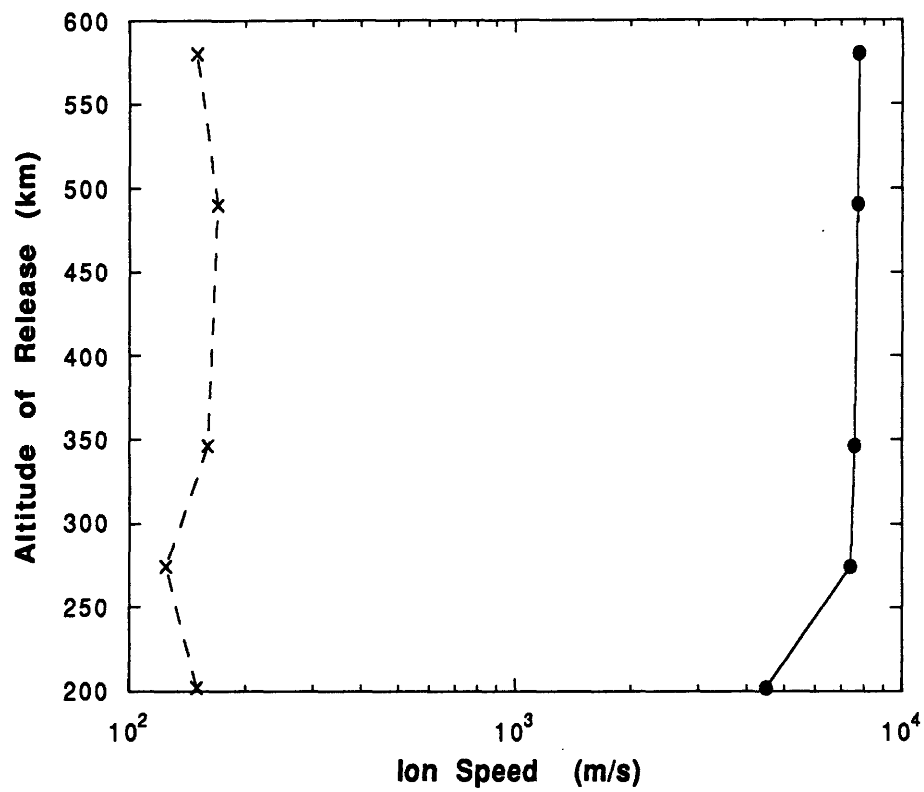

Figure 5.22: The **x** (solid line) and **y** (broken line) components of the contaminant ion velocity at the cloud center plotted against the altitude of the release. The cloud has central density of $N^{\circ}_{\mathrm{H_2O}} = 10^{18}\ \mathrm{m}^{-3}$ and $N^{\circ}_{\mathrm{H_2O^+}} = 10^{13}\ \mathrm{m}^{-3}$. The neutral cloud velocity is $\mathbf{U}_{\mathrm{H_2O}} = -8000\mathbf{x}$ m/s.

Chapter 6

Neutral Flow Model

In this chapter we describe the models used for the neutral flow. The problem of the neutral expansion in a rarefied environment is a subject that has been studied extensively. Two models are presented here. The first is suitable for the expansion of a gas released from a pulsed source, such as a thruster firing, or any type of deliberate or experimental release. The second describes the neutral flow originating from a moving source - such as outgassing from a spacecraft.

6.1 Neutral Gas Releases in a Rarefied Background

The release of neutrals in a rarefied background has been studied extensively from the very beginning of space flight. All expansions initially are in a continuum flow. Self-collisions between the release neutrals dominate the flow. This problem has been examined by *Freeman and Grundy* [1968] for expansion in vacuum and by *Brode and Enstrom* [1969]. As the gas expands self-collisions become rare and the flow is in a free-molecular regime (or collisionless). At latter times collisions with the background become important and the flow finally relaxes a diffusive state [*Bienkowski*, 1964; *Brook and Hamel*, 1972; *Baum*, 1973; *Bernhardt*, 1979].

A critical parameter in characterizing the behavior of released gases in a rarefied background is the equal mass radius α_o [*Baxter and Linson*, 1977]. It is defined as the length of a volume which contains mass of atmospheric molecules equal to the mass of the expanding cloud. If we denote by Q_r the number of released molecules with a mass of released molecule m_r then, the equal mass radius is

$$\alpha_o = \left(\frac{3m_r Q_r}{4\pi n_a m_a}\right)^{1/3} \tag{6.1}$$

If $\alpha_o \leq 3$, the gas will expand for at least 1.5 mean collision times before interactions with the background become significant.

The collision frequency between the released molecules and the ambient can be evaluated from the formula given in *Burgers* [1969].

$$\nu_{ra} = \frac{8}{3\pi} n_a \frac{m_a}{m_r + m_a} \sqrt{\frac{2kT_{ra}}{\mu_{ra}}} \sigma_{ra} \Phi_{ra}(\beta) \tag{6.2}$$

The reduced mass is $\mu_{ra} = m_r m_a/(m_r + m_a)$, the reduced temperature $T_{ra} = (m_a T_r + m_r T_a)/(m_r + m_a)$, and the cross section $\sigma_{ra} = \pi(r_r + r_a)^2$. The term Φ_{ra} is a correction factor to account for the velocity dependence of the collision frequency and depends on the parameter β defined as

$$\beta = \frac{U_r - U_a}{\sqrt{2kT_{ra}/\mu_{ra}}} \tag{6.3}$$

where U_r and U_a are the speeds of the release and ambient neutrals respectively. The expression for Φ is given in *Burgers* [1969] as

$$\Phi = \frac{3\sqrt{\pi}}{8}\left(\beta + \beta^{-1} - \frac{1}{4}\beta^{-3}\right) erf(\beta) + \frac{3}{8}\left(1 + \frac{1}{2}\beta^{-2}\right)\exp(-\beta^2) \tag{6.4}$$

The importance of the correction is evident for increasing values of β. From the definition of the ν_{ra} we can evaluate the mean free path neglecting for the moment the velocity correction term Φ_{ra} as

$$\lambda = \frac{3}{4} \frac{m_r + m_a}{m_a n_a \pi (r_r + r_a)^2} \tag{6.5}$$

We can now evaluate the ratio α_o/λ for typical release materials. The mass of the released material is shown in Table 6.1. In Figure 6.1 we plot the curves for which $\alpha_o/\lambda = 3$ versus the altitude and the amount of relased material, Q_r. The values are calculated with a typical ionosphere and temperature $T_r = T_a = 1000^o$ K. For release conditions above the curves the flow will pass through the free-molecular regime before

#Particles	Mass (kg)		
Q_r	H_2O	CO_2	Ba
10^{23}	0.003	0.0073	0.0225
10^{24}	0.03	0.073	0.25
10^{25}	0.3	0.73	2.25
10^{26}	3	7.3	22.5
10^{27}	30	73	225
10^{28}	300	730	2250

Table 6.1: Number of molecules of the released material Q_r and the corresponding mass in (kgr).

reaching to diffusive equilibrium. For releases of interest it is obvious that there will be an intervening free-molecular regime. The question then is for how long this free-molecular expansion will take place. An estimate comes from the average time between collisions. From the definition of the collision frequency it is given as $\tau_{ra} = \nu^{-1}$ sec. For the same ionospheric conditions as before the collision time is shown in Figure 6.2. For times scales of interest in contamination studies ($\sim 1 - 2$ sec) and for the altitudes of interest the neutral gas flow will be in a free-molecular stage.

6.1.1 Free Molecular Flow from a Pulsed Source

The model adopted here is a simplification of that developed by *Baum* [1972]. If f_r is the distribution function of the released neutrals, it will satisfy Boltzmann's equation

$$\frac{\partial f_r}{\partial t} + \mathbf{v} \cdot \frac{\partial f_r}{\partial x} = \nu_r(n_r\Phi_r - f_r) + \nu_{ra}(n_r\Phi_a - f_r) + \delta(\mathbf{x} - \mathbf{x}_s(t))Q_o(t)\Phi_s(\mathbf{v}) \quad (6.6)$$

where ν_r denote the self-collisions between the release molecules, and ν_{ra} the collisions between the release molecules and the background. The Maxwell distribution function is given by

$$\Phi(\mathbf{v}) = \left(\frac{m}{2\pi kT}\right)^{3/2} \exp\left[-\frac{m}{2kT}(\mathbf{v} - \mathbf{U})^2\right] \quad (6.7)$$

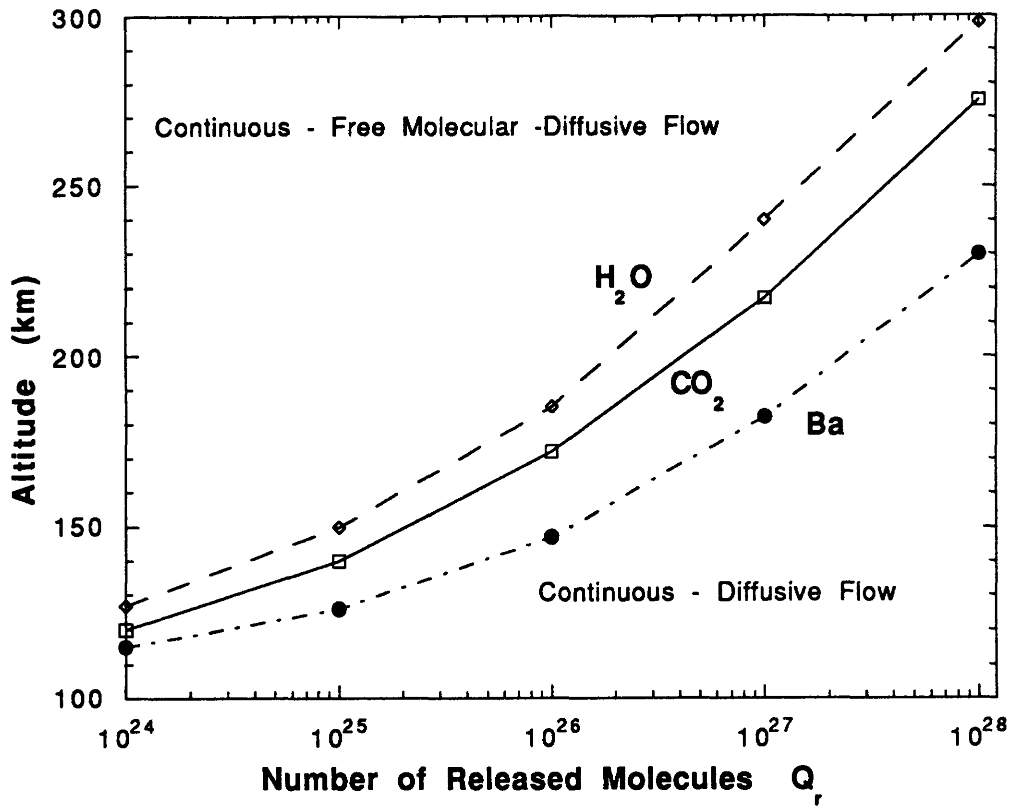

Figure 6.1: Flow regimes for H_2O, CO_2 and Ba released in the ionosphere. Curves are plotted for $\alpha_o/\lambda = 3$. Mid-latitude, summer, daytime conditions with neutral temperature of $T_r = T_a = 1000$ °K.

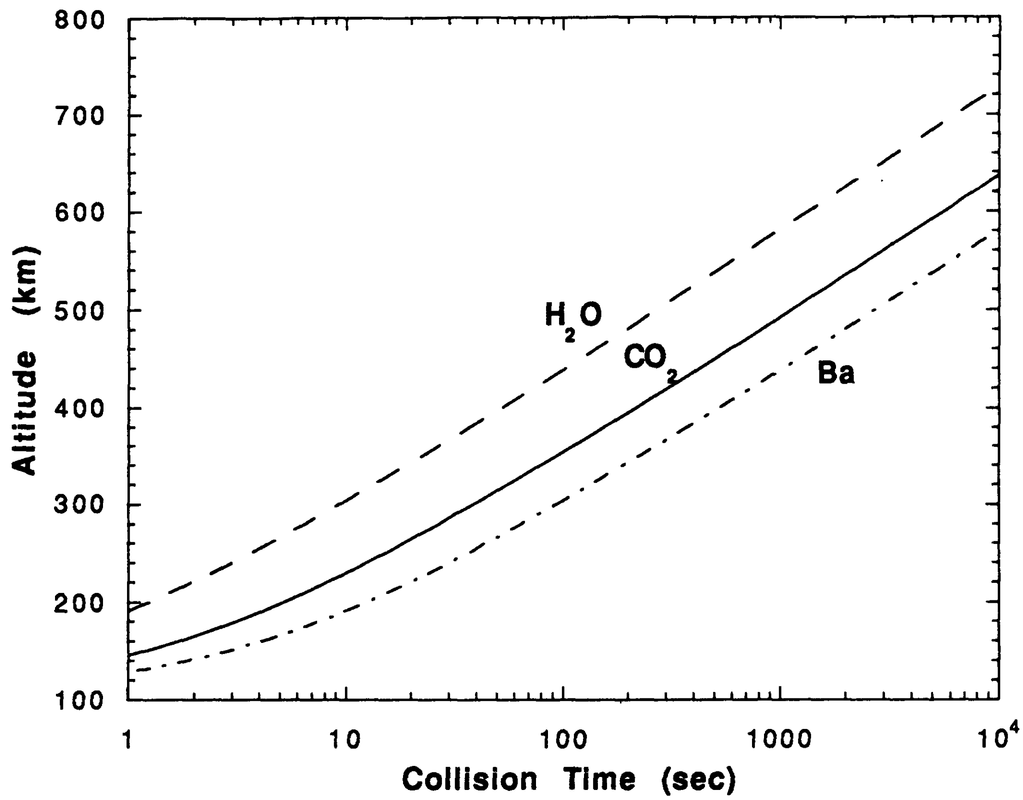

Figure 6.2: Collision times between released H_2O, CO_2 and Ba and the ionospheric neutrals. Mid-latitude, summer, daytime conditions with neutral temperature of $T_r = T_a = 1000$ °K.

The macroscopic velocities are denoted by $\mathbf{U}_a$, $\mathbf{U}_r$ and $\mathbf{U}_s$ for the ambient, the release and the source respectively. The parameter Q_o is the total particle flux emitted by the source which is assumed to operate for time t_o. The conditions at the point of release are prescribed by $\mathbf{U}_s$, T_s. For instance, for a nozzle they will be related with the properties at the nozzle exit.

A formal solution of (6.6) has been derived by *Baum* by taking the Fourier-Laplace transform of Eq. 6.6. In the solution three contributions were present. One comes from the free molecular flow which originates at the sourse; a second contribution is due to a correction of the self-interactions between the release molecules outside the region of the continuum flow; the third comes from the interaction of the free molecular flow with the atmosphere. The second contribution has been neglected being small. The interaction with the atmosphere is given in terms of integrals of the Green's function and for times which are much larger than the collision time, i.e, $T \gg \tau_{ra}$ it gives the diffusive flow. At early times $T < \tau_{ra}$ its contribution is similar to a free molecular flow.

All the velocities here are given in an absolute frame as shown in Figure 6.3. The velocity of the source is the orbital velocity $\mathbf{V}_o$. If the velocity of the released gas at the source with respect to the orbiting source is $\mathbf{U}'_s$ then in the absolute frame it is simply $\mathbf{U}_s = \mathbf{U}'_s + \mathbf{V}_o$. This is a useful reminder since for a thruster firing all of the quantities are given with respect to the nozzle exit. Note that the conditions designated by s should not be confused with those at the exit of the nozzle. They relate by the simple isentropic relations (see Chapter 8). The macroscopic velocity (in the absolute reference frame) of the gas is given by

$$\mathbf{U}_r = \frac{\mathbf{x}}{t} \tag{6.8}$$

and the density by

$$n_r(x,t) = \frac{Q_o t_o}{\pi^{3/2} t^3} \left(\frac{m}{2kT_s}\right)^{3/2} \exp\left[-\frac{m}{2kT_s}|\mathbf{U}_r - \mathbf{U}_s|^2\right] \tag{6.9}$$

If the source, e.g. the spacecraft, is located initially at $\mathbf{x}_o$ as shown in Figure 6.3, then after time t it has moved at $\mathbf{x}_s(t) = \mathbf{x}_o + \mathbf{V}_o t$. The free molecular flow has

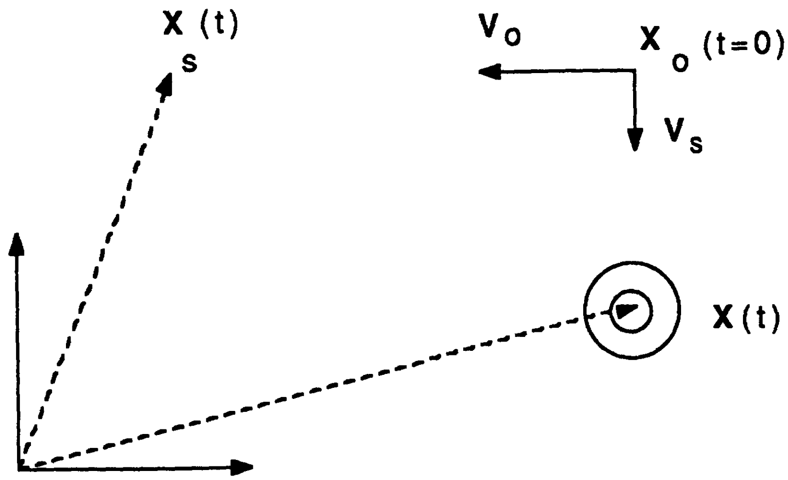

Figure 6.3: Coordinate system in the neutral flow from a pulsed source.

a radial velocity with its origin the point $\mathbf{x_o}$. The density at any time $t > t_o$ is spherically symmetric about the maximum located at $\mathbf{x}(t) = \mathbf{x_o} + \mathbf{U}_s t$ and decreases in magnitudes like $t^{-3}\exp(-t/t_{ra})$. In the example shown in Figure 6.3 the gas velocity at the source has a component equal and in opposite direction to the velocity of the spacecraft.

6.1.2 Diffusive Flow from a Pulsed Source

At times which are greater than the collision times the flow is in the diffusive regime. The density becomes asymptotically symmetric about the initial point of the release. The solution taken by *Baum* is re-written in the following form:

$$n_r(r,t) = \frac{Q_o t_o}{\left(4\pi t \frac{kT_a}{m\nu_a}\right)^{3/2}} \exp\left[-\left(\frac{r}{4kT_a t/m\nu_a}\right)^2\right] \tag{6.10}$$

where m is the reduced mass between the release neutral and the ambient. We denote the neutral diffusion coefficient by $\mathcal{D} = kT_a/m\nu_{ra}$. Then the density written in the above form can be recognized as the familiar solution in spherical coordinates to the

-isotropic- diffusion equation for point source, i.e., to the problem

$$\frac{\partial n}{\partial t} + \nabla \cdot (n_r \mathbf{U}_r) = 0$$
$$\mathbf{U}_r = -\mathcal{D}\frac{\nabla n_r}{n_r} \tag{6.11}$$

There have been more elaborate analytical and numerical models for the 3-D diffusion of neutrals [*Mendillo and Forbes* , 1978; *Bernhardt*, 1979a and b]. These authors have considered effects due to altitude dependent neutral winds, multi-species background, chemical reactions, as well as stationary and moving sources. It is not of interest to reproduce these results in this work. As we have already mentioned, the plasma model developed here could be easily coupled with any 3-D neutral flow model if accurate predictions for specific releases are to be made. It is suffice to examine here the order of magnitude of characteristic parameters in the diffusion regime.

The time scale associated with diffusion was discussed in the preceeding section. It is of the order of the collision time and is given by $\tau_D \sim 1.5\tau_{ra}$. We can obtain an estimate for the length scales of the neutral cloud if we define the diffusive radius of the cloud as $r_D = \sqrt{4\mathcal{D}_r t}$. In Table 6.2 we show typical values of the diffusion coefficient and the cloud radius at the diffusion time, τ_D. The diffusion time increases with altitude and molecular weight of the released material, as Figure 6.2. For instance H_2O at 200 km has $\tau_D \sim 6$ s while at 450 km $\tau_D \sim 150$ s. The important point

Altitude (km)	$\mathcal{D}$ (m^2/s)	$r_D(t = \tau_D)$ (km)
250	$\sim 10^6$	~ 5
350	$\sim 10^7$	~ 70
450	$\sim 10^8$	~ 240

Table 6.2: The diffusion coefficient $\mathcal{D}$ and the radius of the neutral cloud at $t = \tau_D$. Data are for H_2O release at different altitudes.

is that diffusion length scales are much larger than kilometer size. Large simulation regions are not unusual in numerical studies of diffusion (see the references above).

The common characteristic of these studies is that they were addressing large scale, late time phenomena associated with neutral releases. In our work we are interested in early time phenomena. More importantly, we want to resolve characteristics of the order of hundreds of meters rather than kilometer size. From a computational point of view it is not possible to simulate in three dimensions such large regions relevant to diffusion with the discreteness necessary for contamination studies. Neutral releases from orbiting spacecrafts will eventually relax to a diffusive state. However, at time scales of the order of τ_D the spacecraft is out of the region of the neutral cloud and there is no interest- from the contamination point of view- to simulate these late time events (late time being of the order of the diffusive time scale). However, for release experiments both the initial and the late time evolution of the cloud are often required.

6.2 Neutral Flow from a Continuum Source

We derive next a simple model applicable to outgassing or any continuous steady release of neutrals. Consider now the uniformly expanding spherically symmetric flow originating from a moving source. Assume that the neutrals originate on the surface of the source with radius R_s and are depleted through ionization and charge exchange reactions with time scales τ_i and τ_{cx} respectively. The continuity equation for the released neutrals is

$$\frac{1}{r^2}\frac{d}{dr}\left(r^2 U_r n_r\right) = -\frac{n_r}{\tau_i + \tau_{cx}} \tag{6.12}$$

The uniform velocity U_r is taken to be the thermal velocity given by

$$U_r = \sqrt{\frac{2kT_r}{\pi m_r}} \tag{6.13}$$

If the outgassing rate on the surface is given by Q (molecules/sec), the boundary condition applied is

$$Q = n(R_s) 4\pi U_r R_s^2 \tag{6.14}$$

The solution to (6.12) using the boundary condition is

$$n_r = \frac{Q}{4\pi U_r r^2} \exp\left[-\frac{r - R_s}{U_r(\tau_{cx} + \tau_i)}\right] \tag{6.15}$$

Chapter 7

Induced Plasma Environment: Numerical Simulations

In this chapter we present numerical simulations of the induced environment about a spacecraft. We begin with the identification of those spacecraft operations responsible for the creation of the contaminant plasma cloud. The H_2O and H_2O^+ are recognized as the major contaminant species. The chemistry within the water plasma cloud and the implications of the reaction times on the numerical stability are discussed. Parameters used in the numerical simulation are applicable to current and proposed spacecraft. Thruster firings and neutral releases at orbital speeds are investigated. The results are discussed and compared with observations and measurements taken on the Shuttle or during artificial release experiments.

7.1 The Origin of the Contaminant Cloud

There are several operations of a spacecraft which contribute to the creation of the induced contaminant environment. Outgassing from the spacecraft surfaces is one such operation. The rate of outgassing depends critically on the pre-flight conditions and is larger at the beginning of the flight. Another major source of contamination is the thruster firings. One more contribution to contamination comes from operations related to the management of power and life support systems. It is necessary to dispose amounts of liquids, usually water, for heat control, and dispose of water from power and life support systems. We reviewed in Chapter 1 the data from the Shuttle. It is the largest, active vehicle flown. We have pointed out that all the observations on the Shuttle recognized that the dominant contaminant neutral and ion in the induced environment was H_2O and H_2O^+. We review below the typical parameters of various Shuttle operations which generate the water plasma cloud. It will become apparent that the operations responsible for the generation of the induced environment are not unique to the Shuttle. Any large, active spacecraft, such as the proposed Space Station, will perform similar operations. In the simulations to follow we used typical parameters from the Shuttle operations but extended the altitude and latitude range in order to address other possible applications of interest.

The major source of the water plasma cloud about the Shuttle is the reaction control system (RCS) which consists of 38 primary (PRCS) and 6 vernier (VRCS) engines mounted in the front and rear of the vehicle which thrust in all possible directions. These thrusters operate on the reaction between mono-methylhydrazine (CH_3NHNH_2) as the fuel and Nitrogen Tetroxide (N_2O_4) as the oxidizer. The mean mass injection for these thrusters is 1410 g/s for the primaries and 41 g/s for the verniers [*Pickett et al.*, 1985]. The average exhaust velocity of the thruster plume is 3.5 km/s based on a temperature of 3000 °K. The total number of released neutral molecules depends on the duration of the firing and is in the range of 10^{25}-10^{26} for the PRCS and 10^{24}-10^{25} for the VRCS. Among the neutral species in the exhaust gas are H_2O, N_2, CO and H_2. The duration of the thruster firings varies from milliseconds to tens of a second; the number of firings also depends on the mission requirements but is very large. During the STS-3 mission, for example, there were over 40,000 thruster firings.

The other major source of water neutrals in the vicinity of the Shuttle is due to water dumps. This operation is one part of the water management of the orbiter and disposes of excess water generated by the fuel cells. This disposal is done in a nonpropulsive way over a specified period of times. During the STS 3 mission each water dump lasted almost an hour and had an average rate of 64 kg/hour.

Water is also released from thrust-balancing nozzles by the flash evaporator system (FES). These discharges of water are used for heat rejection and for the disposal of water from fuel cells. The water is discharged in a pulsed mode with a variable pulse rate. The direction of the velocity vector of the FES release is always perpendicular to the side surface of the Shuttle.

It is apparent that the above operations are not unique to the Shuttle. For instance, the proposed Space Station will necessary use attitude control thrusters on a much larger scale than the Shuttle. The requirements for the heat control, power and life support systems of the space station are expected to be the largest on any other spacecraft flown to date. Any other spacecraft with large power systems will have the potential of releasing neutrals and/or plasma into the ionosphere.

7.2 Chemistry within the Induced Environment

We model the chemistry of the water neutrals which originate in the vicinity of a spacecraft. Regardless the mode of the released of neutrals they will always have a differential velocity with respect to the ambient O neutrals. If, for example, the water molecules are outgassed, they originate with a velocity, in the absolute frame, which is the sum of the orbital velocity ($\sim$ 8 km/s) and the thermal velocity due to the temperature of the spacecraft. In the case of a thruster firing the released water neutrals will have the exhaust velocity plus the orbital. Thus the released neutrals sweep through the ambient plasma and interact chemically to form the contaminant plasma cloud.

For simplicity we shall consider a plasma cloud consisting of two components, namely, O^+ and H_2O^+ intermixed with a neutral cloud composed of O, H_2O, OH and H. The released H_2O sweeps through the ambient O^+ ions with energies up to 5 eV. Under such conditions ionic water is formed by the charge exchange reaction

$$O^+ + H_2O \overset{k_{cx}}{\rightleftarrows} O + H_2O^+ \tag{7.1}$$

Ionization of the released neutrals although small is included

$$H_2O \xrightarrow{\sigma_{\text{ion}}} H_2O^+ + e \tag{7.2}$$

The created ions are allowed to interact through recombination with the electrons with the following reaction

$$H_2O^+ + e \xrightarrow{k_{\text{rec}}} OH + H \tag{7.3}$$

The charge exchange reaction rate is taken to be $k_{\text{cx}} = 2.4 \times 10^{-15}$ m^3/s [*Bolden and Twiddy*, 1972]. The electron recombination reaction rate is taken to be $k_{\text{rec}} = 3 \times 10^{-13}$ m^3/s [*Murad and Lai*, 1986] and $\sigma_{\text{ion}} = 1.2 \times 10^{-5}$ s^{-1} [*Bernhardt*, 1987]. .

The model developed in Chapters 2 and 3 is applied. The released ions and neutrals referred in the theory by r^+ and r are taken as $r \equiv H_2O$ and $r^+ \equiv H_2O^+$. Similarly, for the ambient ions we take $a^+ \equiv O^+$ and $a \equiv O, H, He$. The density of any species t is denoted by N_t.

We begin with the continuity equations (2.1). The production or loss terms in the continuity of H_2O^+ ions due to chemical reactions are

$$\begin{aligned} S^{\text{cx}}_{H_2O+} &= N_{O+} k_{\text{cx}} N_{H_2O} \\ S^{\text{ion}}_{H_2O+} &= \sigma_{\text{ion}} N_{H_2O} \\ S^{\text{rec}}_{H_2O+} &= -N_{H_2O+} k_{\text{rec}} N_e \end{aligned} \tag{7.4}$$

The loss term in the continuity equation of the ambient ions O^+ is

$$S^{\text{cx}}_{O+} = -N_{O+} k_{\text{cx}} N_{H_2O}$$

The momentum equations for the plasma species are those presented in Chapter 2.3. We included the term $\mathbf{R}_i^b$ to account for momentum transfer due to reactive collision of the ion $i = H_2O^+$ or O^+ in reaction $b = \text{cx}, \text{rec}, \text{ion}$. In general, for the ion i created or lost in a reaction b, the momentum transfer operator has the form

$$\mathbf{R}_i^b = \frac{S_i^b}{N_i}(\mathbf{V}_i - \mathbf{V}_i^b) \tag{7.5}$$

where S_i^b is the rate of production or depletion of the i-th ion in the reaction b and $\mathbf{V}_i^b$ is the velocity with which the ion is created or lost in the reaction. Clearly, with this definition of the momentum operator, there is no average momentum lost for those ions which are depleted in the reactions considered, since these ions are lost with their average velocity. Thus, in the charge exchange reaction the momentum of the O^+ is not changed. Similarly, in the electron recombination the momentum of the H_2O^+ stays the same. However, for the ions which are created it is important to establish the velocity with which they leave the reactions. In the charge exchange reaction we assume that the water ions are created with the water neutral velocity, so $\mathbf{V}^{cx}_{H_2O+} = \mathbf{U}_{H_2O}$. In the ionization reaction we assume that the created water ions keep the bulk velocity of the water neutrals, so that we can write $\mathbf{V}^{ion}_{H_2O+} = \mathbf{U}_{H_2O}$. We can write then the momentum transfer operators due to reactive collisions as follow

$$\mathbf{R}^{cx}_{O+} = 0 \tag{7.6}$$

$$\mathbf{R}^{cx}_{H_2O} = \frac{N_{O+} k_{cx} N_{H_2O}}{\mathrm{N}_{H_2O+}}(\mathbf{V}_{H_2O+} - \mathbf{U}_{H_2O}) \tag{7.7}$$

$$\mathbf{R}^{rec}_{H_2O+} = 0 \tag{7.8}$$

$$\mathbf{R}^{ion}_{H_2O+} = \frac{\sigma_{ion} N_{H_2O}}{\mathrm{N}_{H_2O+}}(\mathbf{V}_{H_2O+} - \mathbf{U}_{H_2O}) \tag{7.9}$$

Then the collision frequencies due to chemical reactions are

$$\begin{aligned}
\nu^{ion}_{O+} &= 0 \\
\nu^{cx}_{H_2O+} &= \frac{N_{O+} k_{cx} N_{H_2O}}{N_{H_2O+}} \\
\nu^{ion}_{H_2O+} &= \frac{\sigma_{ion} N_{H_2O}}{N_{H_2O+}}
\end{aligned} \tag{7.10}$$

From the definition of the total collision frequencies Eq. (2.6) they are given as

$$\nu_{O+} = \sum_n \nu_{O+,n} + \nu_{O+,H_2O} + \nu_{O+,H_2O+} + \nu_{O+,e} \tag{7.11}$$

$$\nu_{H_2O+} = \sum_n \nu_{H_2O+,n} + \nu_{H_2O+,H_2O} + \nu_{H_2O+,O+} + \nu_{H_2O+,e} + \nu^{cx}_{H_2O+} + \nu^{ion}_{H_2O+} \tag{7.12}$$

$$\nu_e = \sum_n \nu_{e,n} + \nu_{e,H_2O} + \nu_{e,H_2O+} + \nu_{e,O+} \tag{7.13}$$

7.2.1 Implications of Chemistry on Numerical Stability

The source and loss terms that appear in the continuity equations play a crucial role in the stability of the numerical solution. In Chapter 4 we derived the maximum time step for stability in the absence of such terms. To examine the role of the source/loss terms we begin with the charge exchange equation. If we ignore transport, then the rate of change of the O^+ is given by

$$\frac{\partial N_{O^+}}{\partial t} = -N_{O^+} k_{cx} N_{H_2O} \tag{7.14}$$

The solution to the above is given by

$$N_{O^+}(t) = N_{O^+}(t=0) \exp\left(-k_{cx} N_{H_2O} t\right) \tag{7.15}$$

For a simple explicit forward time integration scheme stability requires that

$$\Delta t \leq \frac{2}{k_{cx} N_{H_2O}} = 2\tau_{cx} \tag{7.16}$$

where we define the charge exchange reaction time by $\tau_{cx} = 1/k_{cx} N_{H_2O}$. For the range of densities of interest Table 7.1 gives the time step for stability. As the reaction

N_{H_2O} (m^{-3})	τ_{cx} (sec)	Δ t
10^{12}	4.082×10^{2}	8.16×10^{2}
10^{14}	4.082×10^{0}	8.16
10^{16}	4.082×10^{-2}	8.16×10^{-2}
10^{18}	4.082×10^{-4}	8.16×10^{-4}

Table 7.1: Maximum time step for stability due to the charge exchange reaction

time becomes smaller the required time step becomes very small, thus demanding considerable computational time.

We consider next the depletion of H_2O^+ in the recombination reaction (7.3). Using the same arguments as above the reaction time is given by

$$\tau_{rec} = \frac{1}{k_{rec} N_e} \tag{7.17}$$

In Table 7.2 the maximum Δt for conditions anticipated is shown. The electron densities are chosen so that we account for both depletions or enhancements of the ambient

N_e (m^{-3})	τ_{rec} (sec)	Δ t
10^{10}	6.68×10^{2}	1.336×10^{3}
10^{11}	6.68×10^{1}	1.336×10^{2}
10^{12}	6.68×10^{0}	1.336×10^{1}
10^{13}	6.68×10^{-1}	1.336×10^{0}
10^{14}	6.68×10^{-2}	1.336×10^{-1}

Table 7.2: Maximum time step for stability due to the electron recombination reaction

plasma. The slow electron recombination does not impose any serious constraint on the computational time. Even in a case of a three order of magnitude enhancement in the plasma content the time step is well within a reasonable computational time.

Finally, we examine the loss of H_2O due to ionization. In general, for any ionization reaction the ionization time is $\tau_{\rm ion} = 1/\sigma_{\rm ion}$. For H_2O it is $\tau_{ion} \sim 10^5$ sec. Indeed, ionization of water is extremely slow; thus, there is no practical limitation on the time step.

The above analysis implies that the charge exchange reaction is the one that imposes practical constraints on the time-step.

7.3 Radiation within the Induced Environment

The dissociative recombination reaction (7.3) produces OH radicals which are in excited electronic states. These radicals may emit radiation and produce airglow. For the OH produced in the reaction an estimate of 10% will be in the $OH(A^2\Sigma)$ excited state [*Anderson and Bernhardt*, 1978]. We consider only emissions from the transition from the lowest level $A^2\Sigma$ electronic state to the lowest level ground state $X^2\Pi$ according to

$$\mathrm{OH}(\mathrm{A}^2\Sigma, \mathrm{v}' = 0) \xrightarrow{A_{303.6}} \mathrm{OH}(\mathrm{X}^2\Pi, \mathrm{v}'' = 0) + \mathrm{h}\nu \tag{7.18}$$

The Einstein constant is $A_{306.4} = 1.17 \times 10^6$ sec^{-1}. The emitted radiation has a wavelength of 306.4 nm wavelenghth (UV band) and has been measured during the Waterhole release experiments by *Yau et al.* [1985].

The continuity equation of the excited OH radicals is

$$\frac{dN_{\mathrm{OH}}}{dt} = \frac{1}{10} k_{\mathrm{rec}} N_{\mathrm{H_2O^+}} N_e - A_{302.6} N_{\mathrm{OH}} \tag{7.19}$$

From the number density of the excited radicals the volume emission rate $\epsilon_{306.4}(x, y, z\ t)$ (in photons/m^{3}s) can be calculated by

$$\epsilon_{306.4}(x, y, z; t) = A_{302.6} N_{\mathrm{OH}} \tag{7.20}$$

From the volume emission rate we can integrate along a path (line of sight of an instrument for example) and calculate the integrated volume emission rate, i.e., the column emission rate or intensity. In this study we integrate along the **z** direction as,

$$I_{306.4}(x, y; t) = \int \epsilon_{306.4}(x, y, z; t) dz. \tag{7.21}$$

The calculated intensity I is given in units of Rayleighs (1R=10^{10} photons/m^{2}s).

7.4 Thruster Firings from Spacecraft

We present below numerical results from thruster firings simulations. It is assumed that H_2O neutrals are released in a pulsed mode with a specified flow rate. The neutrals expand in a free molecular fashion; their flow is modeled according to the theory presented in Chapter 6. Using typical parameters from the RCS thrusters of the Shuttle it is assumed that the number of release molecules of H_2O is 10^{24}. The neutral (or source) velocity at the release point -in the reference frame of the spacecraft- is denoted by $\mathbf{U}'_s$; in the absolute frame is given by $\mathbf{U}_s = \mathbf{U}'_s + \mathbf{V}_o$ with $\mathbf{V}_o$ to denote the velocity of the spacecraft. The source conditions can be determined by the exit conditions at the nozzle by the use of simple isentropic relations. We recall that according to the flow model described in Chapter 6 this is the regime of the continuum flow outside the exit. For instance, the source velocity and temperature are given in terms of the exit conditions by

$$U_s = U_e\left(\frac{1}{\gamma M_e^2}+1\right) \tag{7.22}$$
$$T_s = T_e\frac{\gamma M_e^2+(\gamma-1)/2}{1+\gamma M_e^2}$$

where M_e is the exit Mach number and γ is the specific heat ratio at the exit. The direction of a velocity vector in the absolute frame (x, y, z), which is also the computational domain, is given by the polar angle $\theta_{o,s}$ measured from the xz plane, and the cone angle $\phi_{o,s}$ measured from the z axis; the subscripts denote the orbital or the source velocity respectively. There are several effects investigated in the simulations. Three different altitudes were considered, 250, 450 and 600 km at mid-latitude and high-latitudes. The altitude and latitude range span most of the applications of interest. The source velocity also varied in order to investigate the effects of orientation of the source velocity with respect to the **B** field. In Table 7.3 the parameters used in the computations are shown. We discuss extensively results that represent typical simulations. We discuss the qualitative and quantitative features of the induced envi-

Altitude (km)	Latitude	$\mathbf{V}_o$			$\mathbf{U}_s'$		
		θ_o^o	ϕ_o^o	$\lvert\mathbf{V}_o\rvert$(km/s)	θ_s^o	ϕ_s^o	$\lvert\mathbf{U}_s'\rvert$(km/s)
250	45,90	-180	0	8	0	0	2
					0	45	3.1
450	45,90	-180	0	8	0	0	2
					0	45	3.1
650	45	-180	0	8	0	0	2

Table 7.3: Parameters for thruster firing simulations.

ronment which *affect* the operation of the spacecraft and can also be *measured*, such as density and velocity of the plasma species, the electrostatic potential, and radiation emission. All results are plotted at a time $t = 0.25$ s after the release. Given that the gyroperiod for the H_2O^+ and O^+ is $\Omega^{-1} \sim 5$ ms the time of 0.25 s corresponds to almost 37 gyroperiods. This is enough time so that substantial drift occurs. At the same time the spacecraft has moved 2 km away from the release point.

7.4.1 Altitude of $h = 250$ km

Case 1: Mid-latitude, $\theta_s = 0°$, $\phi_s = 0°$

We begin with the discussion of results obtained from the simulation of a thruster firing in the anti-orbital velocity. The source velocity of water is $\mathbf{U}'_s = 2000\mathbf{x}$ m/s. In the absolute frame this is a velocity of $\mathbf{U}_s = -6000\mathbf{x}$ m/s.

The force which dominates the dynamic evolution is that due to the motion of the released neutrals, i.e., $\mathbf{F}_n = m_n \nu_{in} \mathbf{U}_n$. In Figure 7.1 we plot the neutral density and the associated velocity vector field. The neutrals initiated at the moment of the pulse of the thruster at $t = 0$ have formed a spherical cloud according to the theory presented in Chapter 6. The maximum density of the neutral cloud travels with the velocity of $\mathbf{U}_s = -6000$ m/s; at $t = 0.25$ s the maximum density is 1.29×10^{16} m^{-3} and is located 1500 m from the origin. This lies at a distance of 500 m behind the spacecraft. The velocity field is that of a radial source located at the origin and expanding in a free molecular fashion.

In Figure 7.2 the formation of the H_2O^+ cloud is shown. On the plane of the release the maximum density is located at about 1000 m from the origin and has a value of 2.72×10^{11} m^{-3} (Figure 7.2(Bottom)). The cloud is extented in the direction of the neutral wind. It shows elongation in the front side and steepening in its back side due to the pile-up of density, a common feature present in numerous 2-D numerical simulations. The cloud is shown to be asymmetric and to be denser in the $\mathbf{U}_{H_2O} \times \mathbf{b}$ direction [*Eccles et al*, 1989]. This preferential pile-up of density is due to momentum transfer and can be explained by looking at the velocity field in the same figure. The velocity field on the release plane shows the effects of the applied neutral wind, diffusion and the ambient electric field; the detail physics of the process has been explained in Chapter 5. The diffusion gives a clockwise rotation to the H_2O^+. There is an additional small unidirectional drift due to the ambient transverse electric field. The significant drift of the cloud is due to the applied neutral wind. The maximum velocity vector on the release plane is 451 m/s and is located in the front side of the plasma cloud where the dense portion of the neutral cloud is located. A simple analysis of the response of a plasma to an applied neutral force $\mathbf{F}_n = m_n \nu_{in} \mathbf{U}_n$ can be obtained from the model equations of Chapter 2 by neglecting charged particle collisions. The transverse velocity then reduces to

$$\mathbf{V}_{\perp t} = \frac{1}{1+k_t^2}\mathbf{U}_{\perp n} + \frac{k_t}{1+k_t^2}\mathbf{U}_{\perp n} \times \mathbf{b} \tag{7.23}$$

where the usual notation is used and $k_t = \Omega_t/\nu_t$. If by $\mathbf{n}$ we denote the direction of the neutral wind, then the ratio of the transverse velocity components is

$$\frac{|\mathbf{V}_{\perp t}^{\mathbf{n}}|}{|\mathbf{V}_{\perp t}^{\mathbf{n}} \times \mathbf{b}|} = k_t \tag{7.24}$$

The magnitude of the induced velocity can also be evaluated from Eq. (7.23) and is given by $V_{\perp t} = (1/1 + k_t^2)^{1/2} U_n$. For small collisionality ratio, i.e., $k_t \ll 1$, both ions and electrons drift with the velocity of the neutral wind; thus no currents are produced within the plasma. In the opposite limit, i.e., $k_t \gg 1$, ions and electrons drift along $\mathbf{n} \times \mathbf{b}$ but in opposite directions; subsequently, there is current flow in the plasma. Following the same arguments, for any arbitrary collisionality ratio there will be current flow in the plasma with the ions gaining a velocity component in the $\mathbf{n} \times \mathbf{b}$ direction. We can also verify that a denser neutral cloud will induce larger drifts since k_t will become smaller (since the collision frequency scales with the neutral density). The above treatment, although simple, does explain the rotation that the ions exhibit in Figure 7.2. In the front side of the plasma cloud the neutral density is larger but still such that $k_t > 1$. Thus, the component along the $\mathbf{n} \times \mathbf{b}$ direction dominates and is added to that due to the diffusion.

The density and ion velocity on a plane 600 m away from the midplane are shown in Figure 7.2(Top). The maximum density is an order of magnitude less than the release plane and the cloud has a more symmetric structure. The neutral wind force is smaller at that plane, since the neutral density drops. The ion velocity shows similar effects as in the release plane but with reduced magnitudes (the maximum is 103 m/s.)

We investigate next the induced perturbations on the ambient plasma. In Figure 7.3 we demonstrate that the O^+ ions form a "hole", a depletion region of kilometer size. The ratio of the density at the minimum to that of the ambient is defined as the strength of the hole $[O^+]_{min}/[O^+]_{amb} = 0.07$. The formation of the depletion is a direct effect of the charge exchange reaction. The symmetric structure of the depletion on the release plane implies that chemistry controls the dynamics of the ambient ions. However, chemistry alone is not responsible for the structure of the "hole": plasma transport plays a key role. The transverse velocity of the ambient has a maximum of 391 m/s on the release plane. The region of the ambient plasma that is forced by the neutral wind exhibits a rotation. Outside of the neutral cloud the ambient ions simply $\mathbf{E}_{\perp o} \times \mathbf{B}$ drift due to the ambient electric field with substantial reduced speeds. The ambient perturbation develops enhancement and depletion regions as we move away from the release plane. On the plane 600 m away from the midplane the strength of the hole is $[O^+]_{min}/[O^+]_{amb} = 0.92$ while the strength of the enhancement is $[O^+]_{max}/[O^+]_{amb} = 1.05$. The drift shows an increase in the center with a maximum of 89 m/s. As we explained in Chapter 5, the dipole field which is established in the release plane due to the action of the neutral wind is mapped along the magnetic field lines and is responsible for the converging flow presented in Figure 7.3(Top).

We will investigate next the parallel plasma flow, a manifestation of the 3-D effects captured in our computations. In Figure 7.4 we plot the density and velocity of the H_2O^+ on the plane (y,z) passing through the cloud's center. We showed in Chapter 5 how the establishment of the Boltzmann potential is associated with the density gradient along $\mathbf{B}$. The cloud shows that it has expanded along $\mathbf{B}$. The velocities along $\mathbf{B}$ (see Figure 7.4(Bottom)) are much larger than the transverse drifts and have a maximum of 1682 m/s. The motion along the field lines depicts the compound effects of diffusion and the parallel component of the neutral force. Recall that the neutrals expand radially from the origin as Figure 7.1(Bottom) shows. We will examine the response of a plasma to an applied parallel force by simplifying the equations of

Chapter 2. The parallel component of the ion velocity is

$$V_{\|r^+} \simeq \frac{\nu_{r+r}}{\nu_{r+r} + \nu_{r+a}} U_{\|r} + \frac{\nu_{r+a}}{\nu_{r+r} + \nu_{r+a}} U_{\|a} \tag{7.25}$$

where a denotes the ambient neutrals. If we scale the collision frequencies with the neutral densities it is apparent that for $N_r \gg N_a$ the ions drift with the applied neutral wind. The parallel flow field is not symmetric. In the region located in the back side of the cloud the velocity is reversed and plasma is shown to converging to the release plane. At the location of the minimum of the depletion region the H_2O^+ ions are accelerated towards the center of the ambient hole.

The parallel density and velocity of the O^+ ions are shown in Figure 7.5. The density shows the formation of both depletion and enhancement regions (Figure 7.5(Top)). The depletion region is formed due to the loss of O^+ in the charge exchange reaction and due to transport. The O^+ ions adjacent to the depletion region are accelerated towards the "hole" in the back side of the depletion as is depicted in Figure 7.5(Bottom). In the front side the ions are pushed away due to the effect of the the Boltzmann potential. In addition, the ambient ions are experiencing the contaminant neutral wind. The O^+ accelerated by the Boltzmann potential and the parallel component of the neutral wind are pushed to the limbs of the cloud and are piled-up. This is a manifestation of the electrostatic "snow-plow" effect. The maximum expansion velocity is 1115 m/s and is experienced as an inflow towards the "hole".

As we discussed in previous chapters, the presence of the plasma cloud leads to the generation of electric field perturbations; the electrostatic potential induced by the presence of the plasma cloud are plotted in Figure 7.6. On the release plane the potential shown in Figure 7.6(b) is the combination of the diffusion field due to the density gradients of the cloud and the dipole due to the action of the neutral wind (see Chapter 5). Note that the neutral force $\mathbf{F}_{H_2O}$ is almost unidirectional, thus establishing a dipole perturbation field. The mapping process is also demonstrated in this simulation. In Figure 7.6(a) we plot the potential 178 km below the release (recall that positive points downwards in the northern hemisphere). Thus, the electric field has been effectively mapped down to the E region with a relative small attenuation with respect to the release plane. The electric field is also mapped to the the upper F region without attenuation as Figure 7.6(c) shows.

Another important parameter is the electron density (often referred to as plasma density). Figure 7.7 shows the plasma density on several transverse planes throughout the computational domain. On the release plane we see the formation of depletion and enhancement regions (Figure 7.7(d)). The electron density is calculated from the quasineutrality condition, $N_e = N_{H_2O^+} + N_{O^+}$; electrons are also lost due to the recombination with the H_2O^+. From the reaction times evaluated in the previous section, and for ion densities predicted here the recombination time is larger than the charge exchange time by almost two orders of magnitude. It is then transport mechanisms that account for the formation of the electron perturbation (via the establishment of the ambient and contaminant density perturbations). Due to the fact that the maximum of the created ions and the "hole" are not co-located, the enhancement is to the side of the maximum of the ion cloud. The rest of the plots in Figure 7.7 show the effect of the induced plasma motion in the ambient plasma. This is a direct consequence of the electric field mapping and clearly shows the phenomenon of "image-formation", i.e., ambient plasma density perturbations. In the E and upper F regions (Figure 7.7(a) and (f) respectively) the appearance of the ripples is the manifestation of the plasma motion induced there.

Finally, Figure 7.8 presents the height integrated UV radiation intensity. It shows that a kilometer size area of UV emission is formed. The maximum intensity is 495 R and is located almost 1000 m behind the spacecraft. The volume emission rate has a structure similar to that of the ion cloud since it is calculated through the recombination reaction of the created H_2O^+.

Case 2: Mid-latitude, $\theta_s = 0^o$, $\phi_s = 45^0$

We continue the discussion with simulation results from a thruster firing with an angle to the orbital velocity. The velocity of the neutrals at the time of the thruster firing is $\mathbf{U}'_s = 2\mathbf{x} + 2.4\mathbf{z}$ km/s. There is a large directional velocity along the **B** lines and it is of interest to investigate such effects.

The neutral gas at $t = 0.25$ s after the firing is shown in Figure 7.9. The maximum of the H_2O density is away from the release plane and is located at $(x = -1500, y = 0, z = 600)$ m plane. The velocity field is similar to that of the simulation just discussed but the neutral force is changed significantly due to change in the neutral density $N_{H_2O}(\mathbf{r},t)$.

The formation of the H_2O^+ cloud is shown in Figure 7.10. On the plane 600 m away from the release plane the cloud shows a maximum density of 2.17×10^{11} m^{-3} (see Figure 7.10(Bottom)). The velocity field is associated with the diffusive clockwise drift, the drift due to the neutral wind and the ambient electric field; the maximum speed is 382 m/s. In the front side of the moving cloud the velocity is mainly due to the contaminant neutral force. On the release plane shown in Figure 7.10(Top) the H_2O^+ cloud is broken in two parts. The maximum density on the release plane is $\sim 10^{10}$ m^{-3} and the maximum velocity is 77 m/s.

In Figure 7.11 we plot the density and the velocity field of H_20^+ on the (x,y=0,z) midplane. The plasma cloud has the characteristics of a plume that expands along $\mathbf{B}$. The maximum of the H_2O^+ density is located on the plane of the maximum neutral density 600 m from the release plane. The velocity field is far from been symmetric, as it was in Case 1. There are two contributions to the parallel flow, as before. The first is due to the diffusive expansion along the $\mathbf{B}$ lines. The second is due to the large component of the neutral force along the $\mathbf{z}$ direction. This enhances the velocities and is directed mainly along $\mathbf{z}$ as Figure 7.11(Bottom) shows. The maximum parallel velocity is also enhanced, in comparison with Case 1 release, and reaches 2395 m/s.

The development of the density perturbation in the O^+ is shown in Figure 7.12 for the $z = 600$ m (Top) and the release plane (Bottom). The depletion formed on a plane at about $z = 600$ m from the release has a strength of 0.25. The velocity field of the O^+ is due to the ambient field outside of the cloud. In the front region of the cloud the O^+ develops drifts similar to those of the H_2O^+ ions with a maximum velocity of 338 m/s. On the release plane the "hole" is much weaker due to the limiting contribution of charge exchange, and the O^+ ions are mostly experiencing an $\mathbf{E} \times \mathbf{B}$ drift. Along the magnetic field lines the structure of the O^+ perturbation is very different from the previous case (compare Figure 7.13 with 7.5). There is a depletion region and an enhancement with a very steep density gradient separating them as Figure 7.13(Top) shows. This density pile-up is again a result of the "snow-plow" effect. The minimum of the O^+ is almost 300 m away from the maximum of the neutral density, i.e., the plane at $z = 600$ m where destruction through charge exchange peaks. Thus, transport plays a crucial role in determining the evolution of the perturbation. The strength of the "hole" produced is $[O^+]_{min}/[O^+]_{amb} \simeq 0.19$; thus the ability to produce a "hole" has weakened in comparison with the previous case. The parallel velocity of the O^+ ions (Figure 7.13(Bottom)) show that there is a unidirectional flow in the positive $\mathbf{z}$ direction with a maximumm of 2153 m/s. This can be explained by noting that below the release plane the O^+ ions are accelerated towards the density minimum. Above the release plane the ambient ions are experiencing a large neutral force component along the $\mathbf{z}$. Note also that the region with the faster expanding ions coincides with that of the neutral cloud. This implies that the large parallel neutral force component dominates the evolution of the plasma cloud.

The integrated intensity of the UV radiation emission is shown in Figure 7.14(Bottom). The pattern is similar to the case before but the maximum intensity is now 555 R. The volume emission rate (in photons/m^{3}s) is plotted on a midplane (x,y=0,z) and depicts the structure of a plume (Figure 7.14(Top)). Thus, intensities calculated along other than lines of sight along the magnetic field will exhibit significant variation.

7.4.2 Altitude of $h = 450$ km

Case 3: Mid-latitude, $\theta_s = 0°$, $\phi_s = 45^0$

We investigate next the effects of altitude on the induced environment. We present results from a thruster firing at an angle to the orbital velocity and at altitude of 450 km, a situation applicable to the proposed Space Station. The source velocity at the release point is $\mathbf{U}'_s = -6000\mathbf{x} + 2400\mathbf{z}$ m/s and the thruster flow rates are similar to Cases 1 and 2 presented above.

In Figure 7.15 the formation of the H_2O^+ cloud is shown. The maximum density is located on a plane 600 m away from the release plane. Although the features of the ion cloud are similar to those for the 250 km simulation (Case 2) the density maximum is smaller and reaches 1.1×10^{11} m^{-3}. This can be attributed to the smaller production of ions through charge exchange due to the limited availability of O^+ at this heigher altitude.

The density and velocity along **B** of the H_2O^+ ions are shown in Figure 7.16. The cloud develops the plume characteristics as Figure 7.16(Top) depicts. The cloud expands along **B** much faster than in Case 2. The maximum parallel velocity has reached 5379 m/s. The increased parallel ion mobilities at higher altitudes result in the faster expansion of the plasma cloud.

The ambient ions shown in Figure 7.17(Top) depict the formation of the depletion and enhancements regions. The minimum of the depletion is located now on the 600 m plane where the density maximum is located. On that plane the strength of the "hole" is $[O^+]_{min}/[O^+]_{amb} \simeq 0.19$. This is of the order of the strength for the 250 km firing. The pile-up of the ambient ions in the direction of the neutral force causes a steep gradient to form at the edges of the plume as shown in Figure 7.17 (Top). The relative strength of the maximum becomes $[O^+]_{max}/[O^+]_{amb} \simeq 1.1$. The ambient plasma velocity is shown in Figure 7.17(Bottom). The ions mostly exhibit a unidirectional flow, a pattern explained by the neutral force and the filling in of the "hole" by the ambient plasma.

The induced flow on the ambient plasma produces plasma density perturbations as it was shown in Cases 1 and 2. Figure 7.18 shows the electron densities at three different layers. On the release plane there is a formation of a depletion and enhancement region, i.e, an "image" cloud. The density maximum coincides with the maximum of the H_2O^+ shown in Figure 7.15(Top). Due to the mapping of the electric field, similar "image" clouds are formed throughout the ionosphere. Figure 7.18(a) presents the development of plasma density perturbation on a plane at the E region while Figure 7.18(b) shows the image cloud formation on a plane located on the upper F region.

Finally, the radiation emission pattern shows similar qualitative characteristics as the release at lower altitudes but with significantly reduced intensities. The UV emission maximum intensity becomes 180 R. This can be attributed to the reduced production of the OH due to lower ionic densities.

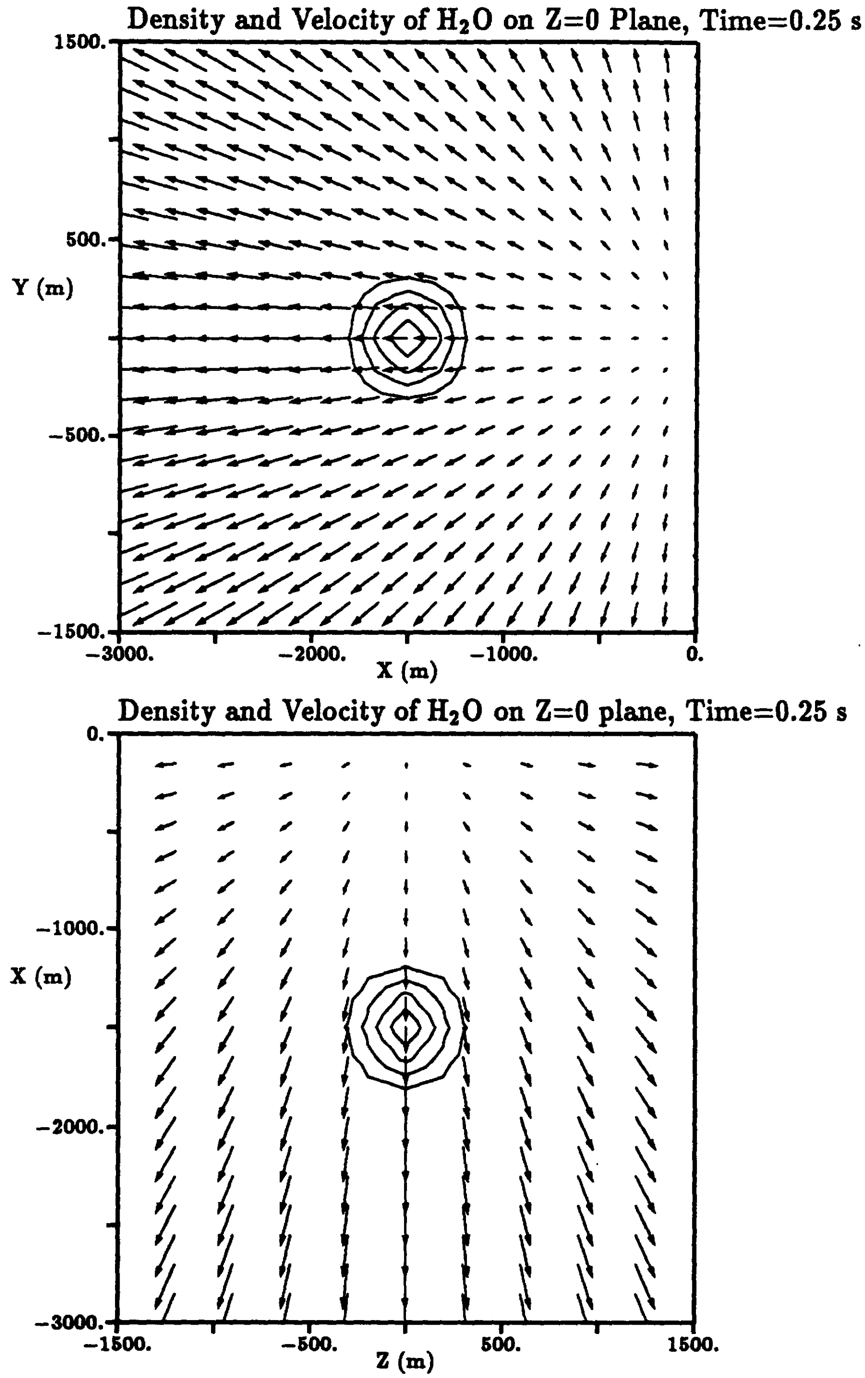

Figure 7.1: Density and velocity of H_2O 0.25 s after the release. (Top) On the plane of maximum density (x,y,z=600) m. (Bottom) On the midplane (x,y=0,z). The maximum neutral density is 1.29×10^{16} m^{-3}. Thruster firing at h = 250 km, $\mathbf{U}_s = -6000\mathbf{x}$ m/s, $\mathbf{V}_o = -8000\mathbf{x}$ m/s.

Contaminant Ions Time=0.25 s

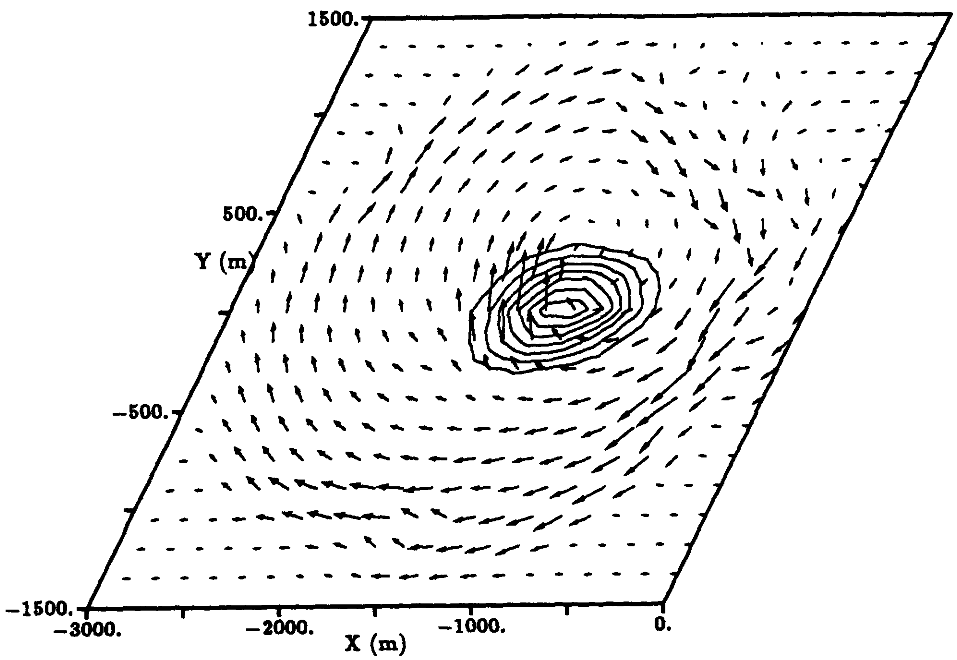

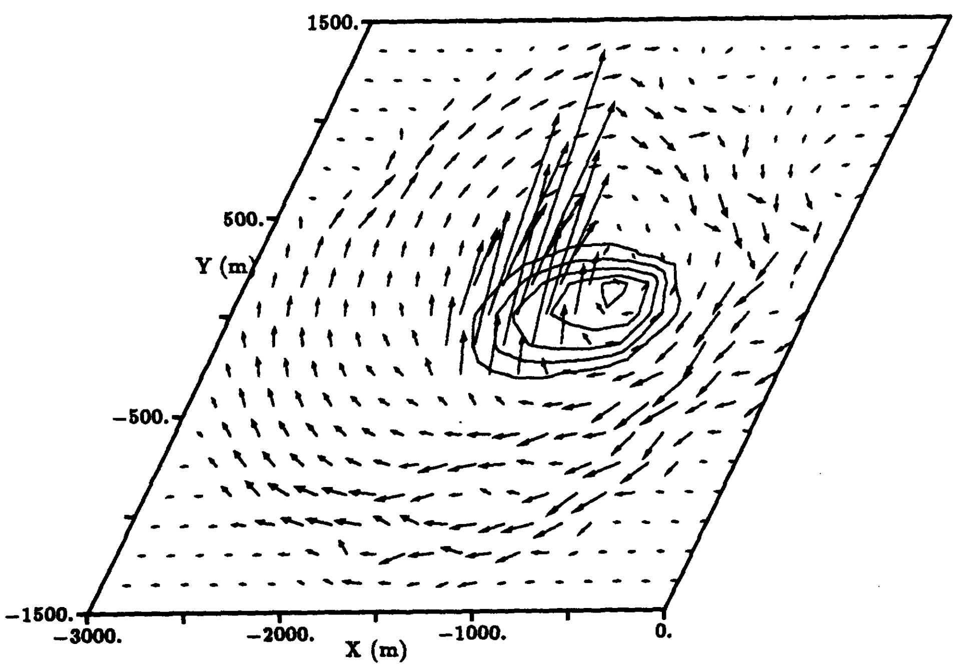

Figure 7.2: The density and velocity of the H_2O^+ ions 0.25 s after the release. (Top) The (x,y,z=600) m plane; contour separation is 0.04 and max=0.3; the maximum velocity vector is 103 m/s. (Bottom) The (x,y,z=0) plane; contour separation is 0.1 and max=1; maximum velocity vector is 451 m/s. Density is normalized to 2.72×10^{11} m^{-3}. Thruster firing at $h = 250$ km with $\mathbf{U}_s = -6000\mathbf{x}$ m/s, $\mathbf{V}_o = -8000\mathbf{x}$ m/s.

Ambient Ions, Time=0.25 s

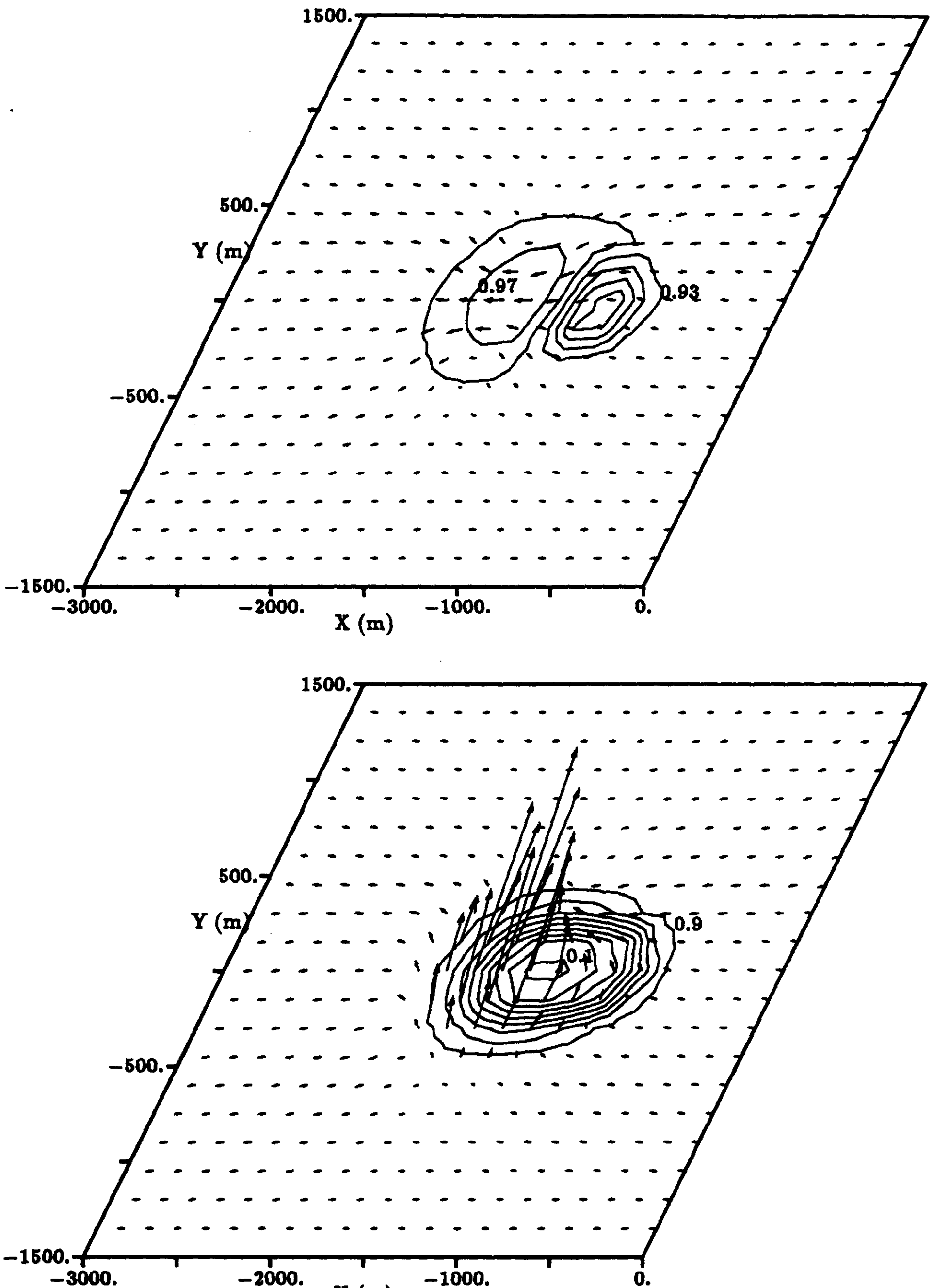

Figure 7.3: The density and velocity of the O^+ ions 0.25 s after the release. (Top) The (x,y,z=600) m plane; contour separation is 0.04 and min=0.68; the maximum velocity vector is 89 m/s. (Bottom) The (x,y,z=0) plane; contour separation is 0.1 and min=0.0676; maximum velocity vector is 391m/s. Density is normalized to 2.99×10^{11} m^{-3}. Thruster firing at $h = 250$ km with $\mathbf{U_s} = -6000\mathbf{x}$ m/s, $\mathbf{V_o} = -8000\mathbf{x}$ m/s.

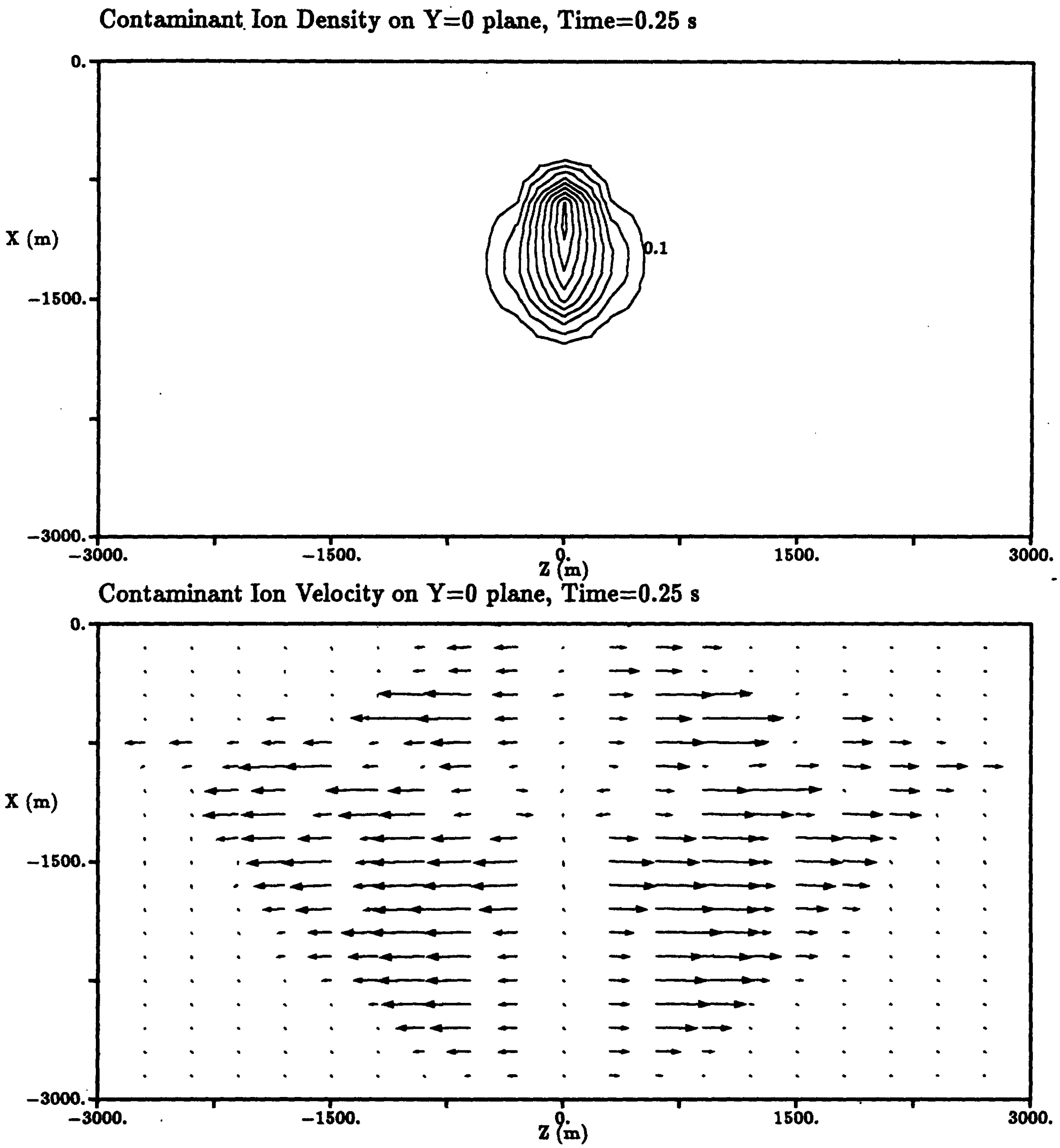

Figure 7.4: The density (Top) and the velocity (Bottom) of the H_2O^+ ions 0.25 s after the release at the (x,y=0,z) plane. Contour separation is 0.1 and normalization is 2.72×10^{11} m^{-3}. Maximum velocity vector is 1682 m/s. Thruster firing at $h = 250$ km with $\mathbf{U}_s = -6000\mathbf{x}$ m/s, $\mathbf{V}_o = -8000\mathbf{x}$ m/s.

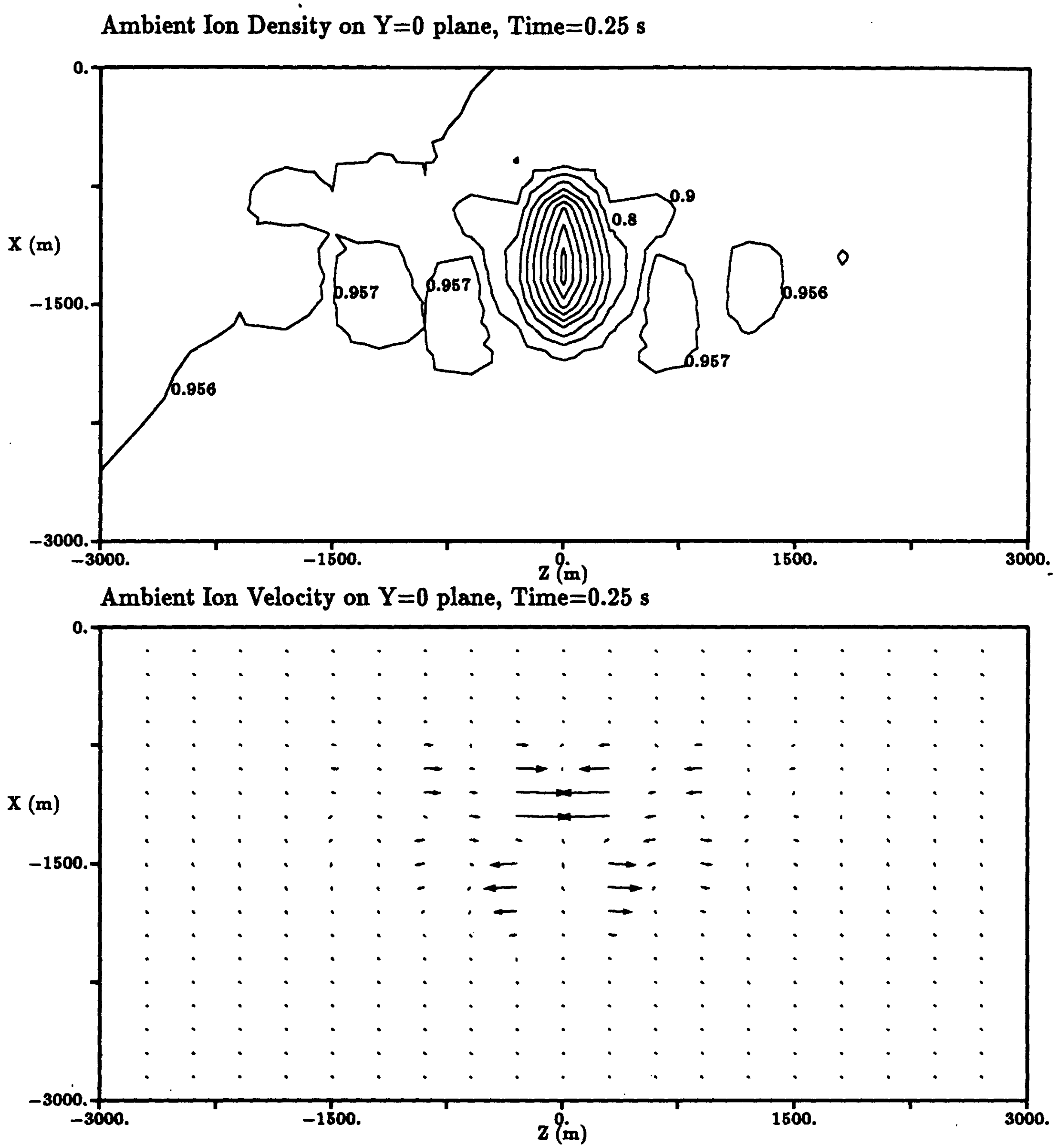

Figure 7.5: The density (Top) and the velocity (Bottom) of the O^+ ions 0.25 s after the release at the (x,y=0,z) plane. Contour separation is 0.1, min=0.067 and normalization is 2.99×10^{11} m^{-3}. Maximum velocity vector is 1115 m/s. Thruster firing at $h = 250$ km with $\mathbf{U}_s = -6000\mathbf{x}$ m/s, $\mathbf{V}_o = -8000\mathbf{x}$ m/s.

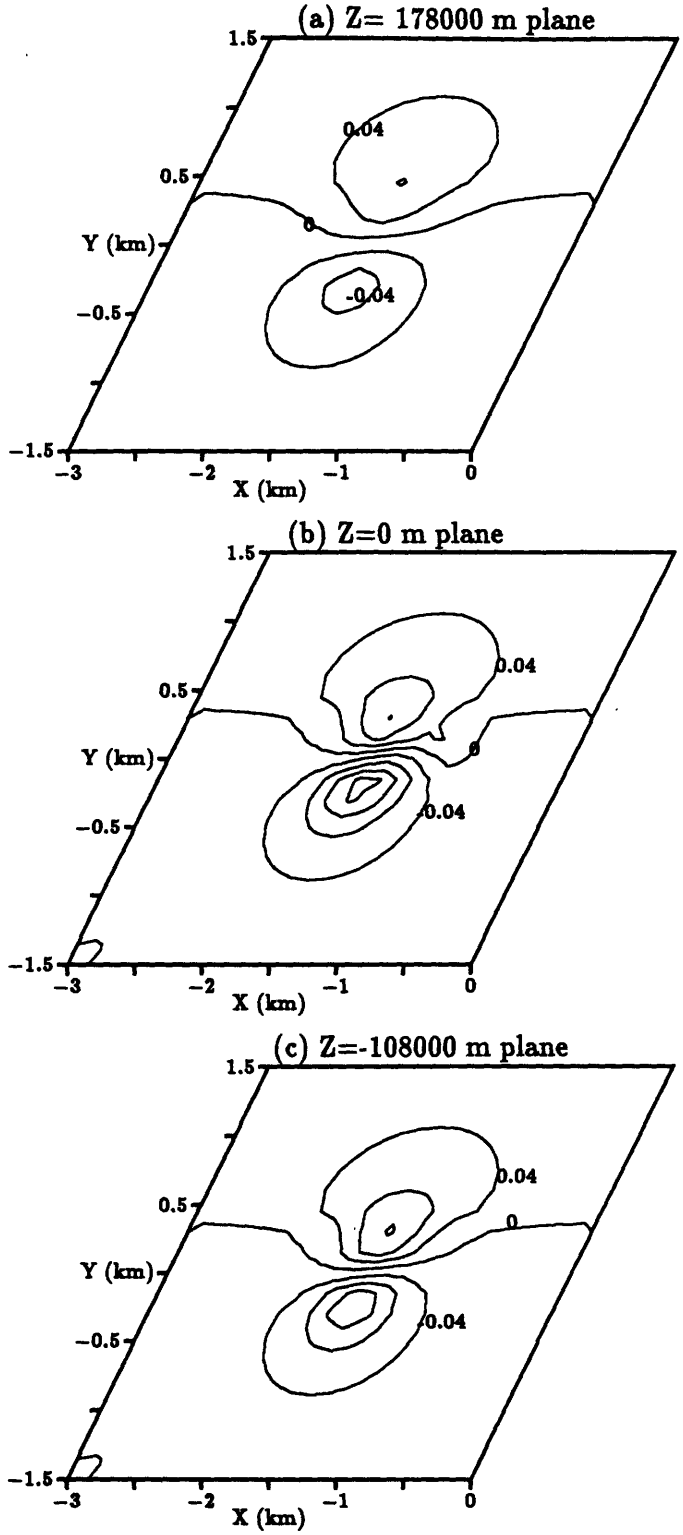

Figure 7.6: The perturbation potential 0.25 s after the release. (a) On (x,y,z=178) km plane. (b) On (x,y,z=0) km plane. (c) On (x,y,z=-108) km plane. Contour separation is 0.04 V. Thruster firing at $h = 250$ km, $\mathbf{U}_s = -6000\mathbf{x}$ m/s, $\mathbf{V}_o = -8000\mathbf{x}$ m/s.

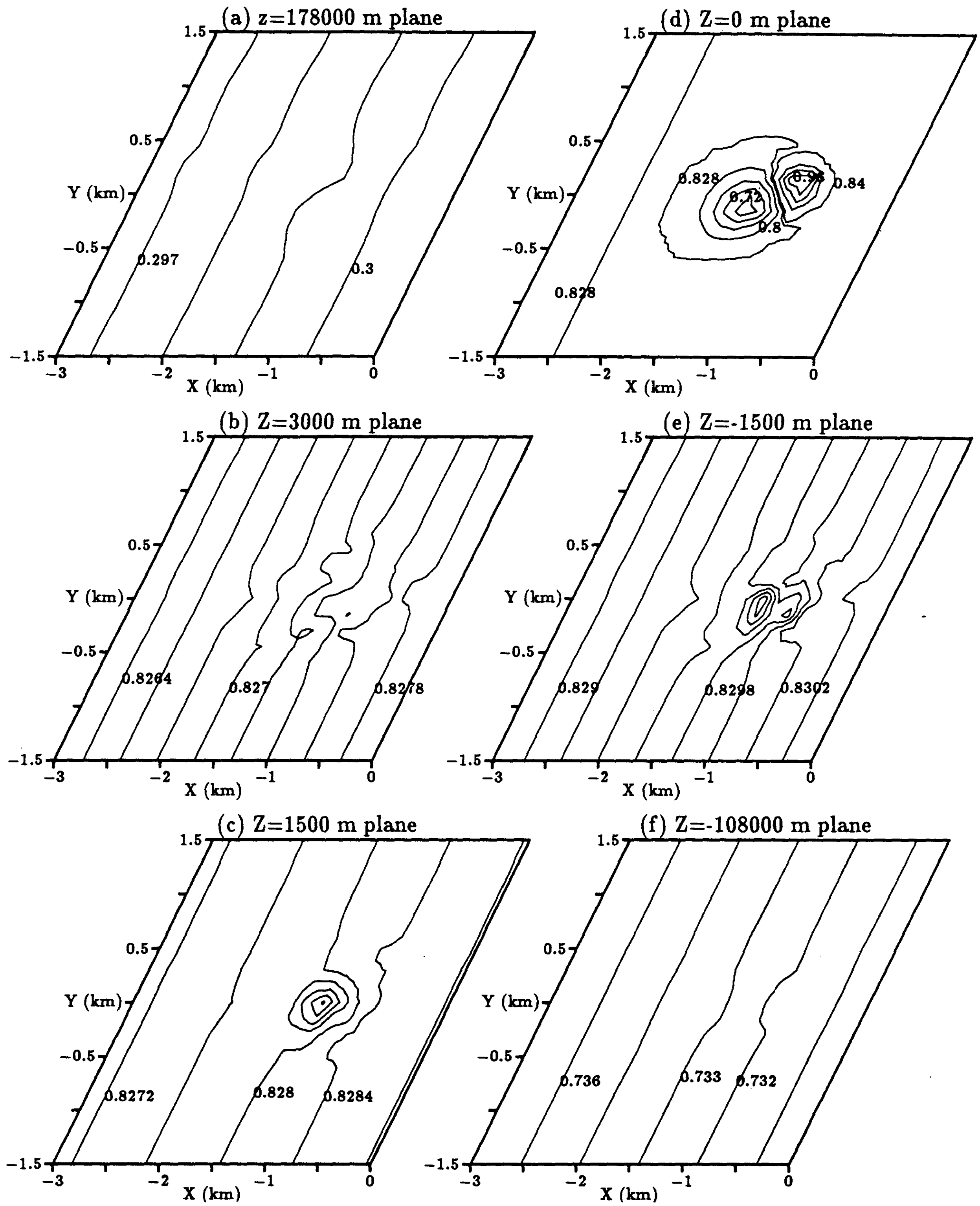

Figure 7.7: The electron density 0.25 s after the release. (a) The (x,y,z=178) km plane; contour separation is 10^{-3}. (b) The (x,y,z=3) km plane; contour separation is 2×10^{-4}. (c) The (x,y,z=1.5) km plane; contour separation is 4×10^{-4}. (d) The (x,y,z=0) km plane; contour separation is 4×10^{-2}. (e) The (x,y,z=-1.5) km plane; contour separation is 2×10^{-4}. (f) The (x,y,z=-108) km plane; contour separation is 10^{-3}. Density is normalized to 3.45×10^{11} m^{-3}. Thruster firing at h = 250 km with $\mathbf{U}_s = -6000\mathbf{x}$ m/s, $\mathbf{V}_o = -8000\mathbf{x}$ m/s.

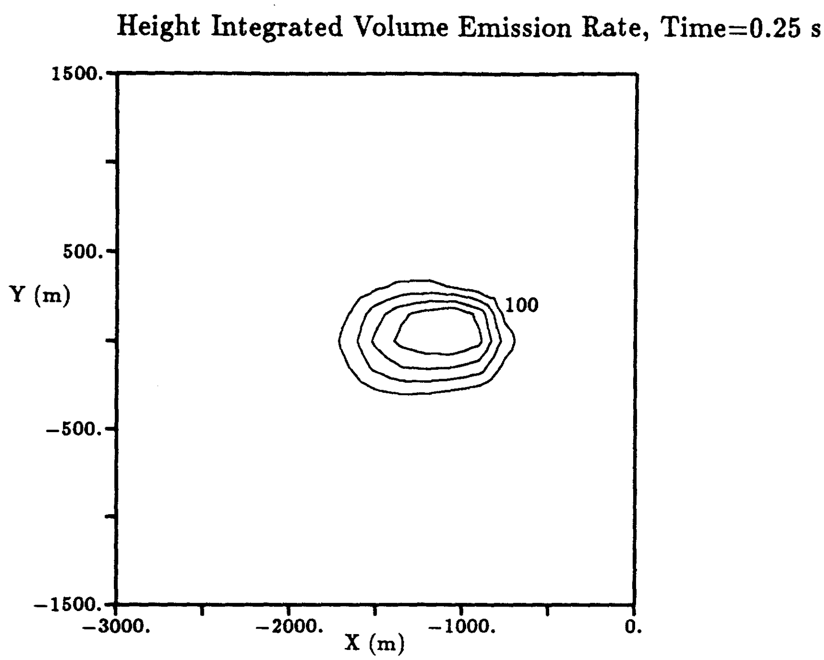

Figure 7.8: Height integrated UV volume emission in Rayleighs 0.25 s after the release. Contour separation is 100 R and maximum is 495 R. Thruster firing at h = 250 km with $\mathbf{U}_s = -6000\mathbf{x}$ m/s, $\mathbf{V}_o = -8000\mathbf{x}$ m/s.

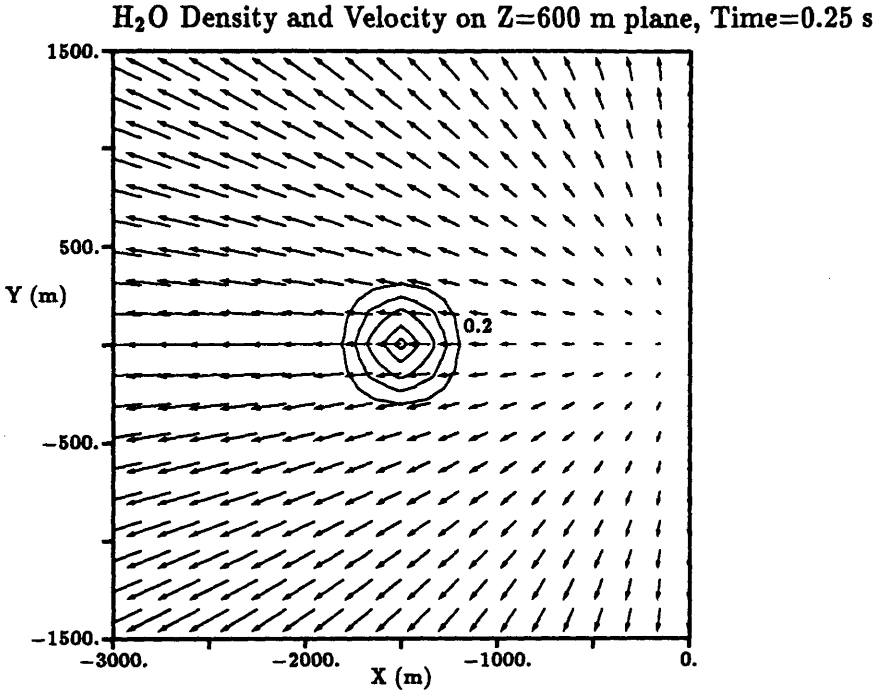

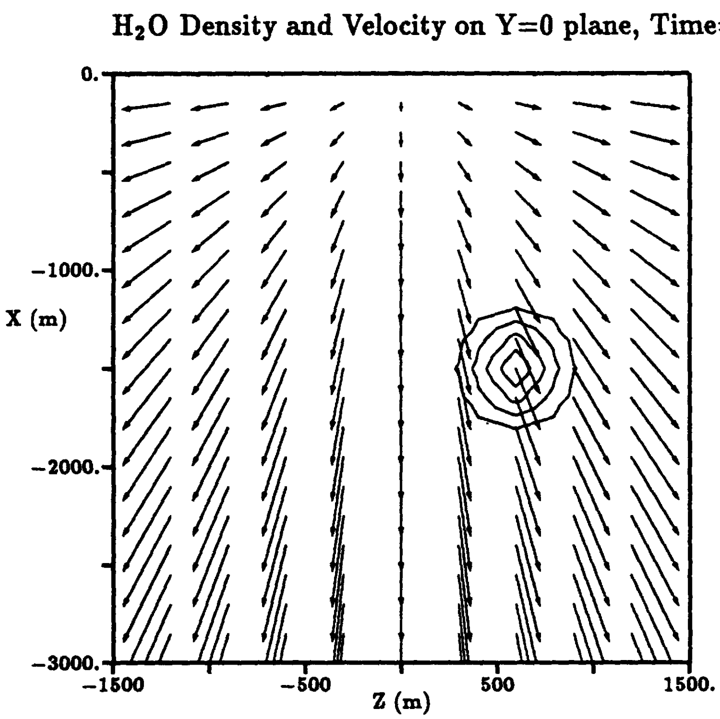

Figure 7.9: Density and Velocity field of H_2O 0.25 s after the release. (Top) On the plane of maximum density (x,y,z=0.6) km. (Bottom) On the midplane (x,y=0,z). The maximum neutral density is 1.29×10^{16} m^{-3}. Thruster firing at h =250 km, $\mathbf{U}_s = -6000\mathbf{x} + 2400\mathbf{z}$ m/s, $\mathbf{V}_o = -8000\mathbf{x}$ m/s.

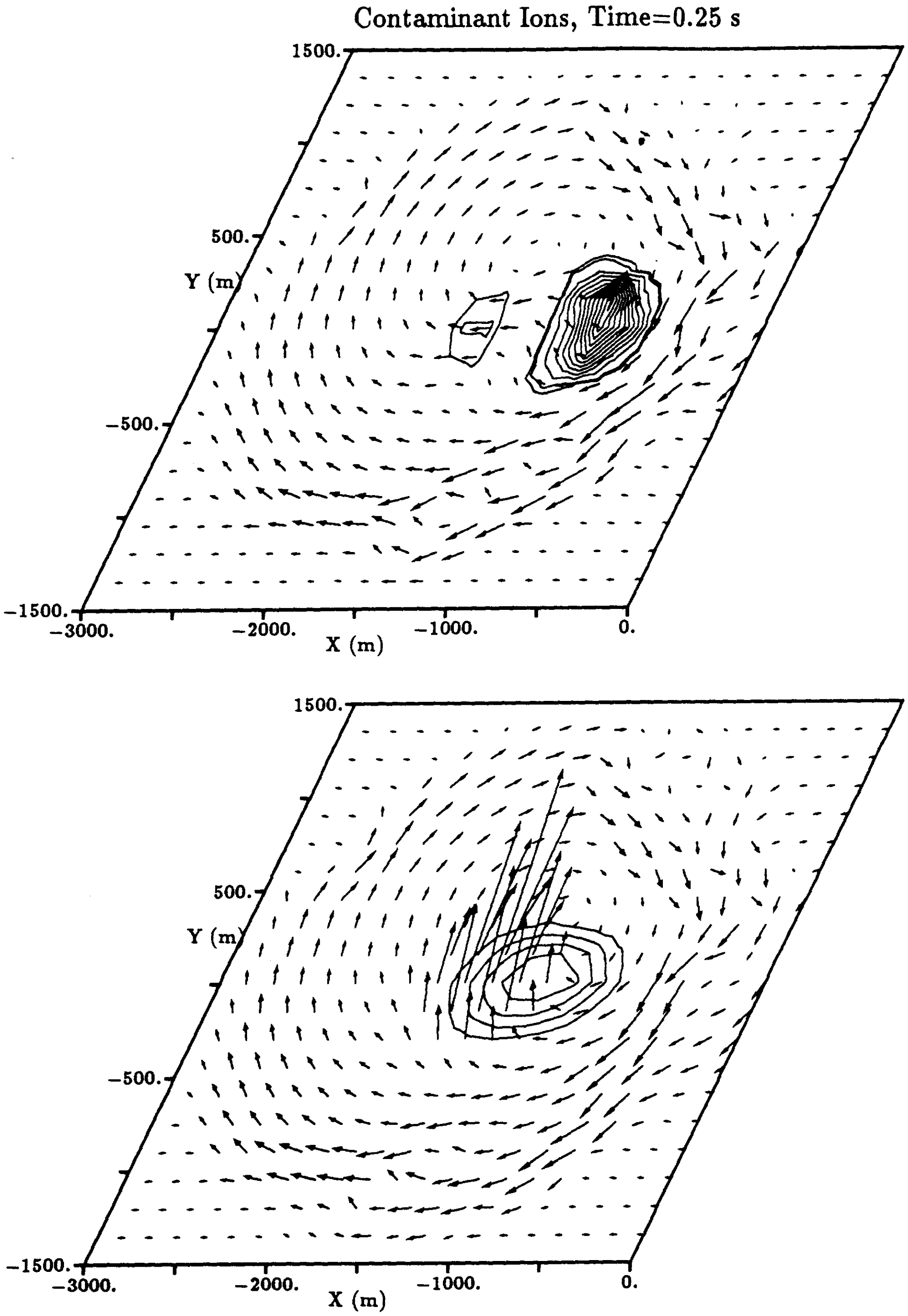

Figure 7.10: The density and velocity of the H_2O^+ ions 0.25 s after the release. (Top) The (x,y,z=600) m plane; contour separation is 0.2 and max=1; maximum velocity vector is 382.5 m/s. (Bottom) The (x,y,z=0) release plane; contour separation is 0.004 and max=0.049; the maximum velocity vector is 76.4 m/s. Density is normalized to 2.17×10^{11} m^{-3}. Thruster firing at h =250 km, $\mathbf{U}_s = -6000\mathbf{x} + 2400\mathbf{z}$ m/s, $\mathbf{V}_o =$ $-8000\mathbf{x}$ m/s.

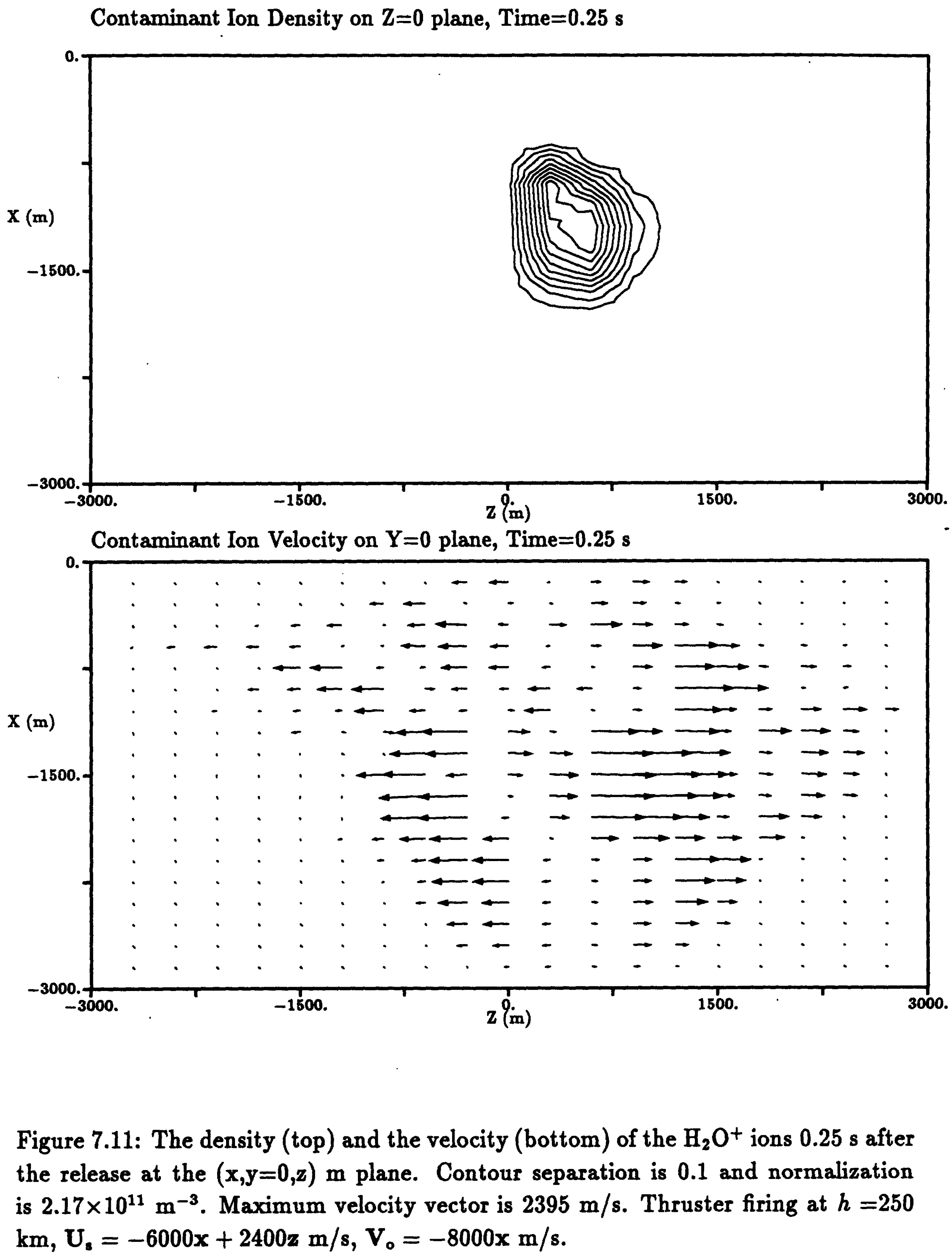

Figure 7.11: The density (top) and the velocity (bottom) of the H_2O^+ ions 0.25 s after the release at the (x,y=0,z) m plane. Contour separation is 0.1 and normalization is 2.17×10^{11} m^{-3}. Maximum velocity vector is 2395 m/s. Thruster firing at h =250 km, $\mathbf{U}_s = -6000\mathbf{x} + 2400\mathbf{z}$ m/s, $\mathbf{V}_o = -8000\mathbf{x}$ m/s.

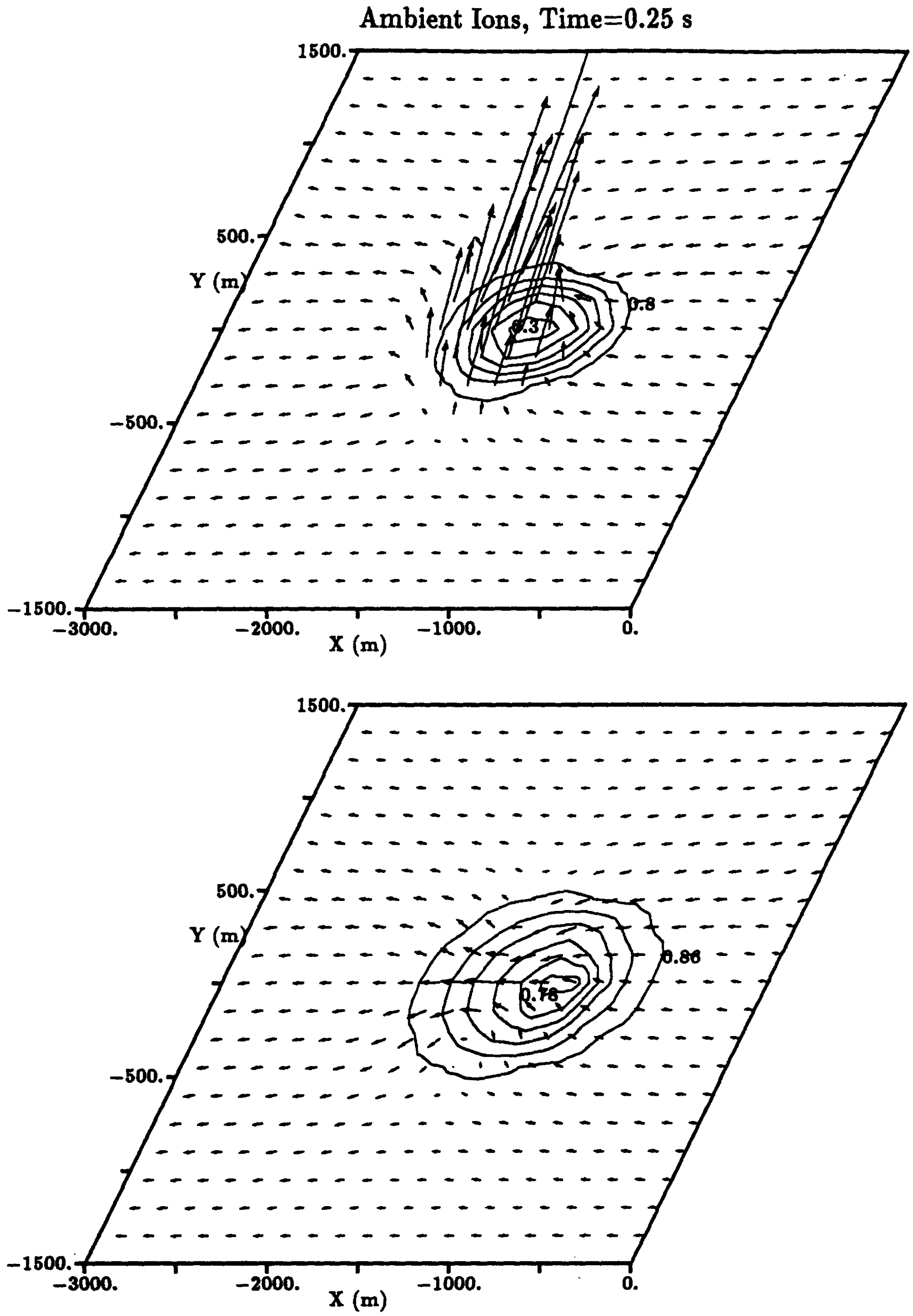

Figure 7.12: The density and velocity of the O^+ ions 0.25 s after the release. (Top) The (x,y,z=600) m plane; contour separation is 0.1 and min=0.2; the maximum velocity vector is 338 m/s. (Bottom) The (x,y,z=0) m release plane; contour separation is 0.1 and min=0.74; maximum velocity vector is 32.5 m/s. Density is normalized to 3.29×10^{11} m^{-3}. Thruster firing at h =250 km, $\mathbf{U}_s = -6000\mathbf{x} + 2400\mathbf{z}$ m/s, $\mathbf{V}_o = -8000\mathbf{x}$ m/s.

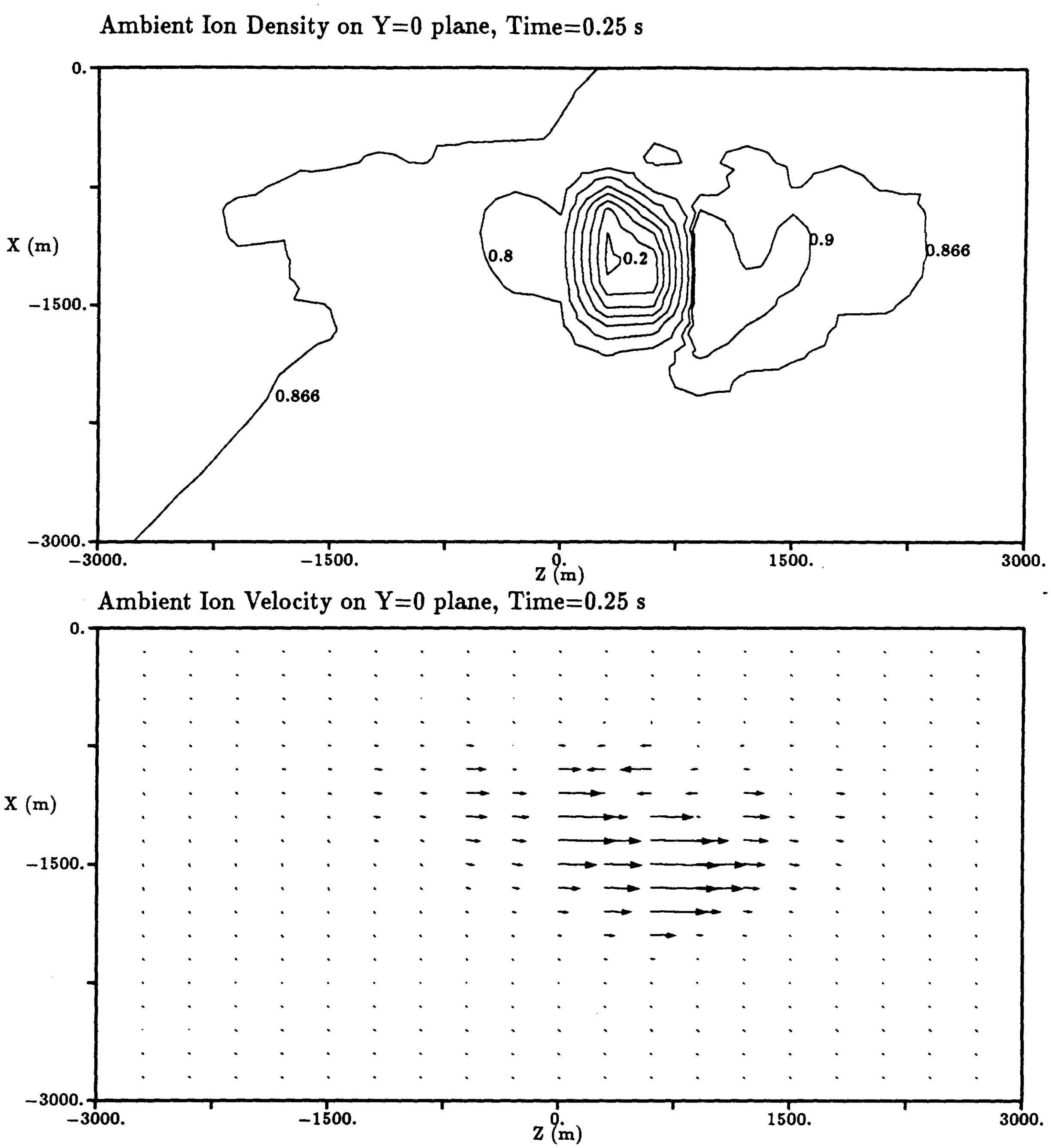

Figure 7.13: The density (Top) and the velocity (Bottom) of the O^+ ions 0.25 s after the release at the (x,y=0,z) plane. Contour separation is 0.1, min=0.179 and normalization is 3.29×10^{11} m^{-3}. Maximum velocity vector is 2153 m/s. Thruster firing at h =250 km, $\mathbf{U}_s = -6000\mathbf{x} + 2400\mathbf{z}$ m/s, $\mathbf{V}_o = -8000\mathbf{x}$ m/s .

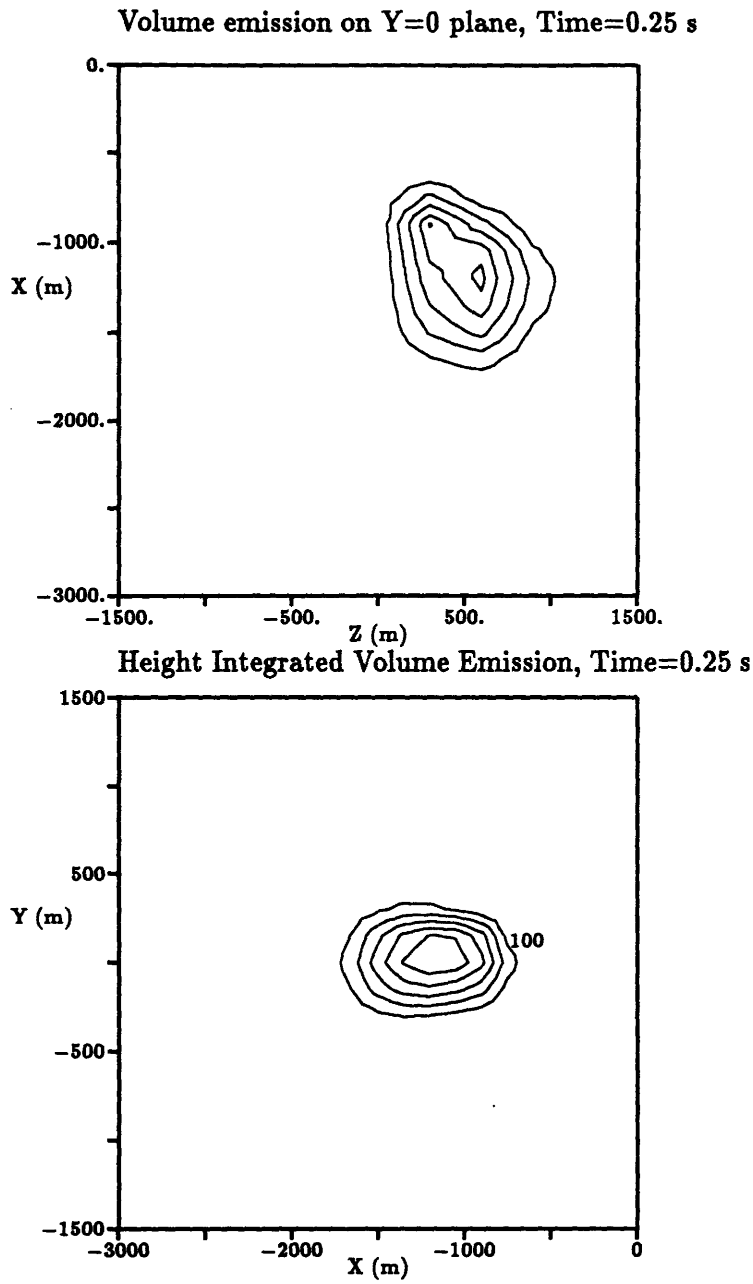

Figure 7.14: (Top) The volume UV emission rate on the midplane (x,y=0,z) m. Outer contour is 0.2, contour separation is 0.2 and normalization is 9.47×10^9 photons/m^{3}s. (Bottom) Height integrated UV emission in Rayleighs. Contour separation is 100 R and maximum is 555 R. Thruster firing at h =250 km, $\mathbf{U_s} = -6000\mathbf{x} + 2400\mathbf{z}$ m/s, $\mathbf{V_o} = -8000\mathbf{x}$ m/s .

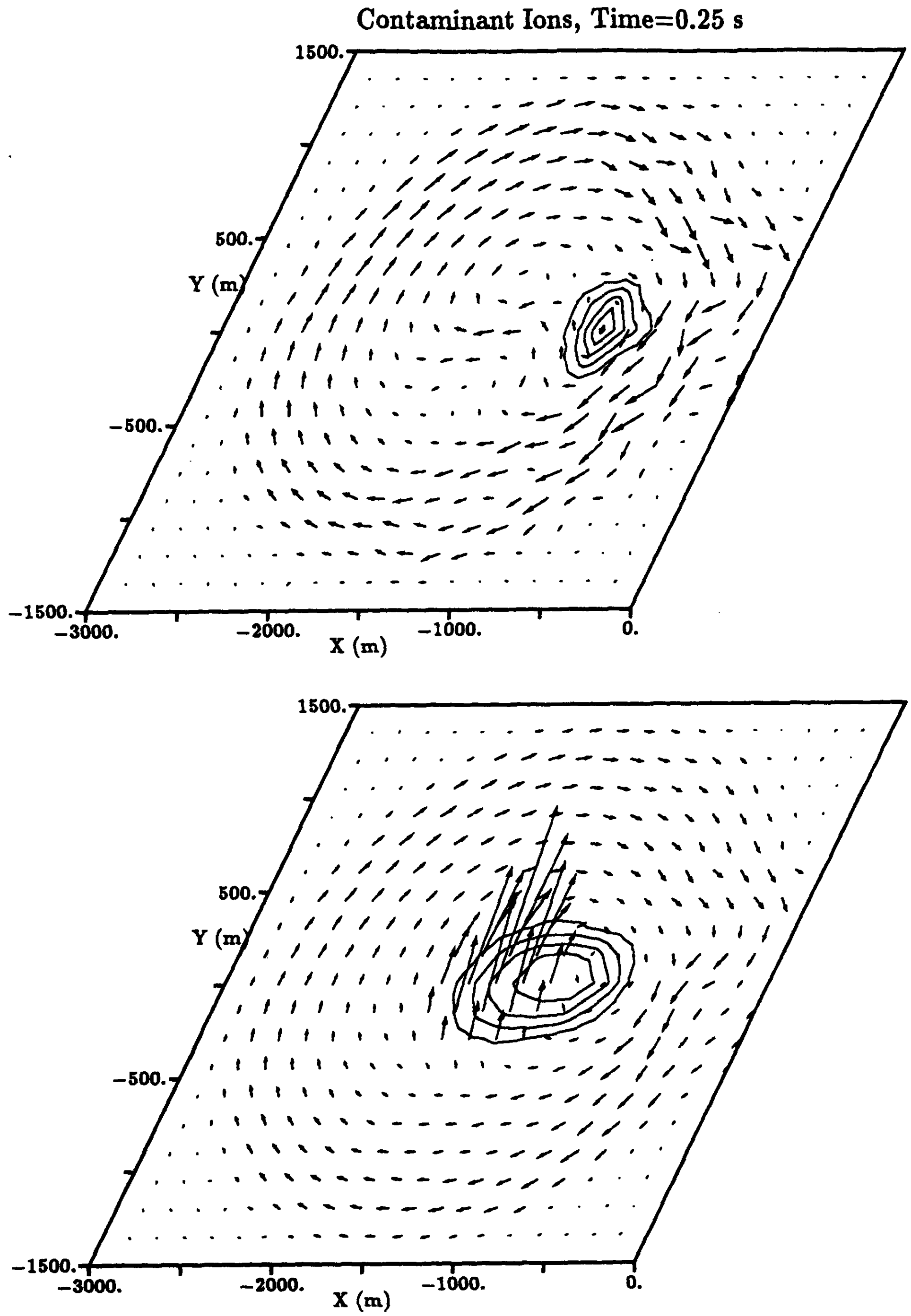

Figure 7.15: The density and velocity of the H_2O^+ ions 0.25 s after the release. (Top) The (x,y,z=600) m plane; contour separation is 0.02 and max=0.1; the maximum velocity vector is 75 m/s. (Bottom) The (x,y,z=0) release plane; contour separation is 0.2 and max=1; maximum velocity vector is 476 m/s. Density is normalized to 1.11×10^{11} m^{-3}. Thruster firing at h = 450 km with $\mathbf{U}_s = -6000\mathbf{x} + 2400\mathbf{z}$ m/s, $\mathbf{V}_o = -8000\mathbf{x}$ m/s.

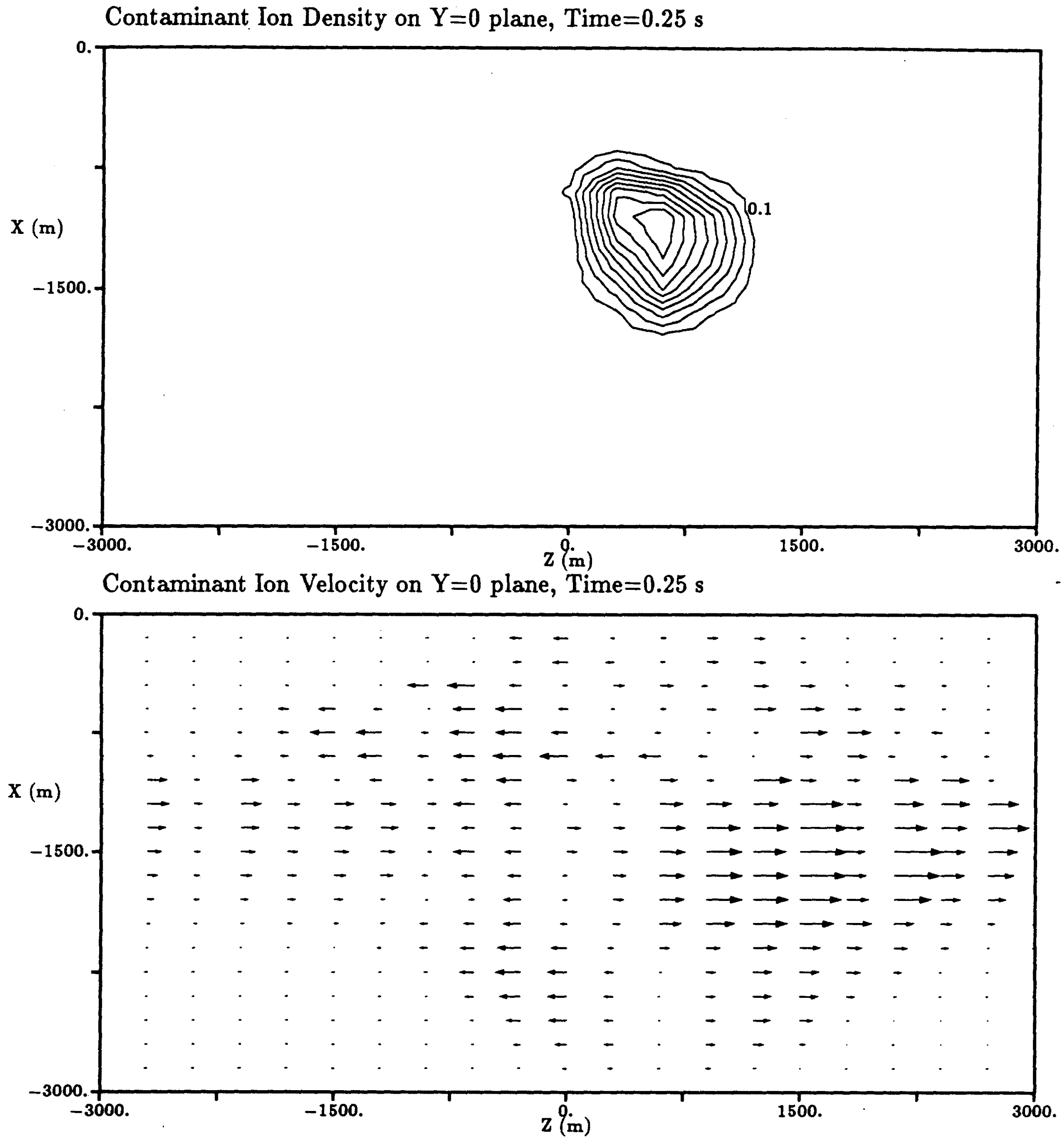

Figure 7.16: The density (Top) and the velocity (Bottom) of the H_2O^+ ions 0.25 s after the release at the (x,y=0,z) m plane. Contour separation is 0.1 and normalization is 1.11×10^{11} m^{-3}. Maximum velocity vector is 5379 m/s. Thruster firing at h = 450 km with $\mathbf{U_s} = -6000\mathbf{x} + 2400\mathbf{z}$ m/s, $\mathbf{V_o} = -8000\mathbf{x}$ m/s.

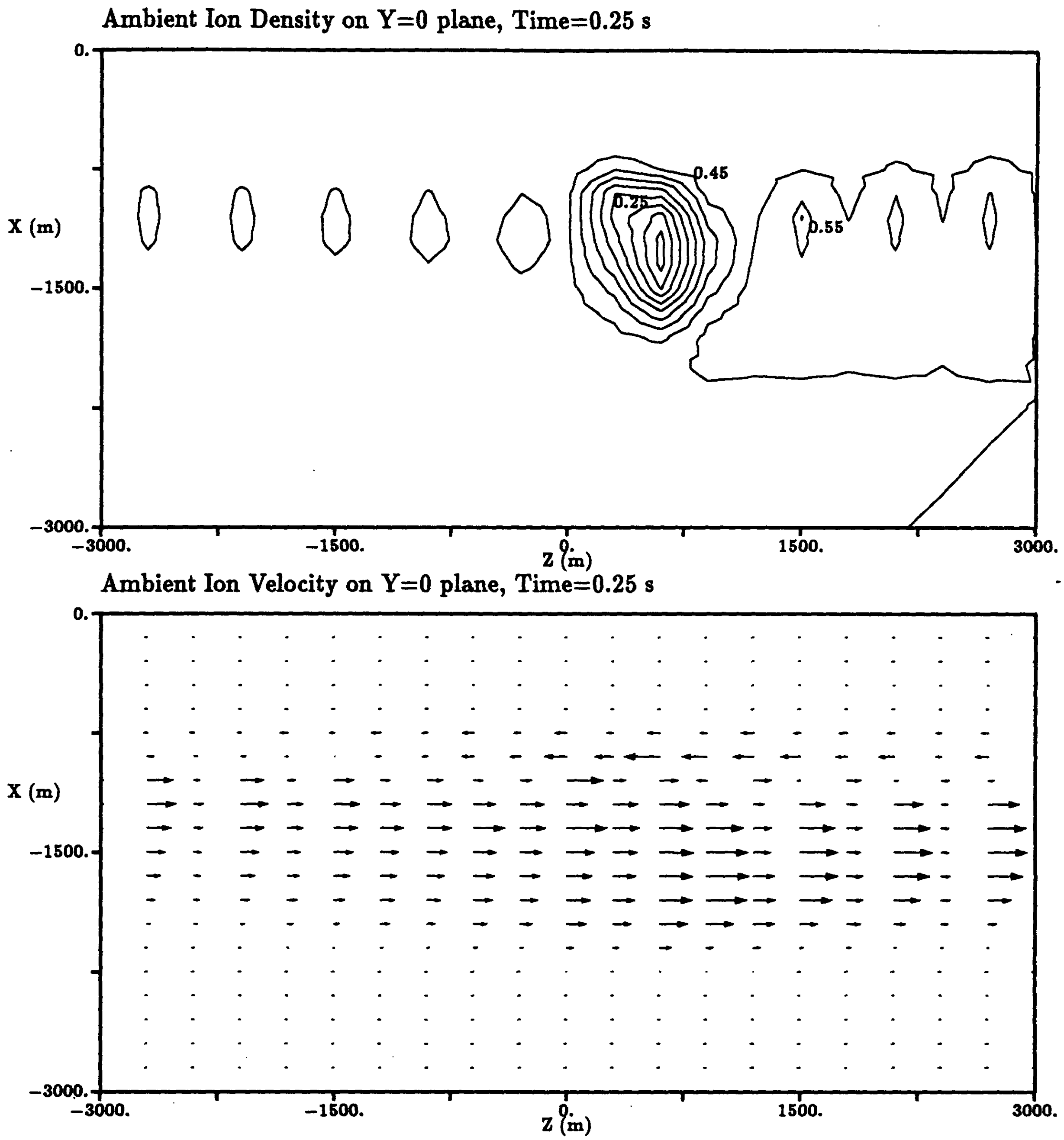

Figure 7.17: The density (Top) and the velocity (Bottom) of the ambient O^+ ions 0.25 s after the release at the (x,y=0,z) plane. Contour separation is 0.05, min=0.089, max=0.55 and normalization is 2.82×10^{11} m^{-3}. Maximum velocity vector is 3501 m/s. Thruster firing at $h = 450$ km with $\mathbf{U_s} = -6000\mathbf{x} + 2400\mathbf{z}$ m/s, $\mathbf{V_o} = -8000\mathbf{x}$ m/s .

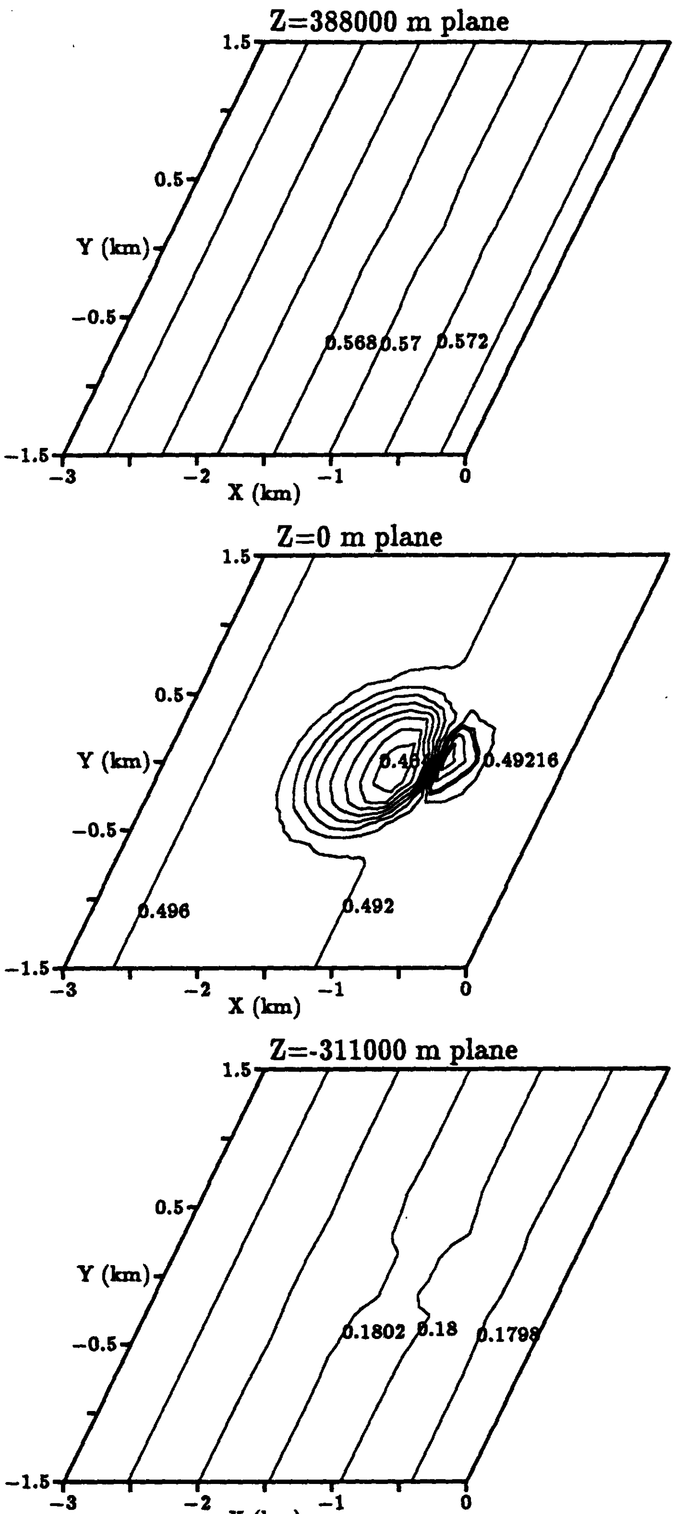

Figure 7.18: The electron density 0.25 s after the release. (a) The (x,y,z=388) km plane; contour separation is 2×10^{-3}. (b) The (x,y,z=0) km plane; contour separation is 4×10^{-3}. (c) The (x,y,z=-311) km plane; contour separation is 2×10^{-3}. Density is normalized to 3.44×10^{11} m^{-3}. Thruster firing at h = 450 km with $\mathbf{U}_s = -6000\mathbf{x} + 2400\mathbf{z}$ m/s, $\mathbf{V}_o = -8000\mathbf{x}$ m/s.

7.5 Release of Neutrals at Orbital Speeds

The second series of simulations investigated the effects on the induced environment due to releases of neutrals at orbital velocities. The application would arise in an instantaneous release from a spacecraft. The source velocity, according to the free molecular flow model, is then $|U_s'| = 0$ and the density maximum propagates with the orbital velocity. This makes the case important in terms of contamination since the released neutral cloud travels with the spacecraft. We examined the release of neutral water. Thus, the results presented below will be similar to those of a pulsed water dump or an instantaneous outgassing process. As in the case of the thruster firings simulations presented above, we examined the role of altitude and latitude on the evolution of the water plasma cloud. We considered orbital releases at altitudes of 250, 450 and 600 km both at mid and high-latitudes. We assumed that the number of released H_2O molecules is 10^{24}, so that comparisons can be drawn with the thruster firing simulations.

We discuss below results of a typical case at time $t = 0.2$ s after the release. The results from the rest of the performed simulations are summarized in the end of this chapter.

7.5.1 Altitude of $h = 250$ km

In Figure 7.19 we show the formation of the H_2O^+ cloud. The density on the release plane (Figure 7.19(Bottom)) has a maximum of 2.53×10^{11} m^{-3}. The cloud shows some steepening in its back side. The velocity field is dictated by the neutral force; the physical mechanisms were explained in the cases considered before. However, the magnitude of the velocity is considerably larger with a maximum of 1078 m/s. The difference between the orbital and other directed releases is due to the larger neutral force that is applied to the ion cloud. The spacecraft initially located at $\mathbf{r} = 0$ has moved to the point (x=-1600,y=0,z=0)m. The maximum of the neutral density co-moves with the spacecraft with a speed of 8000 m/s. According to the results of Chapter 5 the larger neutral force induces larger cloud drifts. On the plane 600 m from the release plane (Figure 7.19(Top)) the H_2O^+ cloud shows a very nonsymmetric structure. The velocity field shows clearly the effects of the diffusion and the dipole field which has mapped along the **B** lines. In the center of the cloud the maximum drift is 60 m/s; thus, there is a large shear in the transverse velocity of the H_2O^+.

The ambient ion density and velocity profiles are shown in Figure 7.20. On the release plane (Figure 7.20(Bottom)) we present the formation of the "hole" with a strength of $[O^+_{min}/[O^+]_{amb} = 0.08$. The velocity field is similar to that of the H_2O^+ ions but with a somewhat reduced magnitude (the maximum is 962 m/s). Figure 7.20(Top) shows the plane 600 m from the release. As in the case of the thruster firing there is a development of an enhancement and depletion region. The dynamics determining this are related to the "snow-plow" effect and that discussion was presented earlier.

The picture of the plasma evolution along the magnetic field lines is shown in Figure 7.21. The H_2O^+ cloud is shown to be symmetric and also to be elongated along **B**. The velocity field shown in Figure 7.21(Bottom) depicts the expansion of the cloud with a maximum velocity of 1618 m/s. The most noticable difference compared with the directed release presented earlier is at the location of the maximum neutral density: there is considerable transverse drift as compared with Case 1.

It is of interest to note that the conditions at the location of the spacecraft, at 1600 m from the origin, are drastically altered. The density of the H_2O^+ density is approximately 1.59×10^{11} m^{-3}. The O^+ has been reduced and the strength of the hole is $[O^+]_{min}/[O^+]_{amb} = 0.3$. The ion velocities, evaluated at the location of the spacecraft, are about 1000 m/s and there is differential direction between the H_2O^+ and O^+.

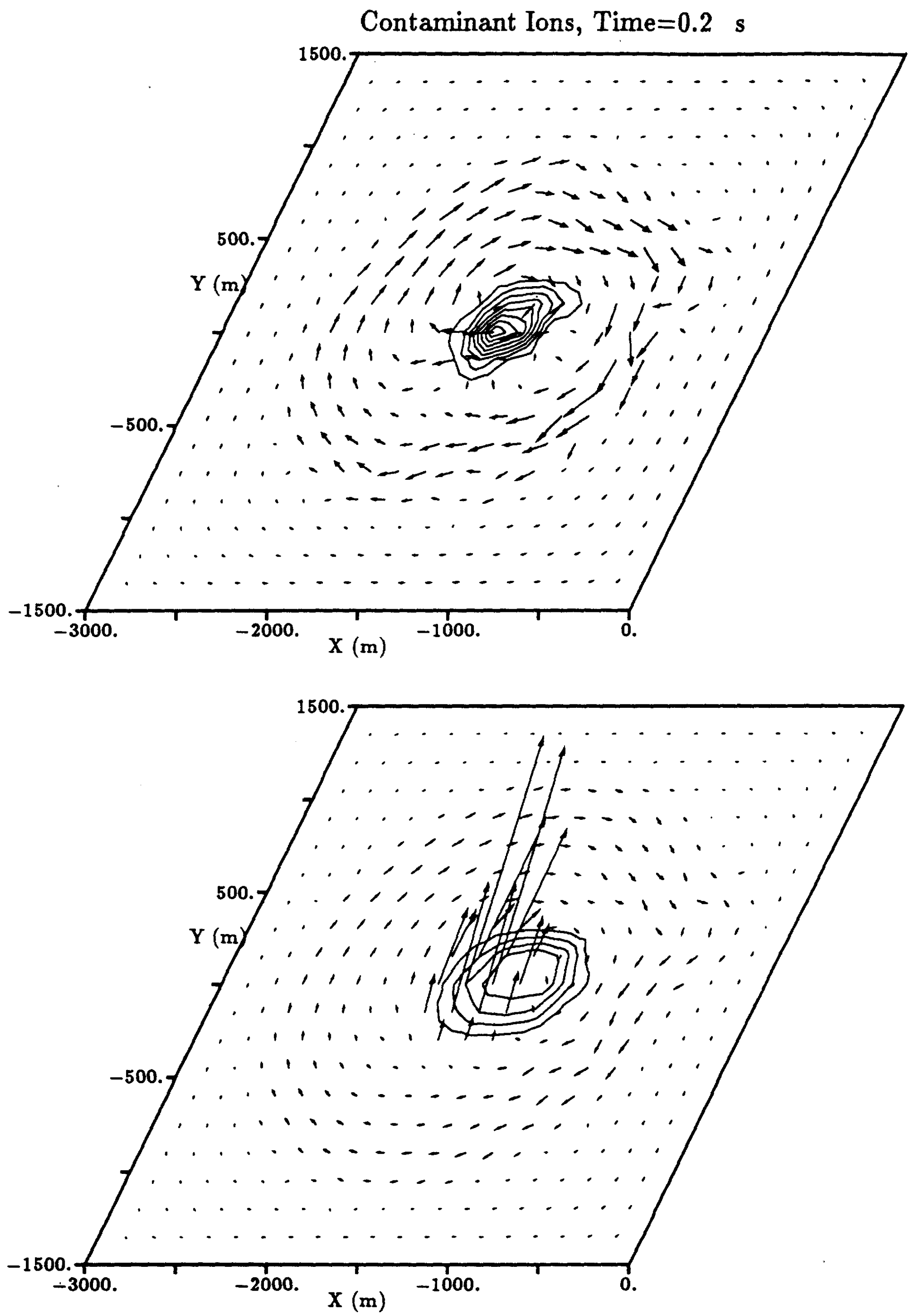

Figure 7.19: The density and velocity of the H_2O^+ ions 0.2 s after the release. (Top) The (x,y,z=600) m plane; contour separation is 5×10^{-4} and max=4.4×10^{-3}; the maximum velocity vector is 60 m/s. (Bottom) The (x,y,y=0) plane; contour separation is 0.2 and max=1; maximum velocity vector is 1078 m/s. Density is normalized to 2.53×10^{11} m^{-3}. Orbital release of water at h = 250 km with $\mathbf{U_s} = \mathbf{V_o} = -8000\mathbf{x}$ m/s.

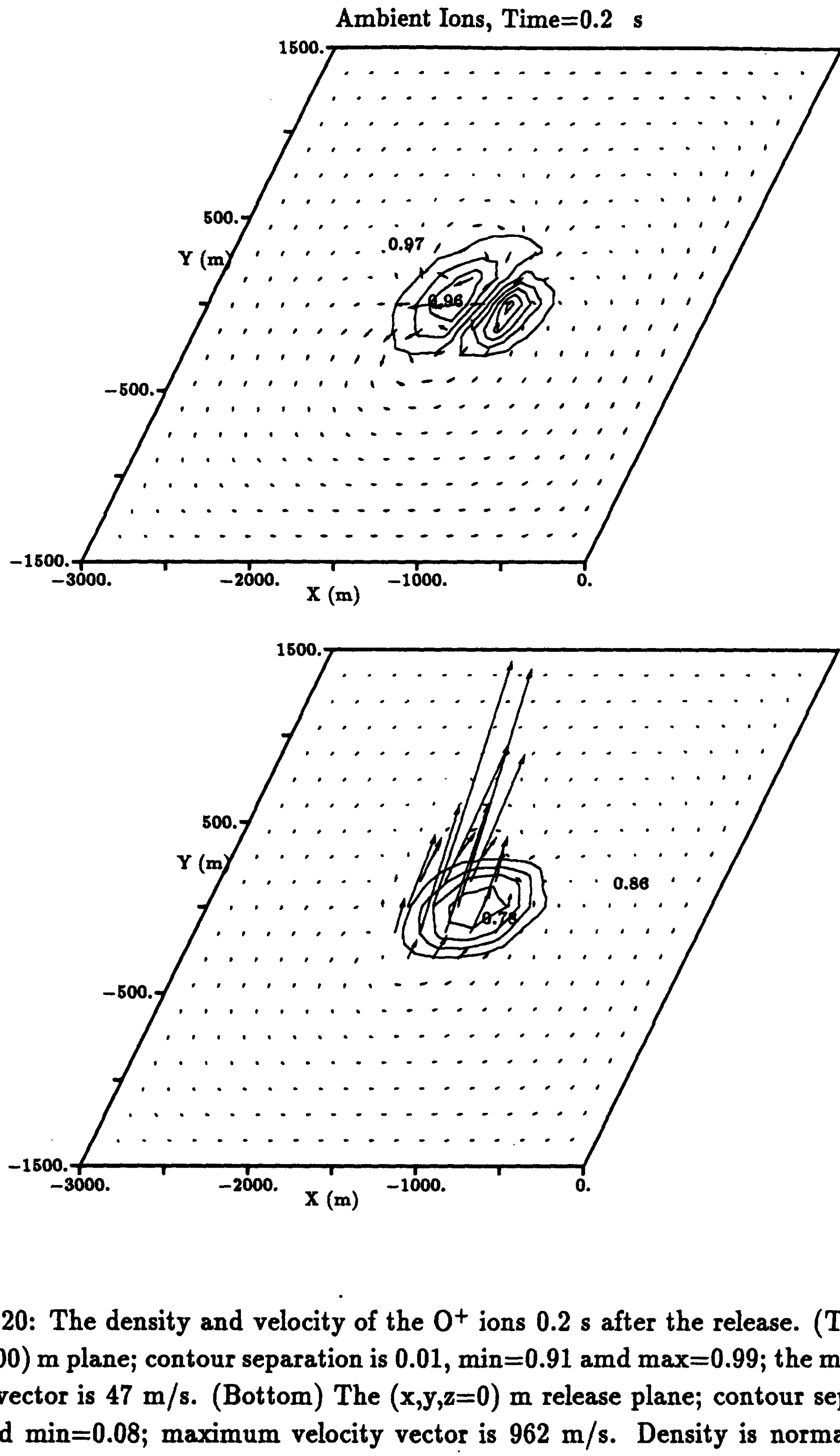

Figure 7.20: The density and velocity of the O^+ ions 0.2 s after the release. (Top) The (x,y,z=600) m plane; contour separation is 0.01, min=0.91 amd max=0.99; the maximum velocity vector is 47 m/s. (Bottom) The (x,y,z=0) m release plane; contour separation is 0.2 and min=0.08; maximum velocity vector is 962 m/s. Density is normalized to 2.95×10^{11} m^{-3}. Orbital release of water at $h = 250$ km with $\mathbf{U_s} = \mathbf{V_o} = -8000\mathbf{x}$ m/s.

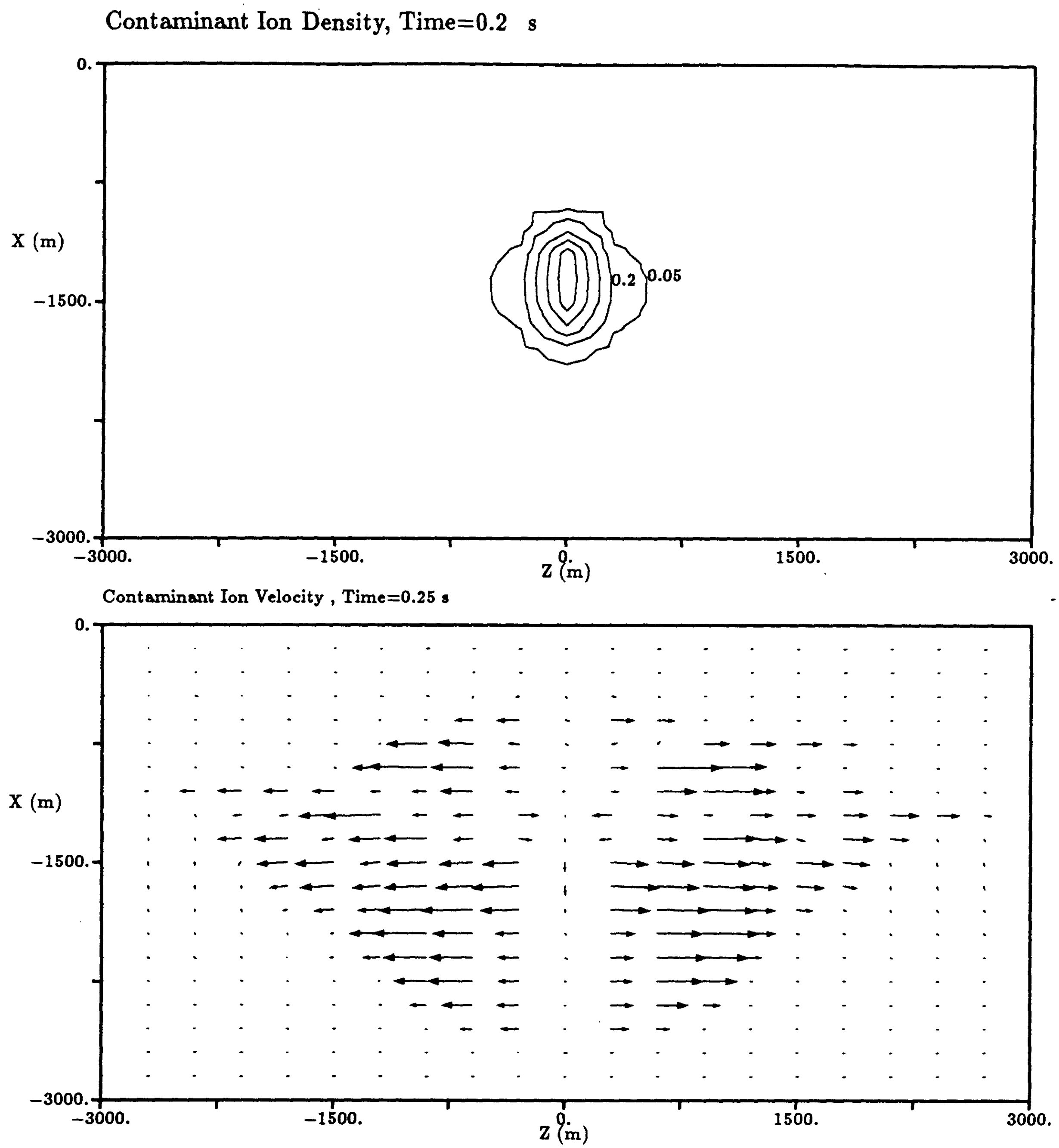

Figure 7.21: The density (top) and the velocity (bottom) of the H_2O^+ ions 0.2 s after the release at the (x,y=0,z) plane. Contour separation is 0.1 and normalization is 2.53×10^{11} m^{-3}. Maximum velocity vector is 1618 m/s. Water orbital release at $h = 250$ km with $\mathbf{U}_s = \mathbf{V}_o = -8000\mathbf{x}$ m/s

7.6 Conclusions - Comparisons with Data

We conclude this chapter by summarizing the results from the numerical simulations. We also compare our results with previous computations and experimental data taken mostly on the Shuttle missions. Data on densities, electric fields, and ion energies on the Shuttle showed variations based on the altitude, operational mode, pre-flight conditions and, most importantly, in the location of the instrument with respect to the orbiter. There are several reasons which prohibit direct comparison of our simulation results with data taken on the Shuttle or during artificial release experiments:

The effects due to the Shuttle geometry, the modified environment according to the definitions given in the introduction are not modeled in our work. This is a result of the large grid cells, relative to the spacecraft dimensions, used in our study.

The conditions under which measurements have been taken are different from those used in the numerical simulations. We modeled a single thruster firing event while on the Shuttle several thrusters fire simultaneously.

Measurements during thruster firings were taken while outgassing was present. Outgassing, which acts as a steady source of contamination, is not taken into account in our thruster firing simulations but is modeled as a separate contamination event.

The measurements are taken at various locations on and around the SSO and at various times after the release events. It is, therefore, difficult to compare a point measurement with the average value over a larger domain predicted by our fluid model.

Although direct comparison is difficult, there are numerous observations that are predicted by our model with respect to the Shuttle cloud or artificial release experiments. For example, the water cloud morphology, the formation of depletion/enhancement regions in the ambient O^+, the "image" cloud formation, and the mapping of the electric fields are some of the plasma phenomena observed during release experiments. Quantitative trends of measurements are also indicated by the model predictions. One of the objectives of this work in the area of *applications* is to provide the designer and the future experimentalist with the large scale picture of the induced environment. These predictions can serve as indicators of trends and phenomena that are to be taken into account in more refined simulations. It is therefore necessary to attempt a comparison with the existing data.

H_2O Densities

The theory governing the neutral water expansion has been presented in Chapter 5. It is evident from the computations that the initial direction of the released gas determines the direction of the motion of the gas cloud with respect to the spacecraft. This has severe consequences in regard to contamination. It was shown that thruster firings which in general have a non-zero angle with the orbital velocity vector result in gas clouds which stay behind and at an angle to the spacecraft. Releases at orbital speeds however, such as outgassing or disposal of liquids, create gas clouds which follow the spacecraft and pose a significant threat for contamination.

Our simulation results can explain several of the neutral species observations on the SSO. The levels of the H_2O densities varied significantly from flight to flight, as well as during the flight. Data from the Spacelab 2 mission suggested that 50 m away from the SSO the density was as high as 6×10^{15} m^{-3} [*Kurth and Frank*, 1990]. During thruster firings the density in the SSO bay reached levels of the order of 10^{18} m^{-3} [*Wulf and Zahn*, 1986]. Measurements taken during the STS-4 mission revealed significantly high water densities up to 10^{18} m^{-3} and, surprisingly, water dumps showed no significant variation of the neutral density. The high outgassing of water was due to heavy rain on the shuttle shortly before the launch [*Hunton and Swider*, 1988]. The neutral density levels in our simulations varied in time as t^{-3} according to Eq. 6.9; at time scales of the order of 0.1-0.2 s after the firing, neutral densities where up to 10^{16} m^{-3} which lies within the typical range measured around the shuttle. This neutral density is associated with the release of 10^{24} H_2O particles. Larger flow rates will significantly enhance the neutral density. Thus, the observed water neutral levels can be attributed to thruster firings under certain conditions which relate to the initial direction of the exhaust gases. With respect to the dimensions of the gas cloud, data from Spacelab 2 revealed that H_2O densities $\geq 10^6$ m^{-3} even at distances of 8 km from the orbiter.

H_2O^+ Densities

All measurements taken on the SSO showed that the dominant contaminant ion is H_2O^+. Our results predict that regardless of the mode of the neutral water release there is a formation of H_2O^+ via charge exchange reaction. It was shown that the characteristics of the structure of the ionic cloud can not be explained by chemistry alone: plasma transport plays a crucial role [see also *Caledonia et al.*, 1986]. The water ions upon their generation are immediately trapped by the magnetic field and then experience the self-consistent perturbation electric field due to the collective behavior of the plasma; the induced drifts define the morphology of the cloud structure. The production of water ions is limited by the availability of the O^+. It is thus expected that water releases in higher altitudes result in less dense clouds. This pattern is depicted in Figure 7.22(Top).

Several simulation results regarding the H_2O^+ cloud are consistent with previous 2-D theories and computations. The cloud is forced by an almost unidirectional neutral wind to drift to a direction and magnitude which depend on the magnitude of the neutral force [*Zalesak et al., 1982*]. The back side of the drifting cloud steepens while the front elongates [*Perkings et al.*, 1973].

All ion measurements on the Shuttle are given in terms of collected current rather than number density. Although currents scale with densities, due to the uncertainties on the species velocity, density comparisons are very difficult. Typical ratios of H_2O^+/O^+ signals were from 2% to 10% [*Narcisi et al.*, 1984]. The water cloud is predicted to form a km size region which compares with the observation that H_2O^+ were found at distances of hundred of meters from the SSO [*Grebowsky et al.*, 1988]. Our model predicts maximum H_2O^+ densities of the order of the ambient. However, the maximum of the plasma cloud remains behind the spacecraft and only during orbital releases, such as a water dump, does it follow the spacecraft. This is in accordance with the observation that H_2O^+ density levels during water dumps reach levels compared to the ambient [*Shawhan et al.*, 1984]. The ion cloud expansion along the magnetic field lines is significant. During thruster firings the plasma cloud elongates along the magnetic field lines and stays behind the spacecraft. Larger flow rates or significant ionization could create denser ion clouds. The localized density enhancements observed about the Shuttle are not a direct result of chemistry but rather relate to plasma transport; this preferential pile-up was shown in the simulations. Thruster firings with a component along the magnetic field create clouds with the characteristics of a plume and significant expansion along **B**.

O^+ Density

Another result of our computations which agrees well with observations is the formation of depletion/enhancement regions of the ambient O^+ during water releases. The formation of "holes" in the ambient ions has first been observed during the launch of Saturn V rocket [Mendillo, 1975]. Since then several water release experiments have been performed and all verified the role of charge exchange in the destruction of the ambient O^+ [*Pongratz*, 1981; *Yau et al.*, 1985].

O^+ depletions have also been observed around the Shuttle during thruster firings or water dumps [*Grebowsky et al.*, 1988]. The level of depletion predicted by our model varies with altitude and with the direction of the thruster firing with respect to the magnetic field lines, as it is shown in Figure 7.22(b). The formation and evolution of the O^+ cloud is dictated by transport and chemistry. The expansion along **B** of the O^+ results in the formation of bumps on the front side of the water ion cloud where the neutral cloud is also located. This is a manifestation of the electrostatic "snow-plow" effect which piles-up density at the edges of the water cloud. The filling-in process of the hole observed during the Waterhole experiments is also predicted by the simulations. The measured levels of O^+ showed considerable variation during the Shuttle flights and operations. This is demonstrated by our model; for instance, the direction of the thrust vector affects the levels of O^+. It is predicted that thruster firings with a velocity component along the magnetic field lines are less effective in producing a "hole". Without the presence of a large component along the magnetic field the strength of the "hole" increases with altitude, i.e., the water release becomes less effective in depleting the ambient O^+ (see Figure 7.22(Bottom)).

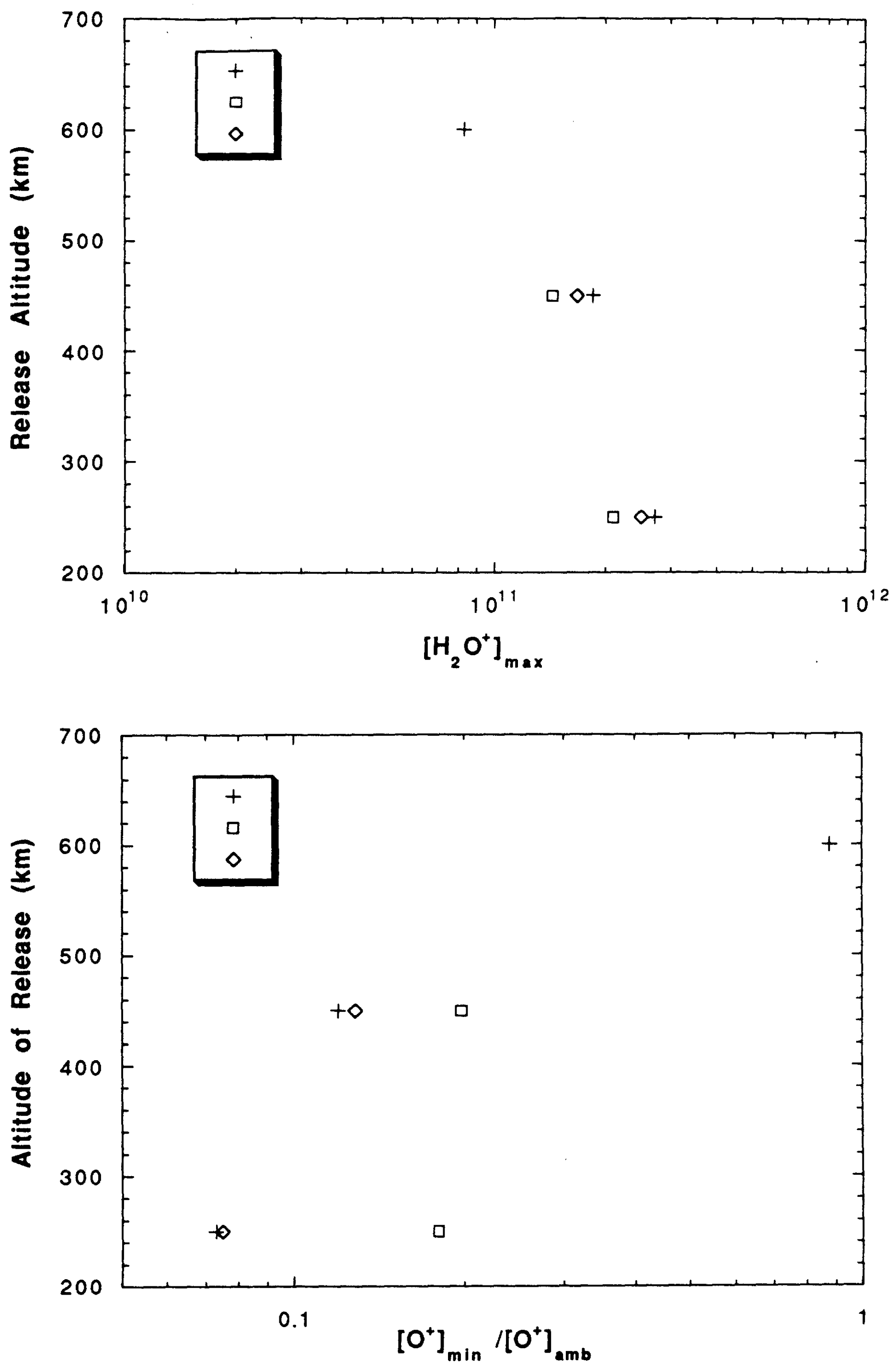

Figure 7.22: (Top) The maximum density of H_2O^+ versus the altitude of the release. (Bottom) The ratio of the maximum depletion of O^+ over the unperturbed value vs the altitude of the release. (Diamond): $\theta_s = 0°$, $\phi_s = 0°$, $|\mathbf{U}|'_s = 2\mathbf{x}$ km/s; (box):$\theta_s = 0°$, $\phi_s = 45°$, $|\mathbf{U}|'_s = 2\mathbf{x} + 2.4\mathbf{z}$ km/s ; (Cross): $\theta_s = 0°$, $\phi_s = 0°$, $|\mathbf{U}|'_s = 0$

Plasma (Electron) Density

The plasma density shows great perturbations with the formation of depletion and enhancement regions. Plasma depletion has been reported during ionospheric modification experiments with water releases [*Yau et al.*, 1985]. Shuttle observations also showed depletions as large as a factor of 10 during thruster firings which compare with simulation results [*Narcisi et al.*, 1984]. However, data from the STS-4 showed plasma enhancements of 3 to 4 orders in magnitude [*Pickett et al.*, 1985]. These effects were more pronounced in the wake of the vehicle and might be very local phenomena due to the Shuttle geometry. Our calculations were not able to predict such large enhancements of the electron density, rather they remained within one order of the ambient. Only in the presence of an anomalous ionization mechanism, such as the critical ionization velocity mechanism, could the plasma density be raised to such levels.

The effects of the release on the unperturbed plasma has also been associated with the formation of "image" clouds [*Lloyd and Haerendel*, 1973; *Scannapieco et al.*, 1974]. This has also been depicted in our simulations. The induced motion on the ambient plasma due to the mapping of electric fields established at the clouds height results in the restructuring of the ambient density profiles.

Plasma Velocities

We explained in detail the physics depicted in the velocity flow field of the ions during releases. In general, the transverse drifts are much smaller than the parallel ones. It is only neutral clouds released at orbital speeds that produce significant transverse drifts in the order of km/s. This is another experimentally verified result. The drift of the cloud relates directly to the established electric fields. In the spacecraft frame one can argue using the familiar notion of shielding of the motional electric field. Data from the STS-4 mission measured streams of very low energy ions, as low as 1.5 eV [*Hunton and Calo*, 1983]. For a practically unshielded cloud both the ambient and contaminant ions should drift away from the spacecraft with 5.3 eV (or 8/km s) in the direction anti-parallel to the orbital velocity. It is the shielding of the motional field that forces the ions to move with speeds as low as 1.4 km/s. The simulation results, as well as those presented in Chapter 5, showed that for neutral clouds with densities above the ambient $\sim 10^{16}\ \mathrm{m}^{-3}$ released at orbital speeds the shielding is of the order of the motional; in such a case the ion velocities -in the spacecraft frame- are significantly reduced and become similar to those observed about the Shuttle. Another observation on the Shuttle showed the existence of multiple localized ion stream flowing at different directions with respect to the orbital velocity. [*Stone et al.*, 1983]. From our simulations it was shown that the ions develop a spatially non-uniform velocity field. Each ion population exhibits a different flow pattern depending upon the conditions of the release and certainly the time of the observation. It has also been verified that ions due to their large velocity component along **B** stream at large angles with respect to the orbital velocity.

Electric Fields

The magnitude and structure of the fields relate directly to the applied forces; the physics involved was represented in depth in Chapter 5. The electric field is shown to be highly localized and anisotropic as anticipated by *Shawhan et al.* [1984]. In certain operations where neutral water is released at orbital speeds and for neutral densities above $10^{16}\ \mathrm{m}^{-3}$, the shielding of the electric field is of the order of the motional which compares well with observation taken during thruster firings [*Shawhan et al.*, 1984].

Radiation Emission from Plume

The study of the radiation environment has significant applications in the signature modification of the spacecraft as well as in the design and operation of sensors on board the spacecraft. In this work we concentrated in ultraviolet emission from the water plasma cloud. It has been recognized recently that the complicated infrared sensors for plume detection could be replaced with simpler UV ones. The plume like characteristics of the thruster firing predicted here resemble UV images of thruster plumes taken by the LACE satellite (see Aviation Week, 4/8/1991). The calculated emission intensities were found to be in the order of hundred of Rayleighs. These intensities are well above the threshold of UV detection levels of about 30 R, as reported during the Waterhole experiments [*Yau et al.*, 1985]. However, larger thruster flow rates or massive neutral water releases will significantly increase the intensity. Numerical experiments with the release of kilograms of water predicted intensity in the order of kR's. Figure 7.23 demonstrates the effects of the simulation parameters of the release on the maximum intensity. It is shown that the major effect is due to altitude which reduces the intensity significantly.

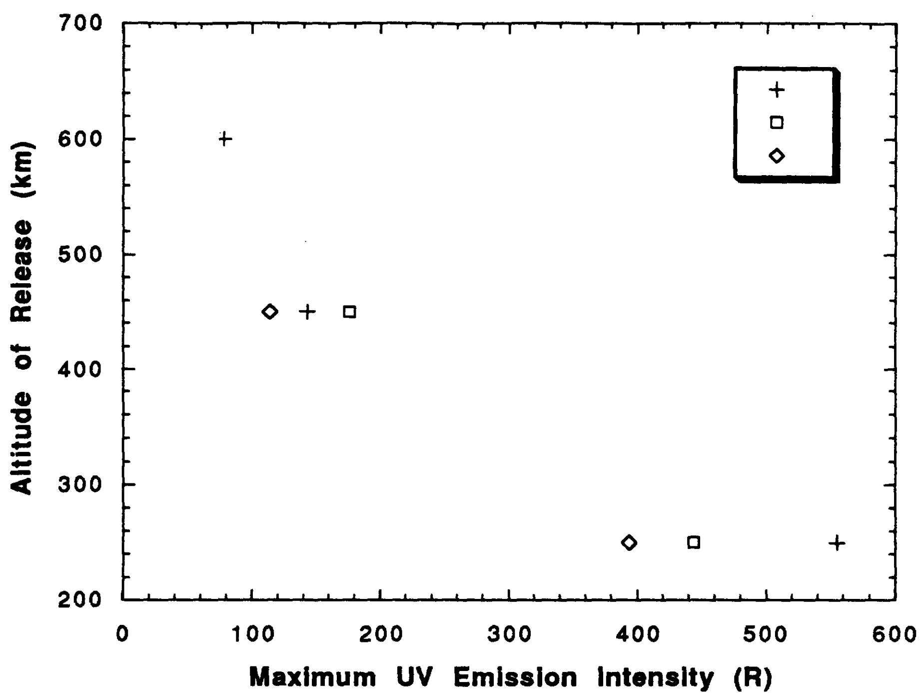

Figure 7.23: The maximum UV intensity. Symbols are the same as in Figure 7.22.

Latitude Effects

Due to the simplicity of current closure in the ambient, releases at higher latitude showed similar results to release at mid-latitudes. Small quantitative differences were attributed to variations with latitude in the ambient neutral and ion density profiles. It should be pointed out that more elaborate equilibrium closure models, for instance, the inclusion of altitude dependent neutral winds or electric fields, would alter the evolution of plasma clouds. From a contamination point of view ambient electric field, which is in the order of millivolts, is not expected to play a role in plasma transport (the induced drifts will be in the order of meters). Similarly, ambient neutral winds, which are in the order of tens of meters, are not expected to affect seriously the cloud evolution compared to the massive neutral wind of the released neutral.

Chapter 8

Conclusions

8.1 Review of Findings

This work was devoted to the development of a 3-D theory and a computational model for the induced plasma environment about a spacecraft. The neutral ion and radiation components of the induced environment were modeled. This is the first comprehensive study of the 3-D evolution of the induced environment; hence, significant effort was put into the understanding of the basic plasma physics processes. The model developed was kept general so that it can be applied to a variety of spacecraft operations and conditions, such as thruster firings, outgassing or artificial release experiments. This work equally addresses issues with respect to *theory*, *numerical methods* and *applications*. There have been several contributions and new findings which are reviewed below. We also present recommendations on the design of spacecraft systems and operations in regard with the induced contaminant environment. The findings of this work can be utilized on spacecraft, such as the Shuttle, the proposed Space Station, or other orbiting platforms.

8.1.1 Contribution to Theory

A general fluid model for the plasma transport was derived. Two ion populations, the ambient and the contaminant, electrons and neutrals are included in the plasma species. The forces included in the momentum balance are due to electric fields, the magnetic field, pressure, gravity, and drag due to collisions. Unlike other models of plasma transport no assumption was made about the differential speed of the ions considered. Thus, all collisions between all particles are included in the formulation. It was shown that for plasma clouds with a length scale of L and velocity V the unsteady and inertia terms can be neglected as long as $V/L \ll \Omega$ or ν, the gyrofrequency or the collision frequency respectively. The role of chemistry in the momentum balance was investigated and the momentum transfer due to inelastic collisions was modeled. With the omission of unsteady and inertia terms the momentum equations were reduced into a system of algebraic equations for the velocity components. The solution to the momentum equations was written in the form of *generalized transport coefficient* tensors operating on the forces considered as

$$\mathbf{V}_t = [\mu_t]\mathbf{E} + \sum [D_t^s] \frac{1}{n_s} \frac{\partial n_s}{\partial \mathbf{x}} + \sum_n [w_t^n] \mathbf{U}_n + [\beta]\mathbf{g} \tag{8.1}$$

The generalized transport coefficients that were derived here can be applied to any plasma in steady state and an arbitrary degree of ionization. In the absence of charged particle collisions they reduce to the well known expression found in the literature. Inertia terms were included perturbatively in the momentum equations.

The fluid transport equations were coupled to the Maxwell equations. Several approximations were applied using the parameters of interest. The displacement current was neglected since changes occur at time scales (τ) such that are $\tau \gg \epsilon_o/\sigma \simeq 10^{-8} - 10^{-3}$ s, where σ denotes the conductivity. Also, the induced magnetic field was neglected since the plasma densities, temperatures and magnetic fields of interest imply a very low β plasma. The plasma was also considered to be quasineutral since length scales of interest are $L \gg \lambda_D$ where the Debye length for the ionosphere is $\lambda_D \simeq 0.2 - 1$ cm. With these approximations the self-consistent electric fields were electrostatic and thus derivable from a potential, i.e., $\mathbf{E} = -\nabla\phi$. The electric currents were formally written from the definition $\mathbf{J} = \sum_t n_t q_t \mathbf{V}_t$ and the substitution of the velocities derived in this work. The equation of charge conservation was formed, $\nabla \cdot \mathbf{J} = 0$. The current balance was determined by direct currents due to electric fields, diffusion currents due to density gradients, currents due to the applied neutral forces (winds) of the ambient and released neutrals, and gravitational drift currents. The current balance equation was written in the from

$$\frac{\partial}{\partial x}\left(\sigma_p\frac{\partial\phi}{\partial x}\right)+\frac{\partial}{\partial y}\left(\sigma_p\frac{\partial\phi}{\partial y}\right)+\frac{\partial}{\partial z}\left(\sigma_z\frac{\partial\phi}{\partial z}\right)=S$$

An analysis of boundary conditions was presented along with a discussion of the current closure in the ambient altitude varying ionosphere. The low E region was regarded as an insulator due to the vanishing transverse and parallel conductivites. The upper F region was also regarded as an insulator due to the vanishing transverse conductivites and the assumption of no current flow into or out from that boundary. It was pointed out that this is only one choice of boundary conditions. If the interest lies in ionospheric-magnetospheric interactions, other boundary conditions should be applied.

A thorough investigation of current closure with the use of *layer* models was pursued. It was necessary to develop a clear understanding of the various closure mechanisms before applying the 3-D numerical model in realistic applications. The current closure via *transverse Pedersen* currents was considered first. It was shown that the charge imbalance created by the presence of the plasma cloud is neutralized by electron flow along the magnetic field lines. For a density perturbation of transverse scale $a_\perp$ the perturbation in the background was found to reach to a distance given by the well known expression $L_{||} \sim a_\perp\sqrt{\sigma_z/\sigma_\perp}$. For the ionosphere the ratio of the conductivities is $10^5 - 10^{12}$, and for transverse scales of interest $a_\perp \geq 500$ m the parallel length scale becomes comparable to the entire ionospheric depth. An expression was derived for the electric field in a plasma cloud due to an applied external field $\mathbf{E}_o$. It is given in terms of the height integrated conductivites as $E = E_o\Sigma_{bP}/(\Sigma_{cP}+\Sigma_{bP})$. Since most of the contribution to the Σ_b comes from the E region and the fact that $L_{||}$ penetrates that region, it was argued that that current closure <u>must</u> include the E region. Such a requirement places a considerable numerical burden since it requires the modeling of large regions.

An analogy has been drawn between a moving conductor in a magnetic field and a moving cloud. Associated with the moving conductor at a velocity $\mathbf{V}_o$ is the *Alfvén wave* field. Due to the motional $\mathbf{E}_m = \mathbf{V}_o \times \mathbf{B}$ field currents flow into the conductor and close out into the ambient plasma in the form of an Alfvén wave. The conditions of applicability of the Alfvén theory were considered. The necessary length that a plasma cloud should have in order to excite such waves was found to be given by $a_\perp \gg 2\pi V_o/\Omega_i$. For cloud drifting with the orbital velocity this requires $a_\perp \gg 250$ m. Slower clouds require much larger transverse scales. Having established the fact that plasma clouds of interest might excite Alfvén waves the implication on the current closure was considered next. A layer model was utilized again. The moving density perturbation generates an electric field which is mapped along the magnetic field lines and drives transverse currents in the background plasma. Both *inertia and Pedersen* currents are allowed to leak the transverse direction. The expression for the self-consistent electric field in the cloud was obtained and is given by $E = E_o(\Sigma_{bP} + \Sigma_W)/(\Sigma_W + \Sigma_{cP} + \Sigma_{bP})$. The wave conductance $\Sigma_W = 1/\mu_o V_A$ provides an additional path for parallel current flow and thus reduces the strength of the electric field within the cloud. It was argued that Alfvén waves can be neglected under the condition that $\Sigma_{bP} > \Sigma_W$. An analysis of the applicability of the above condition was presented. The physics of current closure was discussed for time scales less than $\tau = a_\perp/V_c$. For a given cloud length it was found that there exists an upper bound on the drift velocity V_c for which the wave conductance can be neglected. The Alfvén parallel interaction length given by $L_A \sim 2a_\perp V_A/V_c$ was found to permeate the low E region for most clouds of interest. It was found that only for the nighttime, mid-latitude ionosphere does the wave conductance become large than the Pedersen.

Diffusion was also investigated as a mechanism of current closure. The layer model was utilized for a simple one dimensional density perturbation. The electric field within the cloud was found to be

$$E_\perp = \frac{eD_b^c\frac{\partial N_b^c}{\partial x} + eD_e^c\frac{\partial N_e^c}{\partial x} + eD_c^c\frac{\partial N_c^c}{\partial x} + e(D_b^U + D_e^U)\frac{\partial N^U}{\partial x} + e(D_b^L + D_e^L)\frac{\partial N^U}{\partial x}}{\Sigma_{bP}^U + \Sigma_{bP}^L + \Sigma_{cP}}$$

Two limits were investigated. In the first, the absence of background conductivity (insulating background) leads to the development of ambipolar fields and, thus, transverse diffusion proceeds with the slow electron rate. In the second limit, large background conductivity, the electric field is very effectively short-circuited and diffusion proceeds with the fast ion rate. It was then argued that 3-D diffusion will be greatly altered by the presence of the conducting ambient plasma and transverse diffusion might not be ambipolar.

A *generalized charge conservation* equation was derived. It was shown that, including both the inertia correction to the ion drift and the parallel current carried by the Alfvén wave, the character of the charge conservation equation changes significantly. Rather than attempting a numerical solution to this equation, the polarization currents were included in this work by obtaining the inertia correction to the velocity and adding the divergence of the corresponding current density.

8.1.2 Contributions to Numerical Modeling

One of the key objectives in this study was the development/application of appropriate numerical methods, employed in the solution of the model 3-D equations. There were two types of equations considered: *hyperbolic* and *elliptic*.

The continuity equations of the plasma species are 3-D hyperbolic and can be considered as an example of conservation laws written in the form

$$\frac{\partial U}{\partial t} + \frac{\partial f}{\partial x} + \frac{\partial g}{\partial y} + \frac{\partial h}{\partial z} = 0$$

The numerical solution of such equations suffers from dispersion or dissipation, especially in regions of discontinuities or steep gradients in the state vector U. Since such regions often arise in plasma transport phenomena it was necessary to utilize appropriate numerical schemes. Instead of resorting to the addition of artificial viscocity, the Flux Corrected Transport (FCT) technique was utilized. The algorithm originally developed in 2-D was extented into 3-D. The algorithm developed can be applied as a filter to other CFD schemes. The numerical properties of the high and low order schemes used in the formulation of FCT were investigated. Linear stability analysis was applied and the amplification factor, the maximum time step for stability, and the phase error were derived. A computational example of a 3-D wave propagation was performed. The results demonstrated the ability of the 3D-FCT to handle the propagation of discontinuites without the appearance of non-physical ripples and with a minimum amount of dissipation.

The other numerical challenge in this work was posed by the equation for the electrostatic potential. It is a nonself-adjoint elliptic type of equation, with highly dissimilar coefficient since $\sigma_{\perp} \ll \sigma_z$. It is this inherent difficulty that prohibited the numerical solution of the fully 3-D problem in the past. The discrete potential equation on a non-uniform rectangular grid was derived. For a grid with (nx,ny,nz) points in the (x,y,z) directions the discretization leads to a matrix equation of the form $[a_{NN}][\phi] = [S]$. The matrix $[a]_{NN}$ nonsymmetric, sparse, and large of the order of $N \times N$ with $N = (nx - 2) \times (ny - 2) \times (nz - 2)$. A special storage scheme was developed. The matrix $[a_{NN}]$ was compressed into an $[A]_{N7}$ matrix storing only the seven elements involved in the finite difference discretization around a point (i, j, k). The implementation of Dirichlet and Neumann boundary conditions was presented. A discussion on the methods available for the solution of the derived linear system of equations was presented. It was argued that due to the size and type of the differential equation considered direct methods were prohibited. The alternative was the use of a combination of an *iterative scheme* with appropriate *preconditioning* of the original matrix equation. This strategy was necessary for both computation reasons, i.e., the size of the problem, and for reasons related to the structure of the matrix, i.e., due to its non clustered eigenvalues. The starting algorithm in the computations was an Incomplete Cholesky Decomposition (ICD) applied as a preconditioner to a Conjugate Gradient iteration (ICCG). At later stages of this study the availability of a computer package (NSPCG) offered tremendous variation on the choice of the preconditioner and accelerator. Most of the simulations were run with the use of the ICD as the preconditioner and the General Minimal Residual as the accelerator.

8.1.3 Contributions to Applications - Theory

Current Closure: Initial Time Simulations

The theory developed here was implemented in a computer code. The first series of simulations used preionized plasma clouds and were aimed at the understanding of the 3-D current closure between a plasma cloud and the background. Since this is only the the beginning of such 3-D simulations a thorough investigation of basic plasma physics processes was necessary. These initial-time simulations were:

- Compared with the simple analytic layer models derived in this study.
- Used to examine the role of the magnetic field on the electric field mapping process.
- Elucidated important plasma physics processes, concerning the effects of applied neutral forces, diffusion, and electric fields on a plasma cloud imbeded in a non-uniform background plasma.
- Used as a guide to the understanding of the 3-D evolution of the spacecraft induced environment where more complicated processes are taking place.

A water-bag model was utilized where a plasma sphere was placed in a *uniform background plasma* and an applied externally electric and magnetic fields. In the absence of the magnetic field the conductivites are isotropic and the charge conservation equation can be solved analytically. The property of a plasma to shield the applied electric field was examined. The analytic solution obtained was found to be identical to the numerical. With the presence of a magnetic field the effects of the increased parallel conductivity were investigated. It was shown that the symmetric 3-D dipole present in the case of isotropic conductivites is greatly elongated along $\mathbf{B}$ as the ratio of $\sigma_z/\sigma_\perp$ increases. With values comparable to the ionosphere the field lines become practically equipotential and the transverse electric field is mapped. The numerical interaction length scale was found to be in very good agreement with the theoretical estimate $L_z \sim a_\perp\sqrt{\sigma_z/\sigma_\perp}$.

The current closure processes were examined for plasma clouds imbeded in a *real altitude varying ionosphere.* These are the first computations of this kind and considerable effort was placed upon elucidating phenomena which dictate the evolution of plasma clouds, such as diffusion, applied neutral forces, or electric fields. A series of numerical simulations were performed. The neutral and ion clouds were initialized as Gaussians with prescribed central densities and length scales; parameters were taken so that they span the entire range anticipated about spacecraft.

The problem of 3-D diffusion was considered in the absence of external forces. It was found that diffusion along **B** is ambipolar and proceeds with the slow ion rate. The plasma clouds were shown to rotate slowly around **B** while expanding with much greater speeds along **B**. The overall potential structure, verified the layer model analysis, as well as results from other water-bag and isotropic conductivity models.

The effects of a unidirectional neutral force resulting from the presence of a neutral cloud were also examined. The released neutrals were initialized with a velocity of 8 km/s a situation which would represent the worst scenario for contamination. The central densities of the ion cloud varied from $10^{11} - 10^{13}$ m^{-3} while those of the neutral cloud between $10^{14} - 10^{18}$ m^{-3}. Two extreme situations were demonstrated. Plasma clouds with densities of $n_{r+} \sim 10^{11}$ m^{-3} and $n_r \sim 10^{14}$ m^{-3} represent small perturbations to the ionospheric plasma. It was shown that both the effects of diffusion and the applied neutral wind were present. The diffusion established a Boltzmann electric field while the unidirectional neutral wind established a dipole field. The cloud showed slow rotation around **B** and fast expansion along it. The mapping process of the electric field was also demonstrated. In the opposite extreme of a very strong perturbation the potential and flow field were completely dominated by the strong neutral force. A dipole field was established with a magnitude of ~ 0.23 V/m shielding almost perfectly the applied motional electric field. The obtained ion drift was of the order of 7.5 km/s in the central region of the plasma cloud. Parallel expansion was also present but transverse drifts were dominant. This situation would correspond to a cloud which drifts with the neutral cloud at almost the orbital velocity.

Overall, it was found that in the transverse direction diffusion and the applied unidirectional neutral wind determine the establishment of the electric fields and, consequently, the drifts. In the parallel direction, and due to the absence of any component of neutral wind along **B**, diffusion controls the expansion of the plasma cloud. It was found that with neutral densities above 10^{16} m^{-3} the transverse drifts become comparable to the orbital velocity. These situations are candidates for significant spacecraft contamination.

The effects of altitude of the release were also examined. It was found that with increasing altitude the transverse plasma drifts increased due to better coupling between the cloud and the ambient plasma.

Induced Environment Simulations: Time Evolution

It was recognized in this work that any attempt to model the spacecraft induced plasma environment should account for the detail physics of the (released) neutral flow. The flow of neutrals in a rarefied environment undergoes through various regimes and is a very complex process. The flow regimes resulting from releases of typical contaminants found about spacecrafts were characterized by the use of the equal mass radius α_o. It was shown that for the altitudes, and amount of released material of interest the flow will be in a *free molecular* regime for tens of seconds before relaxing to the *diffusive* state. For time scales of interest in contamination studies, usually of the order of a second, it was necessary to model the free molecular expansion of the released gases. A simple model for such a flow originating from a pulsed source was utilized due to its simplicity and accuracy. More complex neutral models can be easily coupled to the plasma model.

The models for the plasma and neutral transport were applied to study the H_2O and H_2O^+ cloud. These species were identified as the major contaminants about the Shuttle. The review of spacecraft operations responsible for the H_2O found in its vicinity identified three major sources: thruster firing, outgassing, and water dumps from power and life support systems. Chemistry within the contaminant gas cloud plays a crucial role in determining the composition of the induced environment and was included in the formulation. The reaction rates and the implications on the computational time were discussed. It was found that charge exchange posses the stringest condition on the computational time step, which for densities of 10^{18} m^{-3} can be as low as 10^{-4} s. Simulations of thruster firings were performed utilizing typical flow rates of thrusters used in the reaction control system of the Shuttle. A single flow rate was considered with a specified duration of the firing which dumped 10^{24} neutral water molecules. The exhaust velocity was taken to be between 2 and 3.1 km/s and the spacecraft was assumed to fly perpendicular to the magnetic field lines. Several other parameters were varied, such as latitude, altitude (250, 450 and 600 km), and the orientation of the source velocity with respect to the magnetic field.

Regardless of the mode of the water release it was shown that the formation of a H_2O^+ cloud occurred with densities comparable to the ambient O^+. The structure of the cloud was found to be dependent upon such parameters as the direction of the exhaust velocity and the altitude of the release. The worst contamination case was predicted to occur in cases of neutral releases at orbital velocities. It was found that with the considered amount of released material clouds from thruster firing stay behind the spacecraft. However, higher dumping rates might result in clouds that follow the spacecraft. It was demonstrated that the ambient O^+ forms *depletion* and *enhancement* regions. Chemistry and transport determines the evolution of the ionospheric "hole". The strength of the hole was found to depend on the direction of the thruster firing and the altitude. The electron density showed also the formation of density perturbation, i.e., *"image" clouds*. Both enhancement and depletions in the plasma density were predicted. Due to the mapping of the electric field the induced drift showed the formation of "image" clouds in other ionospheric layers far from the location of the spacecraft. The velocity of the species was found to be spatially non-uniform. The transverse drifts were in general smaller than the parallel. However, in releases at orbital speeds the velocities of the species became large and comparable to the orbital.

Special attention was placed in the evaluation of the radiation emission within the plasma cloud. The emissions from a water cloud are expected to be in the ultraviolet band. The height integrated intensity was evaluated. It was found that the intensity of the plume reduces with altitude and was in the order of hundred of Rayleighs. Massive (in the order of a few kilograms) releases were found to have intensities in the order of kR's.

Comparisons of the model predictions with respect to various plasma parameters were found to be in good agreement with experimental data taken during Shuttle missions. This suggests that the model can be used to provide users with an estimate of the conditions that are anticipated to occur around a spacecraft during specific operations.

8.2 Recommendations for Spacecraft Operations

The model developed in this work can be used as a prediction tool for the large scale induced environment. It should also be used as an indication of important effects that must be included in detailed evaluation of the induced environment/spacecraft interactions. There are several recommendations with respect to the environment that can be drawn based on the general conclusions of the analysis performed:

- The spacecraft will be surrounded by a large area where significant amounts of contaminant ions will be present. The ambient neutral, ion and electron density will be greatly perturbed with the appearance of enhancement and depletion regions.

- The perturbed plasma environment suggests that a spacecraft with the potential of releasing neutrals and/or plasma into the ionosphere, will not be a friendly platform for ambient plasma observations.

- The design of experiments, the location of probes and instruments should be based on the prior knowledge of contaminant producing activities.

- The perturbed plasma and neutral environment will interact with power systems, such as exposed high voltage lines and solar arrays. It still remains to determine the nature and the degree of such interactions.

- Deposition of contaminants on surfaces should be expected to increase. In several occasions, ambient and contaminant ions increase their residence time in the vicinity of the spacecraft. The direction of the streaming ions will be greatly modified with respect to the orbital so that the deposition and contamination of surfaces other that those in the ram direction should be expected.

- Charging of spacecraft surfaces should be examined with plasma parameters taken from the induced rather than the ambient environment.

- The wave environment will be significantly enhanced due to instabilities driven within the plasma cloud.

- Significant radiation is expected in the vicinity of the spacecraft. Radiation might be in the IR, UV or optical band depending upon the type of the released material.

- Extra Vehicular Activities (EVA) should be confined to periods where there are not significant thruster activities, or should be performed under closely monitored conditions.

- Releases at orbital speeds, like outgassing, present the worst scenario for contamination. It is thus required that measures should be taken in order to minimize the amount of outgassing.

- Liquids from power supply and life support systems should be disposed in a propulsive mode rather than simply vented from the vehicle.

8.3 Recommendations for Further Research

Improvements - Application of the Current Model

- Extend the range of parameters: Study releases with the use of specific parameters with respect to the type of release, flow rate, amount of released material, latitude, and altitude.

- Neutral Flow Model: Couple the plasma model developed here with more elaborate neutral flow models. This will allow the study of long duration thruster firing.

- Numerical Improvements: Most of the computational time in the current model is spent in the solution of the elliptic equation for the electrostatic potential. Application of a multi-grid technique or other accelerating method which could reduce the computational time is necessary in order to extend the parameter range of the applications.

- Study instabilities: There is a number of important instabilities that could be studied with the use of our model, such as the $\mathbf{E} \times \mathbf{B}$ drift instability and the gravitational drift instability.

- Chemical Release Experiments: Study the evolution of plasma clouds resulting from chemical release experiments, such as the CRRES campaign currently under way. Since our model is the first to account for a realistic altitude ionosphere, it could be used in the assistance and interpretation of data during active experiments. The model could be further enhanced with the application of boundary conditions which take into account ambient fields and neutral winds. These capabilities are included in the current model.

- Ambient Ionospheric Plasma Physics: Study a number of ambient plasma transport phenomena and instabilities. This would require a modification of the applied boundary conditions.

Directions for Further Research

- Develop the theory of plasma transport with the unsteady and inertia terms included in the momentum equations. This would allow us to model rapid plasma expansion phenomena and also extend the altitude range of applications.

- Develop the theory of the electrodynamic interactions in the induced plasma environment in length scales of the order of the spacecraft. This would require inclusion of those interactions due to the geometry of the spacecraft. A possible candidate would be a combination of fluid-particle codes with inclusion of collisional effects.

- Develop the theory of the waves associated with the moving spacecraft-plasma cloud system in a consistent way.

Appendix A

Description of the Computer Code

A.1 Flow Chart of the Code

We begin with the flow chart of the computer code. Given the initial conditions and the distributions $n_{r^+}(\mathbf{r},t)$, $n_{a^+}(\mathbf{r},t)$, $n_r(\mathbf{r},t)$, $n_a(\mathbf{r},t)$ of plasma species at $t = t_o$ we solve for the electric fields. We then evaluate the species velocities and time advance the continuity equations. With the density distributions at $t = t_o + \Delta t$ known we continue the loop until the specified time of interest, $T = n\Delta t$. The equilibrium ambient electric fields are computed with a similar loop, given the distributions of the ambient species.

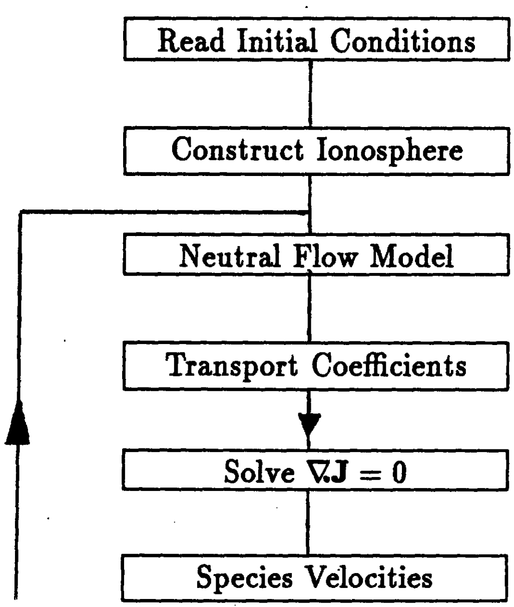

Solve continuity equations

A.2 Functional Description of Subroutines

The calls to the subroutines that appear in the main program CLOUD3D are described below. The function of each subroutine are presented in the boxes.

Read Initial Conditions

SGRIDGEN	Generate Grid
SETDEN	Set up Initial Density Profiles

Neutral Flow model

SCOLRAT	Calculate Collision rates
SCOLFRE	Calculate Collision frequencies
SPEDHALL	Calculate Pedersen,Hall,Parallel Parameters
SDIFFUS	Calculate Diffusion Coefficients
STRANSP	Calculate Mobility Coefficients
SCONDUCT	Calculate Conductivities
SNEWINDC	Calculate Neutral Wind Transport Coeffs
SGRAVITC	Calculate Gravity Transport Coeffs
SAPLELEF	Calculate Applied Electric Field

SSUDUVDF	Calculate Divergence of Diffusion Currents
SSUDIVDF	Divergence of Diffusion Currents
SSUDIVNW	Calculate Divergence of Neutral Winds Currents
SDIVGRAV	Calculate Divergence of Gravity Currents
SDIVEEF	Calculate Divergence of Electric fields
SDIVFPOT	Calculate Divergence of Ambient Fields
SETMAT	Set up matrix equation
SOLVEMAT	Solve the matrix equation
SGETELEF	Evaluate Electric Fields
SVELION	Evaluate Ion, Electron Velocities
SINERTIA	Evaluate Inertia Correction
SCONTIN	Solve Continuity Equations a^+,r^+

There is an additional number of subroutines which are called within the listed subroutines above. Their names and function is as follows:

VECPROD	Evaluate $\mathbf{A} \times \mathbf{B}$
GETDFD	Evaluate the derivatives $\frac{df}{dx}$
DIVMAT	Evaluate $\nabla \cdot \left[[A]\frac{\partial f}{\partial \mathbf{x}}\right]$

SMATVEC	$\mathbf{C} = [A]\mathbf{B}$
GETMAX	Evaluate the maximum of A_{ijk}
SGETCELL	Evaluate cell centered values
SETBOUND	Set up the boundary conditions for potential
LOWF	Low order method for FCT
HIGHF	High order method for FCT
FLIM3D	3D-FCT limiter
GBCOND	Set up boundary conditions for continuity

Bibliography

[1] G.H. Golub abd C.F. Van Loan. *Matrix Computations*. The Johns Hopkins University Press, Baltimore, 1989.

[2] D. N. Anderson and P. A. Bernhardt. Modeling the effects of an H_2 gas release on the equatorial ionosphere. *J. Geophys. Res.*, 83:4777, 1978.

[3] Pongratz M. B. Large scientific releases. *Adv. Space Res.*, 1:253–273, 1981.

[4] P. Banks. Collision frequencies and energy transfer: Electrons. *Planet. Space Sci*, 14:1085, 1968.

[5] P. Banks. Collision frequencies and energy transfer: Ions. *Planet. Space Sci*, 14:1104, 1968.

[6] H. R. Baum. The interaction of a transient exhaust plume with a rarefied atmosphere. *J. Fluid Mech.*, 58:795, 1973.

[7] D.C. Baxter and L.M. Linson. Dynamics of gas clouds released at satellite orbital velocity. *Progr. Astonaut. Aeronaut.*, 51:177, 1977.

[8] P. A. Bernhardt. High-altitude gas release: Transition from collisionless flow to diffusive flow in a nonuniform atmosphere. *J. Geophys. Res.*, 84:4341, 1979.

[9] P. A. Bernhardt. Three-dimensional, time-dependent modeling of neutral gas diffusion in a nonuniform chemically reactive atmosphere. *J. Geophys. Res.*, 84:793, 1979.

[10] P. A. Bernhardt. A critical comparison of ionospheric depletion chemicals. *J. Geophys. Res.*, 92:4617–4628, 1987.

[11] P. A. Bernhardt, B.A. Kashiwa, C.A. Tepley, and S.T. Noble. Spacelab 2 upper atmospheric modification experiment over Arecibo,1, neutral gas dynamics. *Astrophys. Lett and Comm.*, 1988.

[12] P. A. Bernhardt, W.E Swartz, M.C Kelley, M.P Sulzer, and S. T. Noble. Spacelab 2 upper atmospheric modification experiment over Arecibo, 2, plasma dynamics. *Astrophys. Lett and Comm.*, 1988.

[13] G. Bienkowski. Collisionless expansion of gas clouds in the presence of an ambient gas. *Phys. FLuids*, 7:382, 1964.

[14] J. A. Bittencourt. *Fundamentals of plasma physics.* Pergamon Press, 1986.

[15] R. C. Bolden and N. D. Twiddy. A flowing afterglow study of water vapor. *Faraday Disc. Chem. Soc.*, 53:192, 1972.

[16] D. L. Book, J. P. Boris, and K. Hain. Flux Corrected Transport. II. Generalization of the method. *J. Comput. Phys.*, 18:248–283, 1975.

[17] J. P. Boris and D. L. Book. Flux Corrected Transport. I.SHASTA, A fluid algorithm that works. *J. Comput. Phys.*, 11:38–69, 1973.

[18] J. P. Boris and D. L. Book. Flux Corrected Transport. II. Minimal-error FCT algorithms. *J. Comput. Phys.*, 20:397–431, 1976.

[19] H.L. Brode and J.E. Enstrom. Analysis of gas expansion in a rarefied atmosphere. *Phys. FLuids*, 16:1913, 1973.

[20] J.W. Brook and B.B. Hamel. Spherical source flow with finite back pressure. *Phys. FLuids*, 15:1898, 1972.

[21] G. E. Caledonia, J. C. Person, and D. E. Hastings. The interpretation of Space Shuttle measurements of ionic species. *J. Geophys. Res.*, 92:273–281, 1987.

[22] G. R. Carignan and E. M. Miller. Induced environment contaminant monitor: Gaseous constituents. *NASA-TM-82524*, pages 87–101, 1983.

[23] G. W. Castellan. *Physical Chemistry.* Addison Wesley, 1971.

[24] A. Dalgarno, M. R. McDowell, and Williams A. The mobilities of ions in unlike gases. *Proc. R. Soc.*, A250:411, 1958.

[25] J. H. Doles, N. J. Zabusky, and F. W. Perkins. Deformation and striation of plasma clouds in the ionosphere , 3. Numerical simulations of a multilevel model with recombination chemistry. *J. Geophys. Res.*, 81:5987, 1976.

[26] J. F. Drake, M. Mulbrandon, and J. D. Huba. Three-dimensional equilibrium and stability of ionospheric plasma clouds. *Phys. Fluids*, 31:3412, 1988.

[27] J. W. Dungey. The influence of the geomagnetic field on turbulence in the ionosphere. *J. Atmosph. Terr. Phys.*, 8:39–42, 1956.

[28] J. V. Eccles, W. J. Raitt, and P. M. Banks. A numerical model of the electrodynamics of plasma within the contaminant gas cloud of the Space Shuttle Orbiter at LEO. *J. Geophys. Res.*, 91:9049–9063, 1989.

[29] H. K. F. Ehlers, S. Jacobs, L. J. Leger, and E. Miller. Space Shuttle contamination measurements from flights STS-1 through STS-4. *J. Spacecraft and Rockets*, 21:301, 1984.

[30] D. T. Farley. A theory of electrostatic fields in a horizontally stratified ionosphere subject to a vertical magnetic field. *J. Geophys. Res.*, 64:1225, 1959.

[31] J. M. Forbes and M. Mendillo. Diffusion aspects of ionospheric modificatin by the release of highly reactive molecules into the F–region. *J. Atmos. Terr. Phys.*, 38:1299–1307, 1976.

[32] N.C. Freeman and R.E. Grundy. Solutions of the Boltzmann equation in an unsteady cylindrically symmetric expansion. *J. Fluid Mech.*, 31:723, 1968.

[33] N. A. Gatsonis. Theory and numerical analysis of plasma clouds surrounding space systems in low earth orbit. Master's thesis, Mass. Inst. of Technol., Cambridge, 1987.

[34] N. A. Gatsonis and D. E. Hastings. A three-dimensional model and initial time numerical simulation for an artificial plasma cloud in the ionosphere. *J. Geophys. Res.*, 96:7623, 1991.

[35] N. A. Gatsonis and D.E. Hastings. A three-dimensional model for an artificial plasma cloud about a spacecraft in Low Earth Orbit. 1990. AIAA 90-0638.

[36] R.A. Gentry, R.E. Martin, and B.J. Daly. An Eulerian differencing method for unsteady compressible flow problems. *J. Comput. Phys.*, 1, 1966.

[37] J.A. George and J.W. Liu. *Computer Solution of Large Sparse Positive Definite Systems.* Prendice-Hall, Englewood Cliffs, N.J., 1981.

[38] C. K. Goertz. Io's interaction with the plasma torus. *J. Geophys. Res.*, 85:2949–2956, 1980.

[39] C. K. Goertz and R. W. Boswell. Magnetosphere-ionosphere coupling. *J. Geophys. Res.*, 84:7239, 1979.

[40] S. R. Goldman, S.L. Ossakow, and D. L. Book. On the nonlinear motion of a small barium cloud in the ionosphere. *J. Geophys. Res.*, 79:1471, 1974.

[41] J. M. Grebowsky, H. A. Taylor, and M. W. Pharo. Thermal ion perturbations observed in the vicinity of the Space Shuttle. *Planet. Space Sci.*, 35:501–513, 1987.

[42] D. A. Gurnett, W. S. Kurth, and J. T. Steinberg. Plasma wave turbulence around the Shuttle: Results from the Spacelab 2 flight. *Geophys. Res. Lett.*, 15:760–7638, 1988.

[43] G. Haerendel, R. Lust, and E. Rieger. Motion of artificial ion clouds in the upper atmosphere. *Planet. Space Sci.*, 15:1–18, 1967.

[44] L.A. Hageman and D.M. Young. *Applied Iterative Methods.* Academic Press, New York., 1981.

[45] D. E. Hastings and N. A. Gatsonis. The motion of contaminant water plasma clouds about large active space structures. *J. Geophys. Res.*, 94:961, 1989.

[46] D. E. Hastings, N. A. Gatsonis, and T. Mogstad. A simple model for the initial phase of a water plasma cloud about a large structure in space. *J. Geophys. Res.*, 93:1961–1973, 1988.

[47] A. E. Hedin. MSIS-86 thermospheric model. *J. Geophys. Res.*, 92:4649, 1987.

[48] R. A. Heelis, J. F. Vickrey, and N. B. Walker. Magnetic field-aligned coupling effects on ionospheric plasma structure. *J. Geophys. Res.*, 95:7995–8008, 1990.

[49] M.R. Hestenes and E. Stiefel. Methods of conjugate gradients for solving linear systems. *Nat. Bur. Standards J. Res.*, 49:409–436, 1952.

[50] C. W. Hirt. Heuristic stability theory for finite-difference equations. *J. Comput. Phys.*, 2:339–355, 1968.

[51] D. E. Hunton and J. M. Calo. Gas phase interactions in the Shuttle environment. In *AIAA Shuttle Environment and Operations II Conference*, 1985. AIAA 85-6055.

[52] D.E Hunton and W. Swider. Variations of water vapor concentration in the Shuttle environment. *J. Spacecraft and Rockets*, 25:139–145, 1988.

[53] Y. Itikawa. Electrons-atom momentum transfer cross sections. *At. Data Nuclear Data Tab.*, 21:69, 1978.

[54] M. C. Kelley. *The earth's ionosphere.* Academic Press, 1989.

[55] D.S. Kershaw. The incomplete Cholesky-Conjugate gradient method for the iterative solution of systems of linear equations. *J. Comput. Phys.*, 26:43–65, 1978.

[56] Y. Kurihara. On the use of implicit and iterative methods for the time integration of the wave equation. *Monthly Weather Review*, 93:33–46, 1965.

[57] W. S. Kurth and L. A. Frank. Spacelab 2 Plasma Diagnostics Package. *J. Spacecraft and Rockets*, 27:70, 1990.

[58] P. Lax. Weak solutions of nonlinear hyperbolic equations and their numerical computation. *Communications on Pure and Applied Mathematics*, XIII, 1960.

[59] L. M. Linson and J. B. Workman. Formation of striations in ionospheric plasma clouds. *J. Geophys. Res.*, 75:3211, 1970.

[60] K. H Lloyd and G. Haerendel. Numerical modeling of the drift and deformation of ionospheric plasma clouds and their interaction with other layers of the ionosphere. *J. Geophys. Res.*, 78:7389, 1973.

[61] R. Lohner, K. Morgan, J. Peraire, and M. Vahdati. Finite element Flux-Corrected Transport (FEM-FCT) for the Euler and Navier-Stokes equations. *Intern. J. Numer. Meth. Fluids*, 7:1093–1109, 1987.

[62] T.Z. Ma and R.W. Schunk. Plasma cloud expansion in the ionosphere: Three-dimensional simulation. *J. Geophys. Res.*, 96:5793–5810, 1991.

[63] A. J. Mallinckrodt and C. W. Carlson. Relations between transverse electric fields and field-aligned currents. *J. Geophys. Res.*, 83:1426–1432, 1978.

[64] B. E. Mcdonald, M. J. Keskinen, S. L. Ossakow, and S. T. Zalesak. Computer simulation of gradient dirift instability processes in operation Avefria. *J. Geophys. Res.*, 85:2143–2154, 1980.

[65] M. Mendillo and J. M. Forbes. Artificially created holes in the ionosphere. *J. Geophys. Res.*, 83:151, 1978.

[66] M. Mendillo, G.S Hawkins, and J.A Klobuchar. A sudden vanishing of the ionospheric F region due to the launch of Skylab. *J. Geophys. Res.*, 80:2217, 1975.

[67] H. G. Mitchell, J. A. Fedder, J. D. Huba, and S. T. Zalesak. Transverse motion of high–speed barium clouds in the ionosphere. *J. Geophys. Res.*, 90:11091–11095, 1985.

[68] H. G Mitchell, J. A. Fedder, M.J Keskinen, and S. T. Zalesak. A simulation of high-latitude F-layer instabilities in the presence of magnetosphere-ionosphere coupling. *J. Geophys. Res.*, 12:283–286, 1985.

[69] J. A. Mitchell and J. W. McGowan. Experimental studies of electron-ion recombination. In F. Brouillard and J.W McGowan, editors, *Physics of Ion-Ion and Electron-Ion Collisions.* Plenum, New York, 1983.

[70] T.S. Mogstad. Stability theory of plasma clouds about large space vehicles. Master's thesis, Massachusetts Institute of Technology, 1987.

[71] E. Murad and S. T. Lai. Effect of dissociative electron–ion recombination on the propagation of critical ionization discharges. *J. Geophys. Res.*, 91:13745–13749, 1986.

[72] G. Murphy, J. Pickett, N. D'angelo, and W. S. Kurth. Measurements of the plasma parameters in the vicinity of the Space Shuttle. *Planet. Space Sci.*, 34:993–1004, 1986.

[73] G. F. Nalesso and A. R. Jacobson. Shaping of an ion cloud's velocity field by differential breaking due to Alfvén wave dissipation in the ionosphere. *J. Geophys. Res.*, 93:5794, 1988.

[74] R. Narcisi, E. Trzcinski, G. Federico, L. Wlodyke, and D. Delorey. The gaseous environment about the Space Shuttle. *AIAA 83–2659*, 1984.

[75] F. M. Neubauer. Nonlinear standing Alfvén wave current system at Io: Theory. *J. Geophys. Res.*, 85:1171–1178, 1980.

[76] J. Ortega. *Numerical Analysis :A Second Course.* Academic Press, New York, 1972.

[77] F. W. Perkins. Spread F and ionospheric currents. *J. Geophys. Res.*, 78:218, 1973.

[78] F. W. Perkins, N. J. Zabusky, and J. H. Doles. Deformation and striation of plasma clouds in the ionosphere, 1. *J. Geophys. Res.*, 78:697–709, 1973.

[79] J. S. Pickett, G. B. Murphy, W. S. Kurth, C. K. Goertz, and S. D. Shawhan. Effects of chemical releases by the STS 3 orbiter on the ionosphere. *J. Geophys. Res.*, 90:3487–3497, 1985.

[80] M.I. Pudovkin, A.M. Lyatskaya, and I.V. Golovchanskaya. The influence of ionization and recombination processes on the dynamic of ionospheric plasma clouds. *J. Atmos. Terr. Phys.*, 49:1049–1057, 1987.

[81] W. J. Raitt, D. E. Siskind, P. M. Banks, and P. R. Williamson. Measurements of the thermal plasma environment of the Space Shuttle. *Planet. Space Sci.*, 32:457–467, 1984.

[82] K. Rawer and P.A. Bradley, editors. *International Reference Ionosphere -Status 1986/87*, volume 7 (6) of *Adv. Space Res.* 1987.

[83] D. L. Reasoner, S. D. Shawhan, and G. Murphy. Plasma Diagnostics Package measurements of ionospheric ions and Shuttle–induced perturbations. *J. Geophys. Res.*, 91:13463–13471, 1986.

[84] H. Risbeth and O. K. Garriott. *Introduction to Ionospheric Physics*. Academic Press, New York, 1969.

[85] P. J. Roach. *Computational Fluid Dynamics*. Hermosa Publishers, 1976.

[86] Y. Saad and M.H. Shultz. Gmres: A generalized minimal residual algorithm for solving nonsymmetric linear systems. *SIAM J. Sci. Stat. Comput.*, 5:203, 1984.

[87] J. Sanmartin. Theory of a probe in a strong magnetic field. *Phys. Fluids*, 13:103, 1970.

[88] A.J. Scannapieco, S.L. Ossakow, D.L Book, B.E McDonald, and S.R. Goldman. Conductivity ratio effects on the drift and deformation of F region barium clouds coupled to the E region ionosphere. *J. Geophys. Res.*, 79:2913, 1974.

[89] M. Scholer. On the motion of artificial ion clouds in the magnetosphere. *Planet. Space Sci.*, 18:997–1004, 1970.

[90] R. W. Schunk and A. F. Nagy. Electron temperatures in the F region of the ionosphere: Theory and observations. *Rev. Geophys. Space Phys.*, 16:355, 1978.

[91] S. D. Shawhan, G. Murphy, and J. S. Pickett. Plasma Diagnostics Package initial assessment of the Shuttle Orbiter plasma environment. *J. Spacecraft and Rockets*, 21:387, 1984.

[92] A. Simon. Growth and stability of artificial ion clouds in the ionosphere. *J. Geophys. Res.*, 75:6287, 1970.

[93] D. J. Simons, M. B. Pongratz, and S. P. Garry. Prompt striations in ionospheric Barium clouds due to a velocity space instability. *J. Geophys. Res.*, 85:671–677, 1980.

[94] D. E. Siskind, W. J. Raitt, P. M. Banks, and P. R. Williamson. Interactions between the orbiting Space Shuttle and the ionosphere. *Plan. Space Sci.*, 7:881–896, 1984.

[95] J. L. Sperling. Ion–Pedersen drift and parallel electric field effect on plasma jetting. *J. Geophys. Res.*, 88:7095–7106, 1983.

[96] N. H. Stone, U. Samir, K. H. Wright, D. L. Reasoner, and S. D. Shawhan. Multiple ion streams in the near vicinity of the Space Shuttle. *Geophysical Research Letters*, 10:1215–1218, 1983.

[97] B. A. Trubnikov. Particle interactions in a fully ionized plasma. In *Reviews of Plasma Physics*. Consultants Bureau, 1965.

[98] R.S. Varga. *Matrix Iterative Analysis.* Prendice-Hall, Englewood Cliffs, N.J., 1981.

[99] H. J. Volk and G. Haerendel. Striations in ionospheric ion clouds, 1. *J. Geophys. Res.*, 76:4541, 1971.

[100] S.P. Voskoboynikov, V.A. Rozhansky, and L.D. Tsendin. Numerical modeling of three-dimensional plasma clouds evolution in crossed $\vec{E} \times \vec{B}$ fields. *Planet. Space Sci.*, 35:835–844, 1987.

[101] E. Wulf and U. Von Zahn. The Shuttle environment: Effects of thruster firings on gas density and composition in the payload bay. *J. Geophys. Res.*, 91:3270–3278, 1986.

[102] A. W. Yau, B. A. Whalen, F. R. Harris, R. L Gattinger, M. B. Pongratz, and P.A. Bernhardt. Simulations and observations of plasma depletion, ion composition and airglow emissions in two auroral ionospheric depletion experiments. *J. Geophys. Res.*, 90:8387, 1985.

[103] N. J. Zabusky and J. H. Doles. The effects of artificially boundary conditions on numerical simulations of the instability and evolution of barium clouds. *J. Geophys. Res.*, 80:1849, 1975.

[104] N. J. Zabusky, J. H. Doles, and F. W. Perkins. Deformation and striation of plasma clouds in the ionosphere , 2. Numerical simulation of a nonlinear two–dimensional model. *J. Geophys. Res.*, 78:711–724, 1973.

[105] S. T. Zalesak. Fully multidimensional Flux Corrected Transport algorithms for fluids. *J. Comput. Phys.*, 31:335–362, 1979.

[106] S. T. Zalesak. A physical interpretation of the Richtmeyer two–step Lax–Wendroff scheme and its generalization to higher spatial order. In edited by R. Vichnevetsky and R. S. Stepleman, editors, *Advances in Computer Methods for Partial Differential Equations.* Imacs, 1984.

[107] S. T. Zalesak. Very high order and pseudospectral Flux Corrected Transport (FCT) algorithms for conservation laws. In R. Vichnevetsky and R. S. Stepleman, editors, *Advances in Computer Methods for Partial Differential Equations*. Imacs, 1984.

[108] S. T. Zalesak, P. K. Chaturvedi, S. L. Ossakow, and J. A. Fedder. Finite temperature effects on the evolution of ionospheric barium clouds in the presence of a conducting background ionosphere. *J. Geophys. Res.*, 90:4299–4310, 1985.

[109] S. T. Zalesak, J.F. Drake, and J.D. Huba. Dynamics of three-dimensional ionospheric plasma clouds. *Radio Science*, 23:591–598, 1988.

[110] S. T. Zalesak, J.F. Drake, and J.D. Huba. Three-dimensional simulation study of ionospheric plasma clouds. *Geoph. Res. Lett.*, 17:1597–1600, 1990.

[111] S. T. Zalesak, J.A. Fedder, and S. L. Ossakow. Analysis and numerical simulation of the effect of ion Pedersen mobility on ionospheric barium clouds. *J. Geophys. Res.*, 88:8003, 1983.

[112] S. T. Zalesak and S. L. Ossakow. Nonlinear equatorial spread F: Spatially large bubbles resulting from large horizontal scale initial perturbations. *J. Geophys. Res.*, 85:2131–2142, 1980.

[113] S. T. Zalesak, S. L. Ossakow, and P. K. Chaturvedi. Nonlinear equatorial spread F: The effect of neutral winds and background Pedersen conductivity. *J. Geophys. Res.*, 87:151, 1982.

[114] A.P. Zhilinskii and L.D. Tsendin. Collisional diffusion of a partially-ionized plasma in a magnetic field. *Sov. Phys. Usp*, 23:331, 1980.